July 2020

# Solvation Structures and Dynamics of Small Molecules: Experimental and Computational Studies Using Carbonyl Vibrational Modes as Probe

Xiaoliu Zhang
*Louisiana State University and Agricultural and Mechanical College*

# SOLVATION STRUCTURES AND DYNAMICS OF SMALL MOLECULES: EXPERIMENTAL AND COMPUTATIONAL STUDIES USING CARBONYL VIBRATIONAL MODES AS PROBE

A Dissertation

Submitted to the Graduate Faculty of the
Louisiana State University and
Agricultural and Mechanical College
in partial fulfillment of the
requirements for the degree of
Doctor of Philosophy

in

The Department of Chemistry

by
Xiaoliu Zhang
B.S., University of Science and Technology of China, 2014
August 2020

# ACKNOWLEDGEMENTS

I thank and acknowledge my advisor Dr. Daniel G. Kuroda. This dissertation would not have been possible without the help, support, patience and encouragement from him, not to mention his advice, knowledge, and expertise. He set a perfect example for me of being a scientist with his enthuiasm on science, his insistence on searching for the physically intuitive explanation, and his passion on learning things from other fields.

I would like to thank my committee members, Dr. Les Butler, Dr. Megan Macnaughtan, and Dr. Denise DeLorme, for their support and help.

I would like to send my special thanks of gratitude to Dr. Revati Kumar for her help and advice in the computational study.

I would like to thank my group members. I am grateful to Jeramie Rushing and Xiaobing Chen, for reviewing the manuscript in spite of their busy schedule. I thank Susith Kankanamge, who has great lab practical skills and a deep understanding of the theory. I would like to thank him for the help and advice he gave to me, and the warmth and happiness he brought into the office. I express my thanks to Dr. Kristen Fulfer, Dr. Yaowen Cui, and Dr. Habtom Gobeze, for helping me in my study, work, and life. I thank Ernest Nachaki and Rasidah Ali for all the help I receive from them. It has been a great time to work with you all.

I sent my gratitude to my parents, for their support, both emotional and financial, over the years.

At last but not least gratitude goes to all my friends who helped me to complete this project.

# TABLE OF CONTENTS

# ABSTRACT

Solutions are ubiquitous in both the global environment and the human body, and play a significant role in scientific research and industrial production. The structures and dynamics of solutions have been studied for centuries. However, conventional experimental methods, whose intrinsic measuring time is on the order of nanoseconds to microseconds, could not detect the fast dynamics taking place in the solution on the timescale of femto- and pico-second. In this dissertation, the ultrafast two-dimensional infrared (2DIR) spectroscopy was applied to characterize the structure and dynamics in three different types of solutions on the sub-picosecond timescale. Linear Fourier transform infrared spectroscopy (FTIR) and computational calculations were performed to confirm the interpretation of the microscopic framework. Firstly, the ion effect on water structural dynamic properties at high concentration was studied by looking into the solvation shell of acetate ion in $D_2O$ and in 6M NaCl solution. The FTIR lineshape of the carboxylate asymmetric mode and a dynamics component extracted from 2DIR is not affected by the highly concentrated salts, which is proved to be a particularity of the acetate ion by a comparative study on the azide ion. *Ab initio* molecular dynamics (AIMD) simulations confirmed the experimental observations and linked the observed vibrational phenomenon to the thermal rotation of acetate methyl group (—CH3). Secondly, ion solvation structure and dynamics in organic solvents were investigated. By AIMD and *ab initio* umbrella sampling (AIUS), the structure and dynamics of the lithium solvation shell in cyclic and in linear carbonates were compared. The intercalation of entire molecules into the first solvation shell of lithium is found in cyclic carbonate, which leads to a more rigid and more organized solvation structure in cyclic carbonate. Finally, a conductive neutral molecular mixture of acetic acid (HAc) and N-methylimidazole (C1Im) was characterized by both experimental and theoretical methods. The

broadband peaks in FTIR was assigned as delocalized proton stretching mode in HAc-C1Im complexes. AIMD simulation, DFT calculation, and NMR measurements confirmed the existence of proton delocalization in the hydrogen bond between HAc and C1Im.

# CHAPTER 1
# INTRODUCTION

## 1.1. Background

Solutions are ubiquitous in both the environment and the human body. The ocean, which covers more than 70% of the earth's surface, is one of the most common aqueous salt solutions.[1] This large expanse of briny water has a salinity of around 35 parts per thousand on average, and the ions in seawater, *e.g.*, chloride, sodium, magnesium, calcium, and organic carbon ions, maintain a similar proportion to each other even if the salinity is different.[2] The ocean not only nourishes the marine organisms and affects them via osmosis, temperature, and pH,[3-9] but also influences the climate, weather, and air quality of the whole biosphere via the interaction between the ocean and the atmosphere.[10, 11] For example, oceanic $CO_2$ storage is estimated to be 39000 gigatons C, which is 5 times as much as that in the atmosphere. In the past 200 years, the ocean has been absorbing 38% of anthropogenic emission of $CO_2$, decreasing the atmospheric $CO_2$ concentration, and slowing climate warming.[12, 13]

In the human body, most biological processes take place in solutions. The human adult body is composed of up to 60% water by weight, which exists both in the living cells as the intracellular fluid and out of the living cells as the extracellular fluid, maintaining a stable environment with relatively constant pH, osmosis, *et cetera,* for the metabolisms taking place.[14, 15] Moreover, solutions are also indispensable for transferring nutrients, oxygen, carbon dioxide, and waste. By investigating the solution structure and dynamics (*e.g.*, protein folding and ion transport), we can gain a better understanding of biological processes such as digestion, nerve impulse, and blood properties.[16-18]

Solution chemistry also plays an important role in scientific research, as well as in industrial production. The applications include organic synthesis, enzyme catalysis, new battery production, and drug delivery. The significance of solutions is the result of the high chemical reaction rate in solution. The liquid phase, because of its fast diffusion constant compared with the solid phase and its high particle density compared with the gas phase, therefore results in a high particle collision rate, making solutions the most favored medium for chemical processes in nature, daily life, industry, and research. Moreover, the solvent may affect the reactivity by influencing the enthalpy and entropy of the transition state. In particular, the speed of the reaction can change by orders of magnitude when the solvent is changed.[19] The mechanism on how the reaction rate is influenced by the solvents is still being investigated.[20-23] To understand the origin of life, the process of metabolism, the changing of the global environment, and to improve the industrial production as well, solution properties have been widely investigated in the last century.

Experimental methods such as NMR, X-ray scattering, and Raman scattering have been applied to obtain the solvation structure of either ions or protein molecules, as well as the translational and orientational dynamics of solutes on the timescale slower than picosecond.[24-26] Motions on faster timescales are investigated mostly by molecular simulation, where the residence time of the solute, short-time dynamics of libration, and solvation free energy are calculated. Meanwhile, the solvation structures can be visualized via molecular simulation. [25, 27-29] However, the conventional experimental methodologies are not suitable to measure the fast dynamics in solution, since their intrinsic measuring time, which is on the order of nanoseconds to microseconds, is not compatible with the fast motions in the solution, which is usually on the timescale of femto- and picoseconds. Another problem is the conventional methods cannot distinguish the solvation shell dynamics from bulk dynamics.

The development of ultrafast femtosecond laser pulses and the application of ultrafast infrared spectroscopy allow scientists to measure solvation dynamics on the sub-picosecond timescale. The infrared region is investigated because it's on-resonance with the vibrational modes of chemical bonds, which have enough spatial resolution and time resolution for detecting solution processes. Vibrational infrared probes have been used to distinguish structure and dynamics in the solvation shell from the bulk solvent. A good probe is required to have a high signal intensity and high sensitivity to the local environment while introducing very few disturbances to the original system. Several vibrational infrared modes have been tested and proved to be good probes to study changes in the local environment, such as the nitrile stretching mode [30-37] and O-H stretching mode.[38-45] Carbonyl modes, including C=O stretching, COO symmetric stretching, and COO asymmetric stretching were also shown to be good solvation shell probes.[46-55] All of these carbonyl modes have a relatively high absorption coefficient, a sharp absorption peak in the frequency range which seldom overlaps with other highly intense absorption, and a good sensitivity to the local environment from nearby atoms to surrounding molecules, which makes these probes increasingly popular in the spectroscopic field.[54, 56-58]

In this dissertation, C=O vibrational modes were applied as a reliable probe to detect the solvation structure and dynamics of different kinds of solutions.

## 1.2. Previous studies

### 1.2.1. Aqueous salt solution

Water structure and dynamics have been widely investigated via computational simulation and experimental methods.[59-75] The dynamics of the hydrogen bond network has been found to occur over a range of time scales, where the slowest component is assigned to the randomization of the network through concerted hydrogen bond making and breaking rearrangements on the

timescale of 1.7 ps. On the other hand, the fastest component on the time scale of tens of femtosecond is interpreted in different ways, *e.g.*, diffusive changes in the O–H · · · O hydrogen-bond distance or inertial motion.[70, 76, 77] Noteworthy, the orientation relaxation at a time scale of 2.6 ps is also associated with hydrogen bond network rearrangement.[68, 70]

The addition of ions into water leads to dramatic changes in its structural and dynamical properties. Studies on this topic date back to more than 100 years, when Hofmeister proposed the Hofmeister series describing the effects of different salts on protein solubility.[78] Over the last few decades, the structure of the ion solvation shell, *e.g.*, coordination number, mean distances, and spatial configuration, has been revealed via numerous methodologies, including X-ray diffraction, neutron diffraction, EXAFS spectroscopy, XANES spectroscopy, Raman spectroscopy, infrared spectroscopy, NMR relaxation, dielectric relaxation, Rayleigh scattering, Brillouin scattering, and molecular dynamics.[24-26, 79] Most scientists believe that ions have influences on the water structure outside of the ion solvation shell. These long-range influences could be either enhancing ("structure-maker") or destroying ("structure-breaker") the tetrahedral structure of the water hydrogen bond network.[26] Although some researchers claimed that the long-range structuring due to the presence of ions does not exist,[80] the structure making and breaking effect of ions in water or biological systems is still being widely studied.[24, 81] In fact, dynamics of the aqueous salt solutions have been investigated for decades via NMR, Rayleigh scattering, *etc.* at timescales slower than a few picoseconds, until a breakthrough has been made in the past 40 years with the application of ultrafast spectroscopy technique, where the ultrafast aqueous solution dynamics on the timescale of pico- and femtoseconds are detected with ultrafast infrared laser pulses.[25, 59, 82-87] [88, 89]

Ion effects on water structure and dynamics properties and protein folding are concentration-dependent. At very low concentrations (< 0.1 M), electrostatics is dominant compared with specific ion effects. Almost all the studies focus on the intermediate concentration (0.1-2.0 M), where a large amount of solvation shell structures and bulk water exist simultaneously. However, the structural and dynamical properties of aqueous ion solutions at very high concentrations (> 2 M) are scarcely investigated, where all the water molecules are captured by an ion hydration shell, and all the ions "salt out" the proteins.[90]

To fill this gap, a system composed of sodium acetate ($CH_3COONa$) solvated by water with 6 M sodium chloride (NaCl) is investigated in this dissertation (Figure 1.1). The questions of significance remained now are: how does the hydration dynamics of an acetate ion in the vicinity of highly-concentrated salt ions differ from those in pure water; what is the structure of the acetate ion solvation shell; and how is the long-range structuring and interactions? Noticeable, the speciation of the acetate ion in the 6 M NaCl solution is of interest. Infrared and Raman study of the acetate ion in the C-C vibrational region revealed that the acetate forms contact ion pairs with neither sodium nor alkaline-earth ions.[91] A molecular simulation study explained the lack of ion pair formation by thermodynamics, herein the contact ion pair of acetate was found to be of entropic origin, while the solvent-shared ion pair was mainly enthalpically favorable.[92] Therefore, the molecular mechanism behind the lack of contact ion pair formation by the acetate ion is investigated here.

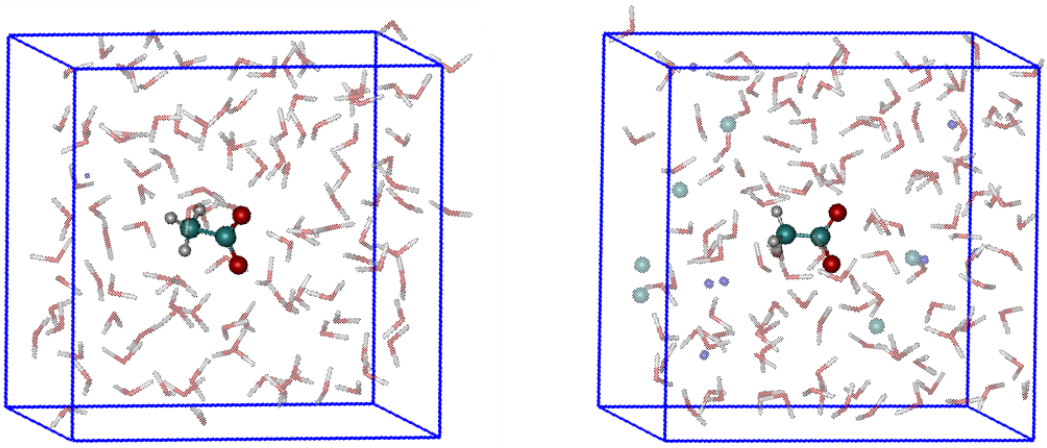

Figure 1.1. Acetate ion solvated in water (left), and acetate ion solvated in 6 M sodium chloride aqueous solution (right). Molecules shown in the ball-and-stick model are acetate ion; molecules in the licorice drawing method are water molecules. The dispersed green and blue balls represent Cl- and Na+ ions respectively.

### 1.2.2. Ions in organic solvent systems

Ions in organic solvent systems have attracted attention in the last few decades. One interest is the ion transfer from water to organic solvents, which is important in ion extraction, membrane transport, and electrode selectivity.[93-96] The Gibbs free energy profile and further structural properties of the process with either monoatomic ions such as F-, Cl-, and Li+, or polyatomic ions such as $Me_4N^+$, $SCN^-$, and $ClO_4^-$ have been obtained experimentally and theoretically.[97-109] These studies reveal the co-extraction of water molecules when transferring ions through the interface, which means the ions do not exist as bare ions in the organic solution but as ion water clusters. Solvation shell components of various ions are investigated, while interactions between ion and hydrated water; ion and the rest solvent molecules; along with hydration shell and organic solvents are demonstrated to be important in determining the solvation shell structural dynamics.

Another popular topic in organic solvents is the solvent effects on chemical reactions taking place in solution. Kinetics, production yield, and selectivity of reactions can be tuned by modifying

the organic solvents. It is found that the rate constant of $CH_3I$ and $Cl^-$ displacement reaction is increased by up to 6 orders of magnitude when changing the solvent from MeOH to DMF. Similar dramatic changes in reaction rate constants are observed in many other chemical reactions. [110] It is found that weak solvation of anion or cation reactants and strong solvation of activated complexes leads to a high reaction rate constant.[111] Solvent effects have also been observed on product yield of organic synthesis.[112] In addition, it was found that the choice of organic solvent has a remarkable effect on the stereoselectivity and enantioselectivity, enhancing the proportion of either *cis*- or *trans*-isomers, and controlling the product chirality in organic synthesis.[113, 114] Efforts have been made to understand the mechanism behind this organic solvent effect. Solute-solvent interactions and solute-solute interactions are investigated in different organic solvents, as a result, the importance of ion pairing was found.[115] The ions are divided into different categories: free ions (FI), solvent separated ion pairs (SSIP), contact ion pairs (CIP), and aggregates (AGG).[116-120] The formation of ion pairs is influenced by the polarity of the solvents. In polar solvents, SSIP and FI are energetically favored, while in nonpolar solvent, CIP is energetically favorable.[121] Ion pairs are believed to change the reaction path, where the CIP is believed to control the selectivity of the reaction.[111, 114]

One more typical example of metal-organic coordination systems is the lithium-ion battery (LIB). A commercial LIB is mainly composed of lithium-ion and linear and cyclic carbonates.[122] The interest in lithium-ion batteries comes from the growing global demand for portable energy storage devices, as well as the advantages of LIB such as low cost, high energy density, and no memory effect.[122-124] There are numerous studies focusing on improvement of the LIB performance, by investigating substitutes on: cation, *e.g.*, $Na^+$; anion, *e.g.*, $PF_6^-$, $AsF_6^-$,

$BF_4$-, and TFSI-; and organic solvents, *e.g.*, carbonates and ethers.[125] However, experimental and theoretical studies have produced conflicting results in structural and dynamical analysis.

The coordination number of lithium ions investigated by ultrafast spectroscopic studies, Raman, and FTIR spectroscopy, is found to be 4 in some studies, differing from 2 or 6 in other studies.[126-132] The controversies also appear in computational studies.[118, 133-148] The implications will be discussed further in chapter four.

The ionic speciation of lithium ions and its counterion in solutions of organic carbonates is also an unsolved problem.[117, 128, 132, 149] Formation of ion pairs and aggregation, wherein the solvent molecules do not solvate the solute completely, decreases the activity coefficient of free ions. Since free ions act as charge carriers in battery solution, the formation of ion pairs and aggregation leads to low conductivity and capacity of the lithium-ion battery. [150] Experimental studies using infrared spectroscopy have obtained different results on ion speciation. An ultrafast vibrational study on the orientational correlation time of C=O stretching mode demonstrated that all lithium ions form contact ion pairs (CIP) with common counterions, *i.e.,* PF6-, BF4-, and ClO4-, in a cyclic carbonate, *i.e.*, ethylene carbonate (EC), at concentrations higher than 0.5 M.[128] However, other studies using the same method focusing on the same vibrational mode pointed out that at those concentrations, the predominant ion species are FI and CIP in cyclic carbonate and FI and SSIP in linear carbonate.[117, 126] Similarly, computational calculations also showed inconsistencies. Classical MD indicated a large population of CIP existing in lithium hexaflourophosphate solutions of EC.[146] In contrast, the potential energy surface for the lithium tetrafluoroborate in EC at CAM-B3LYP/6-31G(d) level suggested that SSIPs are the most energetically favorable species.[143] Moreover, another study using the energy representation method for $LiBF_4$ and $LiPF_6$ in both propylene carbonate (PC) and dimethyl carbonate (DMC)

claimed that CIP is the most energetically favorable species irrespective of the dielectric constant of the carbonate.[147]

Debates also focus on the rate of the solvent exchange process. The mobility of lithium ion is a determining factor in battery performance since the ion mobility in solutions is much slower than the electron mobility in the wire as a charge carrier. Microscopic fluxional solvent exchange processes are important in understanding the macroscopic battery property of lithium ion mobility. The mobility of the lithium ion is mainly determined by the properties of the solvent molecules, which affects the diffusion of the lithium ion by the solvent-solute interactions and the solvent-solvent interactions.[122, 125] Although the solvent-solute interactions between the lithium ion and either the cyclic or linear carbonates have been investigated through the viewpoint of the equilibrium structure, still the picture of the solute-solvent dynamics is not clear.[132, 151-158] The competition between the entropically favored linear carbonates and the enthalpically favored cyclic carbonates demands the understanding of solvent exchange dynamics in different carbonate solutions.[159] In this case, ultrafast infrared spectroscopy has been applied for its sensitivity and time resolution. (See in Chapter 2) However, previous ultrafast spectroscopies resulted in controversies. Minhaeng Cho and his group predicted a fast solvent exchange between the lithium ion and linear carbonate in both single solvent and co-solvent systems. Here, both the formation and dissociation processes of Li+---carbonate complex is on the timescale of less than 5 ps.[129, 160] On the other hand, another study pointed out that the experimental signature assigned to solvent exchange arises from a vibrational energy transfer mechanism due to deformations of the solvation shell of the lithium ion.[126]

In this project, systems of $LiPF_6$ solvated in cyclic carbonate and linear carbonate (Figure 1.2) will be investigated by *ab initio* molecular dynamics and umbrella sampling to illustrate the coordination number, ion speciation, and solvent exchange rate in the solution.

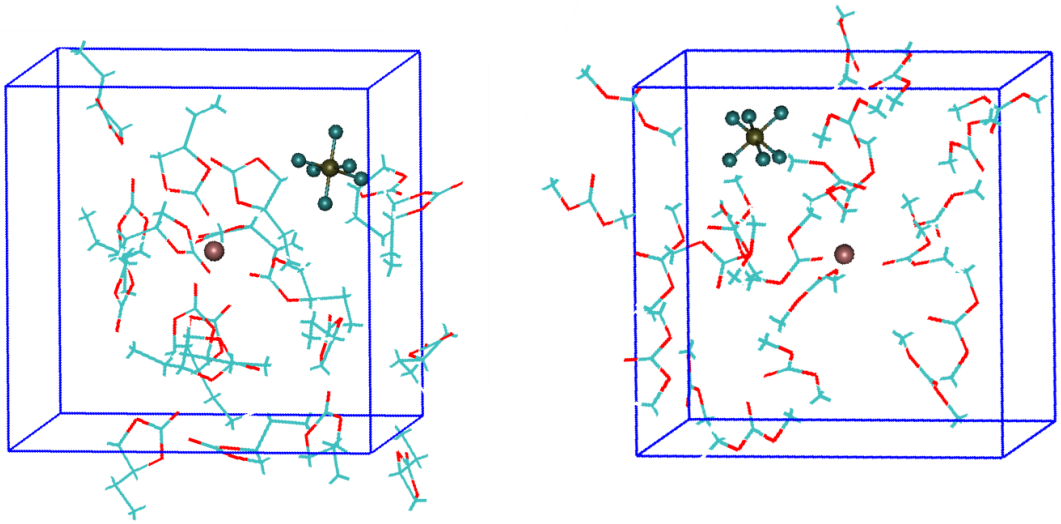

Figure 1.2. $LiPF_6$ solvated in cyclic (butylene carbonate, left), and linear (dimethyl carbonate, right) carbonates. The brown ball at the center of the box represents Li+, while the green balls in octahedron shape represent PF6- ion, and the carbonates are represented by lines.

### 1.2.3. Neutral molecular mixture

Liquid phase solutions can be simply divided into three categories: ions solvated by neutral molecules, mixtures of neutral species, and mixtures of ions, namely ionic liquids. Systems discussed in Section 1.2.1 and 1.2.2 are in the first category, and the second category will be introduced in this section. The study of a solution containing two neutral organic species appealed to an increasing number of scientists because of its unique conductivity behavior: the equimolar mixture of acetic acid (HAc) and N-methylimidazole ($C_1Im$) was found to have a conductivity 4 orders of magnitude higher than neat HAc and 2 orders of magnitude higher than $C_1Im$ (shown in Figure 1.3), while the mixture was found to be composed of only the electronically neutral molecular species.[161-166] The Grotthuss mechanism was then proposed to be the main mechanism for the conductive property of the neutral molecular mixture and was investigated by

both experiments and computational simulation,[165, 167] leading to a desire for understanding the microscopic structure of hydrogen-bond network, as well as the proton motions related to the conductivity behavior.

Regarding the solution structure, there is a debate about whether the system is composed of neutral molecules, acid and base ions, or the complexes formed by base and acid molecules. As mentioned before, the HAc and $C_1$Im mixture was found to have a conductivity 4 orders of magnitude higher than its neat acid and 2 orders of magnitude higher than its neat base, which is often related to a protic ionic liquid, especially when the system is composed of a Brønsted acid and a Brønsted base. This assumption is in agreement with previous NMR studies, where the ionicity of the equimolar mixture is found to be 92.8% by concentration-dependent NMR experiment, and both the proton transfer enthalpy and entropy are found to be -9.33 kJ/mol, and 11.29 $J\cdot(mol\cdot K)^{-1}$ respectively by temperature-dependent NMR studies.[168] However, Raman spectroscopy by Umebayashi group on the frequency range of C=C and C=O vibration absorption showed that electrically neutral molecular species predominantly exist in the equimolar mixture.[161] This result also agrees with the fact that ΔpKa value between HAc and $C_1$Im is as small as 2.4, which means the proton transfer is incomplete and the solution is characterized as a poor ionic liquid.[161, 169-171]

Meanwhile, the Umebayashi group calculated the energy difference between molecular complexes and their corresponding conjugated ion structures. The conjugated $[Ac]^-$ -- $[C_1hIm]^+$ state has ~7 kJ/mol higher free energy compared with the molecular complexes by PCM calculations using acetonitrile as a medium.[161] According to the Bell–Evans–Polanyi principle,[172, 173] their group considered the activation energy of the proton transfer process to be small, which is comparable with thermal energy at room temperature, indicating fast proton

transfer and reorientation of the surrounding neutral molecules.[161] This fast proton transfer leads to the breakout finding of the Grutthuss mechanism from not only the *ab initio* molecular dynamics (AIMD) simulation, but also the spectroscopy signatures of Raman, X-ray scattering, and NMR, which can explain the high conductivity in the neutral molecular system.[165, 167] The AIMD calculation obtained the fraction of neutral molecules to be 75-80% in the equimolar mixture,[165] which is in agreement with the results of Raman measurements. Moreover, measurements of different molar ratios of this HAc/$C_1$Im mixture have been applied to obtain the conductivity curve, and two electrical conductivity maxima were found, at x(HAc)=0.65 and x(HAc)=0.85 respectively.[163, 164] This two-maximum conductivity curve indicates a more intricate picture wherein the speciation may change with the molar ratio of the mixture. Furthermore, there is another question about the assignment of the broadband peak in infrared spectroscopy on the frequency range of 1800 $cm^{-1}$ to 3000 $cm^{-1}$, which is not shown in Umebayashi's paper.

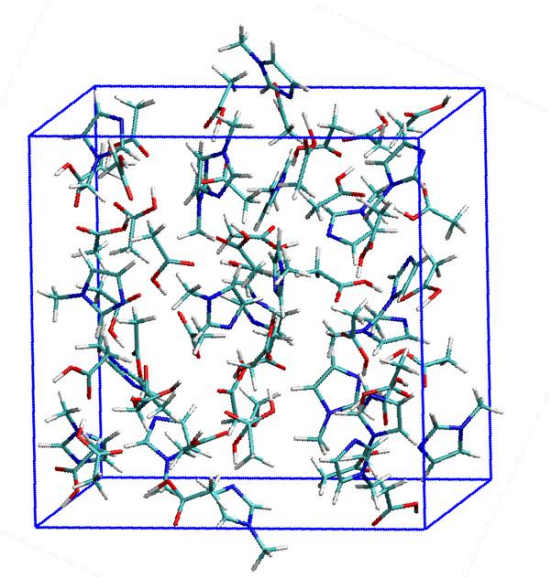

Figure 1.3. Acetic acid and N-methylimidazole molecular mixture. The red, green, blue, and white colors represent oxygen, carbon, nitrogen, and hydrogen atom respectively.

As a result, problems remain in this system: Is it composed of ions, neutral species, or neither of them; what are the structures of the complexes; how do they change with HAc concentration; and which conformers of the complexes are responsible for conductive behavior?

### 1.3. Outline of this thesis

The objective of the work described in this thesis is to investigate the solvation structure and dynamics of small molecule solutions with C=O stretch mode as a probe using FTIR and 2DIR spectroscopy assisted with molecular dynamics simulation. In chapter 2, the theory of third-order nonlinear response, the ultrafast pulse generation, and the 2DIR experiment setup are described. Then, the interpretation of spectral signature of 2DIR, like the spectral diffusion and the crosspeak, is introduced.

In chapter 3, the solvation dynamics of sodium acetate in water and in 6 M sodium chloride solution is investigated by linear and two-dimensional infrared spectroscopies using the carboxylate asymmetric stretch mode of the acetate ion as a probe. The linear IR spectra showed that the carboxylate asymmetric stretch central frequency and bandwidth are not significantly perturbed by the presence of a large amount of sodium chloride. Then, the frequency-frequency autocorrelation functions (FFCF) extracted from the time evolution of 2DIR spectra revealed that a dynamical component having a picosecond time constant is also not affected by the presence of high salt concentrations. Next, the asymmetric stretch of the azide ion in both the pure water and a highly-concentrated salt solution was investigated by linear infrared and 2DIR spectroscopies as a contrast. Finally, *ab initio* molecular dynamics simulations and a frequency map are calculated to confirm experimental observations and linked the observed vibrational phenomenon to the hydrogen bond structure and dynamics of the acetate first solvation shell, which is governed by the thermal rotation of its methyl group (–CH3).

In Chapter 4, the solvation shell structure and dynamics of lithium ion in linear and cyclic carbonates are investigated by *ab initio* molecular dynamics (AIMD) simulation and *ab initio* umbrella sampling (AIUS). The solvation shell structures in each carbonate solvent were characterized by radial distribution function between lithium ion and either the oxygen or the carbon of the carbonyl, demonstrating that the molecular arrangement of the carbonates directly coordinating $Li^+$ is not significantly altered by the carbonate chemical nature. The ion speciation was then investigated via radial distribution function between $Li^+$ and $PF_6^-$ and potential of mean force obtained from AIMD, showing significantly different pictures between cyclic and linear carbonates, which could be associated with the intercalation phenomenon observed in cyclic carbonates. In addition, the solvation shell dynamics was interrogated by the autocorrelation function of the structure factor in each frame. Finally, the solvent exchange process with a transition state was studied by AIUS and AIMD, revealing the dynamics of the geometrical changes of the carbonates solvating $Li^+$ at the timescale of tenths of picoseconds, while the ion pairing and solvent chemical exchange processes were found to be at time scales at least an order of magnitude larger than tenth.

In Chapter 5, FTIR, 2DIR, and AIMD simulation are applied to investigate the structure of a mixture composed of acetic acid and N-methylimidazole. Conductivities and viscosities of the mixture at different molar ratios were measured by a conductivity meter and a viscometer. Broadband FTIR absorption centered at ~1800 $cm^{-1}$ and ~2500 $cm^{-1}$ was observed over a large range of HAc molar fractions (0.05-0.97), which is an evidence of delocalized protons. Concentrate-dependent AIMD simulations indicated the existence of delocalized protons and revealed that there are two kinds of complexes existing in solution. One is formed by HAc with several $C_1Im$ and is the dominant species at low x(HAc); the other is $C_1Im$ with several HAc and

is the dominant species at high x(HAc). DFT calculations of representative structures taken from AIMD simulation confirmed the existence of the delocalized proton. Finally, the flat-bottom potential energy surface determined from DFT calculation and pump-probe spectra finally confirmed the proton delocalization existence in both complexes.

### 1.4. References


1. Castro, P. and M. Huber, *Marine biology. WCB*. 1997, McGraw-Hill, New York.
2. Schleicher, K.E. and A. Bradshaw, *A Conductivity Bridge for Measurement of the Salinity of Sea Water1*. ICES Journal of Marine Science, 1956. **22**(1): p. 9-20.
3. Missimer, T.M. and R.G. Maliva, *Environmental issues in seawater reverse osmosis desalination: Intakes and outfalls.* Desalination, 2018. **434**: p. 198-215.
4. Poloczanska, E., et al., *Climate change and Australian marine life*. Oceanography and marine biology, 2007. **45**: p. 407.
5. Pörtner, H.O., M. Langenbuch, and B. Michaelidis, *Synergistic effects of temperature extremes, hypoxia, and increases in CO2 on marine animals: From Earth history to global change.* Journal of Geophysical Research: Oceans, 2005. **110**(C9).
6. Pörtner, H.-O., *Ecosystem effects of ocean acidification in times of ocean warming: a physiologist's view.* Marine Ecology Progress Series, 2008. **373**: p. 203-217.
7. Turley, C., et al., *Reviewing the impact of increased atmospheric CO2 on oceanic pH and the marine ecosystem.* Avoiding dangerous climate change, 2006. **8**: p. 65-70.
8. Auerbach, D.I., et al., *Impacts of ocean CO 2 disposal on marine life: I. A toxicological assessment integrating constant-concentration laboratory assay data with variable-concentration field exposure.* Environmental Modeling & Assessment, 1997. **2**(4): p. 333-343.
9. Joint, I., S.C. Doney, and D.M. Karl, *Will ocean acidification affect marine microbes?* The ISME journal, 2011. **5**(1): p. 1-7.
10. Jickells, T., et al., *Global iron connections between desert dust, ocean biogeochemistry, and climate.* science, 2005. **308**(5718): p. 67-71.
11. Hansen, J., et al., *Climate response times: Dependence on climate sensitivity and ocean mixing.* Science, 1985. **229**(4716): p. 857-859.
12. Rackley, S.A., *Chapter 12 - Ocean Storage*, in *Carbon Capture and Storage*, S.A. Rackley, Editor. 2010, Butterworth-Heinemann: Boston. p. 267-286.

13. Riemer, P., *Greenhouse gas mitigation technologies, an overview of the CO2 capture, storage and future activities of the IEA Greenhouse Gas R&D programme.* Energy Conversion and Management, 1996. **37**(6): p. 665-670.

14. Watson, P.E., I.D. Watson, and R.D. Batt, *Total body water volumes for adult males and females estimated from simple anthropometric measurements.* The American Journal of Clinical Nutrition, 1980. **33**(1): p. 27-39.

15. Koeppen, B.M. and J.T. Hansen, *Netter's Atlas of Human Physiology*. 2002: Elsevier Inc.

16. Sandle, G., *Salt and water absorption in the human colon: a modern appraisal.* Gut, 1998. **43**(2): p. 294-299.

17. Gavras, I. and H. Gavras, *'Volume-expanded'hypertension: the effect of fluid overload and the role of the sympathetic nervous system in salt-dependent hypertension.* Journal of hypertension, 2012. **30**(4): p. 655-659.

18. Meneton, P., et al., *Links between dietary salt intake, renal salt handling, blood pressure, and cardiovascular diseases.* Physiological reviews, 2005. **85**(2): p. 679-715.

19. Singh, A., *Solvent Effect on the Enthalpy and Entropy of Activation for the Hydrolysis of Ethyl Cinnamate in Mixed Solvent System.* Journal of Phy. Chem. Biophys, 2017. **7**.

20. Sullivan, B.P. and T.J. Meyer, *Kinetics and mechanism of carbon dioxide insertion into a metal-hydride bond. A large solvent effect and an inverse kinetic isotope effect.* Organometallics, 1986. **5**(7): p. 1500-1502.

21. Ruiz-Lopez, M., et al., *Solvent effects on the mechanism and selectivities of asymmetric Diels-Alder reactions.* Journal of the American Chemical Society, 1993. **115**(19): p. 8780-8787.

22. Pedrielli, P., G.F. Pedulli, and L.H. Skibsted, *Antioxidant mechanism of flavonoids. Solvent effect on rate constant for chain-breaking reaction of quercetin and epicatechin in autoxidation of methyl linoleate.* Journal of Agricultural and Food Chemistry, 2001. **49**(6): p. 3034-3040.

23. Cole, R.B. and A.K. Harrata, *Solvent effect on analyte charge state, signal intensity, and stability in negative ion electrospray mass spectrometry; implications for the mechanism of negative ion formation.* Journal of the American Society for Mass Spectrometry, 1993. **4**(7): p. 546-556.

24. Marcus, Y., *Effect of Ions on the Structure of Water: Structure Making and Breaking.* Chemical Reviews, 2009. **109**(3): p. 1346-1370.

25. Bakker, H., *Structural dynamics of aqueous salt solutions.* Chemical reviews, 2008. **108**(4): p. 1456-1473.

26. Ohtaki, H. and T. Radnai, *Structure and dynamics of hydrated ions.* Chemical Reviews, 1993. **93**(3): p. 1157-1204.

27. Ladanyi, B.M. and R.M. Stratt, *Short-Time Dynamics of Solvation: Linear Solvation Theory for Polar Solvents.* The Journal of Physical Chemistry, 1995. **99**(9): p. 2502-2511.

28. Skyner, R., et al., *A review of methods for the calculation of solution free energies and the modelling of systems in solution.* Physical Chemistry Chemical Physics, 2015. **17**(9): p. 6174-6191.

29. Allen, M.P. and D.J. Tildesley, *Computer simulation of liquids*. 2017: Oxford university press.

30. Fafarman, A.T., et al., *Quantitative, directional measurement of electric field heterogeneity in the active site of ketosteroid isomerase.* Proceedings of the National Academy of Sciences, 2012. **109**(6): p. E299-E308.

31. Kim, H. and M. Cho, *Infrared probes for studying the structure and dynamics of biomolecules.* Chemical reviews, 2013. **113**(8): p. 5817-5847.

32. Lindquist, B.A., K.E. Furse, and S.A. Corcelli, *Nitrile groups as vibrational probes of biomolecular structure and dynamics: an overview.* Physical Chemistry Chemical Physics, 2009. **11**(37): p. 8119-8132.

33. Waegele, M.M., R.M. Culik, and F. Gai, *Site-specific spectroscopic reporters of the local electric field, hydration, structure, and dynamics of biomolecules.* The journal of physical chemistry letters, 2011. **2**(20): p. 2598-2609.

34. Bazewicz, C.G., et al., *Expanding the utility of 4-cyano-l-phenylalanine as a vibrational reporter of protein environments.* The Journal of Physical Chemistry B, 2012. **116**(35): p. 10824-10831.

35. Zimmermann, J., et al., *Cyano groups as probes of protein microenvironments and dynamics.* Angewandte Chemie International Edition, 2011. **50**(36): p. 8333-8337.

36. Waegele, M.M., M.J. Tucker, and F. Gai, *5-Cyanotryptophan as an infrared probe of local hydration status of proteins.* Chemical physics letters, 2009. **478**(4-6): p. 249-253.

37. Andrews, S.S. and S.G. Boxer, *Vibrational Stark Effects of Nitriles II. Physical Origins of Stark Effects from Experiment and Perturbation Models.* The Journal of Physical Chemistry A, 2002. **106**(3): p. 469-477.

38. Fournier, J.A., et al., *Broadband 2D IR spectroscopy reveals dominant asymmetric H 5 O 2+ proton hydration structures in acid solutions.* Nature chemistry, 2018. **10**(9): p. 932.

39. Dahms, F., et al., *Large-amplitude transfer motion of hydrated excess protons mapped by ultrafast 2D IR spectroscopy.* Science, 2017. **357**(6350): p. 491-495.

40. Stenger, J., et al., *Coherent response of hydrogen bonds in liquids probed by ultrafast vibrational spectroscopy.* The Journal of Physical Chemistry A, 2001. **105**(13): p. 2929-2932.

41. Rezus, Y., D. Madsen, and H. Bakker, *Orientational dynamics of hydrogen-bonded phenol.* The Journal of chemical physics, 2004. **121**(21): p. 10599-10604.

42. Cringus, D., et al., *Hydrogen bonding and vibrational energy relaxation in water–acetonitrile mixtures.* The Journal of Physical Chemistry B, 2004. **108**(29): p. 10376-10387.

43. Woutersen, a., U. Emmerichs, and H. Bakker, *Femtosecond mid-IR pump-probe spectroscopy of liquid water: Evidence for a two-component structure.* Science, 1997. **278**(5338): p. 658-660.

44. Levinger, N.E., P.H. Davis, and M. Fayer, *Vibrational relaxation of the free terminal hydroxyl stretch in methanol oligomers: Indirect pathway to hydrogen bond breaking.* The Journal of Chemical Physics, 2001. **115**(20): p. 9352-9360.

45. Ashihara, S., et al., *Vibrational couplings and ultrafast relaxation of the O–H bending mode in liquid H2O.* Chemical physics letters, 2006. **424**(1-3): p. 66-70.

46. Kuroda, D.G. and R.M. Hochstrasser, *Dynamic structures of aqueous oxalate and the effects of counterions seen by 2D IR.* Physical Chemistry Chemical Physics, 2012. **14**(18): p. 6219-6224.

47. Kuroda, D.G. and R.M. Hochstrasser, *Two-dimensional infrared spectral signature and hydration of the oxalate dianion.* The Journal of chemical physics, 2011. **135**(20): p. 204502.

48. Chuntonov, L., et al., *Kinetics of exchange between zero-, one-, and two-hydrogen-bonded states of methyl and ethyl acetate in methanol.* The Journal of Physical Chemistry B, 2015. **119**(12): p. 4512-4520.

49. Kuroda, D.G., D.Y. Vorobyev, and R.M. Hochstrasser, *Ultrafast relaxation and 2D IR of the aqueous trifluorocarboxylate ion.* The Journal of chemical physics, 2010. **132**(4): p. 044501.

50. Li, T., et al., *Hydration and vibrational dynamics of betaine (N, N, N-trimethylglycine).* The Journal of chemical physics, 2015. **142**(21): p. 212438.

51. Huerta-Viga, A., et al., *A salt-bridge structure in solution revealed by 2D-IR spectroscopy.* Physical Chemistry Chemical Physics, 2014. **16**(30): p. 15784-15786.

52. Bagchi, S., et al., *2D-IR experiments and simulations of the coupling between amide-I and ionizable side chains in proteins: Application to the Villin headpiece.* The journal of physical chemistry B, 2009. **113**(32): p. 11260-11273.

53. Lim, M. and R.M. Hochstrasser, *Unusual vibrational dynamics of the acetic acid dimer.* The Journal of Chemical Physics, 2001. **115**(16): p. 7629-7643.

54. Banno, M., K. Ohta, and K. Tominaga, *Ultrafast Dynamics of the Carbonyl Stretching Vibration in Acetic Acid in Aqueous Solution Studied by Sub-Picosecond Infrared Spectroscopy.* The Journal of Physical Chemistry A, 2008. **112**(18): p. 4170-4175.

55. Fried, S.D., S. Bagchi, and S.G. Boxer, *Measuring electrostatic fields in both hydrogen-bonding and non-hydrogen-bonding environments using carbonyl vibrational probes.* Journal of the American Chemical Society, 2013. **135**(30): p. 11181-11192.

56. Choi, J.-H. and M. Cho, *Vibrational solvatochromism and electrochromism of infrared probe molecules containing C≡O, C≡N, C=O, or C−F vibrational chromophore.* The Journal of Chemical Physics, 2011. **134**(15): p. 154513.

57. Park, E.S., et al., *Vibrational stark spectroscopy in proteins: A probe and calibration for electrostatic fields.* The Journal of Physical Chemistry B, 1999. **103**(45): p. 9813-9817.

58. Pazos, I.M., et al., *Ester Carbonyl Vibration as a Sensitive Probe of Protein Local Electric Field.* Angewandte Chemie International Edition, 2014. **53**(24): p. 6080-6084.

59. Jimenez, R., et al., *Femtosecond solvation dynamics of water.* Nature, 1994. **369**(6480): p. 471-473.

60. Palese, S., et al., *Femtosecond optical Kerr effect studies of water.* The Journal of Physical Chemistry, 1994. **98**(25): p. 6308-6316.

61. Thrane, L., et al., *THz reflection spectroscopy of liquid water.* Chemical Physics Letters, 1995. **240**(4): p. 330-333.

62. Kindt, J. and C. Schmuttenmaer, *Far-infrared dielectric properties of polar liquids probed by femtosecond terahertz pulse spectroscopy.* The Journal of Physical Chemistry, 1996. **100**(24): p. 10373-10379.

63. Carey, D.M. and G.M. Korenowski, *Measurement of the Raman spectrum of liquid water.* The Journal of chemical physics, 1998. **108**(7): p. 2669-2675.

64. Mizoguchi, K., Y. Hori, and Y. Tominaga, *Study on dynamical structure in water and heavy water by low-frequency Raman spectroscopy.* The Journal of chemical physics, 1992. **97**(3): p. 1961-1968.

65. Walrafen, G., *Raman spectrum of water: transverse and longitudinal acoustic modes below. apprxeq. 300 cm-1 and optic modes above. apprxeq. 300 cm-1.* Journal of physical chemistry, 1990. **94**(6): p. 2237-2239.

66. Rey, R., K.B. Møller, and J.T. Hynes, *Hydrogen Bond Dynamics in Water and Ultrafast Infrared Spectroscopy.* The Journal of Physical Chemistry A, 2002. **106**(50): p. 11993-11996.

67. Fecko, C.J., et al., *Ultrafast Hydrogen-Bond Dynamics in the Infrared Spectroscopy of Water.* Science, 2003. **301**(5640): p. 1698-1702.

68. Rezus, Y.L.A. and H.J. Bakker, *On the orientational relaxation of HDO in liquid water.* The Journal of Chemical Physics, 2005. **123**(11): p. 114502.

69. Asbury, J.B., et al., *Water Dynamics: Vibrational Echo Correlation Spectroscopy and Comparison to Molecular Dynamics Simulations.* The Journal of Physical Chemistry A, 2004. **108**(7): p. 1107-1119.

70. Moilanen, D.E., et al., *Water inertial reorientation: Hydrogen bond strength and the angular potential.* Proceedings of the National Academy of Sciences, 2008. **105**(14): p. 5295-5300.

71. Ohmine, I. and H. Tanaka, *Fluctuation, relaxations, and hydration in liquid water. Hydrogen-bond rearrangement dynamics.* Chemical reviews, 1993. **93**(7): p. 2545-2566.

72. Woutersen, S., U. Emmerichs, and H.J. Bakker, *Femtosecond Mid-IR Pump-Probe Spectroscopy of Liquid Water: Evidence for a Two-Component Structure.* Science, 1997. **278**(5338): p. 658.

73. Laenen, R., C. Rauscher, and A. Laubereau, *Dynamics of local substructures in water observed by ultrafast infrared hole burning.* Physical review letters, 1998. **80**(12): p. 2622.

74. Steinel, T., et al., *Watching hydrogen bonds break: A transient absorption study of water.* The Journal of Physical Chemistry A, 2004. **108**(50): p. 10957-10964.

75. Cowan, M., et al., *Ultrafast memory loss and energy redistribution in the hydrogen bond network of liquid H 2 O.* Nature, 2005. **434**(7030): p. 199-202.

76. Gale, G., et al., *Femtosecond dynamics of hydrogen bonds in liquid water: A real time study.* Physical review letters, 1999. **82**(5): p. 1068.

77. Woutersen, S. and H.J. Bakker, *Hydrogen bond in liquid water as a Brownian oscillator.* Physical review letters, 1999. **83**(10): p. 2077.

78. Hofmeister, F., *Zur Lehre von der Wirkung der Salze.* Archiv für experimentelle Pathologie und Pharmakologie, 1888. **24**(4): p. 247-260.

79. D'Angelo, P., et al., *Combined XANES and EXAFS analysis of ${\mathrm{Co}}^{2+},$ ${\mathrm{Ni}}^{2+},$ and ${\mathrm{Zn}}^{2+}$ aqueous solutions.* Physical Review B, 2002. **66**(6): p. 064209.

80. Franks, F., *Water a comprehensive treatise: volume 4: aqueous solutions of amphiphiles and macromolecules*. 2013: Springer Science & Business Media.

81. Garcia-Celma, J.J., et al., *Specific anion and cation binding to lipid membranes investigated on a solid supported membrane.* Langmuir, 2007. **23**(20): p. 10074-10080.

82. Fayer, M.D., et al., *Water Dynamics in Salt Solutions Studied with Ultrafast Two-Dimensional Infrared (2D IR) Vibrational Echo Spectroscopy.* Accounts of Chemical Research, 2009. **42**(9): p. 1210-1219.

83. Akio, S. and T. Yoshihiro, *NMR Studies on Reorientational Motion of Hydrated D2O Molecules in Tetraalkylammonium Bromide Dilute Aqueous Solutions.* Bulletin of the Chemical Society of Japan, 1990. **63**(11): p. 3255-3259.

84. Mancinelli, R., et al., *Hydration of Sodium, Potassium, and Chloride Ions in Solution and the Concept of Structure Maker/Breaker.* The Journal of Physical Chemistry B, 2007. **111**(48): p. 13570-13577.

85. Laage, D. and J.T. Hynes, *On the Residence Time for Water in a Solute Hydration Shell: Application to Aqueous Halide Solutions.* The Journal of Physical Chemistry B, 2008. **112**(26): p. 7697-7701.

86. Smith, J.D., R.J. Saykally, and P.L. Geissler, *The Effects of Dissolved Halide Anions on Hydrogen Bonding in Liquid Water.* Journal of the American Chemical Society, 2007. **129**(45): p. 13847-13856.

87. Kropman, M.F. and H.J. Bakker, *Vibrational relaxation of liquid water in ionic solvation shells.* Chemical Physics Letters, 2003. **370**(5): p. 741-746.

88. Heilweil, E.J., et al., *Vibrational energy relaxation of the cyanide ion in aqueous solution.* The Journal of Chemical Physics, 1982. **76**(11): p. 5632-5634.

89. Nibbering, E.T. and T. Elsaesser, *Ultrafast vibrational dynamics of hydrogen bonds in the condensed phase.* Chemical Reviews, 2004. **104**(4): p. 1887-1914.

90. Kunz, W., *Specific ion effects in colloidal and biological systems.* Current Opinion in Colloid & Interface Science, 2010. **15**(1-2): p. 34-39.

91. Quiles, F. and A. Burneau, *Infrared and Raman spectra of alkaline-earth and copper(II) acetates in aqueous solutions.* Vibrational Spectroscopy, 1998. **16**(2): p. 105-117.

92. Hajari, T., P. Ganguly, and N.F.A. van der Vegt, *Enthalpy-Entropy of Cation Association with the Acetate Anion in Water.* Journal of Chemical Theory and Computation, 2012. **8**(10): p. 3804-3809.

93. Eisenman, G. and J.A. Dani, *An introduction to molecular architecture and permeability of ion channels.* Annual review of biophysics and biophysical chemistry, 1987. **16**(1): p. 205-226.

94. Gouaux, E. and R. MacKinnon, *Principles of selective ion transport in channels and pumps.* science, 2005. **310**(5753): p. 1461-1465.

95. Cox, M., M. Hidalgo, and M. Valiente, *Solvent Extraction for the 21st Century.* SCI, London, 2001.

96. Albanese, D., et al., *Key role of water for nucleophilic substitutions in phase-transfer-catalyzed processes: A mini-review.* Industrial & engineering chemistry research, 2001. **40**(11): p. 2396-2401.

97. Rose, D. and I. Benjamin, *Free Energy of Transfer of Hydrated Ion Clusters from Water to an Immiscible Organic Solvent.* The Journal of Physical Chemistry B, 2009. **113**(27): p. 9296-9303.

98. Osakai, T., A. Ogata, and K. Ebina, *Hydration of Ions in Organic Solvent and Its Significance in the Gibbs Energy of Ion Transfer between Two Immiscible Liquids.* The Journal of Physical Chemistry B, 1997. **101**(41): p. 8341-8348.

99. Hundhammer, B. and T. Solomon, *Determination of standard Gibbs energies of ion partition between water and organic solvents by cyclic voltammetry: Part I.* Journal of electroanalytical chemistry and interfacial electrochemistry, 1983. **157**(1): p. 19-26.

100. Samec, Z., V. Mareček, and M.P. Colombini, *Standard Gibbs energies of transfer of alkali metal cations from water to 1, 2-dichloroethane: A critique.* Journal of electroanalytical chemistry and interfacial electrochemistry, 1988. **257**(1-2): p. 147-154.

101. Sabela, A., et al., *Standard Gibbs energies of transfer of univalent ions from water to 1, 2-dichloroethane.* Electrochimica acta, 1992. **37**(2): p. 231-235.

102. Rose, D. and I. Benjamin, *Free Energy of Transfer of Hydrated Ion Clusters from Water to an Immiscible Organic Solvent.* Journal of Physical Chemistry B, 2009. **113**(27): p. 9296-9303.

103. Rais, J., T. Okada, and J. Alexova, *Gibbs energies of transfer of alkali metal cations between mutually saturated water-solvent systems determined from extraction experiments with radiotracer Cs-137.* Journal of Physical Chemistry B, 2006. **110**(16): p. 8432-8440.

104. Arnett, E.M., B. Chawla, and N.J. Hornung, *The hydration of anions in nonaqueous media.* Journal of Solution Chemistry, 1977. **6**(12): p. 781-818.

105. Mikio, K., T. Kyoji, and I. Tadashi, *THE COEXTRACTION OF WATER WITH ALKALI AND ALKALINE EARTH METALS HEXANITRODIPKENYLAMINATES AND ANALOGOUS AMINATES.* Chemistry Letters, 1972. **1**(5): p. 417-420.

106. Osakai, T., et al., *Proton NMR Study on Selective Hydration of Anions in Nitrobenzene.* The Journal of Physical Chemistry B, 2000. **104**(50): p. 12021-12027.

107. Benjamin, I., *Mechanism and Dynamics of Ion Transfer Across a Liquid-Liquid Interface.* Science, 1993. **261**(5128): p. 1558-1560.

108. Schweighofer, K.J. and I. Benjamin, *Transfer of Small Ions across the Water/1,2-Dichloroethane Interface.* The Journal of Physical Chemistry, 1995. **99**(24): p. 9974-9985.

109. Wick, C.D. and L.X. Dang, *Molecular Dynamics Study of Ion Transfer and Distribution at the Interface of Water and 1,2-Dichlorethane.* The Journal of Physical Chemistry C, 2008. **112**(3): p. 647-649.

110. Alexander, R., et al., *Solvation of ions. XIV. Protic-dipolar aprotic solvent effects on rates of bimolecular reactions. Solvent activity coefficients of reactants and transition states at 25°.* Journal of the American Chemical Society, 1968. **90**(19): p. 5049-5069.

111. Barthel, J., et al., *Non-aqueous electrolyte solutions in chemistry and modern technology*, in *Physical and inorganic chemistry*. 1983, Springer. p. 33-144.

112. Mąkosza, M. and M. Wawrzyniewicz, *Reactions of organic anions. XXIV. Catalytic method for preparation of dichlorocyclopropane derivatives in aqueous medium.* Tetrahedron Letters, 1969. **10**(53): p. 4659-4662.

113. BODEN, R.M. and B. RM, *A mild method for preparing trans-alkenes; crown ether catalysis of the Wittig reaction.* 1975.

114. Brak, K. and E.N. Jacobsen, *Asymmetric Ion-Pairing Catalysis.* Angewandte Chemie International Edition, 2013. **52**(2): p. 534-561.

115. Darensbourg, M.Y., *Ion pairing effects on transition metal carbonyl anions.* Prog. Inorg. Chem, 1985. **33**: p. 221-274.

116. Aroca, R., et al., *Vibrational spectra and ion-pair properties of lithium hexafluorophosphate in ethylene carbonate based mixed-solvent systems for lithium batteries.* Journal of Solution Chemistry, 2000. **29**(10): p. 1047-1060.

117. Fulfer, K.D. and D.G. Kuroda, *Ion speciation of lithium hexafluorophosphate in dimethyl carbonate solutions: an infrared spectroscopy study.* Physical Chemistry Chemical Physics, 2018. **20**(35): p. 22710-22718.

118. Borodin, O. and G.D. Smith, *Quantum chemistry and molecular dynamics simulation study of dimethyl carbonate: ethylene carbonate electrolytes doped with LiPF6.* The Journal of Physical Chemistry B, 2009. **113**(6): p. 1763-1776.

119. Han, S.-D., et al., *Solvate structures and computational/spectroscopic characterization of LiPF6 electrolytes.* The Journal of Physical Chemistry C, 2015. **119**(16): p. 8492-8500.

120. Afroz, T., et al., *Structural interactions within lithium salt solvates: acyclic carbonates and esters.* The Journal of Physical Chemistry C, 2015. **119**(13): p. 7022-7027.

121. Winstein, S., et al., *Salt effects and ion-pairs in solvolysis1.* Journal of the American chemical society, 1954. **76**(9): p. 2597-2598.

122. Xu, K., *Electrolytes and interphases in Li-ion batteries and beyond.* Chemical reviews, 2014. **114**(23): p. 11503-11618.

123. Bockris, J.O.M. and A.K. Reddy, *Modern electrochemistry 2B: electrodics in chemistry, engineering, biology and environmental science*. Vol. 2. 2000: Springer Science & Business Media.

124. Lucht, B.L., T. Markmaitree, and L. Yang, *Lithium–Ion Batteries.* Encyclopedia of Inorganic and Bioinorganic Chemistry, 2011.

125. Xu, K., *Nonaqueous Liquid Electrolytes for Lithium-Based Rechargeable Batteries.* Chemical Reviews, 2004. **104**(10): p. 4303-4418.

126. Fulfer, K.D. and D.G. Kuroda, *Solvation Structure and Dynamics of the Lithium Ion in Organic Carbonate-Based Electrolytes: A Time-Dependent Infrared Spectroscopy Study.* The Journal of Physical Chemistry C, 2016. **120**(42): p. 24011-24022.

127. Fulfer, K.D. and D.G. Kuroda, *A comparison of the solvation structure and dynamics of the lithium ion in linear organic carbonates with different alkyl chain lengths.* Physical Chemistry Chemical Physics, 2017. **19**(36): p. 25140-25150.

128. Jiang, B., et al., *The Anion Effect on Li+ Ion Coordination Structure in Ethylene Carbonate Solutions.* The Journal of Physical Chemistry Letters, 2016. **7**(18): p. 3554-3559.

129. Liang, C., K. Kwak, and M. Cho, *Revealing the Solvation Structure and Dynamics of Carbonate Electrolytes in Lithium-Ion Batteries by Two-Dimensional Infrared Spectrum Modeling.* The Journal of Physical Chemistry Letters, 2017. **8**(23): p. 5779-5784.

130. Allen, J.L., et al., *Combined quantum chemical/Raman spectroscopic analyses of Li+ cation solvation: Cyclic carbonate solvents-Ethylene carbonate and propylene carbonate.* Journal of Power Sources, 2014. **267**: p. 821-830.

131. Giorgini, M.G., et al., *Solvation Structure around the Li+ Ion in Mixed Cyclic/Linear Carbonate Solutions Unveiled by the Raman Noncoincidence Effect.* Journal of Physical Chemistry Letters, 2015. **6**(16): p. 3296-3302.

132. Seo, D.M., et al., *Role of Mixed Solvation and Ion Pairing in the Solution Structure of Lithium Ion Battery Electrolytes.* The Journal of Physical Chemistry C, 2015. **119**(25): p. 14038-14046.

133. Pollard, T.P. and T.L. Beck, *Structure and polarization near the Li+ ion in ethylene and propylene carbonates.* The Journal of Chemical Physics, 2017. **147**(16): p. 161710.

134. Postupna, O.O., et al., *Microscopic Structure and Dynamics of LiBF4 Solutions in Cyclic and Linear Carbonates.* The Journal of Physical Chemistry B, 2011. **115**(49): p. 14563-14571.

135. Ong, M.T., et al., *Complex ion dynamics in carbonate lithium-ion battery electrolytes.* The Journal of Physical Chemistry C, 2017. **121**(12): p. 6589-6595.

136. Borodin, O., et al., *Competitive lithium solvation of linear and cyclic carbonates from quantum chemistry.* Physical Chemistry Chemical Physics, 2016. **18**(1): p. 164-175.

137. Ong, M.T., et al., *Lithium Ion Solvation and Diffusion in Bulk Organic Electrolytes from First-Principles and Classical Reactive Molecular Dynamics.* The Journal of Physical Chemistry B, 2015. **119**(4): p. 1535-1545.

138. Ganesh, P., D.-e. Jiang, and P.R.C. Kent, *Accurate Static and Dynamic Properties of Liquid Electrolytes for Li-Ion Batteries from ab initio Molecular Dynamics.* The Journal of Physical Chemistry B, 2011. **115**(12): p. 3085-3090.

139. Tang, Z.-K., J.S. Tse, and L.-M. Liu, *Unusual Li-Ion Transfer Mechanism in Liquid Electrolytes: A First-Principles Study.* The Journal of Physical Chemistry Letters, 2016. **7**(22): p. 4795-4801.

140. Wang, J., et al., *Superconcentrated electrolytes for a high-voltage lithium-ion battery.* Nature communications, 2016. **7**: p. 12032.

141. Tachikawa, H. and S. Abe, *Solvent Stripping Dynamics of Lithium ion solvated by ethylene carbonates: A direct ab-initio molecular (AIMD) Study.* Electrochimica Acta, 2014. **120**: p. 57-64.

142. Li, T. and P.B. Balbuena, *Theoretical Studies of Lithium Perchlorate in Ethylene Carbonate, Propylene Carbonate, and Their Mixtures.* Journal of The Electrochemical Society, 1999. **146**(10): p. 3613-3622.

143. Tachikawa, H., *Mechanism of Dissolution of a Lithium Salt in an Electrolytic Solvent in a Lithium Ion Secondary Battery: A Direct Ab Initio Molecular Dynamics (AIMD) Study.* ChemPhysChem, 2014. **15**(8): p. 1604-1610.

144. Flores, E., et al., *Solvation structure in dilute to highly concentrated electrolytes for lithium-ion and sodium-ion batteries.* Electrochimica Acta, 2017. **233**: p. 134-141.

145. Chaudhari, M.I., et al., *Scaling Atomic Partial Charges of Carbonate Solvents for Lithium Ion Solvation and Diffusion.* Journal of Chemical Theory and Computation, 2016. **12**(12): p. 5709-5718.

146. Kumar, N. and J.M. Seminario, *Lithium-Ion Model Behavior in an Ethylene Carbonate Electrolyte Using Molecular Dynamics.* The Journal of Physical Chemistry C, 2016. **120**(30): p. 16322-16332.

147. Takeuchi, M., et al., *Free-Energy and Structural Analysis of Ion Solvation and Contact Ion-Pair Formation of Li+ with BF4– and PF6– in Water and Carbonate Solvents.* The Journal of Physical Chemistry B, 2012. **116**(22): p. 6476-6487.

148. Jorn, R., et al., *Atomistic Modeling of the Electrode–Electrolyte Interface in Li-Ion Energy Storage Systems: Electrolyte Structuring.* The Journal of Physical Chemistry C, 2013. **117**(8): p. 3747-3761.

149. Chapman, N., et al., *Spectroscopic and Density Functional Theory Characterization of Common Lithium Salt Solvates in Carbonate Electrolytes for Lithium Batteries.* The Journal of Physical Chemistry C, 2017. **121**(4): p. 2135-2148.

150. Blomgren, G.E., *Properties and structures of electrolyte solutions for lithium batteries.* Journal of Power Sources, 1985. **14**(1): p. 39-44.

151. Jow, T.R., et al., *Electrolytes for lithium and lithium-ion batteries*. Vol. 58. 2014: Springer.

152. Doucey, L., et al., *A study of the Li/Li+ couple in DMC and PC solvents: part 1: characterization of LiAsF6/DMC and LiAsF6/PC solutions.* Electrochimica acta, 1999. **44**(14): p. 2371-2377.

153. Kameda, Y., et al., *Solvation structure of Li+ in concentrated LiPF6− propylene carbonate solutions.* The Journal of Physical Chemistry B, 2007. **111**(22): p. 6104-6109.

154. Smith, J.W., et al., *X-Ray absorption spectroscopy of LiBF 4 in propylene carbonate: a model lithium ion battery electrolyte.* Physical Chemistry Chemical Physics, 2014. **16**(43): p. 23568-23575.

155. Morita, M., et al., *A Raman spectroscopic study of organic electrolyte solutions based on binary solvent systems of ethylene carbonate with low viscosity solvents which dissolve different lithium salts.* Journal of the Chemical Society, Faraday Transactions, 1998. **94**(23): p. 3451-3456.

156. Xuan, X., et al., *Vibrational spectroscopic studies on ion solvation of lithium perchlorate in propylene carbonate+ N, N-dimethylformamide mixtures.* Spectrochimica Acta Part A: Molecular and Biomolecular Spectroscopy, 2000. **56**(11): p. 2131-2139.

157. Giorgini, M.G., et al., *Solvation structure around the Li+ ion in mixed cyclic/linear carbonate solutions unveiled by the Raman noncoincidence effect.* The Journal of Physical Chemistry Letters, 2015. **6**(16): p. 3296-3302.

158. Bogle, X., et al., *Understanding Li+–solvent interaction in nonaqueous carbonate electrolytes with 17O NMR.* The journal of physical chemistry letters, 2013. **4**(10): p. 1664-1668.

159. Bohets, H. and B.J. van der Veken, *On the conformational behavior of dimethyl carbonate.* Physical Chemistry Chemical Physics, 1999. **1**(8): p. 1817-1826.

160. Lee, K.-K., et al., *Ultrafast fluxional exchange dynamics in electrolyte solvation sheath of lithium ion battery.* Nature Communications, 2017. **8**: p. 14658.

161. Doi, H., et al., *A New Proton Conductive Liquid with No Ions: Pseudo-Protic Ionic Liquids.* Chemistry – A European Journal, 2013. **19**(35): p. 11522-11526.

162. MacFarlane, D.R., et al., *Lewis base ionic liquids.* Chemical Communications, 2006(18): p. 1905-1917.

163. Treble, R.G., K.E. Johnson, and E. Tosh, *The volatilities and conductivities of ionic liquids — GC–MS methodology and preliminary studies of acetic acid – base systems.* Canadian Journal of Chemistry, 2006. **84**(6): p. 915-924.

164. Yoshimura, N., et al., *Electronic States of Acetic Acid in a Binary Mixture of Acetic Acid and 1-Methylimidazole Depend on the Environment.* The Journal of Physical Chemistry B, 2019. **123**(6): p. 1332-1339.

165. Ingenmey, J., S. Gehrke, and B. Kirchner, *How to harvest Grotthuss diffusion in protic ionic liquid electrolyte systems.* ChemSusChem, 2018. **11**(12): p. 1900-1910.

166. Chen, K., et al., *Equilibrium in protic ionic liquids: The degree of proton transfer and thermodynamic properties.* The Journal of Physical Chemistry B, 2017. **122**(1): p. 309-315.

167. Watanabe, H., et al., *Possible Proton Conduction Mechanism in Pseudo-Protic Ionic Liquids: A Concept of Specific Proton Conduction.* The Journal of Physical Chemistry B, 2019. **123**(29): p. 6244-6252.

168. Chen, K., et al., *Equilibrium in Protic Ionic Liquids: The Degree of Proton Transfer and Thermodynamic Properties.* The Journal of Physical Chemistry B, 2018. **122**(1): p. 309-315.

169. Yoshizawa, M., W. Xu, and C.A. Angell, *Ionic Liquids by Proton Transfer: Vapor Pressure, Conductivity, and the Relevance of ΔpKa from Aqueous Solutions.* Journal of the American Chemical Society, 2003. **125**(50): p. 15411-15419.

170. Xu, W. and C.A. Angell, *Solvent-Free Electrolytes with Aqueous Solution-Like Conductivities.* Science, 2003. **302**(5644): p. 422-425.

171. Belieres, J.-P. and C.A. Angell, *Protic Ionic Liquids: Preparation, Characterization, and Proton Free Energy Level Representation.* The Journal of Physical Chemistry B, 2007. **111**(18): p. 4926-4937.

172. Bell, R.P., *The theory of reactions involving proton transfers.* Proceedings of the Royal Society of London. Series A-Mathematical and Physical Sciences, 1936. **154**(882): p. 414-429.

173. Evans, M.G. and M. Polanyi, *Inertia and driving force of chemical reactions.* Transactions of the Faraday Society, 1938. **34**(0): p. 11-24.

# CHAPTER 2
# LINEAR AND NONLINEAR INFRARED SPECTROSCOPY

## 2.1. Light-matter interactions

In molecular spectroscopy, photons are used to investigate the matter through light-matter interactions. Albeit the molecules cannot be observed directly through this method, information on molecular structure and dynamics is obtained from analyzing the detected spectra. To extract microscopic information in spectroscopy, a quantitative formalism of the light-matter interaction process is required. For this purpose, following the description popularized by Mukamel, Boyd, and Cho, a semi-classical treatment is applied, which means the material system is described quantum mechanically, while the time-dependent electromagnetic field is treated classically.[1-3]

### 2.1.1. Time-dependent Schrödinger equation

One of the most simplified models for a molecule interacting with a photon consists of a single molecule system that can be described by a single wavefunction, which is defined as a *pure state*, and an external electric field. The time-dependent Hamiltonian of an isolated vibrator is expressed as:

$$\hat{H}(t) = \hat{H}_0 + \hat{W}(t) \qquad (1)$$

where $\hat{H}_0$ is the Hamiltonian for the isolated molecule, and $\hat{W}(t)$ is the quantum mechanical operator for the interaction energy generated by the external time-dependent electromagnetic field and the dipole moment of the molecule. The interaction energy $\hat{W}(t)$ then is described as

$$\hat{W}(t) = -\vec{\mu} \cdot \vec{E}(t) \qquad (2)$$

where $\vec{\mu}$ is the molecule's dipole moment and $\vec{E}(t)$ is the external time-dependent electromagnetic field. Consider the electromagnetic field simply as

$$E(t) = E'(t)\cos(\omega t) \tag{3}$$

where $E'(t)$ is the time-dependent amplitude.

The time-evolution of the molecular state is given by solving the time-dependent Schrodinger equation:

$$\frac{\partial}{\partial t}|\psi(t)\rangle = -\frac{i}{\hbar}\widehat{H}(t)|\psi(t)\rangle. \tag{4}$$

When the external electric field $\widehat{W}(t)$ is much smaller than the internal field $\widehat{H}_0$, the external field exerted on the molecule can only disturb the coefficients of the wavefunctions, but not the eigenstates themselves. As a result, the wavefunction $\psi(t)$ can be expanded with the eigenstates of the isolated molecule Hamiltonian $\widehat{H}_0$ as a basis:

$$|\psi(t)\rangle = \sum_n c_n(t)|n\rangle, \tag{5}$$

where $c_n(t)$ is the time dependent probability coefficient, and

$$\widehat{H}_0|n\rangle = E_n|n\rangle. \tag{6}$$

Substitute equation (6) into equation (4):

$$\frac{\partial}{\partial t}c_m(t) = -\frac{i}{\hbar}\sum_n H_{mn}\, c_n(t), \tag{7}$$

where $H_{mn} = \langle m|\widehat{H}(t)|n\rangle$.

### 2.1.2. Density matrix of pure state and Liouville–von Neumann equation

The matrix $\| H \|$ above is another way of representing a quantum operator. With a well-defined orthogonal wavefunction basis set, operator $\hat{A}$ can be represented by a matrix with the matrix elements defined by:

$$A_{mn} = \langle m|\hat{A}|n\rangle. \tag{8}$$

The density matrix is an operator to describe self-interaction, defined as the outer product of a wavefunction and its complex conjugate:

$$\rho \equiv |\psi\rangle\langle\psi|, \tag{9}$$

with $\rho_{mn} = \langle m|\psi\rangle\langle\psi|n\rangle = c_m c_n^*$.

In infrared spectroscopy, the states with most measurable population are $|0\rangle$ and $|1\rangle$. Consider a system in which only those two states can be accessed by the laser pulse. After a laser pulse, according to Equation (5), the system is in a superposition of $|0\rangle$ and $|1\rangle$:

$$\begin{aligned} |\psi_{01}(t)\rangle &= c_0(t)|0\rangle + c_1(t)|1\rangle \\ &= c_0 e^{-iE_0 t/\hbar}|0\rangle + c_1 e^{-iE_1 t/\hbar}|1\rangle . \end{aligned} \tag{10}$$

$$\begin{aligned} \rho = |\psi_{01}\rangle\langle\psi_{01}| &= \begin{pmatrix} c_0(t)c_0^*(t) & c_0(t)c_1^*(t) \\ c_1(t)c_0^*(t) & c_1(t)c_1^*(t) \end{pmatrix} \\ &= \begin{pmatrix} c_0^2 & c_0 c_1^* e^{i\omega_{01}t} \\ c_1 c_0^* e^{-i\omega_{01}t} & c_1^2 \end{pmatrix}, \end{aligned} \tag{11}$$

where $\omega_{01}$ is the angular frequency that is corresponding to the energy difference between ground state $|0\rangle$ and first excited state $|1\rangle$ .

The diagonal terms of $\| \rho \|$ correspond to the probability of the system being in a certain basis set state, and the sum of them is 1 when the wavefunction $|\psi\rangle$ is normalized. The off-diagonal terms are coherence, which is the oscillatory process that interacts with the external field and emits a field.

When the density matrix is a diagonal matrix, the system described by the wavefunction $|\psi\rangle$ is in a *population state*. In the case of a pure state, a population state can only be a system composed of a single basis set (eigenstate/eigenfunction). When the off-diagonal terms in the density matrix are not all zero, the system is in a *coherent state*.

With a density matrix, the expectation of an operator $\hat{A}$ can be easily written as:

$$\langle \hat{A} \rangle = \langle \psi(t) | \hat{A} | \psi(t) \rangle = \sum_{mn} \rho_{nm} A_{mn} = Tr\big(\rho(t)\hat{A}\big) \equiv \langle \rho(t)\hat{A} \rangle, \qquad (12)$$

and the time evolution of the density matrix is:

$$\frac{d}{dt}\rho(t) = -\frac{i}{\hbar}\hat{H}(t)\rho(t) + \frac{i}{\hbar}\rho(t)\hat{H}(t) = -\frac{i}{\hbar}\big[\hat{H}(t), \rho(t)\big], \qquad (13)$$

which is the *Liouville-von Neumann* equation.

So far, with the application of matrix in the field of quantum mechanics, the eigenstate, the wavefunction, and the operator can be represented as basis set, vector, and matrix respectively. As a result, the complicated integral calculation is transferred into simple matrix operation. The other advantage of using density matrix will be introduced in the next section.

### 2.1.3. Molecular ensemble and dephasing

An isolated molecule model is not sufficient to describe the real light-matter interaction in condensed phase. In condensed phase, the vibrational frequency and quantum states are slightly distinct from molecule to molecule because of the different surrounding environment they experience and different spatial structures they have. Therefore, a statistical treatment is required, and the density matrix again shows its convenience in describing a molecular ensemble. Density matrix of an ensemble is defined as:

$$\rho = \sum_s p_s |\psi_s\rangle\langle\psi_s| \tag{14}$$

where $p_s$ is the probability of the state $|\psi_s\rangle$ in the ensemble, and $\sum_s p_s = 1$. Density matrix of an ensemble also fulfills the Liouville-von Neumann equation.

In $|0\rangle$ and $|1\rangle$ two states system, after substitution Equation (11) into Equation (14), the density matrix of ensemble after a laser pulse is:

$$\begin{aligned}\rho = \sum_s p_s |\psi_s\rangle\langle\psi_s| &= \begin{pmatrix} \langle c_0(t)c_0^*(t)\rangle & \langle c_0(t)c_1^*(t)\rangle \\ \langle c_1(t)c_0^*(t)\rangle & \langle c_1(t)c_1^*(t)\rangle \end{pmatrix} \\ &= \begin{pmatrix} \langle c_0^2\rangle & \langle c_0 c_1^* e^{i\omega_{01}t}\rangle \\ \langle c_1 c_0^* e^{-i\omega_{01}t}\rangle & \langle c_1^2\rangle \end{pmatrix}.\end{aligned} \tag{15}$$

The symbol $\langle \dots \rangle$ here represents ensemble average.

As time evolves, systems in the excited state $|1\rangle$ move to the ground state $|0\rangle$, which is the *vibrational population relaxation*. The vibrational relaxation results in a decay of $|1\rangle$ state population $\rho_{11}$ with time constant $T_1$ along with an increasing of $|0\rangle$ state population $\rho_{00}$:

$$\rho_{11}(t) = \rho_{11}(0)e^{-t/T_1}, \tag{16}$$

$$\rho_{00}(t) = 1 - \rho_{11}(t). \tag{17}$$

The *homogeneous dephasing* is a decay in the off-diagonal terms of the density matrix, characterized with a homogeneous dephasing time $T_2$:

$$\rho_{01}(t) = c_0 c_1^* e^{i\omega_{01}t} e^{-t/T_2} \tag{18}$$

$$\rho_{10}(t) = c_1 c_0^* e^{-i\omega_{01}t} e^{-\frac{t}{T_2}}. \tag{19}$$

$T_1$ contributes to $T_2$ through the decrease of off-diagonal elements. The relationship between $T_1$ and $T_2$ is described as:

$$\frac{1}{T_2} = \frac{1}{2T_1} + \frac{1}{T_2^*}, \tag{20}$$

where $T_2^*$ is the *pure dephasing*.

### 2.1.4. Perturbation theory

To separate the time propagation caused by external electric field and that intrinsic to the molecule itself, the wavefunction $|\psi(t)\rangle$ can be written in the form of the *interaction picture*:

$$|\psi(t)\rangle \equiv e^{-\frac{i}{\hbar}\hat{H}_0(t-t_0)}|\psi_I(t)\rangle \tag{21}$$

where $e^{-\frac{i}{\hbar}\hat{H}_0(t-t_0)}$ is the time evolution component under the effect of intrinsic Hamiltonian $\hat{H}_0$ for the isolated molecule, and the time propagation caused by a laser pulse is described by $|\psi_I(t)\rangle$. $|\psi(t)\rangle$ represents an ensemble density matrix.

The time evolution of $|\psi_I(t)\rangle$ can be written in a similar form to the Schrodinger equation, thus the Liouville-von Neumann equation is valid for $|\psi_I(t)\rangle$:

$$\frac{\partial}{\partial t}|\psi_I(t)\rangle = -\frac{i}{\hbar}\widehat{W_I}(t)|\psi_I(t)\rangle \tag{22}$$

where $\widehat{W_I}(t)$ is defined as:

$$\widehat{W}_I(t) \equiv e^{\frac{i}{\hbar}\widehat{H}_0(t-t_0)}\widehat{W}(t_0)e^{-\frac{i}{\hbar}\widehat{H}_0(t-t_0)}. \tag{23}$$

Substitute Eq. (21), Eq. (22) and Eq. (23) to the definition of density matrix, then the density matrix described in interaction picture is:

$$|\psi(t)\rangle\langle\psi(t)| = e^{-\frac{i}{\hbar}\widehat{H}_0(t-t_0)}|\psi_I(t)\rangle\langle\psi_I(t)|e^{\frac{i}{\hbar}\widehat{H}_0(t-t_0)}. \tag{24}$$

Or written as:

$$\rho(t) = e^{-\frac{i}{\hbar}\widehat{H}_0(t-t_0)}\rho_I(t)e^{\frac{i}{\hbar}\widehat{H}_0(t-t_0)}. \tag{25}$$

$\rho_I(t)$ also fulfills the Liouville-von Neumann equation:

$$\frac{d}{dt}\rho_I(t) = -\frac{i}{\hbar}\left[\widehat{W}_I(t), \rho_I(t)\right]. \tag{26}$$

Thus, the perturbative expansion of $\rho_I(t)$ is:

$$\rho_I(t) = \rho_I(t_0) + \sum_{n=1}^{\infty}\left(-\frac{i}{\hbar}\right)^n \int_{t_0}^{t} d\tau_n \int_{t_0}^{\tau_n} d\tau_{n-1} \dots \int_{t_0}^{\tau_2} d\tau_1 \left[\widehat{W}_I(\tau_n), \left[\widehat{W}_I(\tau_{n-1}), \dots \left[\widehat{W}_I(\tau_1), \rho_I(t)\right] \dots\right]\right]. \tag{27}$$

Go back to the density matrix under the full Hamiltonian $\rho(t)$:

$$\rho(t) = \rho(t_0) + \sum_{n=1}^{\infty}\left(-\frac{i}{\hbar}\right)^n \int_{t_0}^{t} d\tau_n \int_{t_0}^{\tau_n} d\tau_{n-1} \dots \int_{t_0}^{\tau_2} d\tau_1 \; e^{-\frac{i}{\hbar}\widehat{H}_0(t-t_0)}\left[\widehat{W}_I(\tau_n), \left[\widehat{W}_I(\tau_{n-1}), \dots \left[\widehat{W}_I(\tau_1), \rho(t_0)\right] \dots\right]\right] e^{\frac{i}{\hbar}\widehat{H}_0(t-t_0)}. \tag{28}$$

Substitute Equation (2) into Equation (28):

$$\rho(t) = \rho(t_0) + \sum_{n=1}^{\infty} \left(-\frac{i}{\hbar}\right)^n \int_{t_0}^{t} d\tau_n \int_{t_0}^{\tau_n} d\tau_{n-1} \dots \int_{t_0}^{\tau_2} d\tau_1 \, E(\tau_n)E(\tau_{n-1}) \dots E($$
$$e^{-\frac{i}{\hbar}\hat{H}_0(t-t_0)}\left[\hat{\mu}_I(\tau_n), [\hat{\mu}_I(\tau_{n-1}), \dots [\hat{\mu}_I(\tau_1), \rho(t_0)] \dots ]\right] e^{\frac{i}{\hbar}\hat{H}_0(t-t_0)}, \quad (29)$$

Where

$$\hat{\mu}_I(t) \equiv e^{\frac{i}{\hbar}\hat{H}_0(t-t_0)} \hat{\mu}(t_0) e^{-\frac{i}{\hbar}\hat{H}_0(t-t_0)}. \quad (30)$$

In the following part, the subscript *I* of interaction picture is discarded. The Schrodinger picture and the interaction picture are distinguished by $\hat{\mu}$ and $\hat{\mu}(t)$, since the former is time-independent and the latter is time-dependent.

### 2.1.5. Nonlinear polarization and response function

In the picture of linear and nonlinear spectroscopy, the macroscopic polarization is a significant bridge between the incident photon and the signal photon. It is induced by the external electromagnetic field, and radiates the signal electromagnetic field.

The perturbative expansion of the macroscopic polarization is:

$$\bar{P}(t) = P^{(0)} + P^{(1)} + P^{(2)} + P^{(3)} + \cdots, \quad (31)$$

where $P^{(n)}$ is the nth-order polarization resulting from n incident fields.

The ensemble average of P(t) can be obtained from the density matrix as:

$$\bar{P}(t) = Tr\left(\hat{\mu}\rho(t)\right) = Tr\left(\hat{\mu}\rho^{(0)}(t)\right) + Tr\left(\hat{\mu}\rho^{(1)}(t)\right) + Tr\left(\hat{\mu}\rho^{(2)}(t)\right) + \cdots \quad (32)$$

Substitute Equation (29) into Equation (32):

$$\overline{P^{(n)}}(t) = Tr\left(\hat{\mu}\rho^{(n)}(t)\right) = \langle\hat{\mu}\rho^{(n)}(t)\rangle$$

$$= -\left(-\frac{i}{\hbar}\right)^{n} \int_{t_0}^{t} d\tau_n \int_{t_0}^{\tau_n} d\tau_{n-1} \dots \int_{t_0}^{\tau_2} d\tau_1 \, E(\tau_n)E(\tau_{n-1}) \dots E(\tau_1) \tag{33}$$

$$\langle\hat{\mu}(t)\left[\hat{\mu}(\tau_n), [\hat{\mu}(\tau_{n-1}), \dots [\hat{\mu}(\tau_1), \rho(t_0)] \dots\right]\rangle.$$

Assume $\rho(t_0)$ is the time-independent density matrix under the internal Hamiltonian $\widehat{H}_0$, so send $t_0 \to -\infty$. Set $\tau_1 = 0$, and use the time interval $t$ instead of absolute time $\tau$:

$$\begin{gathered} t_1 = \tau_2 - \tau_1 \\ t_2 = \tau_3 - \tau_2 \\ \dots\dots \\ t_n = \tau - \tau_n \end{gathered} \tag{34}$$

The nth-order polarization can be written as the convolution of n incident fields and an nth-order response function $R^{(n)}$:

$$\overline{P^{(n)}}(t) = \int_0^{\infty} dt_n \int_0^{\infty} dt_{n-1} \dots \int_0^{\infty} dt_1 \, E(t - t_n)E(t - t_n - t_{n-1}) \dots$$
$$E(t - t_n - t_{n-1} - \dots - t_1)R^{(n)}(t_n, \dots, t_1), \tag{35}$$

where the response function $R^{(n)}$ is described as:

$$R^{(n)}(t_n, \dots, t_1) =$$
$$-(-\frac{i}{\hbar})^n\langle\hat{\mu}(t_n + \dots + t_1)[\hat{\mu}(t_{n-1} + \dots + t_1), \dots, [\hat{\mu}(0), \rho(-\infty)] \dots]\rangle \tag{36}$$

In the linear spectroscopy, where n=1, the macroscopic polarization is describes as:

$$\overline{P^{(1)}}(t) = \int_0^\infty dt_1 \, E(t - t_1) R^{(1)}(t_1), \tag{37}$$

where

$$R^{(1)}(t_1) = \frac{i}{\hbar} \langle \hat{\mu}(t_1)[\hat{\mu}(0), \rho(-\infty)] \rangle. \tag{38}$$

The relationship between macroscopic polarization and emitted light is described as:

$$E_{sig}(t) = iP(t). \tag{39}$$

Substitute Equation (39) and Equation (38) to Equation (37), an opposite sign between incident electric field $E(t)$ and emitted signal $E_{sig}(t)$ is obtained. This destructive inference between emitted light and incident light causes the decrease of optical density of light after the sample, which is described as the absorption process in linear spectroscopy.

In third-order nonlinear spectroscopy, the third-order polarization generated by three external electromagnetic fields is described as:

$$\begin{aligned} \overline{P^{(3)}}(t) = \int_0^\infty dt_1 \int_0^\infty dt_2 \int_0^\infty dt_3 \, E(t - t_3) E(t - t_3 - t_2) \\ E(t - t_3 - t_2 - t_1) R^{(3)}(t_1, t_2, t_3), \end{aligned} \tag{40}$$

Where

$$R^{(3)}(t_1, t_2, t_3) = (\frac{i}{\hbar})^3 \langle \hat{\mu}(t_1 + t_2 + t_3) \left[ \hat{\mu}(t_1 + t_2), \left[ \hat{\mu}(t_1), [\hat{\mu}(0), \rho(-\infty)] \right] \right] \rangle \tag{41}$$

### 2.1.6. Rotating wave approximation and Feynman diagrams

In the previous part, the macroscopic polarization is derived with a simplified description of electric field $E(t)$. Here, a more sophisticated description of the electric field is taken as a real sine or cosine function, which can be written as the summation of a pair of complex conjugates:

$$E_0(t) = 2E'(t)\cos(\theta) = E'(t)\left(e^{-i\omega t} + e^{+i\omega t}\right) = E(t) + E^*(t), \qquad (42)$$

where $E'(t)$ is the amplitude. Take the linear interaction for instance, the convolution of the electric field and molecular response can be rewritten as:

$$\begin{aligned}
\overline{P^{(1)}}(t) &= \int_0^\infty dt_1\,[E(t-t_1) + E^*(t-t_1)]R^{(1)}(t_1) \\
&= \frac{i}{\hbar}\int_0^\infty dt_1\,[E(t-t_1) + E^*(t-t_1)]\langle\hat{\mu}(t_1)[\hat{\mu}(0),\rho(-\infty)]\rangle \\
&= \frac{i}{\hbar}\int_0^\infty dt_1\,E(t-t_1)\langle\hat{\mu}(t_1)\hat{\mu}(0)\rho(-\infty)\rangle \\
&+ \frac{i}{\hbar}\int_0^\infty dt_1\,E^*(t-t_1)\langle\hat{\mu}(t_1)\hat{\mu}(0)\rho(-\infty)\rangle \\
&- \frac{i}{\hbar}\int_0^\infty dt_1\,E^*(t-t_1)\langle\rho(-\infty)\hat{\mu}(0)\hat{\mu}(t_1)\rangle \\
&- \frac{i}{\hbar}\int_0^\infty dt_1\,E(t-t_1)\langle\rho(-\infty)\hat{\mu}(0)\hat{\mu}(t_1)\rangle.
\end{aligned} \qquad (43)$$

Consider the dephasing between 0 and $t_1$:

$$\begin{aligned}\overline{P^{(1)}}(t) = &\frac{i}{\hbar}\mu_{01}^2 e^{-i\omega t}\int_0^\infty dt_1\, E'(t-t_1)e^{-\frac{t_1}{T_2}} \\ &+\frac{i}{\hbar}\mu_{01}^2 e^{i\omega t}\int_0^\infty dt_1\, E'(t-t_1)e^{-\frac{t_1}{T_2}}e^{-2i\omega t} \\ &-\frac{i}{\hbar}\mu_{01}^2 e^{i\omega t}\int_0^\infty dt_1\, E'(t-t_1)e^{-\frac{t_1}{T_2}} \\ &-\frac{i}{\hbar}\mu_{01}^2 e^{-i\omega t}\int_0^\infty dt_1\, E'(t-t_1)e^{-t_1/T_2}e^{2i\omega t}.\end{aligned} \tag{44}$$

The second and fourth integral have a fast oscillating component $e^{\pm 2i\omega t}$, causing the convolution average to 0 over time. Therefore, compared with the first and third integral, the second and the fourth can be neglected. This is the r*otating wave approximation*, and it reduces the number of convolutions that need to be considered by half:

$$\begin{aligned}\overline{P^{(1)}}(t) = &\frac{i}{\hbar}\mu_{01}^2 e^{-i\omega t}\int_0^\infty dt_1\, E'(t-t_1)e^{-\frac{t_1}{T_2}} \\ &-\frac{i}{\hbar}\mu_{01}^2 e^{i\omega t}\int_0^\infty dt_1\, E'(t-t_1)e^{-\frac{t_1}{T_2}}.\end{aligned} \tag{45}$$

To simplify the tedious convolution notation, a Feynman diagram is adopted to trace the coherence under the interaction between the electric field and the density matrix at different times graphically.

Below is an example of Feynman diagrams (Figure 2.1), displaying the four components in Equation (44). The vertical double line represents the *ket* (left) and *bra* (right) of the density matrix. From bottom to top is the time evolution, as shown by the arrow on the left side. The arrow pointing in or out from the density matrix represents the interaction with the dipole operator. An operator acting on *ket* corresponds to an arrow on the left side, and an operator acting on *bra*

corresponds to an arrow on the right side. The direction of the arrow is determined by the electric field. $E(t) = E'(t)e^{-i\omega t}$ is represented by a right-pointing arrow. Its complex conjugate $E'(t) = E'(t)e^{+i\omega t}$ is represented by a left-pointing arrow. The system propagates under its internal Hamiltonian in time intervals between laser pulses, experiencing processes including dephasing.

Feynman diagrams helps to identify which pathways need to be taken into consideration. In Figure 2.1, the first arrow in the pathways corresponding to $R_2^{(1)}$ and $R_4^{(1)}$ is pointing away from the density matrix, which represents emission of light and de-excitation of state. It means that the pulse tries to de-excite the ground state, which is rarely possible and in agreement with the rotating wave approximation results.

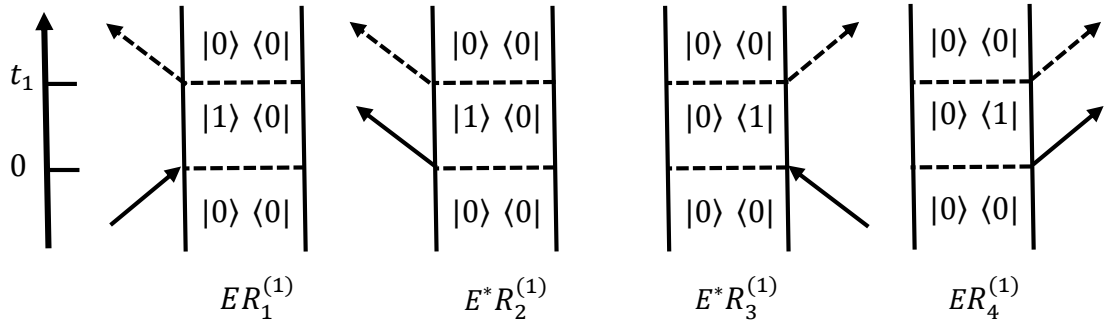


Figure 2.1. Feynman diagrams of four components in Equation (44).

### 2.1.7. Pathways in third-order spectroscopy

Similar to linear interaction, by instituting Equation (42) into third-order polarization, $2 \times 2^3 = 16$ components are obtained.

$$R^{(3)}(t_1, t_2, t_3) = \left(\frac{i}{\hbar}\right)^3 \langle \hat{\mu}(t_1 + t_2 + t_3) \left[\hat{\mu}(t_1 + t_2), \left[\hat{\mu}(t_1), [\hat{\mu}(0), \rho(-\infty)]\right]\right]\rangle \quad (46)$$

Denote $\hat{\mu}(0)$, $\hat{\mu}(t_1)$, $\hat{\mu}(t_1+t_2)$, $\hat{\mu}(t_1+t_2+t_3)$ as $\hat{\mu}_0$, $\hat{\mu}_1$, $\hat{\mu}_2$, and $\hat{\mu}_3$. Discard half of the 16 components according to rotating wave approximation; the remaining 8 pathways are described as:

$$R_1(t_1,t_2,t_3) = (\frac{i}{\hbar})^3\langle\hat{\mu}_3\hat{\mu}_1\rho(-\infty)\hat{\mu}_0\hat{\mu}_2\rangle \quad (47)$$

$$R_2(t_1,t_2,t_3) = (\frac{i}{\hbar})^3\langle\hat{\mu}_3\hat{\mu}_2\,\rho(-\infty)\hat{\mu}_0\hat{\mu}_1\rangle \quad (48)$$

$$R_4(t_1,t_2,t_3) = (\frac{i}{\hbar})^3\langle\hat{\mu}_3\hat{\mu}_0\,\rho(-\infty)\hat{\mu}_1\hat{\mu}_2\,\rangle \quad (49)$$

$$R_5(t_1,t_2,t_3) = (\frac{i}{\hbar})^3\langle\hat{\mu}_3\hat{\mu}_2\hat{\mu}_1\hat{\mu}_0\,\rho(-\infty)\,\rangle \quad (50)$$

$$R_1{}^*(t_1,t_2,t_3) = (\frac{i}{\hbar})^3\langle\hat{\mu}_2\hat{\mu}_0\rho(-\infty)\hat{\mu}_1\hat{\mu}_3\rangle \quad (51)$$

$$R_2{}^*(t_1,t_2,t_3) = (\frac{i}{\hbar})^3\langle\hat{\mu}_1\hat{\mu}_0\rho(-\infty)\hat{\mu}_2\hat{\mu}_3\rangle \quad (52)$$

$$R_4{}^*(t_1,t_2,t_3) = (\frac{i}{\hbar})^3\langle\hat{\mu}_2\hat{\mu}_1\rho(-\infty)\hat{\mu}_0\hat{\mu}_3\rangle \quad (53)$$

$$R_5{}^*(t_1,t_2,t_3) = (\frac{i}{\hbar})^3\langle\rho(-\infty)\hat{\mu}_0\hat{\mu}_1\hat{\mu}_2\hat{\mu}_3\rangle \quad (54)$$

$R_1{}^*$, $R_2{}^*$, $R_4{}^*$, and $R_5{}^*$ are the complex conjugates of $R_1$, $R_2$, $R_4$, and $R_5$ respectively. The pathways of $R_1$, $R_2$, $R_4$, and $R_5$ are shown by Feynman diagrams in Figure 2.2. $R_3$, and $R_6$ are omitted here, since they involved three-level system. These Feynman diagrams are shown in Figure 2.3.

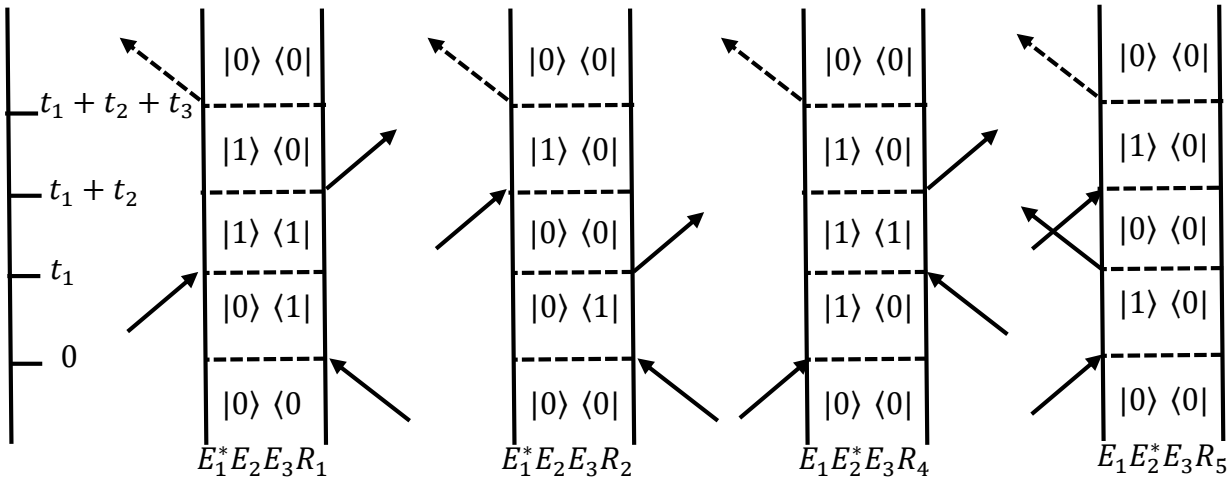


Figure 2.2. Feynman diagrams of third-order nonlinear response in two-level system.

Information of rephasing and non-rephasing is obtained from the Feynman diagrams. In the pathways $R_1$ and $R_2$, the two coherent states are $|0\rangle\langle 1|$ and $|1\rangle\langle 0|$, which are opposite. $|0\rangle\langle 1|$ coherence is generated by $e^{i\omega t_1}$ oscillation of the density matrix off-diagonal element, while $|1\rangle\langle 0|$ coherence is generated by $e^{-i\omega t_3}$ oscillation. Therefore, the dephasing in the time interval $t_1$ is compensated by the dephasing in the reversed direction in the time interval $t_3$. At the time $t_3 = t_1$, the initial phase condition is totally restored, so the $R_1$ and $R_2$ are named as *rephasing* pathways. In $R_4$ and $R_5$, the first and second coherent states are identical, which leads to a continuous increasing in dephasing. $R_4$ and $R_5$ are *non-rephasing* pathways.

The emitted signal generated by different pathways has its specific direction, so that the collection of signals generated by certain specific pathways without huge background of other beams is accessible. The direction of emitted light fulfills the phasing-matching condition, which will be discussed in Section 2.3.

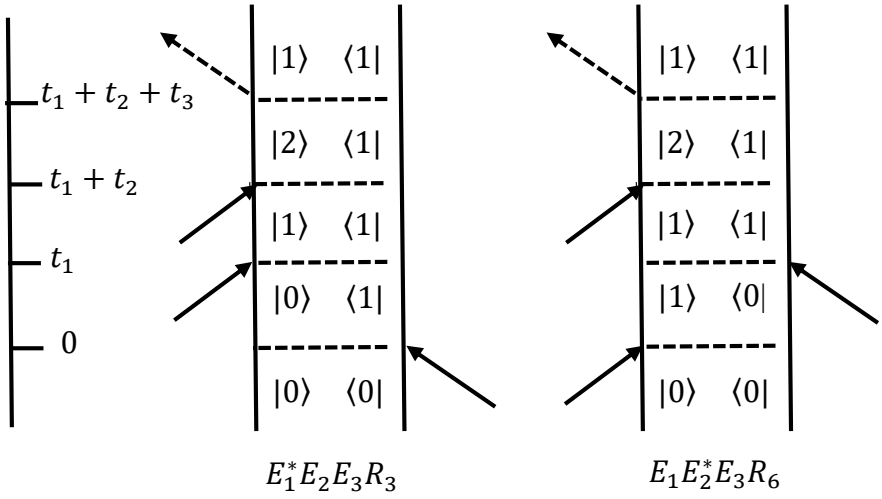

Figure 2.3. Feynman diagram of three-level system.

## 2.2. Vibrational lineshape and spectra signatures

In the last section, we discussed the interaction between the molecular ensemble and the external electric field, going through the macroscopic polarization changes induced by laser pulse, and the emitted field generated by the oscillating polarization of the molecules. In this chapter, we are going into the spectra. Lineshape of linear and third-order nonlinear spectroscopy will be derived based on the emitted signal developed previously. Models will be built to interpret the relationship between macroscopic spectral signatures we observe, *i.e.*, diagonal peak and crosspeak, and microscopic properties we want to investigate, i.*e.*, dynamics and structure in the solution.

### 2.2.1. Linear spectroscopy lineshape

In typical linear infrared spectroscopy, the detector measures the intensity of the vector summation of both the incident electric field and signal. By taking the Fourier transform, the signal gathered by the detector is described as:

$$\mathrm{S}(\omega) \propto \left| \int_0^{+\infty} \left\{ E(t) + E_{sig}^{(1)}(t) \right\} e^{i\omega t} dt \right|^2$$

$$\propto I_0(\omega) + 2\mathrm{Re}\left\{ \int_0^{+\infty} E(t) e^{i\omega t} dt \cdot \int_0^{+\infty} E_{sig}^{(1)}(t) e^{i\omega t} dt \right\} + I_{sig}^{(1)}(\omega)$$

$$\approx I_0(\omega) + 2\mathrm{Re}\left\{ E(\omega) \cdot E_{sig}^{(1)}(\omega) \right\}. \qquad (55)$$

The intensity of the pure signal is much smaller than the intensity of incident light, so $I_{sig}^{(1)}(\omega)$ is neglected. The signal is detected and amplified by the interference between incident light $E$ and signal itself $E_{sig}^{(1)}$, which is called as *heterodyned detection*.

The absorption in spectroscopy is defined as the additive inverse of the logarithm of the signal to incident ratio. Using the Taylor expansion of ln(x), the absorption can be described as:

$$\mathrm{A}(\omega) = -\log\left( \frac{S(\omega)}{I_0(\omega)} \right) \approx 2\mathrm{Re}\left\{ E(\omega) \cdot E_{sig}^{(1)}(\omega) \right\}. \qquad (56)$$

Assume the electric field of incident pulse is a δ function, and the dipole moment is a constant along time-evolution, substitute Equation (55), （39）, and (45), the lineshape of absorption is described as a Lorentzian line:

$$A(\omega) \propto \mu_{01}^2 \frac{\frac{1}{T_2}}{(\omega - \omega_0)^2 + \frac{1}{T_2^2}}. \quad (57)$$

### 2.2.2. Homogeneous and inhomogeneous dephasing

In the previous sections, the dephasing is treated simply with a homogeneous dephasing factor $e^{-t/T_2}$, by assuming the frequency $\omega_{01}$ of an oscillator does not change along time propagation. In this simplified case, the dephasing is caused by the increasing destructive interference among the emitted light from different molecules, which is called *homogeneous dephasing*. Now consider the time evolution of the molecular internal Hamiltonian influenced by the time evolution of the molecular environment, which leads to the *inhomogeneous dephasing*. Kubo's theory is applied to describe the dephasing in the solution, where the molecular oscillator is treated quantum mechanically and the solution environment is treated classically.[4]

The time-dependent transition frequency is described as:

$$\omega_{01}(t) = \omega_{01} + \delta\omega_{01}(t), \quad (58)$$

where $\omega_{01}$ is the average of $\omega_{01}(t)$, and $\delta\omega_{01}(t)$ is the fluctuation deviation from mean value at time $t$. It fulfills the equation:

$$\langle \delta\omega_{01}(t) \rangle = 0. \quad (59)$$

The coherent element in the density matrix $e^{\pm i\omega t} e^{-t/T_2}$ now can be described as:

$$e^{\pm i\omega_0 t} \langle \exp(-i \int_0^t d\tau \, \delta\omega_{01}(\tau)) \rangle. \quad (60)$$

The time integral represents the time-dependent frequency fluctuation of a single molecule, and the $\langle ... \rangle$ represents ensemble average of molecules. Plug Equation (60) into Equation (38), and assume the dipole moment is a constant when the environment fluctuates:

$$R^{(1)}(t_1) = i\mu_{01}^2 e^{\pm i\omega_0 t} \langle \exp(-i \int_0^{t_1} d\tau \, \delta\omega_{01}(\tau)) \rangle \tag{61}$$

Denoting $\langle \exp(-i \int_0^{t_1} d\tau \, \delta\omega_{01}(\tau)) \rangle$ as $\exp(-g(t))$, the dephasing term can be rewritten in the formulation of Taylor expansion:

$$\begin{aligned} &\langle \exp\left( -i \int_0^{t_1} d\tau \, \delta\omega_{01}(\tau) \right) \rangle \\ &\quad = 1 - i \int_0^{t_1} d\tau \, \langle \delta\omega_{01}(\tau) \rangle \\ &\quad - \frac{1}{2} \int_0^{t_1} \int_0^{t_1} d\tau' d\tau'' \, \langle \delta\omega_{01}(\tau') \delta\omega_{01}(\tau'') \rangle + \cdots \\ &\quad \equiv \exp\big(-g(t)\big) = 1 - g(t) + \frac{1}{2} g^2(t) + \cdots \end{aligned} \tag{62}$$

Expand $g(t)$ in powers of $\delta\omega_{01}$:

$$g(t) = g_1(t) + g_2(t) + \cdots, \tag{63}$$

where $g_n(t)$ is on the order of $\mathrm{O}(\delta\omega_{01}^n)$. Substituting Equation (63) into (62), $g_1(t)$ is found to be 0. Therefore, $g(t)$ can be written as $g_2(t)$ on the order of $\mathrm{O}(\delta\omega_{01}^2)$:

$$g(t) = g_2(t) = \frac{1}{2} \int_0^{t_1} \int_0^{t_1} d\tau' d\tau'' \, \langle \delta\omega_{01}(\tau') \delta\omega_{01}(\tau'') \rangle, \tag{64}$$

which can be rewritten as:

$$g(t) = \frac{1}{2}\int_0^t \int_0^{\tau'} d\tau' d\tau'' \langle \delta\omega_{01}(\tau'')\delta\omega_{01}(0)\rangle. \quad (65)$$

$g(t)$ is called as the lineshape function, and $\langle \delta\omega_{01}(\tau'')\delta\omega_{01}(0)\rangle$ is the frequency-frequency correlation function (FFCF). Substituting Equation (65) into Equation (61), the emitted signal of linear spectroscopy on frequency domain after Fourier transform is described as:

$$\mathrm{S}(\omega) \propto \mathrm{Re}\left\{\int_0^{+\infty} e^{i(\omega-\omega_{01})t} e^{-g(t)} dt\right\}, \quad (66)$$

where the information of the FFCF exists but hidden in the convolution.

### 2.2.3. Dynamics in FFCF and spectral diffusion

According to Kubo's theory, assume the frequency fluctuation is a Markov process, FFCF can be described as the product of the square of the fluctuation amplitude $\Delta^2$ and an exponential decay with a correlation decay time $\tau$:

$$\langle \delta\omega(t)\delta\omega(0)\rangle = \Delta^2 e^{-\frac{t}{\tau}} \quad (67)$$

Kubo lineshape function is obtained after two integrals:

$$g(t) = \frac{1}{2}\int_0^t \int_0^{\tau'} d\tau' d\tau'' \langle \delta\omega_{01}(\tau'')\delta\omega_{01}(0)\rangle = \Delta^2\tau^2(e^{-\frac{t}{\tau}} + \frac{t}{\tau} - 1) \quad (68)$$

When $t \gg \tau$, the frequency fluctuations are small or fast, and the dephasing dynamics is fast. The Kubo function is in the *homogeneous limit*, which can be written as

$$g(t) = -\Delta^2\tau t. \quad (69)$$

Define the pure homogeneous dephasing time as:

$$T_2^* = \frac{1}{\Delta^2 \tau}, \tag{70}$$

Equation (69) can be rewritten as:

$$g(t) = e^{-\frac{t}{T_2^*}}. \tag{71}$$

Substituting Equation (71) to Equation (66), the frequency domain linear spectra is:

$$S(\omega) \propto \frac{1}{(\omega - \omega_{01})^2 - \frac{1}{T_2^{*2}}}, \tag{72}$$

which is a Lorentzian function with a full width half maximum of $1/T_2^*$. This reduces to Equation (57), where we treated the dephasing simply with a homogeneous dephasing factor. *Motionally narrowed* Lorentzian lineshape will be observed, since $1/T_2^*$ is smaller than the frequency fluctuation distribution Δ.

When $\tau \gg t$, which is corresponding to the slow frequency fluctuation of molecules, it is the *inhomogeneous limit*. Therefore, the FFCF is a constant:

$$\langle \delta\omega(t)\delta\omega(0) \rangle = \Delta^2 \tag{73}$$

The Kubo lineshape function can be rewritten as:

$$g(t) = \frac{\Delta^2 \tau^2}{2}, \tag{74}$$

So the frequency-domain linear spectra is obtained as:

$$\mathrm{S}(\omega) \propto \mathrm{Re}\left\{ \int_0^{+\infty} e^{i(\omega - \omega_{01})t} e^{-g(t)} dt \right\} \propto e^{-\frac{(\omega - \omega_{01})^2}{2\Delta^2}}, \tag{75}$$

which is a Guassian function with a full width half maximum of Δ.

For the case between homogeneous limit and inhomogeneous limit, the spectra is a convolution of a Lorentzian function and a Gaussian function, which is a Voigt profile. In the case that the frequency fluctuation has more than one physical process, the FFCF will have more than one exponential decay components, with each component has a correlation decay time of each physical process.

In the 2DIR spectroscopy, frequency fluctuation results in the *spectral diffusion* phenomenon. It is a time-propagation diagonal peak shape change, from a tilted shape elongated along the diagonal line to a rounder and more upright shape, which can be simply understood as the probe frequency gets deviated from the pump frequency as waiting time increases because of the frequency fluctuation. FFCF can be obtained directly from the 2DIR spectroscopy using the central line slope or the nodal line slope.[5, 6]

### 2.2.4. Anharmonicity

Consider a third-order nonlinear response process. After first two laser pulses, the system is located in population states of $|1\rangle\langle 1|$ or $|0\rangle\langle 0|$. After this point, there are three possible processes.

For those at ground state $|0\rangle\langle 0|$, the third pulse generates a coherence state between $|0\rangle$ and $|1\rangle$, and goes back to $|0\rangle$ population state with a decreasing of absorption at frequency $\omega_{01}$, which is called as the *ground-state bleach*.

For those at excited state $|1\rangle\langle 1|$, the third pulse can leads to either a coherence between ground state $|0\rangle$ and first excited state $|1\rangle$, or a coherence between first excited state $|1\rangle$ and second excited state $|2\rangle$. The former causes a decreasing in absorption at frequency $\omega_{01}$, and the

latter causes an increasing in the absorption at frequency $\omega_{12}$, which are named as the *stimulated emission* and *excited absorption* respectively.

The three processes result in two points on the 2DIR spectra. At same pump frequency $\omega_{01}$, the ground-state bleach and stimulated emission locates at $(\omega_{01}, \omega_{01})$, while the excited absorption locates at $(\omega_{01}, \omega_{12})$. It results in the phenomenon that the diagonal peaks in 2DIR appear in pairs. The frequency difference between these two peaks rises from the anharmonicity of the oscillator energy potential surface. In a conventional potential well of oscillator, including the harmonic oscillator, $\omega_{01}$ is larger than $\omega_{12}$, which means the excited absorption shifts to lower frequency compared with ground-state bleach and stimulated emission on the diagonal line. When the anharmonicity is reversed, which occurs in the very steep potential well as observed in delocalized excess protons in water cluster, the excited absorption shifts to higher frequency compared with ground-state bleach and stimulated emission. When the anharmonicity is 0, the two peaks overlap.

### 2.2.5. Crosspeak

In 2DIR spectra, there also sometimes exists crosspeak besides the diagonal peaks. Crosspeaks appear off the diagonal line, with its pump and probe pulses having different central frequencies.

Static crosspeak appearing at very short waiting time $t_2$ on the order of femtoseconds can be related to the coupling among different vibrational modes. When the local modes are strongly coupled, delocalized states are formed, which is called as the *vibrational exciton*. The Hamiltonian of coupling between two vibrational modes focused on the transition between the ground state and the first-excited state is described as:

$$\widehat{H} = \begin{pmatrix} \hbar\omega_1 & \beta_{12} \\ \beta_{21} & \hbar\omega_2 \end{pmatrix}, \tag{76}$$

where $\omega_1$ and $\omega_2$ are corresponding to the Hamiltonian of isolated vibrational modes respectively, and $\beta_{12}$ and $\beta_{21}$ is the coupling constant. Assume $\beta_{12} = \beta_{21}$.

In weak coupling limit, where $\beta_{12} \ll |\hbar\omega_1 - \hbar\omega_2|$, the Eigen value of energy is solved as:[7]

$$E_{1,2}^{exciton} = \hbar\omega_{1,2} \mp \frac{2\beta_{12}^2}{\hbar\omega_2 - \hbar\omega_1}. \tag{77}$$

In strong coupling limit, where $\beta_{12} \gg |\hbar\omega_1 - \hbar\omega_2|$, the Eigen value of energy is:

$$E_{1,2}^{exciton} = \frac{\hbar\omega_1 + \hbar\omega_2}{2} \mp \beta_{12}. \tag{78}$$

The anharmonicity of the crosspeaks varies from that of corresponding diagonal peaks because of the delocalization. In the case of strong coupling, anharmonicity of crosspeaks is much larger than diagonal peaks, and in the case of weak coupling, anharmonicity of crosspeaks is smaller than diagonal peaks.

Static crosspeak can also come from an intramolecular coupling called *Fermi resonance*. Fermi resonance appears when a transition accidentally has a similar frequency as an overtone or a combination mode. Moreover, this resonance is unpredictable before doing experiment, and is an obstacle when analyzing 2DIR data.

The time evolution of crosspeak could be related to different dynamic processes. One possible reason is the *population transfer*, which happens between the coupled vibrational modes that have similar vibrational energies. This time evolution could also yield from the so-called chemical exchange. In this case, the oscillator exists in two distinguished types of environment in solution, which means they do not result in small deviations around the same central frequency, but two distinguished peaks with two different central frequencies instead. In the process of

chemical exchange, the molecule is pumped is one environment, and probed when it moves to the other environment.

## 2.3. Implementation of 2DIR spectroscopy

### 2.3.1. Generation of ultrafast femtosecond laser pulse

The source of the ultrafast laser pulse for 2DIR set-up is generated by *Mai Tai* SP mode-locked Ti:Sapphire laser with a *Spitfire Ace* regenerative Ti:sapphire amplifier. The *Mai Tai* SP laser consists of a CW diode-pumped, intracavity, solid-state laser chamber and a Ti:Sapphire laser chamber. In the first chamber, the output of diode laser is used to pump $Nd^{3+}$ ion in Nd:$YVO_4$ medium, and the frequency-doubled output (532 nm) of Nd:$YVO_4$ laser using second harmonic generation is used to pump the Ti:Sapphire laser in the second chamber. In the second chamber, the material responsible for lasing is the Ti:Sapphire rod in the cavity between two mirrors. An acousto-optic modulator is applied to achieve the mode-locked operation. The output of Ti:Sapphire laser with a wavelength of 800 nm then undergoes a tuning process and enters the *Spitfire* amplifier. The amplifier consists of a stretcher, which lowers the pulse power to avoid threshold damage, a cavity, which amplifies the pulse, and a compressor, which compresses the pulse period. The *Mai Tai* laser along with *Spitfire* generates stable pulses centered at 800 nm with a repetition rate of 5 kHz and an average power of 1 W.

A chiller is used to water-cool and control the temperature of the crystals in CW pump laser and Ti:Sapphire laser to ensure a stable laser performance. The laser head is sealed to prevent dust and air moisture.

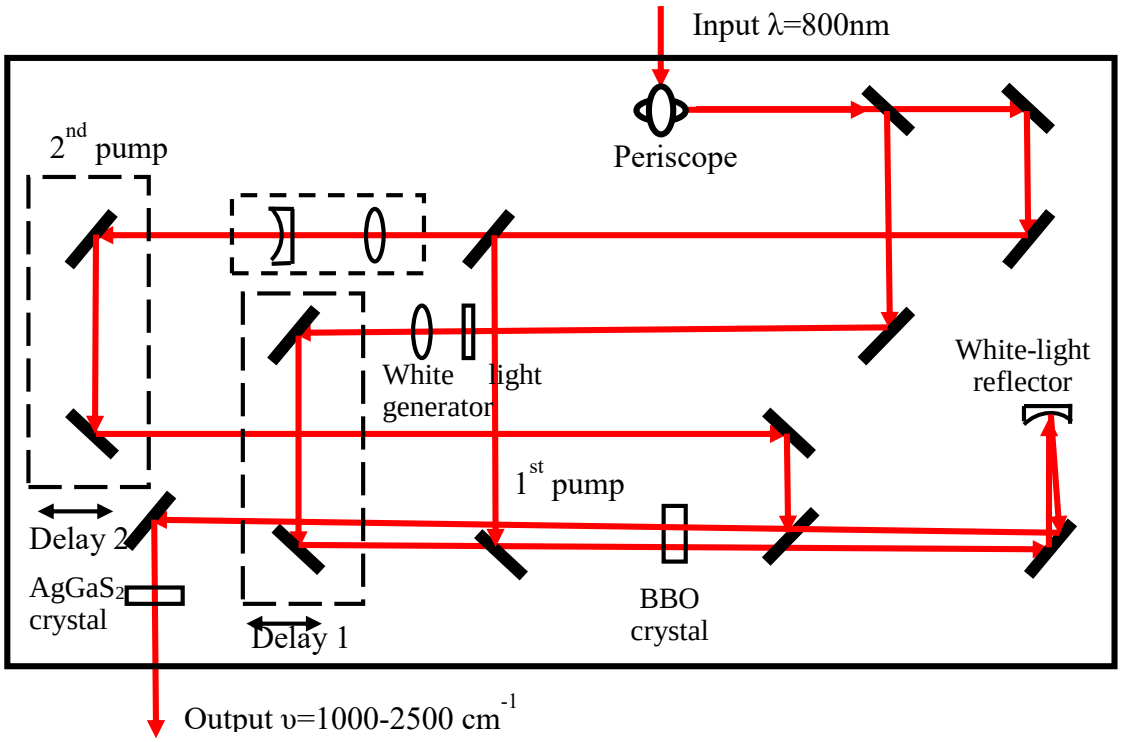


Figure 2.4. Set-up for the ultrafast optical parametric amplifier

The vibrational frequency of investigated modes is in the mid-infrared region. As a result, an optical parametric amplifier (OPA) is applied to generate stable ultrafast pulses in the infrared region with the 800 nm pulse from the amplifier. The simplified set-up of OPA-800C system is shown in Figure 2.4. The input light is split into two beams after the first beam splitter. About 96% of the energy is transmitted and used for the OPA pump. The 4% reflected light is used to generate a white light as a seed pulse for wavelength extension by focusing on a 2 mm thick sapphire plate. The pump beam passes the second beam splitter and is split again into two beams. Pump 1 and the re-collimated delayed white light focus on a BBO crystal ($\beta$-$BaB_2O_4$, type II) to pre-amplify the frequency component. Pump 2 then hits the pre-amplified continuum reflected back by the white-light reflector on the same BBO crystal at another spot to generate a signal and an idler. The signal and idler cover the wavelength from 1.1 µm to 1.6 µm, and from 1.6 µm to 3.0 µm respectively.

Finally, the signal and idler generate an ultrafast infrared laser pulse with the wavelength from 3 μm to 10 μm on the $AgGaS_2$ crystal (type II) by difference frequency generation.

### 2.3.2. 2DIR experimental set-up

Ultrafast laser pulses from OPA is split into four beams after two beam splitters. Three of them are used as external electric fields applied on the investigated sample, which is prepared between two windows that do not have absorption in the frequency region we look into (usually $CaF_{2)}$. The path length of the lights is determined by the thickness of the spacer put between the two windows.

The emitted light is detected in the direction determined by the *phase-matching condition*. Light propagates in the space is not only a function of time t and phase $\phi$, but also related to the propagation vector $k$, and its position. Therefore, an electric field can be described as:

$$E = E' e^{-i(\vec{k}\cdot\vec{r}-\omega t+\phi)}. \tag{79}$$

Denote the propagation vector of three pulses as $\vec{k}_1$, $\vec{k}_2$, and $\vec{k}_3$ at the time sequence. All of them are at different directions. The third-order macroscopic polarizations of rephasing pathway $R_1$ and non-rephasing pathway $R_4$ are described as:

$$P_1^{(3)} \propto e^{i(-\vec{k}_1+\vec{k}_2+\vec{k}_3)\cdot\vec{r}} e^{i(-\phi_1+\phi_2+\phi_3)} \int_0^\infty dt_3 \int_0^\infty dt_2 \int_0^\infty dt_1 \, E_3''(t-t_3) \cdot E_2''(t-t_3-t_2) \cdot E_1''^{*}(t-t_3-t_2-t_1) R_1(t_1,t_2,t_3), \tag{80}$$

and:

$$P_4^{(3)} \propto e^{i(\vec{k}_1-\vec{k}_2+\vec{k}_3)\cdot\vec{r}} e^{i(\phi_1-\phi_2+\phi_3)} \int_0^\infty dt_3 \int_0^\infty dt_2 \int_0^\infty dt_1 \, E_3''(t-t_3) \cdot E_2''^{*}(t-t_3-t_2) \cdot E_1''(t-t_3-t_2-t_1) R_4(t_1,t_2,t_3). \quad (81)$$

So the propagation vector of $P_1^{(3)}$ is $-\vec{k}_1+\vec{k}_2+\vec{k}_3$, and the propagation vector of $P_4^{(3)}$ is $\vec{k}_1-\vec{k}_2+\vec{k}_3$. The rephasing signals then can be separated from non-rephasing ones, but not among themselves. To collect both rephasing and non-rephasing signals, although it is possible to put two detectors in different directions, it is more convenient to exchange the pulse sequence of $\vec{k}_1$ and $\vec{k}_2$. $P_{1,4}^{(3)}$ is positive only if $t_1 \geq 0, t_2 \geq 0$, and $t_3 \geq 0$. Therefore, if $\vec{k}_2$ arrives the sample before $\vec{k}_1$ by scanning the time stage of pulses, the other type of signal can be collected in the same phasing matching direction. This configuration of three incident pulses is called as *boxcar configuration.*

The emitted light is heterodyned detected by the fourth pulse, *i.e.*, local oscillator, from the beam splitter to amplify the signal, which is called *heterodyne detection*. The intensity of the interference is detected by a nitrogen-cooled 64-element MCT array detector through a monochromator.

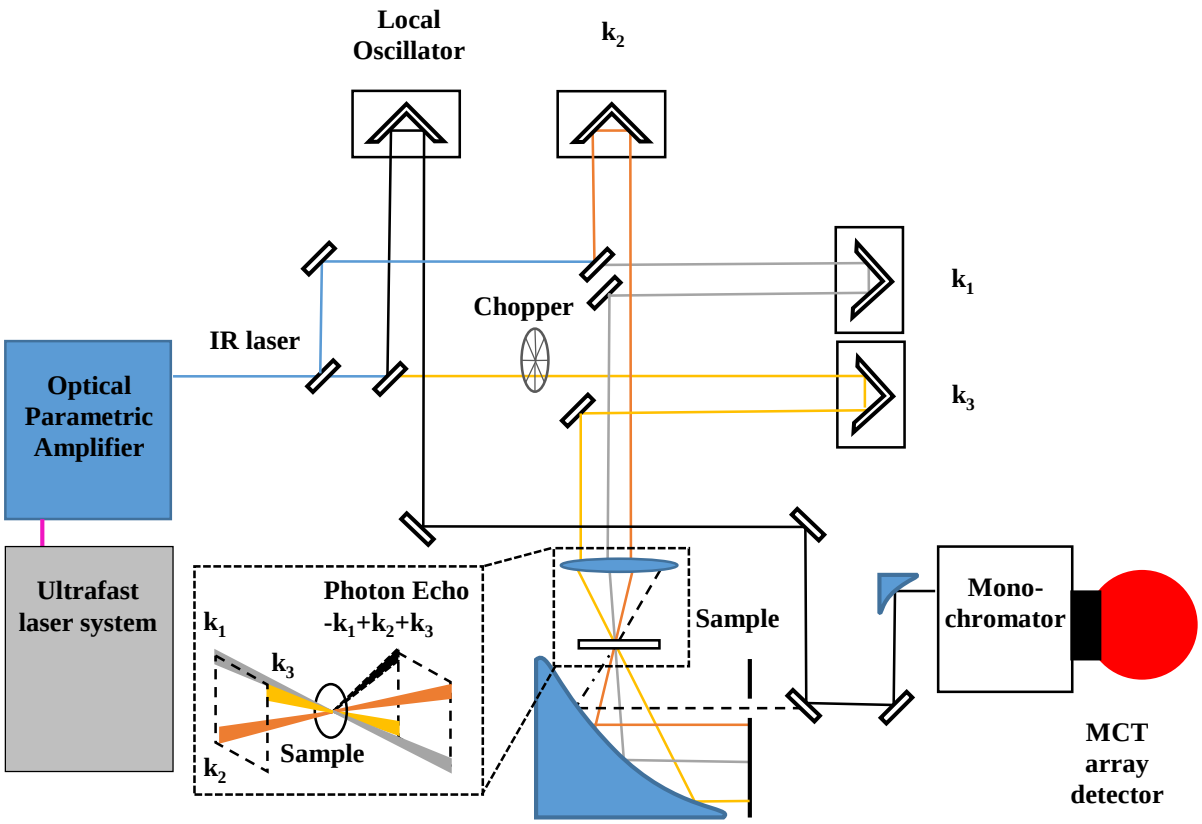


Figure 2.5. Scheme of 2DIR set-up.

## 2.4. Computational methods

Molecular dynamics (MD) simulation is a useful tool to help investigate the dynamics and structure in the many-body systems by simulating it numerically on the atom scale. Experimental spectroscopy measures macroscopic properties directly and investigates microscopic structure and dynamics by making assumptions and building models that relate to the microscopic properties with the macroscopic ones. MD simulation looks into the microscopic processes directly, and becomes a good tool besides the experimental methods.

The input for an MD simulation is the initial position, velocity, and the mass of all the atoms in the system, then the movement of all atoms is calculated for each time step, which is

normally on the order of femtosecond when investigating the dynamics in the condensed phase. In each step, forces on each atom are obtained first, then the new positions and velocities can be calculated. In this section, both the classical MD simulation and *ab initio* MD simulation will be discussed.

### 2.4.1. Classical MD simulation

Classical MD simulation treats every single atom (or united atoms) under Newton's Law. The implement is to calculate forces from a parameterized force field, which is firstly building a model to describe interactions and then either fitting the variables from experimental data, or from high-level calculations.

The overall energy potential is typically divided into four components:

$$V(\vec{r}) = V_{bonded} + V_{non-bonded} + V_{restraints} + V_{field}. \quad (82)$$

The bonded interaction potential $V_{bonded}$ is represented by terms dependent on bond length, bond angles, and torsional angles respectively.

The 2-body pair potential is described as a harmonic vibrational potential between the two covalently bonded atoms $i$ and $j$:

$$V_{bond}(r_{ij}) = \frac{1}{2} k_{ij}^{b} (r_{ij} - r_{ij}^{0})^2, \quad (83)$$

where $k_{ij}^{b}$ is the spring constant, $r_{ij}$ is the distance between two atoms, and $r_{ij}^{0}$ is the equilibrium distance.

The 3-body angular potential is also described by a harmonic vibrational potential, but among three covalently bonded atoms $i$, $j$, and $k$:

$$V_{angle}(\theta_{ijk}) = \frac{1}{2} k_{ijk}^{\theta} (\theta_{ijk} - \theta_{ijk}^{0})^2, \tag{84}$$

where $k_{ijk}^{\theta}$ is the angle force constant, $\theta_{ijk}$ is the angle in radians between $\overrightarrow{r_{ij}}$, and $\overrightarrow{r_{kj}}$, and $\theta_{ijk}^{0}$ is the equilibrium angle.

The 4-body dihedral angle (torsion) potential is divided into two categories: proper dihedral angle and improper dihedral angle. The former is formed by four consecutive atoms, while the latter is formed by three atoms centered around a fourth atom. The quartet potentials are described by:

$$V_{proper\ torsion}(\phi_{ijkl}) = k_{ijkl}^{C}(1 + \cos(n\phi_{ijkl} - \phi_0)), \tag{85}$$

$$V_{improper\ torsion}(\phi_{ijkl}) = \frac{1}{2} k_{ijkl}^{H} (\phi_{ijkl} - \phi_{ijkl}^{0})^2. \tag{86}$$

$k_{ijkl}^{C}$ is the force constant of the cosine type, and $k_{ijkl}^{H}$ is the force constant of the improper torsion . $\phi_{ijkl}$ is the angle between the plane going through the atoms i, j, k, and the plane going through j, k, l. $\phi_0$ and $\phi_{ijkl}^{0}$ are the equilibrium torsion, where the energy potential has its minimum value. $n$ is the multiplicity, which is the number of minima in the interaction potential as the dihedral angle rotates 360 degrees.

Non-bonded n-body interactions $V_{non-bonded}$ are treated by an effective pair potential for simplicity and computational efficiency.

The most famous potential model for non-bonded interactions is the Lennard Jones potential, which describes the Van der Waals potential as:

$$V_{LJ} = \sum_{\mathrm{I<J}} 4\varepsilon[\left(\frac{\sigma}{\mathrm{R_{LJ}}}\right)^{12} - \left(\frac{\sigma}{\mathrm{R_{LJ}}}\right)^{6}] \quad (87)$$

where ε is the depth of the potential well, σ is the finite distance where the potential is zero, r is the distance between the atoms.

Another common model for non-bonded interaction potential is the Coulomb potential, which describes the electrostatic interaction between two atoms:

$$V_{\mathrm{Coul}} = \sum_{\mathrm{i<j}} \frac{1}{4\pi\varepsilon_0} \frac{q_i q_j}{\varepsilon_R r_{ij}}, \quad (88)$$

where $q_i$ and $q_j$ are charges of the two atoms respectively. $\varepsilon_0$ is the permittivity of vacuum, $\varepsilon_R$ is the dielectric constant of the media, and $r_{ij}$ is the distance between two atoms.

Restraint potentials $V_{restraints}$ are used to restraint the motion of systems to avoid disastrous deviation, to fit for specific experimental data, or to accomplish sampling. Restraint potentials are not real potential and have numerous types, such as position restraint, angle restraint, torsion restraint, distance restraint, and orientation restraint, to implement different needs in computational simulation.

Fields $V_{field}$ are usually applied to describe two things: external potentials exerted on the system, which could be external electromagnetic field or flow; and continuum solvation, which approximates the solvent as the implicit continuous medium with several properties such as dielectric constant instead of the explicit solvent molecules.

Verlet algorithm is often applied in order to obtain the time propagation of velocity and position in each step.[8] The iteration is:

$$r(t + \delta t) = 2r(t) - r(t - \delta t) + f(t)/m \cdot \delta t^2, \quad (89)$$

Periodic boundary conditions are applied to minimize the edge effect and maintain the macroscopic behavior of the system. It is implemented by filling the universe with infinitive periodic replicas of fundamental boxes, which means a particle exiting one side of the box will enter the box from the opposite side. The cubic box is the most common box shape, while other shapes such as rhombic dodecahedron, truncated octahedron, are also available. *Minimum image convention* is used to ensure a correct short-range interaction picture, and long-range interactions and fluctuations with wavelength larger than box size might be not well described.

The classical MD simulation is convenient because it's much faster compared with *ab initio* simulation. This classical MD treatment can simulate large systems for very slow dynamics without consuming too much time. The disadvantages include, it is not as exact as the quantum treatment which solves Schrodinger equations. Especially when there is charge transfer, proton hopping, and other quantum effects, the classical MD cannot predict the system evolution correctly. Another problem is that one force field is fitted for one specific kind of system, so if the system is not parametrized before, you have to build a new force field yourself.

### 2.4.2. AIMD simulation

AIMD simulation invented by Car and Parrinello is a lot more exact compared with classical MD simulation since it does not have any empirical potential parameters. All the potentials are solved by time-dependent Schrodinger function. [9]

Solving the time-dependent Schrodinger function of the many-body system is prohibitively expensive. It became reachable after the Density Functional Theory (DFT) was proposed.[10]

Although other methods such as MP2 are developed and applied, DFT is still the most popular one.[11]

DFT method is based on the *Born–Oppenheimer (BO) approximation*, wherein the motions of nuclei and motions of electrons can be treated separately. Instead of using a big amount of wavefunctions to describe each electron respectively, DFT theory describes the electron structure of the whole system using only one potential, and all the interaction terms are hidden, which reduces the quantity of interest from 3n dimensions to 3 dimensions. System of n electrons can be studied as a set of n one-electron Schrödinger-like equations, which are called *Kohn–Sham equations*: [12]

$$-\frac{1}{2}\nabla^2 + V_{eff}(r)\varphi_i(r) = \epsilon_i\varphi_i(r). \tag{90}$$

The first term is kinetic energy functional, and the second term effective potential is:

$$V_{eff} = V_{ext} + \int \frac{n(r')}{|r - r'|}\ dr' + \frac{\delta E_{xc}[n(r)]}{\delta n(r)}, \tag{91}$$

where $V_{ext}$ is the external potential functional, $\int \frac{n(r\prime)}{|r - r\prime|}\ dr'$ is called the Hartree term, which describes the direct Coulomb interaction between electron, and the last term $\int \frac{n(r\prime)}{|r - r\prime|}\ dr'$ represents exchange-correlation energy.

Currently, it is proved that to obtain the exact exchange-correlation functional is prohibitive.[13] Therefore, approximations need to be made, and the exchange-correlation functionless of different level of approximation are developed. The accuracy increases as more complicated models are developed: Local Density Approximation (LDA), Generalized Gradient Approximation (GGA), meta-GGA, Hybrid Functional (HF) and *etc.*.[14]

## 2.5. Conclusion

In this chapter, we discussed the light-matter interaction in the infrared spectroscopy, derived the molecular response function for linear and nonlinear processes, and went through both the rephasing and non-rephasing pathways. Then we derived the frequency domain spectra that could be gathered from the detector while building a relationship between the 2DIR observables and the physical processes. After that, setups for the ultrafast infrared pulse generation, and for the 2DIR experiment are discussed. Finally, computational methods to simulate the molecular dynamics are introduced.

## 2.6. References


1. Mukamel, S., *Principles of nonlinear optical spectroscopy*. Vol. 29. 1995: Oxford university press New York.
2. Boyd, R.W., *Nonlinear optics*. 2003: Elsevier.
3. Cho, M., *Two-dimensional optical spectroscopy*. 2009: CRC press.
4. Kubo, R., *A stochastic theory of line shape.* Stochastic processes in chemical physics, 1969. **15**: p. 101-127.
5. Kwac, K. and M. Cho, *Molecular dynamics simulation study of N-methylacetamide in water. I. Amide I mode frequency fluctuation.* The Journal of chemical physics, 2003. **119**(4): p. 2247-2255.
6. Kwak, K., et al., *Frequency-frequency correlation functions and apodization in two-dimensional infrared vibrational echo spectroscopy: A new approach.* The Journal of chemical physics, 2007. **127**(12): p. 124503.
7. Hamm, P. and M. Zanni, *Concepts and methods of 2D infrared spectroscopy*. 2011: Cambridge University Press.
8. Verlet, L., *Computer "Experiments" on Classical Fluids. I. Thermodynamical Properties of Lennard-Jones Molecules.* Physical Review, 1967. **159**(1): p. 98-103.
9. Car, R. and M. Parrinello, *Unified approach for molecular dynamics and density-functional theory.* Physical review letters, 1985. **55**(22): p. 2471.

10. Parr, R.G., *Density functional theory of atoms and molecules*, in *Horizons of Quantum Chemistry*. 1980, Springer. p. 5-15.

11. Del Ben, M., et al., *Bulk liquid water at ambient temperature and pressure from MP2 theory.* The Journal of Physical Chemistry Letters, 2013. **4**(21): p. 3753-3759.

12. Kohn, W. and L.J. Sham, *Self-Consistent Equations Including Exchange and Correlation Effects.* Physical Review, 1965. **140**(4A): p. A1133-A1138.

13. Schuch, N. and F. Verstraete, *Computational complexity of interacting electrons and fundamental limitations of density functional theory.* Nature Physics, 2009. **5**(10): p. 732.

14. Perdew, J.P. and K. Schmidt, *Jacob's ladder of density functional approximations for the exchange-correlation energy.* AIP Conference Proceedings, 2001. **577**(1): p. 1-20.

# CHAPTER 3
# ACETATE ION AND ITS INTERESTING SOLVATION SHELL STRUCTURE AND DYNAMICS

## 3.1. Introduction

Ions are crucial species in medicine, biology, chemistry, and engineering due to their participation in important processes like nerve signaling,[1] ion transport through membranes,[2] chemical synthesis,[3] and electrochemical energy conversion.[3] Thus, in general, a basic characterization of the microscopic and macroscopic solvation phenomena of ions is extremely important from both a scientific and an engineering point of view. Ions are classified into two categories. The first category involves simple inorganic ions like $Na^+$, $Zn^{2+}$, and $Cl^-$, which are formed by reducing or oxidizing the atomic elements. The second category comprises ionized polyatomic molecular species; i.e., molecular ions, such as acetate, nitrate, and phosphate ions. Although simple inorganic and molecular ions share similar interactions with water molecules, the small difference in the interaction potential leads to large differences in the structure and dynamics of their hydration shell.[3]

One of first studies on ion hydration dates back more than 100 years, when Hofmeister showed the salting-out and salting-in effects that different ions exert on proteins, which is now known as the famous Hofmeister series.[4] The discovery of this series led to the definition of kosmotropes and chaotropes; i.e., water structure makers and breakers.[5] Interestingly, the

Reproduced from Zhang, X., R. Kumar, and D.G. Kuroda, *Acetate ion and its interesting solvation shell structure and dynamics.* The Journal of Chemical Physics, 2018. **148**(9): p. 094506, with the permission of AIP Publishing

definition of water structure makers and breakers did not arise from a microscopic analysis of the water structure, but from the macroscopic effects of the ions, such as protein precipitation, bacterial growth, etc.[6] However, it was until the last two decades, that the microscopic structure and dynamics of the ion hydration shell started to be directly investigated via advanced ultrafast laser spectroscopies and, in particular, third order non-linear infrared spectroscopy.[3] As a result, the hydration dynamics and structure of molecular ions, such as thiocyanate,[7-9] azide,[10-12] guanidinium,[13] oxalate,[14-16] phosphate,[17] nitrate,[18] hydroxide,[19, 20] borohydride,[21] etc. had been now studied. In addition, solvation structure of other ions like alkali halides have been indirectly investigated.[22-24] Notably, the hydration structure and dynamics of the acetate ion, an equally important molecular ion, has not been fully investigated yet.

Acetate ($CH_3COO^-$) is an ion with large applications in industry and important implications in life. In fact, the acetate ion is crucial for the synthesis of numerous derivatives like acetyl coenzyme A, citric acid, and oxaloacetate in cell organisms.[25] In addition, acetate ion is an analogue of a moiety commonly found in many important biomolecules, such as amino acids, lipids, and osmolytes, where the carboxylate group is covalently attached to a larger structure through a hydrophobic methylene group (-$CH_2$-).[25] Previous studies on the acetate ion solvation showed its interesting and unique properties.[4, 26-31] However, some of these studies reached contradictory conclusions. For example, the order of the activity coefficients for given concentration alkali in acetate ($Li^+ < Na^+ < K^+ < Rb^+ < Cs^+$) was found to be reversed in comparison with alkali chloride salts, and was explained by "localized hydrolysis."[26] In contrast, it was postulated that acetate ions are structure-makers because the hydrophobic group (methyl, -$CH_3$) has a comparatively larger effect than its hydrophilic groups (carboxylate, -$CO_2^-$).[4]

Moreover, a dielectric relaxation spectroscopy (DRS) study showed that the acetate ion presents two slow components in the dielectric spectrum, which were assigned to the hydration dynamics of the carboxylate and methyl groups, respectively. However, the dynamical component corresponding to the methyl group was observed to be fragile and to decrease markedly with increasing concentration.[27] Finally, it was found experimentally that the acetate ion presents a lower diffusivity than that predicted by the Stoke-Einstein relation indicating a tight binding to its solvation shell.[30] The observation is in agreement with the acetate Jones-Dolle's B-coefficient of $B = 0.10 \pm .02\ M^{-1}$ derived from Ref. [32]. Furthermore, it has been previously demonstrated by Hamm and Laage groups that those ions that bind tightly to its solvation shell should slowdown the rearrangements of the hydrogen bond network.[33, 34]

Other studies indirectly probing the hydration particularity of acetate have shown experimentally that the acetate ion does not form contact ion pairs.[29] A molecular simulation study explained the lack of ion pair formation by thermodynamics, since the contact ion pair of acetate was found to be of entropic origin, while the solvent-shared ion pair was mainly enthalpically favorable.[28] Thus, it remains as an open question whether the water solvation shell around the acetate ion is strengthened or weakened by the acetate ion. Furthermore, the molecular mechanism behind the lack of contact ion pair formation by the acetate ion is still unknown. To this end, a detailed microscopic description of the hydration shell dynamics and structure of acetate ion in solution is needed.

In this study, dilute solutions of sodium acetate (0.1M) in pure $D_2O$ (referred as water in the rest of the manuscript) and in 6M NaCl solution are studied via linear and non-linear infrared (IR) spectroscopies and *ab initio* molecular dynamics simulation (AIMD). The selected non-linear

spectroscopy is two dimensional infrared spectroscopy (2DIR) because it can measure the dynamics of solvent motions from femtoseconds to picosecond timescales.[35] The IR studies are focused on the carboxylate asymmetric stretch mode of the acetate ion to investigate its hydration shell dynamics, because it has been previously established that this group is a sensitive probe to the local environment for other ions,[14, 16, 36, 37] zwitterions,[38] and peptides.[39, 40] The experimental findings are complemented with AIMD simulations and a frequency map to uncover and/or confirm the molecular processes giving rise to the observed vibrational dynamics of the acetate ion.

### 3.2. Experimental and theoretical methods

#### 3.2.1. Sample preparation

Deuterium oxide ($D_2O$, >=99.75 % D) was obtained from Acros Organics. Sodium acetate ($NaC_2H_3O_2$, 99%), sodium azide ($NaN_3$, 99.8%), and sodium chloride (NaCl, 99.0%) were purchased from MCB reagents, Sigma Aldrich, and Fisher Chemical, respectively. All chemicals were used without further purification, except for the sodium acetate that was dried in the vacuum oven previous to its use. Sodium acetate and sodium azide were dissolved in $D_2O$ and 6M NaCl $D_2O$ solution, respectively, to obtain 0.1M solutions. The acetate and azide samples were held in between two $CaF_2$ windows separated by a spacer of 12 μm and 25 μm, respectively. All experiments were measured at room temperature (23 ℃).

### 3.2.2. Infrared spectroscopies

The Fourier transform IR (FTIR) spectra were collected with a Bruker Tensor 27 spectrometer with a resolution of 0.5 $cm^{-1}$. Each reported FTIR spectrum is an average of 40 scans.

The setup used consists of the typical boxcar configuration photon echo setup with heterodyne detection.[35] In short, broadband IR pulses, with a temporal width of ~60 fs, are generated by a Ti:Sapphire amplifier (Spectra Physics Spitfire Ace) with a 5 kHz repetition rate in combination with an optical parametric amplifier (Spectra Physics OPA-800C) and difference generation crystal. The non-linear response of the sample is produced by focusing and temporally and spatially overlapping three split replicas (wave vectors: $\mathbf{k}_1$, $\mathbf{k}_2$, and $\mathbf{k}_3$) of the original IR pulse at the sample using the boxcar configuration. The photon echo signal produced by the sample is collected in the phase matching direction ($-\mathbf{k}_1 + \mathbf{k}_2 + \mathbf{k}_3$) and heterodyned with a fourth IR pulse (local oscillator) for detection. The detection occurs in a liquid nitrogen cooled 64 element MCT array detector (Infrared Systems Development) after the photon echo and local oscillator are dispersed in a Triax monochromator (100 grooves/mm). Two pulse sequences, rephasing (with a time order $\mathbf{k}_1 < \mathbf{k}_2 < \mathbf{k}_3$) and non-rephasing (with a time order $\mathbf{k}_2 < \mathbf{k}_1 < \mathbf{k}_3$) are measured to obtain the 2DIR spectra. The coherence time interval $\tau$ was scanned from -3500 fs to 3500 fs with a step of 5 fs, and the waiting time T was scanned with a step of 150 fs from 0 ps to 2.1 ps. In all the cases, the local oscillator preceded the photon echo signal by ~1 ps. The 2DIR spectra were obtained by a double Fourier Transformation on the photon echo signal from ($\tau$, $T_w$, t) to ($\omega_\tau$, $T_w$, $\omega_t$), while $T_w$ is kept as a parameter. A detail explanation of this analysis can be found elsewhere.[41]

### 3.2.3. *Ab initio* molecular dynamics (AIMD) simulation

The system was selected to be model via AIMD simulations because of the reproducibility of the self-diffusion coefficient of water molecules in solutions with high salt concentration.[42] The simulation boxes for sodium acetate in water and sodium acetate in salt solutions were built by Packmol.[43] Due to high computational cost of the AIMD, the selected box size was 15Å×15Å×15Å. In this box, the 0.1M sodium acetate solution was represented by 113 water molecules and one sodium acetate molecule, while the 0.1M sodium acetate salt solution consisted of 121 water molecules, six $Na^+$ ion, six $Cl^-$ ion, and one sodium acetate molecule, or equivalent 3 M NaCl. Note that the 3 M NaCl solution was used because the simulation at 6 M NaCl produced phase separations. The concentration of acetate in simulation is larger than 0.1M due to the limitation of the box size for performing AIMD simulations. However, the box contains only one acetate ion, which inhibits acetate-acetate interactions, and it is sufficiently large to accommodate both ions without forming ion pairs all the time.

Classical molecular dynamics simulations (MD) were first performed to achieve equilibrated states which are later used as starting points for the AIMD simulations. Classic MD simulations with periodic boundary conditions were carried out by Large-scale Atomic/Molecular Massively Parallel Simulator (LAMMPS)[44] with the input files generated by moltemplate software[45] using the Optimized Potentials for Liquid Simulations (OPLSAA) force field.[46] The TIP3P water model was chosen for describing the water molecules in the solution.[47] The systems first underwent a 1 ns canonical simulation (in the NVT ensemble) followed by a 1 ns isothermal-isobaric simulation (in the NPT ensemble) to achieve equilibrium. Finally, the whole system underwent another 5 ns of canonical simulation as production run. In all cases, the

simulation temperature was 300 K and Nose-Hoover thermostat with a damping constant of 100 fs was used. In the NPT simulation, a Nose-Hoover barostat with a damping constant of 1 ps was used. The time step in all the simulations was 1 fs. About 15 snapshots from the final NVT simulation of each system were randomly chosen and used as starting configurations for the AIMD simulations.

The AIMD simulations were performed using the CP2K software package.[48] The simulations were carried out using the BLYP functional with TZV2P basis set and GTH pseudopotentials for the inter core electrons.[49] The functional as well as the basis set were selected because they have been shown to reproduce both the structural and dynamical properties of water.[50] All simulations were carried out in the NVT ensemble with periodic boundary conditions and a temperature of 300K. The temperature was maintained by using a Nose-Hoover thermostat with a 100 fs temperature damping constant. For sodium acetate in water, 13 trajectories of AIMD simulation were obtained, each having a temporal length of 6.5 ps with a step of 0.5 fs. The first 0.5 ps in each trajectory was discarded from the analysis to assure that the system had reached equilibrium. For sodium acetate in NaCl solution, only nine of the 15 original trajectories were used because the other six have contact ion pairs, but the vibrational signature of ion pairs is spectrally separated from that of the free ion (see below). In addition, the inclusion of ion pairs fail to produce a good estimate of the FFCF (not shown). Each trajectory for the acetate ion in NaCl solution has a temporal length of 7 ps with a time step of 0.5 fs. In this case, the first 1 ps of the trajectory was discarded to allow the system to reach equilibrium conditions.

### 3.2.4. Theoretical frequency-frequency correlation function

A density functional theory (DFT) map developed for the acetate ion was used to derive the frequency fluctuations of its carboxylate asymmetric stretch mode in pure water and in NaCl solution from the AIMD simulation.[40] The DFT map relates the solvent structural fluctuation with the vibrational frequency by empirically linking the vibrational mode frequency with electric fields exerted by the solvent molecules on the atoms involved in the vibrational mode. In this case, the vibrational mode is the asymmetric stretch of acetate and the electric fields are computed on the carbon and oxygen atoms of the carboxylate group.[40] The frequency of the mode is calculated based on the equation, $\omega[\boldsymbol{E}(\boldsymbol{r})] = \Sigma\, C_{ij} E_i(r_j)$, where $\omega[\boldsymbol{E}(\boldsymbol{r})]$ is the frequency of the transition between ground state and first excited state in the electric field $\boldsymbol{E}$, $E_i$ is the electrostatic field or its gradient, $C_{ij}$ is the empirically determined electrostatic parameters obtained from the DFT map, $i$ is the directions of the field or the gradient ($i$ = x, y, z, xx, yy, zz, xy), and $j$ represents the atom at which the fields and the gradients are calculated.

The instantaneous frequencies of the carboxylate asymmetric stretch mode were calculated at each time step in the AIMD simulation trajectory using the DFT map. The electric fields and gradients generated by water molecules from the first solvation shell were computed from the coordinates of AIMD trajectories. Note that the charges of the water molecules were assumed to be those from the TIP3P water model because this model was used for creating the DFT map.[40, 47] The fluctuation of the instantaneous frequencies ($\omega(t)$) was computed as: $\delta\omega(t) = \omega(t) - \langle\omega\rangle$), where $\langle\omega\rangle$ is the average of the frequency of all the trajectories. The frequency-frequency correlation function (FFCF) was computed as the average of the individual correlation functions (i.e., $\langle\delta\omega(0)\delta\omega(t)\rangle$) derived for each trajectory.

## 3.3. Results

### 3.3.1. FTIR spectroscopy

The FTIR spectra of 0.1M sodium acetate in $D_2O$ and in 6M NaCl solution are shown in Figure 3.1. The solvent subtracted spectra exhibits two peaks located at ~1420 $cm^{-1}$ and ~1560 $cm^{-1}$. The high frequency peak has been previously assigned to the antisymmetric stretching mode of the carboxylate group ($AS_{COO}$), and the partially overlapped peak at ~1420 $cm^{-1}$ to its symmetric stretching mode.[51] At low frequencies, there is another small peak at ~ 1350 $cm^{-1}$, which is likely from the symmetric $CH_3$ deformation.[52] The comparison between the spectra of sodium acetate in 6M NaCl solution and in $D_2O$ shows that there is no obvious difference in bandwidth and central frequency for the modes observed in this region, aside from the difference in the low frequency part due to background subtraction errors caused by the presence of both the combination mode of $D_2O$ at ~1555 $cm^{-1}$ and the bending mode at ~1210 $cm^{-1}$.[53] Furthermore, the bands of the $AS_{COO}$ observed for the acetate ion in $D_2O$ and NaCl solutions have almost a perfect overlap (inset Figure 3.1). Finally, the IR spectrum of acetate in the carboxylate symmetric and asymmetric stretch region does not appear to be concentration dependent (Figure 3.2).

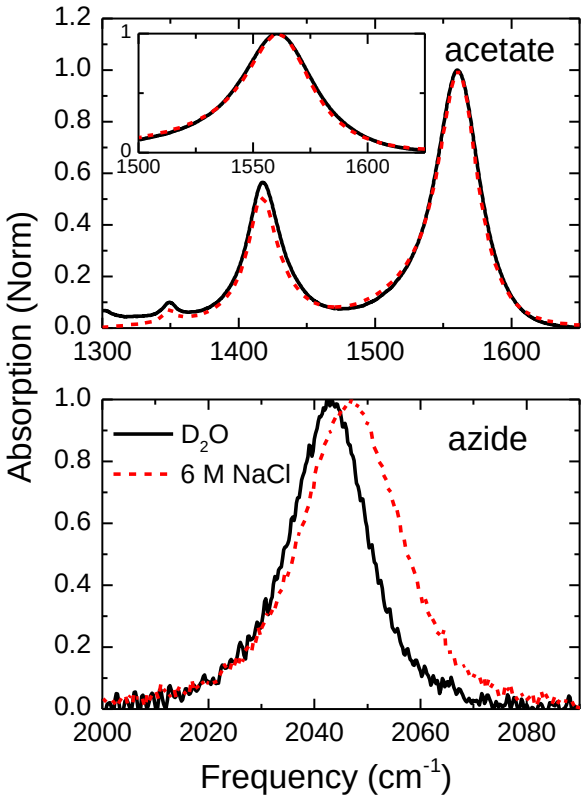


Figure 3.1. Solvent subtracted FTIR spectra of 0.1 M sodium acetate (top panel) and 0.1 M sodium azide (bottom panel) in the asymmetric stretch region of O=C=O and N=N=N. Black solid and red dashed lines correspond to $D_2O$ and 6M NaCl solutions, respectively.

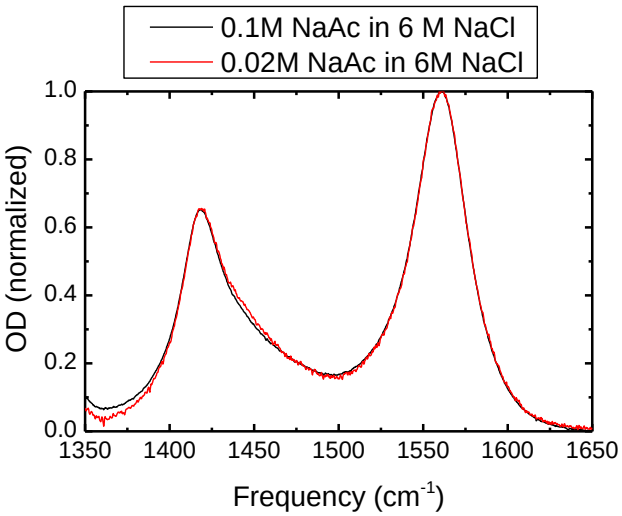


Figure 3.2. Concentration dependence of the carboxylate symmetric and asymmetric stretch of carboxylate in acetate.

### 3.3.2. Two dimensional infrared spectroscopy (2DIR)

The 2DIR spectra of sodium acetate in $D_2O$ and in sodium chloride solution at the frequency range of the $AS_{COO}$ for different waiting times ($T_W$) is shown in Figure 3.3. In these 2D spectra, the horizontal ($\omega_t$) and vertical ($\omega_\tau$) axes represent the probe and pump frequencies, respectively. Each 2DIR spectrum shows a negative peak (blue right peak) and a positive peak (red left peak), which are related to the transitions of the $AS_{COO}$ from the vibrational ground state to the first excited state ($\nu$=0 to $\nu$=1), and from the first excited state to the second excited state ($\nu$=1 to $\nu$=2), respectively. The ~30 $cm^{-1}$ separation between the negative peak and the positive evidences the anharmonic nature of the vibrational potential of the $AS_{COO}$ mode. Note that the peaks observed in any 2DIR spectra do not contain the contact ion-pair transition since those appear at ~1580 $cm^{-1}$ (Figure 3.4) and ion-pair vibrational frequency assignment is in agreement not only with the peak position for the contact ion-pair formed by another carboxylate containing ion,[37] but also with theoretical studies.[54] Moreover, the peak at 1590 $cm^{-1}$ shows the expected increase in intensity with NaCl concentration, though it has a very small contribution in both cases (Figure 3.4.). In addition, the 2DIR spectra appears to show of fifth order signals in the region corresponding to the $\nu$=2 to $\nu$=3 transitions, which is assigned to fifth order and not a cascade signal,[55] due to the presence of the diagonal peak (Figure 3.4.). The presence of high order processes is not new and is likely to arise from the large transition dipole of the asymmetric stretch of carboxylate asymmetric stretch. However, it is expected that will have a small contribution to the overall signal.[55]

The time evolution of 2DIR shows that at short waiting times the 2DIR peaks are more elongated and tilted along the diagonal line ($\omega_t = \omega_\tau$, black line in the 2D plots of Figure 3.3.), and

as $T_W$ increases the 2DIR peaks become rounder and less tilted along the diagonal. The change in the elongation and tilt of the peaks is due to the loss of correlation between pump and probe frequencies as a result of motions of the solvent molecules in the solvation shell of the acetate ion; i.e., spectral diffusion.[35] Interestingly, the rate at which the $AS_{COO}$ loses its correlation appears to be different in the two samples, as evidenced by the tilt of the 2D peaks which is still observed in the 2DIR spectrum at $T_W$ = 2.1 ps of 6M NaCl sample, and is not clear in the 2DIR peaks of the acetate ion in $D_2O$.

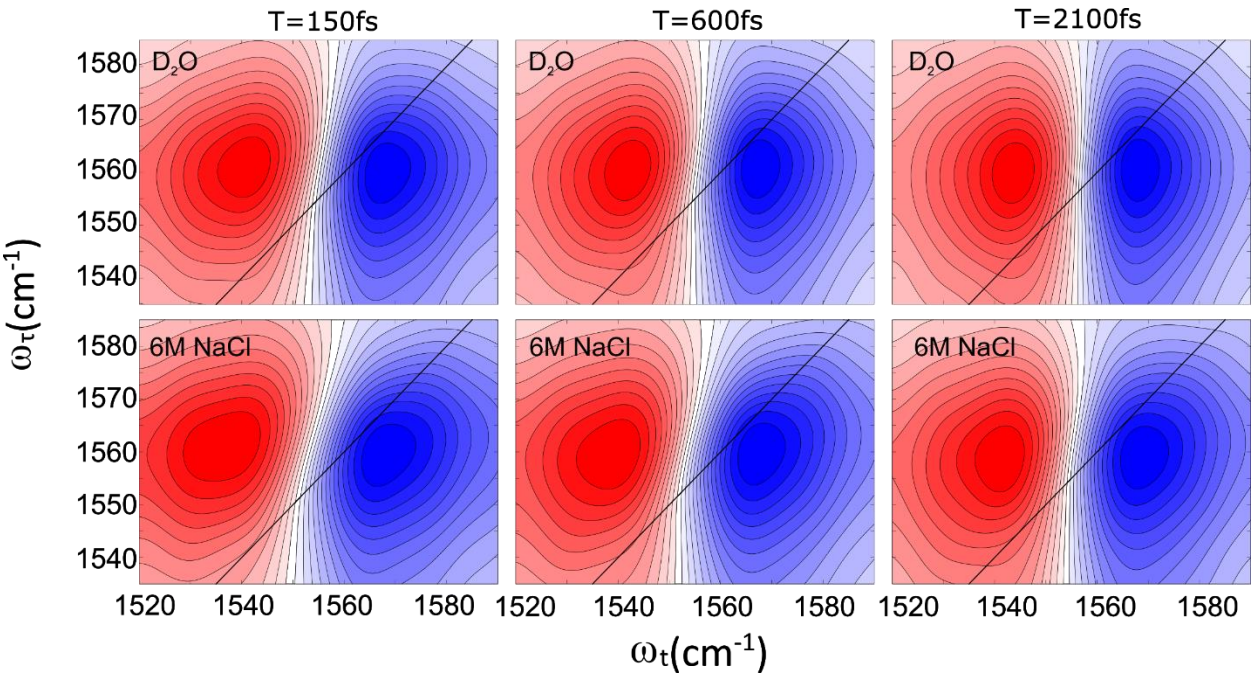


Figure 3.3. 2DIR spectra as function of waiting time of sodium acetate in $D_2O$ (top) and in 6M NaCl (bottom) solution.

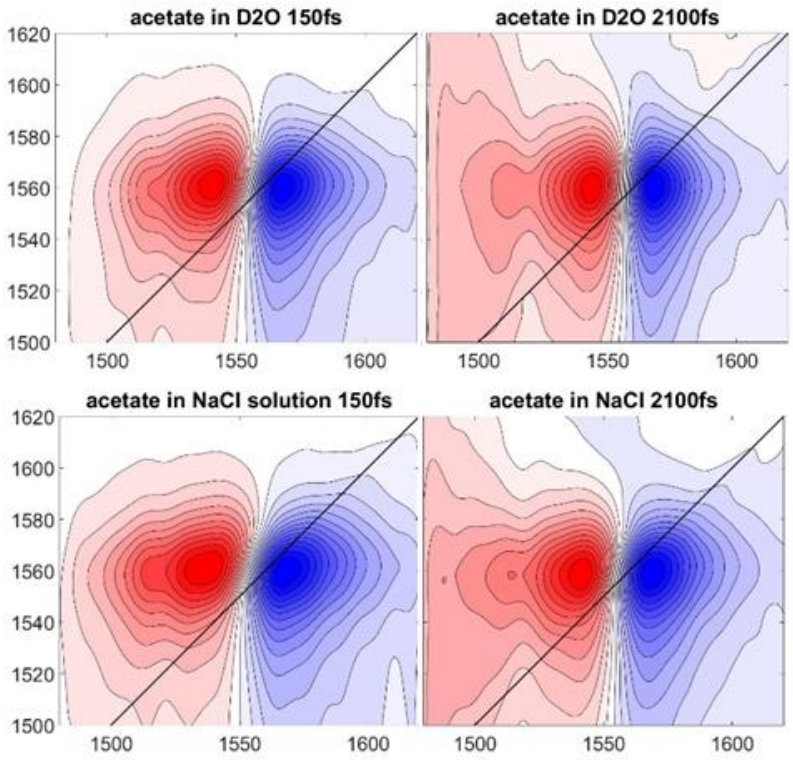


Figure 3.4. 2DIR spectra of acetate at larger frequency windows, showing that the main peaks do not contain the contact ion-pair transition.

### 3.4. Discussion

The FTIR absorption spectra of the $AS_{COO}$ mode of the acetate ion in $D_2O$ and in NaCl solutions (Figure 3.1) is not well modeled with two Voigt profiles, which is in agreement with a previous report.[31] As seen in the FTIR spectra, the derived central frequency of the $AS_{COO}$ mode is statistically the same for the two solutions (Table ). The results indicate that the interaction between acetate and sodium ions is very weak even at a 6M NaCl concentration, where the ratio of sodium to acetate ions is ~8:1. The weak interaction is also evidenced by the lack of a noticeable contact ion pair peak in the linear IR spectra, which is only barely noticeable in the 2DIR spectra (Figure 3.4). In addition, the lack of formation of contact ion pairs by the acetate ion is also in agreement with a previous study.[29]

Table 3.1. Parameters derived from the FTIR spectra of sodium acetate and azide in water and NaCl solution.

| Ion | Parameter | $D_2O$ | 6M NaCl | Difference |
|---|---|---|---|---|
| Acetate | $\omega_0$ ($cm^{-1}$)* | 1561.3 ± 0.1 | 1561.4 ± 0.1 | 0.1 |
| Acetate | FWHM ($cm^{-1}$)** | 38.6 ± 0.5 | 36.4 ± 0.5 | -2.4 (-6%) |
| Azide | $\omega_0$ ($cm^{-1}$)* | 2042.7 ± 0.1 | 2046.7 ± 0.1 | 4.0 (0.2%) |
| Azide | FWHM ($cm^{-1}$)** | 17.1 ± 0.5 | 21.4 ± 0.5 | 4.3 (25%) |

*Computed by fitting with a Voigt profile.
**Derived directly from the normalized FTIR.

Similar to the central frequency, the full width at half maximum (FWHM) of the $AS_{COO}$ band remains fairly constant when the solution has large amounts of NaCl (Table 3.1.). While the slight difference in the width of the band might be real, it only represents a change of less than 6% with respect to the $D_2O$ solution. To verify that the bandwidth of the $AS_{COO}$ band is particularly different from other ions, the change in asymmetric stretch mode is compared with that of the azide ion ($N_3^-$). Note that the azide ion was selected due to the similarity of the normal mode; i.e., asymmetric stretch involving three atoms. In addition, the azide ion has a B-coefficient of -0.014 $M^{-1}$, which is similar to that of the chloride ion (B = -0.014).[56] Thus, it is not expected that the azide ion will perturb significantly the water or salt solution structures.[33, 34]

In contrast with the acetate ion, FWHM and central frequency of the $N_3^-$ asymmetric stretch of the azide ion show a ~4 $cm^{-1}$ blueshift and 25% bandwidth when the concentration of sodium and chloride ions is set to 6M, displaying the expected sensitivity of the ion to changes in the concentration of ions in the water solution. In addition, the lack of change in the central frequency of the $AS_{COO}$ of the acetate ion suggests that the carboxylate group of acetate maintains a similar interaction with the solvent in both $D_2O$ and NaCl solutions. The lack of change in bandwidth of the $AS_{COO}$ band points to an unexpected similarity in the vibrational dynamical components giving rise to the lineshape of the acetate $AS_{COO}$.

The semi-classical theory predicts that the FTIR lineshape depends on the vibrational lifetime ($T_{10}$), rotational diffusion ($D$), and the FFCF through its lineshape function (g(t)). The mathematical expression of the FTIR lineshape is given by:[35]

$$S(\omega) \propto Re \int_0^\infty e^{i(\omega-\omega_{01})t}\, e^{-t/2T_{10}} e^{-2Dt} e^{-g(t)} dt, \quad (1)$$

where $\omega_{01}$ is the transition frequency and $g(t)$ is the double integral of the frequency-frequency autocorrelation function (FFCF); i.e., $g(t) = \int_0^t \int_0^{\tau'} d\tau' d\tau'' < \delta\omega_{01}(\tau'')\delta\omega_{01}(0) >$ . The analytical form of the FTIR lineshape and the striking similarity in the FWHM of the $AS_{COO}$ could indicate the change of two or more of its parameters in opposite directions such that the total effect is cancelled out. However, the vibrational lifetime derived from the waiting time dependence of the 2DIR spectra shows that the $T_{10}$ of the $AS_{COO}$ does not change significantly between the two samples (Figure 3.5). Note that the $T_{10}$ values are in agreement with a previous study.[31] It is also possible that the lack of change in the lineshape width is caused by a compensation in the rotational diffusion ($D$). However, the extremely short lifetime of the vibrational transition does not allow us to measure a reliable value of $D$. To discard this effect, the $D$ value of another acetate ion (trifluoroacetate)[37] with a slightly longer $T_{10}$ is used. In this case, the reorientational motion of the $AS_{COO}$ of trifluoroacetate ($\tau_c = 1/6D = 4.3\, ps$) reveals that the rotation diffusion only accounts for a very small percentage of the total lineshape width (~1 $cm^{-1}$). Furthermore, theoretical results from the AIMD simulation support a slow decay of the orientational correlation function (see below, Figure 3.6, and Table 3.2). Another possibility arises from a similarity in all the parameters of the Eqn. (1) for both the $D_2O$ and 6M NaCl acetate solutions. However, as previously mentioned the dynamics of the FFCF is not the same in both samples. Thus, it is likely

that the similarity in the lineshape width is caused by the compensation of the parameters within the FFCF. To assess this last possibility, all the FFCF parameters are required.

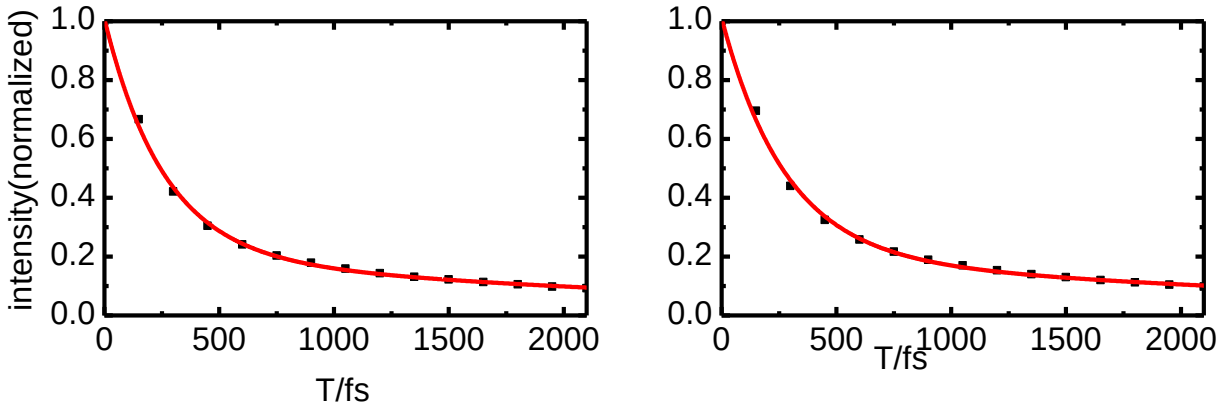


Figure 3.5. The vibrational lifetime derived from the waiting time dependence of sodium acetate in D2O (left) and in NaCl (right).

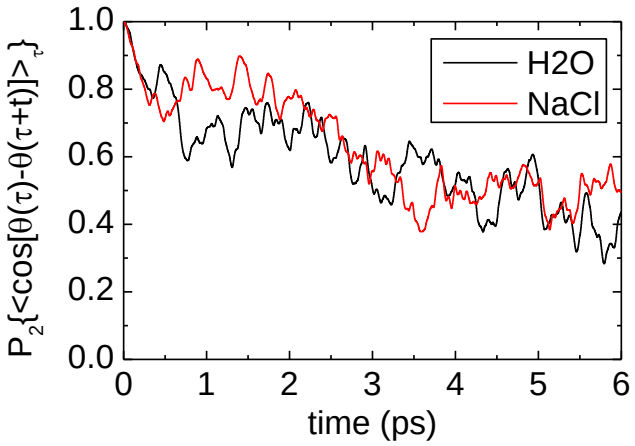


Figure 3.6. Dipole reorientation dynamics of the $AS_{COO}$ computed from the AIMD. The exponential characteristic decay times were found to be 8.8 ± 0.1 ps and 8.2 ± 0.1 ps for water and NaCl solutions, respectively.

Table 3.2. Exponential decay fitting parameters of $P_2\{<\cos[\theta(\tau)-\theta(\tau+t)]>\}$

| Sample | $A_1$ | $\tau_1$ (ps) | $A_2$ | $\tau_2$ (ps) |
|---|---|---|---|---|
| Water | 0.22±0.01 | 0.17±0.01 | 0.81±0.01 | 8.20±0.01 |
| NaCl solution | 0.16±0.01 | 0.06±0.01 | 0.89±0.01 | 8.81±0.01 |

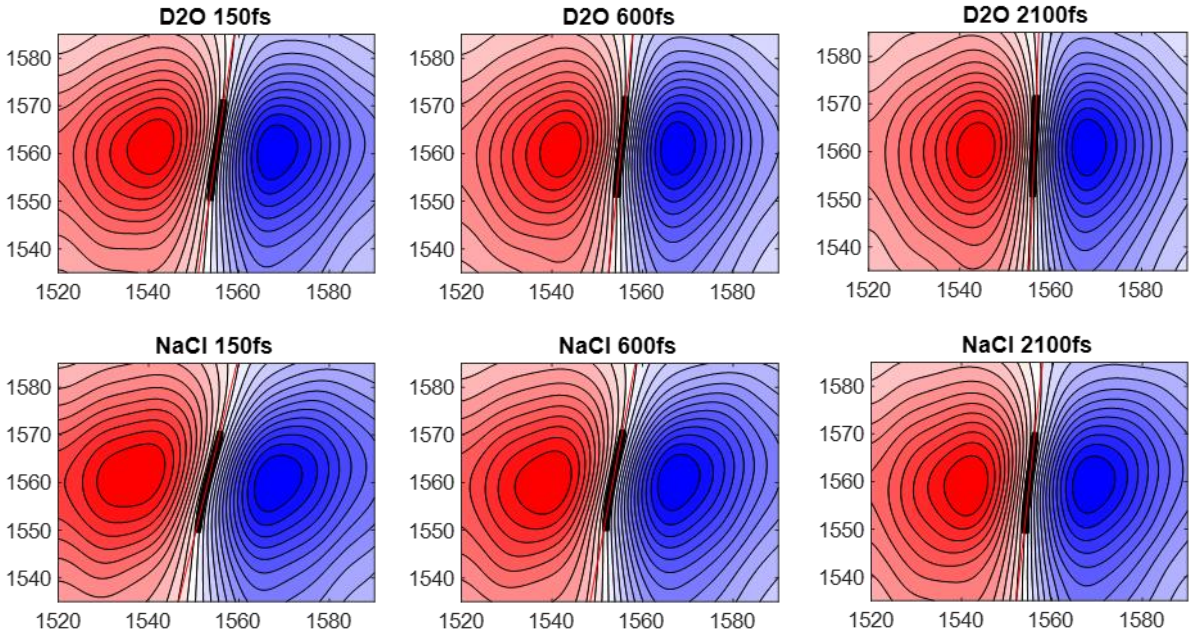


Figure 3.7. 2DIR spectra of acetate in $D_2O$ (top panels) and salts solutions (lower panels). Black point corresponds to the points used to calculate the inverse slope and red line is the linear fitting of the points.

The decorrelation times of the FFCF of the $AS_{COO}$ are extracted from the $T_W$ evolution of the 2DIR spectra. Here, the characteristic times of the FFCF for both samples were derived from the inverse of slope of the zero contour line separating the negative and positive peaks (Figure 3.7) because it has been shown that this spectral feature correctly describes the dynamics of the FFCF.[57, 58] Note that the inverse slope was calculated in a range of ±10 $cm^{-1}$ of the central frequency. The time dependence of the inverse slope for the $AS_{COO}$ in water and salt solutions is shown in Figure 3.8. The inverse slope presents different values at short waiting times for the $AS_{COO}$ in water (~0.15 at $T_W$ = 0.15 ps) and in 6M NaCl solution (~0.25 at $T_W$ = 0.15 ps) indicating an increase in the contribution of inhomogeneous part of FFCF with addition of NaCl.[59] This increment cannot be due to a change in the vibrational lifetime ($T_{10}$) of the acetate ion in both solutions since they are very similar (Figure 3.5). In addition, the inverse slope decreases to ~0.04

at the longest waiting time measured ($T_W$= 2.1 ps) for acetate in $D_2O$, while the value for the 6M NaCl sample at the same waiting time is ~0.1. The change in the inverse slope at longer waiting times evidences the rise of a slow dynamical component with increasing amounts of sodium chloride in the solution.

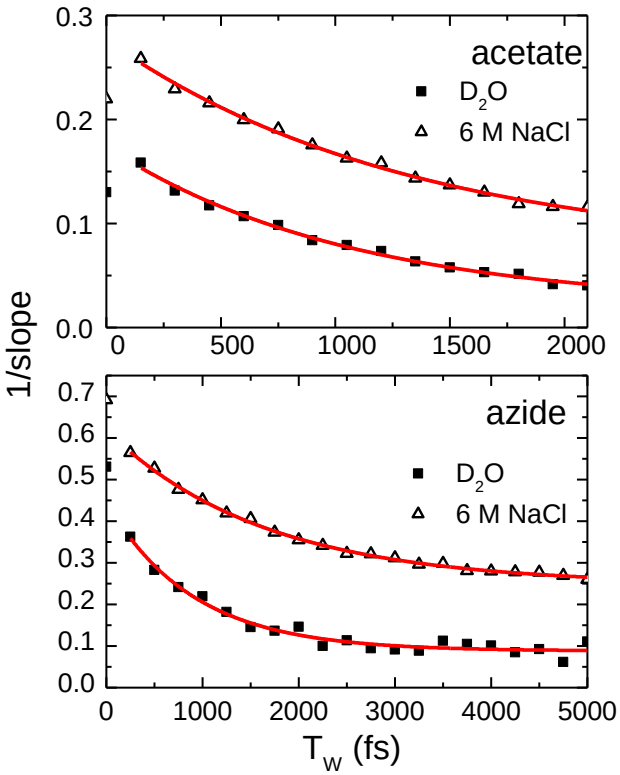


Figure 3.8. Inverse of slope vs. waiting time ($T_W$) for the asymmetric stretch of sodium acetate (top panel) and azide (bottom panel). Black filled squares and open triangles correspond to the experimental inverse slope of the ions in water and NaCl solutions, respectively. The red line represents its exponential decay fitting as described in the text. Note that the first data point at $T_W$ = 0 fs is excluded from the fitting due to the influence of non-resonance signals from the sample and sample cell components.

The waiting time evolution of the inverse of slope for both water and salt solutions were modeled with an exponential decay function of the form: $f(t) = y_0 + Ae^{-\frac{t}{\tau_1}}$, where $y_0$ is the offset, A is the amplitude of the dynamical component, and $\tau_1$ its characteristic time. The parameters of

the fitting are listed in Table 3.3. Interestingly, the only observed decay time ($\tau_1$) is ~1.2 ps, irrespective of the salt concentration, and is on the same timescale as the FFCF decay time of the aqueous trifluorocarboxylate ion (~0.8 ps).[37] It was previously established that the picosecond characteristic time of the FFCF is related to the hydrogen bond network reorganization dynamics around the carboxylate group of the acetate ion.[37] The similarity between the decay time in both $D_2O$ and 6M NaCl solutions suggests that the carboxylate group of acetate ion must be sensing the same type of water dynamics in both solutions. While it is possible that the NaCl does not influence the hydrogen bond network reorganization dynamics of water, previous experimental studies have demonstrated definitively that the water slow down its dynamics in the presence of salts like NaBr.[60] Furthermore, the inverse slope derived from the 2DIR of sodium azide in the same conditions (Figure 3.9) shows a factor of two in slowdown of the FFCF dynamics of the $N_3^-$ asymmetric stretch mode (Table 3.3), which corroborates the expected slowdown in the motions of water. Overall the FFCF modeling agree with the most likely scenario for explaining the similarity in the $AS_{COO}$ lineshape where the changes in the lineshape function (g(t)) are self-compensated by the weight and contribution of the different FFCF components, though the component with a characteristic time of ~1.2 ps remains unchanged in the two samples.

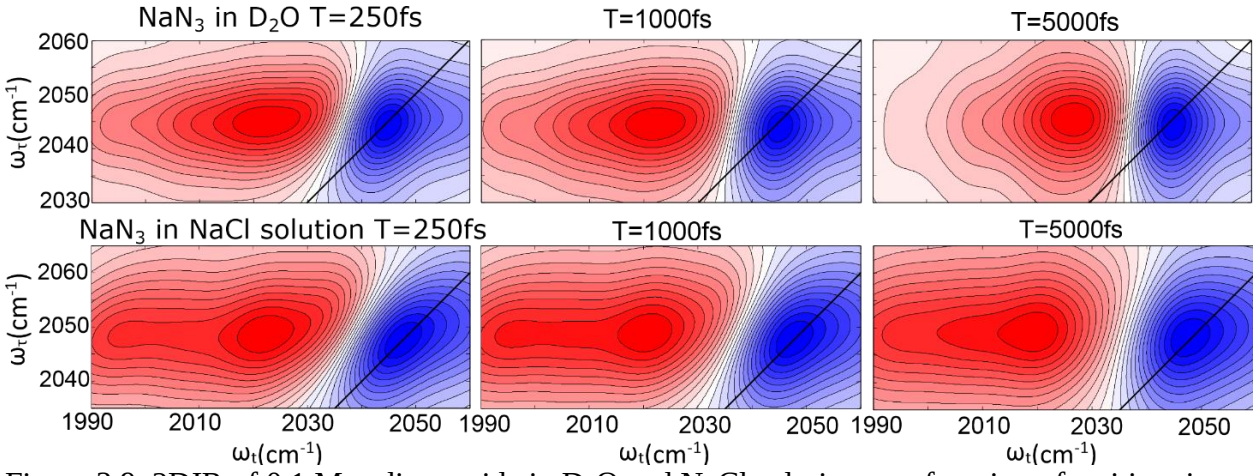

Figure 3.9. 2DIR of 0.1 M sodium azide in $D_2O$ and NaCl solution as a function of waiting time.

Table 3.3. Parameters derived from modeling the inverse slope with an exponential function as described in the text.

| Ion | Solvent | $y_0$ | A | $\tau_1$/ps |
|---|---|---|---|---|
| Acetate | $D_2O$ | 0.02±0.01 | 0.15±0.01 | 1.1±0.1 |
| Acetate | 6M NaCl | 0.07±0.01 | 0.21±0.01 | 1.3±0.1 |
| Azide | $D_2O$ | 0.09±0.01 | 0.36±0.02 | 0.9±0.1 |
| Azide | 6M NaCl | 0.25±0.01 | 0.37±0.01 | 1.6±0.1 |

The characterization of all the parameters of the FFCF is performed by finding the values that correctly predict the experimental FWHM of the $AS_{COO}$ (Table 3.3), as well as the inverse slope at 0.15 ps and 2.1 ps (Figure 3.9) using the response function representation of the third order non-linear signal[61] in a similar manner as the studies in Ref. [62] and [37]. The proposed FFCF has a functional form based on the standard Kubo formalism,[63]

$$\mathrm{FFCF(t)} = \frac{\delta(t)}{T_2^*} + \Delta_1^2 e^{-\frac{t}{\tau_1}} + \Delta_2^2 \text{ , (3)}$$

where $T_2^*$ represents a homogeneous dephasing component, $\Delta_1$ and $\tau_1$ are the amplitude and decay time of a component which cannot be described by either inhomogeneous or homogeneous limit,

and $\Delta_2$ is the amplitude of an inhomogeneous component.[35] The results of the modeling (Table 3.4) show that the acetate ion in $D_2O$ only requires a homogeneous component and a Kubo function, while the acetate ion solution in 6M NaCl requires an additional inhomogeneous component to correctly describe the three experimental parameters. It is interesting to observe that the homogeneous component becomes increasingly slow with the addition of salt, while the amplitude of the fluctuation of the ~1.2 ps component remains unchanged. Moreover, the appearance of an inhomogeneous component could indicate the presence of slower water dynamics which is likely to arise from the transformation of a fast dynamical component (originally represented by a homogeneous contribution), to an extremely slow component (given by the inhomogeneous contribution). However, it is also possible that the band is composed of two different transitions arising from solvent separated ion-pairs as it will be shown in the later sections of the manuscript.

Table 3.4. Lineshape function parameters derived from modeling the FWHM of the IR spectrum as well as the inverse of the slope at 0.15 ps and 2.1 ps.

| Solvent | $\omega_{10}$ ($cm^{-1}$) | $\Delta_1$ ($ps^{-1}$) | $\Delta_2$ ($ps^{-1}$) | $T_2$* (ps) |
|---|---|---|---|---|
| $D_2O$ | 1561 | 1.6 ± 0.1 | -- | 0.9 ± 0.1 |
| NaCl [1] | 1561 | 1.6 ± 0.1 | 0.9 ± 0.1 | 2.0 ± 0.1 |
| NaCl [2] | 1557 | 1.6 ± 0.1 | -- | 1.5 ± 0.1 |
| NaCl [2] | 1565 | 1.6 ± 0.1 | -- | 1.5 ± 0.1 |

[1] Modeled with one transition
[2] Modeled with two transitions

To understand the molecular processes that give rise to the observed vibrational dynamics, the solvation of the acetate ion was further studied by AIMD simulations. The local environment surrounding the acetate ions in the two different solutions is first evaluated from the radial distribution function (RDF) between the carbon atom of the carboxylate group and the oxygen atoms of water (Figure 3.10). The computed RDFs show a complete overlap up to 4.15 Å indicating not only that the acetate ion has the similar amount of water molecules in its first

solvation shell, but also that the sodium and chloride ions do not perturb significantly the acetate first solvation shell. Moreover, the radial distribution function for the acetate ion in water is found to be in agreement with previous theoretical study.[64] In addition, the RDF shows that the acetate ion in water has a second and third solvation shells, as evidenced by the two peaks at ~5 Å and ~7 Å. In contrast, at high NaCl concentration the structure of the second and third solvation shells are significantly affected, as seen by the lower amplitude of the peak ~5 Å and by the lack of a third peak in the RDF. The numbers of water molecules in the first solvation shell were computed to be ~7.0 and ~6.4 for water and 6M NaCl solutions, respectively. This result indicates that acetate forms on average three hydrogen bonds with each of its oxygen atoms which is consistent with the observation of a previous study.[64]

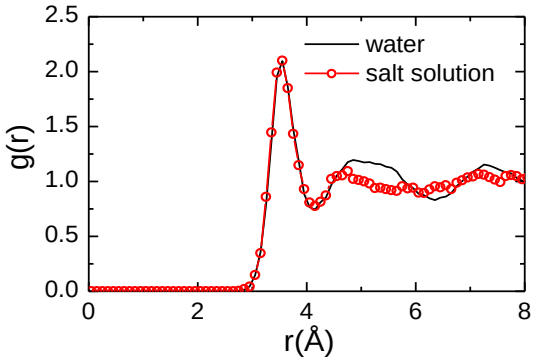


Figure 3.10. Radial distribution function between carbon in carboxyl group and oxygen in water molecule in sodium acetate water solution (black line) and sodium acetate NaCl solution (red open circles).

The FFCF dynamics of the acetate ion in both solutions was also derived from the AIMD simulations (Figure 3.12). The computed FFCFs (see theoretical methods) shows a dynamic process with at least two different time scales. Interestingly, the variance of the frequency fluctuations remains almost invariant with the addition of large quantities of sodium and chloride ions. The characteristic times of the FFCF dynamics were quantified by modeling its time

dependence with a sum of three exponential decay functions; i.e., $\mathrm{FFCF(t)} = \sum A_i^2 e^{-\frac{t}{\tau' i}}$. The parameters from the fitting are shown in Table 3.4. Similarly to the experimental FFCF, $\tau'_3$ is assigned to the global structural rearrangement of hydrogen bond network arising from rotational jumps and hydrogen bond making and breaking.[60, 65] Notably, the slow characteristic time of the FFCF ($\tau'_3$) remains fairly unchanged in both the water and salt solutions which is in reasonable agreement with experimental results. The other two fast correlation times ($\tau'_1$ and $\tau'_2$) are related to the water molecule libration motions[60, 66] and to the internal bending and stretching motions of water molecules.[60, 67] Moreover, the presence of two fast dynamical components ($\tau'_1$ and $\tau'_2$) supports the needed homogeneous component in the modeling of the experimental FFCF, as previously described.

The simulated FFCF does not capture the presence of the slow component seen experimentally, which could be due to the small time window (~50 ps) obtained from the AIMD. However, the FFCF computed from classical MD simulations also does not predict the slow dynamical component on a time window of ~450 ps (Figure 3.11), which allows us to discard the temporal sampling as the cause of the lack of a slow component. Thus, it is likely that the slow component arises from two slowly exchanging configurations of the hydrated acetate ion. While one possibility could come from slow solvent exchange due to the overlapping solvation shells between acetate and sodium ions, the hydrogen bond dynamics between the acetate ion and water molecules does not seem to be affected by the salt concentration (see below). Thus, it is likely that the effect is caused by the presence of solvent separated ion pairs (SIP). In a SIP, the central frequency of the $AS_{COO}$ could be shifted by a water mediated charge transfer between sodium and acetate ions (electronic effect). In this case, SIPs should have a slightly different $AS_{COO}$ central

frequency, which will essentially split the band and give rise to the observed inhomogeneous component of the FFCF (Table 3.4). In addition, the presence of two transitions could explain why the FWHM for the $AS_{COO}$ (~30 $cm^{-1}$, Table 3.5) derived from the theoretical FFCF is narrower in both water and salt solutions when compared to the experimental value (Table 3.1) since the calculation assumes a single transition when computing the FFCF.

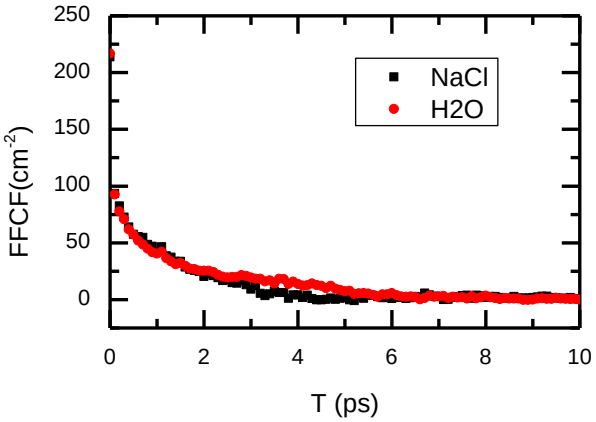


Figure 3.11. FFCF computed from the classical MD simulations for 45 temporal windows of 10 ps each.

The simulation of the temporal evolution of 2DIR spectra using a pair of transitions (Table 3.4) reproduces the experimental slope values and the FWHM of the $AS_{COO}$. However, the simulation also requires a frequency difference of ~9 $cm^{-1}$ between the band maxima. The calculated split should shift the central frequency of the transition, but this effect is not observed in the FTIR. However, it also possible that there is an accidental cancellation of effects from ion paring and the change in the dielectric constant of the medium due to the addition of the salt. It is important to note that this effect will not be capture by calculating the FFCF from the theory because if the shift in the frequency arise from electronic effects, such as charge transfer, it will require the inclusion of both transitions with their corresponding gas phase frequencies and the identification of these species in the trajectory to compute the theoretical FFCF. The determination

of the involvement of such species will require a thorough investigation and vibrational characterization of the species formed during the MD simulation, which is beyond the scope of this paper.

The presence of a second transition is an interesting topic on its own, but it does not explain the picosecond FFCF dynamics of the acetate ion and its lack of sensitivity to salt concentration. The AIMD simulations allow us to discard any possible effect of the randomization of the orientational distribution of the carboxylate group as a source of the fast decorrelation of the FFCF.[68] To this end, the anisotropy of the $AS_{COO}$ is computed from the second order correlation function of the orientation of the $AS_{COO}$ transition dipole ($R(t) = 2/5\langle P_2[\boldsymbol{u}(0) \cdot \boldsymbol{u}(t)]\rangle$), where $\mathbf{u}(t)$ is the transition dipole and is represented here by the unit vector joining the two oxygen atoms of the carboxylate group, $P_2$ is the second order Legendre polynomial, and the angle brackets indicate the ensemble average. The computed anisotropy (Figure 3.6 and Table 3.2) shows a very slow decay with a time constant of ~8 ps in both NaCl and $D_2O$. The result indicates that the reorientation-induced contribution plays little to no role in the FFCF.

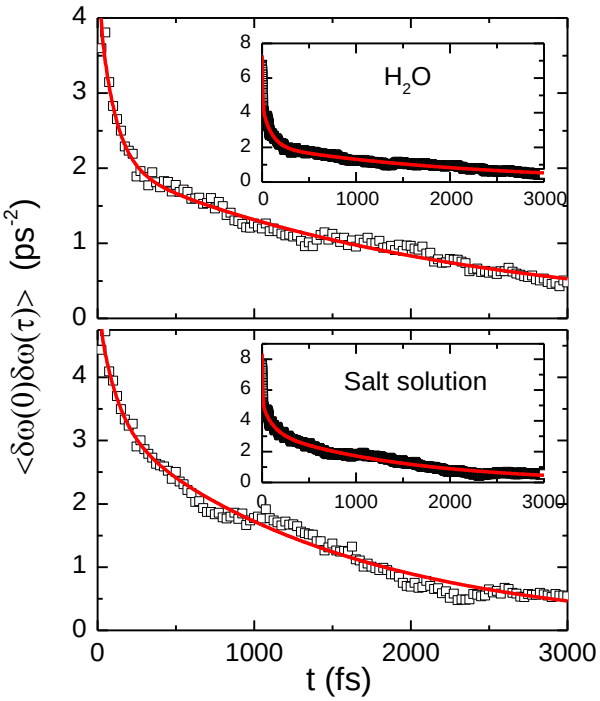


Figure 3.12. Autocorrelation function of the frequency fluctuations (FFCF) computed from the AIMD and the frequency map. Top and bottom panels correspond to sodium acetate in water and in NaCl solution, respectively. Black open squares correspond to the computed FFCF and the red line to the fitting with a sum of exponential functions as described in the text. While the plots highlight the slow decay times, the insets show the whole correlation function.

Table 3.5. Parameters from fitting of the theoretical FFCF and HBCF of sodium acetate solutions.

| Metric | Sample | $\Delta_1$ ($ps^{-1}$) | $\tau_1$ (fs) | $\Delta_2$ ($ps^{-1}$) | $\tau_2$ (fs) | $\Delta_3$ ($ps^{-1}$) | $\tau_3$ (fs) | FWHM ($cm^{-1}$) |
|---|---|---|---|---|---|---|---|---|
| FFCF | water | 1.7±0.1 | 6.8±0.2 | 1.5±0.1 | 99±2 | 1.5±0.1 | 2190±50 | 30.1±0.3 |
| FFCF | NaCl | 1.8±0.1 | 6.9±0.3 | 1.3±0.1 | 116±3 | 1.8±0.1 | 1530±30 | 33±1 |
| | | $A_1$ | | $A_2$ | | $A_3$ | | |
| HBCF (acetate-water) | water | 1.05±0.01 | 5.5±0.1 | 0.19±0.01 | 85±3 | 0.07±0.01 | 590±20 | |
| HBCF (acetate-water) | NaCl | 1.03±0.01 | 5.7±0.1 | 0.16±0.01 | 94±4 | 0.09±0.01 | 800±20 | |
| HBCF (water-water) | water | 0.68±0.01 | 5.1±0.1 | 0.26±0.01 | 76±2 | 0.20±0.01 | 520±5 | |
| HBCF (water-water) | NaCl | 0.68±0.01 | 5.2±0.1 | 0.22±0.01 | 71±2 | 0.13±0.01 | 1120±20 | |

The molecular mechanism behind the lack of change of the ~1-2 ps component of the calculated and measured FFCF with the addition of salt was studied by computing the hydrogen bond dynamics of the acetate and water from the AIMD simulation. The number of hydrogen bonds between acetate and water was used in this case because it has been previously shown that the frequency fluctuations in the acetate ion are dominated by a rearrangement of the hydrogen bonds around the oxygen atoms of the carboxylate. For this purpose, the distance between oxygen atoms of the ion acetate and water molecules was used as parameter to define the existence of a hydrogen bond.[69] Figure 3.13 shows the correlation functions of the number of hydrogen bonds (HBCF) between the acetate ion and water molecules for both solutions. It is clear that the hydrogen-bond dynamics between the acetate ion and water molecules are very similar in water and salt solutions. The modeling of the HBCF with the sum of three exponential decays of the form: $\mathrm{HBCF(t)} = \sum A_i \ e^{-\frac{t}{\tau'' i}}$, reveals the presence of two short characteristic times ($\tau''_1$ and $\tau''_2$) with no obvious difference for both samples, and a long characteristic time ($\tau''_3$) that increases from ~600 fs in $D_2O$ to ~800 fs in NaCl (Table 3.5). Although the change in $\tau''_3$ indicates that the sodium and chloride ions alter the dynamics of hydrogen bond between the acetate ion and water, the observed change is not large. Interestingly, a similar analysis of the HBCF among water molecules outside of the solvation shell (Figure 3.13) shows an analogous picture for $\tau''_1$ and $\tau''_2$, but completely different for the long correlation time $\tau''_3$. Again, the modeling of the water-water HBCF with a sum of three exponential functions (Table 3.5) reveals that the third decay time ($\tau''_3$) has a large increase in its value when the solution has a significant amount of sodium and chloride ions. In contrast, the presence of ions does not seem to affect the other two decay times ($\tau''_1$ and $\tau''_2$). The difference between the acetate-water and water-water HBCF confirms the known

slowdown of water hydrogen bond dynamics with the addition of NaCl.[60] In addition, it verifies that the invariance of the acetate-water hydrogen bond in the presence of large quantities of sodium and chloride ions is not an artifact of the AIMD. Moreover, it further supports of our experimental observation in which the FFCF dynamics remains unchanged in solutions saturated with NaCl, but does not provide the molecular mechanism behind this effect.

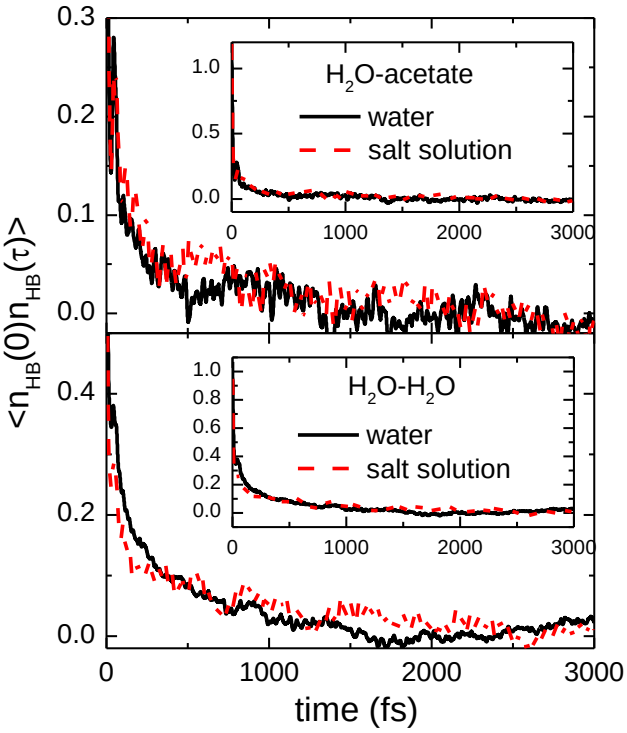


Figure 3.13. Hydrogen bond autocorrelation function. Top panel shows the HBCF between acetate and water molecules and bottom panel displays the HBCF between water molecules outside of solvation shell. Solid black and red dashed lines correspond to acetate in water and in NaCl solutions, respectively. While the plots highlight the slow decay times, the insets show the whole correlation function.

The simplicity of the acetate ion allows us to uncover the molecular mechanism responsible for the interesting solvation shell dynamics of the ion. Acetate has only one substituent that can affect the solvation shell of its $COO^-$ group; i.e., its methyl group. It is well known that the energetics of the rotation of methyl groups is well within thermal energy.[70-72] Thus, it is not

surprising that the acetate ion controls its solvation shell by the thermal rotation of its methyl group. To test this hypothesis, the correlation between the number of hydrogen bonds formed between water and one oxygen atom of the acetate ion and the HCCO dihedral angle of acetate is computed. The correlation numbers between these two variables are found to be ~ -0.6 for both water and salt solutions (Figure 3.13) which indicates that the HCCO dihedral angle directly affects the hydrogen bonding occurring at the carboxylate group. The dynamics of the dihedral angle is derived from the correlation function: $C(t) = \langle cos[\theta(\tau) - \theta(\tau + t)] \rangle_\tau$, where $\theta$ is the dihedral angle and $t$ is the residence time in a single dihedral angle conformation (see Figure 3.14).[73] The characteristic times of the dynamics computed by modeling the data with the sum of two exponential decays reveals the presence of two residence times: one on the order of ~100 fs and the other larger than 1 ps (Table 3.6). While the values of the characteristic times might not be very precise due to the short time window used to evaluate this correlation function, they still show that the rotation dynamics of the methyl group has a comparable time scale to that observed for the FFCF. The fast rotational dynamics of the methyl group as well as the observed correlation between the number of hydrogen bonds in the carboxylate group and the dihedral angle strongly supports the proposed molecular mechanism in which the rotation of the methyl group controls the structure and dynamics of the acetate first hydration shell. The observed mechanism has multiple implications in the properties of the carboxylate group. For example, it provides a molecular framework for describing why carboxylate groups do not tend to favor the formation of contact ion pairs with alkali metals.

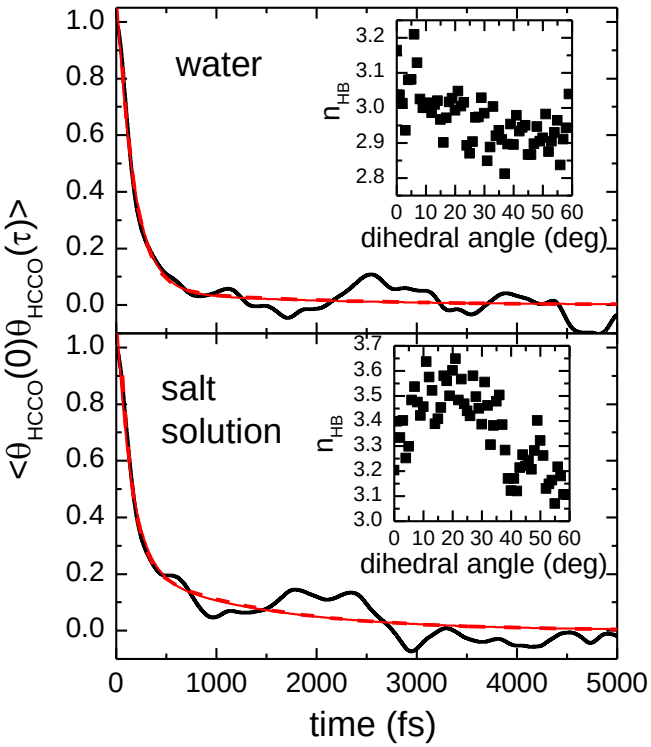


Figure 3.14. Dihedral autocorrelation function of HCCO. Top and bottom panel correspond the autocorrelation for water and NaCl solutions, respectively. Black line is the computed autocorrelation and the red dashed line is fitting with a sum of exponential decays. Inset show the number of hydrogen bonds in one oxygen atom of the carboxylate as a function of the HCCO dihedral angle.

Table 3.6. Exponential decay fitting ($f(t) = \sum A_i \ e^{-\frac{t}{\tau_i}}$,)parameters

| Sample | $A_1$ | $\tau_1$ (fs) | $A_2$ | $\tau_2$ (fs) |
|---|---|---|---|---|
| Water | 1.0±0.01 | 174±2 | 0.06±0.01 | 1760±120 |
| NaCl solution | 0.90±0.01 | 150±2 | 0.22±0.01 | 1320±30 |

### 3.5. Summary

The solvation shell dynamics of acetate ion in $D_2O$ and 6M NaCl solution was successfully studied by FTIR and 2DIR experiments. The linear IR spectroscopy of the acetate $AS_{COO}$ mode revealed that its IR lineshape is not affected by the high concentration of sodium and chloride ions. In addition, the FFCF deducted from the photon echo experiments revealed a ~1 ps component

which is also not affected by the concentration of ions. A comparison with the effect on the asymmetric stretch of the azide ion showed that the lack of change in the $AS_{COO}$ lineshape and FFCF dynamics is a particularity of the acetate ion. AIMD simulations confirmed that the hydration shell structure and dynamics of acetate ion is not affected by the presence of large quantities of ions, while substantial amounts of charged species produced a slowdown in the hydrogen bond dynamics of water molecules outside the acetate first hydration shell. Moreover, the FFCF and lineshape derived for the acetate $AS_{COO}$ from AIMD simulations and a DFT-frequency map presented a reasonable agreement with the experiments, but they fail to explain the observed inhomogeneous components of the FFCF. Our results and modeling suggest that the inhomogeneous component could arise from the presence of solvent separated ion pairs. Finally, the computational modeling provided a molecular framework for understanding the vibrational spectra and dynamics of the acetate ion. In this case, the thermal rotation of the acetate methyl group ($–CH_3$) is found to be responsible for controlling the structure and dynamics of the water molecules in the first solvation shell. Our experiments provide the molecular basis for rationalizing why osmolytes and zwitterions containing the carboxylate group, such as betaine, avoid the formation of ion pairs and maintain their high water solvation number, even in solutions with high salt concentrations.

### 3.6. References


1. Hodgkin, A.L. and A.F. Huxley, *A Quantitative Description of Membrane Current and Its Application to Conduction and Excitation in Nerve.* Journal of Physiology-London, 1952. **117**(4): p. 500-544.

2. Lombard, J., *Once upon a time the cell membranes: 175 years of cell boundary research.* Biology Direct, 2014. **9**: p. 32.

3. Marcus, Y., *Ions in solution and their solvation*. 2015, Hoboken, New Jersey: John Wiley & Sons, Inc. x, 298 pages.

4. Hofmeister, F., *Zur lehre von der wirkung der salze.* Naunyn-Schmiedeberg's Archives of Pharmacology, 1888. **25**(1): p. 1-30.

5. Collins, K.D. and M.W. Washabaugh, *The Hofmeister Effect and the Behavior of Water at Interfaces.* Quarterly Reviews of Biophysics, 1985. **18**(4): p. 323-422.

6. Zhang, Y.J. and P.S. Cremer, *Interactions between macromolecules and ions: the Hofmeister series.* Current Opinion in Chemical Biology, 2006. **10**(6): p. 658-663.

7. Czurlok, D., et al., *Femtosecond 2DIR spectroscopy of the nitrile stretching vibration of thiocyanate anions in liquid-to-supercritical heavy water. Spectral diffusion and libration-induced hydrogen-bond dynamics.* Physical Chemistry Chemical Physics, 2015. **17**(44): p. 29776-29785.

8. Chen, H.L., et al., *Vibrational Energy Transfer: An Angstrom Molecular Ruler in Studies of Ion Pairing and Clustering in Aqueous Solutions.* Journal of Physical Chemistry B, 2015. **119**(12): p. 4333-4349.

9. Gaffney, K.J., et al., *H-bond switching and ligand exchange dynamics in aqueous ionic solution.* Chemical Physics Letters, 2011. **504**(1-3): p. 1-6.

10. Kuo, C.-H., et al., *Correlation of the Vibrations of the Aqueous Azide Ion with the O−H Modes of Bound Water Molecules.* Journal of Physical Chemistry B, 2007. **111**(50): p. 14028-14033.

11. Guo, Q., et al., *Line shape analysis of two-dimensional infrared spectra.* Journal of Chemical Physics, 2015. **142**(21): p. 212427.

12. Hamm, P., M. Lim, and R.M. Hochstrasser, *Non-Markovian dynamics of the vibrations of ions in water from femtosecond infrared three-pulse photon echoes.* Physical Review Letters, 1998. **81**(24): p. 5326-5329.

13. Vorobyev, D.Y., et al., *Water-Induced Relaxation of a Degenerate Vibration of Guanidinium Using 2D IR Echo Spectroscopy.* Journal of Physical Chemistry B, 2010. **114**(8): p. 2944-2953.

14. Kuroda, D.G. and R.M. Hochstrasser, *Dynamic structures of aqueous oxalate and the effects of counterions seen by 2D IR.* Physical Chemistry Chemical Physics, 2012. **14**(18): p. 6219-6224.

15. Kuroda, D.G., et al., *Vibrational dynamics of a non-degenerate ultrafast rotor: The (C12,C13)-oxalate ion.* Journal of Chemical Physics, 2013. **139**(16): p. 164514.

16. Kuroda, D.G. and R.M. Hochstrasser, *Two-dimensional infrared spectral signature and hydration of the oxalate dianion.* Journal of Chemical Physics, 2011. **135**(20): p. 204502.

17. Costard, R., et al., *Ultrafast phosphate hydration dynamics in bulk H2O.* Journal of Chemical Physics, 2015. **142**(21): p. 212406.

18. Thogersen, J., et al., *Hydration Dynamics of Aqueous Nitrate.* Journal of Physical Chemistry B, 2013. **117**(12): p. 3376-3388.

19. Mandal, A., et al., *Collective vibrations of water-solvated hydroxide ions investigated with broadband 2DIR spectroscopy.* Journal of Chemical Physics, 2014. **140**(20): p. 204508.

20. Mandal, A. and A. Tokmakoff, *Vibrational dynamics of aqueous hydroxide solutions probed using broadband 2DIR spectroscopy.* Journal of Chemical Physics, 2015. **143**(19): p. 194501.

21. Giammanco, C.H., P.L. Kramer, and M.D. Fayer, *Dynamics of Dihydrogen Bonding in Aqueous Solutions of Sodium Borohydride.* Journal of Physical Chemistry B, 2015. **119**(8): p. 3546-3559.

22. Bakker, H.J., M.F. Kropman, and A.W. Omta, *Effect of ions on the structure and dynamics of liquid water.* Journal of Physics-Condensed Matter, 2005. **17**(45): p. S3215-S3224.

23. van der Post, S.T. and H.J. Bakker, *The combined effect of cations and anions on the dynamics of water.* Physical Chemistry Chemical Physics, 2012. **14**(18): p. 6280-6288.

24. Bakker, H.J., *Structural dynamics of aqueous salt solutions.* Chemical Reviews, 2008. **108**(4): p. 1456-1473.

25. Nelson, D.L., M.M. Cox, and A.L. Lehninger, *Lehninger principles of biochemistry*. Seventh edition. ed. 2017, New York, NY; Houndmills, Basingstoke: W.H. Freeman and Company ; Macmillan Higher Education. xxxiv, 1172, AS34, G20, I45 pages.

26. Robinson, R.A. and H.S. Harned, *Some aspects of the thermodynamics of strong electrolytes from electromotive force and vapor pressure measurements.* Chemical Reviews, 1941. **28**(3): p. 419-476.

27. Rahman, H.M.A., G. Hefter, and R. Buchner, *Hydration of Formate and Acetate Ions by Dielectric Relaxation Spectroscopy.* Journal of Physical Chemistry B, 2012. **116**(1): p. 314-323.

28. Hajari, T., P. Ganguly, and N.F.A. van der Vegt, *Enthalpy-Entropy of Cation Association with the Acetate Anion in Water.* Journal of Chemical Theory and Computation, 2012. **8**(10): p. 3804-3809.

29. Quiles, F. and A. Burneau, *Infrared and Raman spectra of alkaline-earth and copper(II) acetates in aqueous solutions.* Vibrational Spectroscopy, 1998. **16**(2): p. 105-117.

30. Banerjee, P., S. Yashonath, and B. Bagchi, *Rotation driven translational diffusion of polyatomic ions in water: A novel mechanism for breakdown of Stokes-Einstein relation.* Journal of Chemical Physics, 2017. **146**(16): p. 164502.

31. Banno, M., K. Ohta, and K. Tominaga, *Vibrational dynamics of acetate in D2O studied by infrared pump-probe spectroscopy.* Physical Chemistry Chemical Physics, 2012. **14**(18): p. 6359-6366.

32. Sanyal, S.K. and S.K. Mandal, *Viscosity B-Coefficients of Alkyl Carboxylates.* Electrochimica Acta, 1983. **28**(12): p. 1875-1876.

33. Shalit, A., et al., *Terahertz echoes reveal the inhomogeneity of aqueous salt solutions.* Nature Chemistry, 2017. **9**(3): p. 273-278.

34. Stirnemann, G., et al., *Mechanisms of Acceleration and Retardation of Water Dynamics by Ions.* Journal of the American Chemical Society, 2013. **135**(32): p. 11824-11831.

35. Hamm, P. and M.T. Zanni, *Concepts and methods of 2d infrared spectroscopy*. 2011, Cambridge ; New York: Cambridge University Pres. ix, 286 p.

36. Chuntonov, L., et al., *Kinetics of Exchange between Zero-, One-, and Two-Hydrogen-Bonded States of Methyl and Ethyl Acetate in Methanol.* Journal of Physical Chemistry B, 2015. **119**(12): p. 4512-4520.

37. Kuroda, D.G., D.Y. Vorobyev, and R.M. Hochstrasser, *Ultrafast relaxation and 2D IR of the aqueous trifluorocarboxylate ion.* Journal of Chemical Physics, 2010. **132**(4): p. 044501.

38. Li, T., et al., *Hydration and vibrational dynamics of betaine (N,N,N-trimethylglycine).* Journal of Chemical Physics, 2015. **142**(21): p. 212438.

39. Huerta-Viga, A., et al., *A salt-bridge structure in solution revealed by 2D-IR spectroscopy.* Physical Chemistry Chemical Physics, 2014. **16**(30): p. 15784-15786.

40. Bagchi, S., et al., *2D-IR Experiments and Simulations of the Coupling between Amide-I and Ionizable Side Chains in Proteins: Application to the Villin Headpiece.* Journal of Physical Chemistry B, 2009. **113**(32): p. 11260-11273.

41. Fulfer, K.D. and D.G. Kuroda, *A comparison of the solvation structure and dynamics of the lithium ion in linear organic carbonates with different alkyl chain lengths.* Physical Chemistry Chemical Physics, 2017. **19**(36): p. 25140-25150.

42. Ding, Y., A.A. Hassanali, and M. Parrinello, *Anomalous water diffusion in salt solutions.* Proceedings of the National Academy of Sciences of the United States of America, 2014. **111**(9): p. 3310-3315.

43. Martinez, L., et al., *PACKMOL: A Package for Building Initial Configurations for Molecular Dynamics Simulations.* Journal of Computational Chemistry, 2009. **30**(13): p. 2157-2164.

44. Plimpton, S., *Fast Parallel Algorithms for Short-Range Molecular-Dynamics.* Journal of Computational Physics, 1995. **117**(1): p. 1-19.

45. Jewett, A.I., Z.Y. Zhuang, and J.E. Shea, *Moltemplate a Coarse-Grained Model Assembly Tool.* Biophysical Journal, 2013. **104**(2): p. 169a-169a.

46. Jorgensen, W.L., D.S. Maxwell, and J. Tirado-Rives, *Development and Testing of the OPLS All-Atom Force Field on Conformational Energetics and Properties of Organic Liquids.* Journal of the American Chemical Society, 1996. **118**(45): p. 11225-11236.

47. Jorgensen, W.L., et al., *Comparison of Simple Potential Functions for Simulating Liquid Water.* Journal of Chemical Physics, 1983. **79**(2): p. 926-935.

48. VandeVondele, J., et al., *QUICKSTEP: Fast and accurate density functional calculations using a mixed Gaussian and plane waves approach.* Computer Physics Communications, 2005. **167**(2): p. 103-128.

49. Goedecker, S., M. Teter, and J. Hutter, *Separable dual-space Gaussian pseudopotentials.* Physical Review B, 1996. **54**(3): p. 1703-1710.

50. Lin, I.C., et al., *Structure and Dynamics of Liquid Water from ab Initio Molecular Dynamics-Comparison of BLYP, PBE, and revPBE Density Functionals with and without van der Waals Corrections.* Journal of Chemical Theory and Computation, 2012. **8**(10): p. 3902-3910.

51. Jones, L.H. and E. Mclaren, *Infrared Spectra of Ch3coona and Cd3coona and Assignments of Vibrational Frequencies.* Journal of Chemical Physics, 1954. **22**(11): p. 1796-1800.

52. Ito, K. and H.J. Bernstein, *THE VIBRATIONAL SPECTRA OF THE FORMATE, ACETATE, AND OXALATE IONS.* Canadian Journal of Chemistry, 1956. **34**(2): p. 170-178.

53. Falk, M., *Frequencies of H□ O□ H, H□ O□ D and D□ O□ D bending fundamentals in liquid water.* Journal of Raman Spectroscopy, 1990. **21**(9): p. 563-567.

54. Nara, M., H. Torii, and M. Tasumi, *Correlation between the vibrational frequencies of the carboxylate group and the types of its coordination to a metal ion: An ab initio molecular orbital study.* Journal of Physical Chemistry, 1996. **100**(51): p. 19812-19817.

55. Fulmer, E.C., F. Ding, and M.T. Zanni, *Heterodyned fifth-order 2D-IR spectroscopy of the azide ion in an ionic glass.* Journal of Chemical Physics, 2005. **122**(3): p. 034302.

56. Jenkins, H.D.B. and Y. Marcus, *Viscosity B-Coefficients of the Aqueous Cyanide and Azide Ions.* Journal of Solution Chemistry, 1993. **22**(1): p. 95-98.

57. Kwac, K. and M.H. Cho, *Molecular dynamics simulation study of N-methylacetamide in water. II. Two-dimensional infrared pump-probe spectra.* Journal of Chemical Physics, 2003. **119**(4): p. 2256-2263.

58. Kim, Y.S., et al., *2D IR provides evidence for mobile water molecules in beta-amyloid fibrils.* Proceedings of the National Academy of Sciences of the United States of America, 2009. **106**(42): p. 17751-17756.

59. Kwak, K., et al., *Frequency-frequency correlation functions and apodization in two-dimensional infrared vibrational echo spectroscopy: A new approach.* Journal of Chemical Physics, 2007. **127**(12): p. 124503.

60. Fayer, M.D., et al., *Water Dynamics in Salt Solutions Studied with Ultrafast Two-Dimensional Infrared (2D IR) Vibrational Echo Spectroscopy.* Accounts of Chemical Research, 2009. **42**(9): p. 1210-1219.

61. Mukamel, S., *Principles of nonlinear optical spectroscopy*. Oxford series in optical and imaging sciences. 1995, New York: Oxford University Press. xviii, 543 p.

62. Park, S., K. Kwak, and M.D. Fayer, *Ultrafast 2D-IR vibrational echo spectroscopy: a probe of molecular dynamics.* Laser Physics Letters, 2007. **4**(10): p. 704-718.

63. Kubo, R., *A Stochastic Theory of Line Shape*, in *Advances in Chemical Physics*. 2007, John Wiley & Sons, Inc. p. 101-127.

64. Houriez, C., M. Meot-Ner, and M. Masella, *Simulated Solvation of Organic Ions II: Study of Linear Alkylated Carboxylate Ions in Water Nanodrops and in Liquid Water. Propensity for Air/Water Interface and Convergence to Bulk Solvation Properties.* Journal of Physical Chemistry B, 2015. **119**(36): p. 12094-12107.

65. Laage, D. and J.T. Hynes, *A molecular jump mechanism of water reorientation.* Science, 2006. **311**(5762): p. 832-835.

66. Moilanen, D.E., et al., *Water inertial reorientation: Hydrogen bond strength and the angular potential.* Proceedings of the National Academy of Sciences of the United States of America, 2008. **105**(14): p. 5295-5300.

67. Sonoda, M.T., et al., *A review on the dynamics of water.* Brazilian Journal of Physics, 2004. **34**(1): p. 3-16.

68. Kramer, P.L., J. Nishida, and M.D. Fayer, *Separation of experimental 2D IR frequency-frequency correlation functions into structural and reorientation-induced contributions.* Journal of Chemical Physics, 2015. **143**(12): p. 124505.

69. Kumar, R., J.R. Schmidt, and J.L. Skinner, *Hydrogen bonding definitions and dynamics in liquid water.* Journal of Chemical Physics, 2007. **126**(20): p. 204107.

70. Pitzer, K.S., *Potential Energies for Rotation About Single Bonds.* Discussions of the Faraday Society, 1951(10): p. 66-73.

71. Mellink, W.A. and R. Kaptein, *Determination of the methyl group rotation energy barrier in some substituted tricyclo [3.1.0.02,6]hexanes by carbon-13 spinlattice relaxation.* Organic Magnetic Resonance, 1980. **13**(4): p. 279-281.

72. Zheng, J.R., et al., *Ultrafast carbon-carbon single-bond rotational isomerization in room-temperature solution.* Science, 2006. **313**(5795): p. 1951-1955.

73. vanderSpoel, D. and H.J.C. Berendsen, *Molecular dynamics simulations of leu-enkephalin in water and DMSO.* Biophysical Journal, 1997. **72**(5): p. 2032-2041.

# CHAPTER 4
# AN *AB INITIO* MOLECULAR DYNAIMCS STUDY OF THE SOLVATION STRUCTURE AND ULTRAFAST DYNAMICS OF LITHIUM SALTS IN ORGANIC CARBONATES: A COMPARISON BETWEEN LINEAR AND CYCLIC CARBONATES

## 4.1. Introduction

Lithium ion batteries with carbonate electrolytes have been extensively used in portable energy devices due to their advantages such as low cost, high energy density, and no memory effect. However, this technology still suffers from some drawbacks such as limited thermal stability and low efficiency compared to its theoretical value. In most current commercial lithium ion batteries, the electrolyte is composed of both a linear carbonate, such as dimethyl carbonate (DMC, Scheme 4.1) or ethyl methyl carbonate (EMC), and a cyclic carbonate, like ethylene carbonate (EC) or butylene carbonate (BC).[1] The mixture is needed to gain the best physicochemical properties of each solvent, namely, the high dielectric constant of the cyclic carbonate and the low viscosity of the linear carbonate. Previous studies have demonstrated that the solvent used in the electrolytes influences the battery performance through the ionic conductivity, which is determined by the solvation and diffusion of lithium ions (Li+),[2] and by forming the solid-electrolyte interphase, which avoids the degradation of the battery capacity.[3] In addition, it has been proven that the stability of lithium ion batteries can be improved by modifying the solvent composition of the electrolyte.[4, 5] Thus, to improve the overall battery

Reproduced from Zhang, X. and D.G. Kuroda, *An ab initio molecular dynamics study of the solvation structure and ultrafast dynamics of lithium salts in organic carbonates: A comparison between linear and cyclic carbonates.* The Journal of Chemical Physics, 2019. **150**(18): p. 184501, with the permission of AIP Publishing

stability and efficiency, the interactions among electrolyte components should be investigated and optimized.

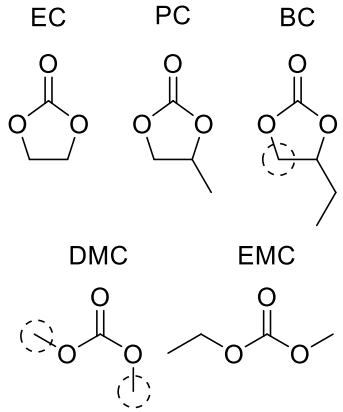


Scheme 4.1. Chemical structure of carbonates. Ethylene carbonate (EC), propylene carbonate (PC), butylene carbonate (BC), dimethyl carbonate (DMC), and ethyl methyl carbonate (EMC). Dashed circle denotes the methylene and methyl carbons used for calculating the radial distribution functions.

Numerous studies have investigated the solvation structure and dynamics of lithium ion electrolytes using experimental methodologies, such as X-ray scattering,[6, 7] nuclear magnetic resonance,[8-12] Raman spectroscopy,[12-17] and linear and ultrafast infrared spectroscopy.[18-22] Similarly, several theoretical studies using different levels of theory have also been presented.[23-28] While it has been a long time since the physicochemical properties of cyclic and linear carbonates, such as dielectric constant, viscosity, and electrochemical stability, have been presented,[1] the molecular level description of the organic carbonate behavior is still scarce. In particular, some studies have focused on the mixture of cyclic and linear carbonate solutions using experimental and theoretical methods to obtain the composition and dynamics of the mixed solvation shell.[18, 28-30] However, due to the complexity of the system, namely, fast exchange of solvent molecules and different speciation of the ionic species, the knowledge derived from such systems has been rather limited. On the other hand, only a few studies have investigated the

differences of solvation structure and interactions between the two types of carbonate solutions.[31, 32]

Lately, there have been a significant number of studies using vibrational spectroscopy to the study the solvation of Li+ in organic carbonates.[12-17, 31-34] In particular, some studies have used ultrafast IR spectroscopy to investigate the solvation structure and dynamics of Li+ in organic carbonates.[18, 20-22, 35] However, it appears that the ultrafast spectroscopy work has produced more contradictions than agreements. For example, the coordination number of lithium ion by carbonates has been found to be 4 by some of the ultrafast spectroscopic studies,[21, 22] while others predicted the coordination number of 2 and 6.[19, 35] Moreover, the disagreement in the Li+ solvation number is also found across vibrational spectroscopies, such as Raman[36, 37] and FTIR.[31] In addition, there have been contradictions in the ionic speciation of lithium ions and its counter ion in solutions of organic carbonates.[20, 31, 32, 35] For example, some studies have claimed that the majority of the lithium ions are found forming contact ion pairs (CIP),[35] whereas others predicted an speciation based majorly on solvent separated ion pairs (SSIP) and free ions for the same solutions.[20] Finally, one study predicted a fast solvent exchange of those organic carbonate in the first solvation shell of the lithium ion,[18, 19] while another study pointed out that the experimental signature assigned to solvent exchange arises from a vibrational energy transfer mechanism due to deformations of the solvation shell of the lithium ion.[21] In addition, this last work had shown a significant difference in the solvation shell dynamics between linear and cyclic carbonates which have opposing dynamical trends with lithium salt concentration.[21] As a consequence, further study is needed to disambiguate the interactions and motions of the molecular components in lithium salt solutions of linear and cyclic carbonates. To this end, we present here

a theoretical study based on ab initio molecular dynamics simulations. In particular, this theoretical study is focused on disambiguating the ultrafast processes and the molecular mechanism measured by the different ultrafast vibrational studies.

Molecular dynamics (MD) simulations of lithium salts in linear and cyclic carbonate solutions have been widely studied using classical potentials (GAFF [10, 38] and OPLS-AA[39]), modified or self-developed polarizable empirical potentials,[25, 29, 39-42] semi-empirical quantum mechanical potentials (PM7),[24] and ab initio-based potentials.[2, 4, 23, 28, 43-48] Although the number of studies is significant, the contradictions seen in the experiments are also observed in the theoretical work. For example, some studies show a coordination number of 6 for the lithium ion using classical MD simulations,[23, 40] whereas a tetrahedral structure with a coordination number of 4 for the lithium solvation shell in linear and cyclic carbonates was observed in all the ab initio studies,[2, 4, 23, 28, 43-48] PM7 calculations,[24] and the classical MDs with custom/modified force fields.[25, 29, 39, 42, 49] However, it has been demonstrated independently by Rick's and Rempe's groups that well-optimized polarizable or quantum-based well-modified or quantum models are required to accurately reproduce the solvation properties of the lithium ions in carbonates.[38, 39] These last studies might explain why classical MDs with off-the-shell potentials are likely to fail in properly describing the lithium ion solvation and speciation in organic carbonates.

The speciation of the lithium ion in organic carbonates has been also investigated theoretically. As with the solvent coordination number, the speciation predicted theoretically also showed inconsistencies among different studies. For example, classical MD shows a large population of CIP existing in lithium hexaflourophosphate solutions of ethylene carbonate

(EC).[25] In contrast, the potential energy surface for the lithium tetrafluoroborate in EC at CAM-B3LYP/6-31G(d) level suggests that SSIPs are the most energetically favorable species.[48] Another study using energy representation method for LiBF4 and LiPF6 in propylene carbonate (PC) and dimethyl carbonate (DMC) suggested that CIP is most energetically favorable species irrespective of the dielectric constant of the carbonate.[42] In addition, ab initio MD study predicted a lithium ion solvation energy as high as 140 kcal/mol in EC.[46] Interestingly, the solvent exchange between first- and second-solvation shell was studied by two groups using classical and quantum MDs. The solvent exchange was not observed within the 30 ps AIMD simulation containing LiPF6 in EC or PC,[2] but a classical MD predicted a fast exchange of molecules in the lithium first solvation shell.[18]

In the present work, ab initio molecular dynamics simulations (AIMD) based on density functional theory are used to investigate the solvation structure and dynamics of the lithium ion in both linear and cyclic carbonates. We have chosen AIMD because the electrons are treated quantum mechanically without the need of extra empirical parameters. This methodology has shown a significant predictive power on exploring chemical process that are difficult to probe experimentally.[50, 51] The AIMD simulations used here are based on the PBE functional, which has a proven record of accurately capturing the structure and dynamical properties of the lithium solvation shell as well as the other relevant reactions in carbonate-based electrolytes.[2, 23, 43, 51] However, the cost of such computation is currently exceedingly high and limits the possible time window. To avoid the sampling problems associated with the short time window investigated by the AIMD, the present study also used ab initio umbrella sampling (AIUS) to calculate the

potential of mean force (PMF) and their corresponding probability distributions involved in the processes of ion pairing and solvent exchange.

The paper is organized as follows. Section II discusses the theoretical methods. The results and discussion are presented in Section III, followed by Conclusions in Section IV.

## 4.2. Theoretical methods

### 4.2.1. *Ab Initio* Molecular Dynamics Simulations (AIMD)

The AIMD simulation was carried out with the CP2K package (ver 3.0).[52] The electronic structure was calculated via Quickstep module[52] using the PBE functional with the D2[53] dispersion scheme and the TZ2VP basis set, with Goedecker-Teler-Hutter (GTH) pseudopotentials.[54-56] Periodic boundary conditions were applied to all the systems, and the Nosé-Hoover thermostat was used to keep the temperature as a constant of 300 K with the temperature damping constant of 100 fs. Self-consistent field (SCF) convergence criterion was set to $5.0 \times 10^{-7}$ Hartree. The cyclic carbonate system was composed of 1 lithium ion (Li+), 1 hexafluorophosphate ion ($PF_6^-$), and 19 butylene carbonate (BC) molecules in a cubic box with a length of ~16 Å. Note that BC was selected because it is the only cyclic organic carbonate that could be studied directly using ultrafast IR spectroscopy.[21] In the case of the linear carbonate, the system was composed of 1 Li+, 1 $PF_6$-, and 23 DMC molecules in a cubic box with a length of ~17 Å. In both cases, the box composition is representative of low concentration $LiPF_6$-carbonate solutions (i.e., c < 1M) because it has been observed that aggregates are not present at significant concentrations in these solutions.[20, 31, 57, 58]

To obtain the initial box, Li+ coordinated with 4 carbonates were firstly optimized by using Gaussian09.[59] Note that we have selected DMC molecules with cis-trans conformation because the stabilization energy is similar to those with a mixture of cis-cis and cis-trans conformations (Figure 4.1). In addition, it has been previously demonstrated that entropy does not play a significant role in the solvation energetics.[28] The optimized structure was then submerged in a box containing the rest of the carbonate molecules using Packmol.[60] The system with restraints in the positions of the four coordinated oxygens of the carbonyl in each carbonate underwent a 10 ns NVT, 10 ns NPT, and 15 ns NVT process using LAMMPS software package and OPLSAA force field.[61, 62] These first steps were required to assure the equilibration of the box while maintaining the correct solvation structure around Li+. In the case of linear carbonate, the *cis-trans* isomers were used for coordinated linear carbonates, while the rest of the box was filled with *cis-cis* DMC. The presence of different isomers of the linear carbonate was needed because it has been found that *cis-cis* DMC has lower free energy,[31] whereas the solvation shell of Li+ complex significantly stabilize the *cis-trans* conformer.[29, 31] The initial configurations for the AIMD simulations were obtained from the last 15 ns of the NVT MD. In the AIMD, the systems were equilibrated for ~5 ps, and the production run was carried out in the NVT ensemble for another 200 ps. In each case, the time step of the AIMD was 0.5 fs.

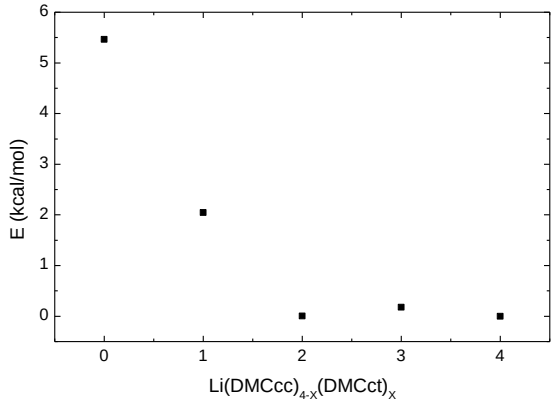


Figure 4.1. Relative solvation energy calculated using PBE/6-31+G(d,p) in gas phase for Li+ containing different number of DMC cis-trans (DMCct) and cis-cis (DMCcc) conformers in the solvation shell.

### 4.2.2. *Ab Initio* Umbrella Sampling (AIUS)

The potential of mean force along different reaction pathways involving ion pair formation and solvent exchange was obtained at the *ab initio* level using the umbrella sampling method. This methodology allowed us to evaluate the convergence of the computationally demanding AIMD as well as estimate the probability distributions and energetics of species with a low probability of occurring. The reaction coordinate in AIUS simulations was set as the distance between Li+ and the phosphorus atom of the counterion for calculating the ion pairing and between Li+ and a carbonyl oxygen for solvent exchange. Approximately 20 windows were employed in each AIUS simulation. Harmonic potentials were adopted as the biasing constraint in the form of

$$U_i(x) = \frac{1}{2}k(x - x_i)^2,$$

where $i$ represents the $i^{\text{th}}$ biasing potential, spring constant $k$ varies from 10.04 kcal/mol/Å$^2$ to 25.1 kcal/mol/Å$^2$, and $x_i$ is the reaction coordinate of the center of each harmonic biasing potential. Initial configurations with a reaction coordinate of ~7 Å were taken from the snapshots of the

AIMD simulation, and then driven from ~7 Å to ~2 Å (forming process) by sequentially applying the ~20 biasing potentials for windows of ~14 ps each. In each window, the first 2 ps were discarded due to system equilibration. A similar method was used to simulate the breaking process, but in this case, the system was driven using a reaction coordinate that was varied from ~2 Å to ~7 Å. The weighted histogram analysis method (WHAM) was used to unbias the system and obtain the free energy of the proposed reaction coordinate (PMF).[63-66]

### 4.3. Results and discussion

#### 4.3.1. Cation solvation

The geometry and composition of the solvation shell structure as a function of the molecular structure of the organic carbonate were first investigated by measuring the radial distribution functions (RDF, g(r)) and angular and distance distributions from the canonical AIMD. The g(r) and the integrated g(r) between Li+ and the carbonyl oxygen ($O_C$) of the carbonate (Figure ) shows a very sharp first peak located at 1.95 Å irrespective of the carbonate structure, which is in agreement with previous experimental and computational results.[2, 24, 44] A second maximum located at ~7.5 Å, barely noticed in the g(r), indicates a separation of ~5.5 Å between first and second solvation shell. A coordination number of 4 is deduced from the integrated g(r) at a distance of 4 Å validating the tetrahedral solvation structure of lithium in both BC and DMC solutions observed experimentally.[21] The presence and location of the second solvation shell is in agreement with previous studies.[23, 67] As expected, the g(r) between the lithium and carbonyl carbon ($C_C$) shows the same results as between the Li+ and $O_C$ (Figure 4.2(b)); i.e., an overlapped lineshape with a coordination number of 4. However, the first maximum in the RDF of Li+-$C_C$ is located at 2.95 Å. The presence of the maxima at ~3 Å implies that the carbonyl groups are not

pointing directly towards Li+, but they are slightly tilted. In addition, RDFs of Li+-$C_C$ of BC and DMC samples showed 2 peaks and 1 peak in the range of 4-8 Å, respectively. The presence of a second peak in the g(r) of Li+-$C_C$ is not a contradiction between the two RDFs, but an indication of the intercalation of BC molecules in the first solvation shell of Li+ as will be discussed later.

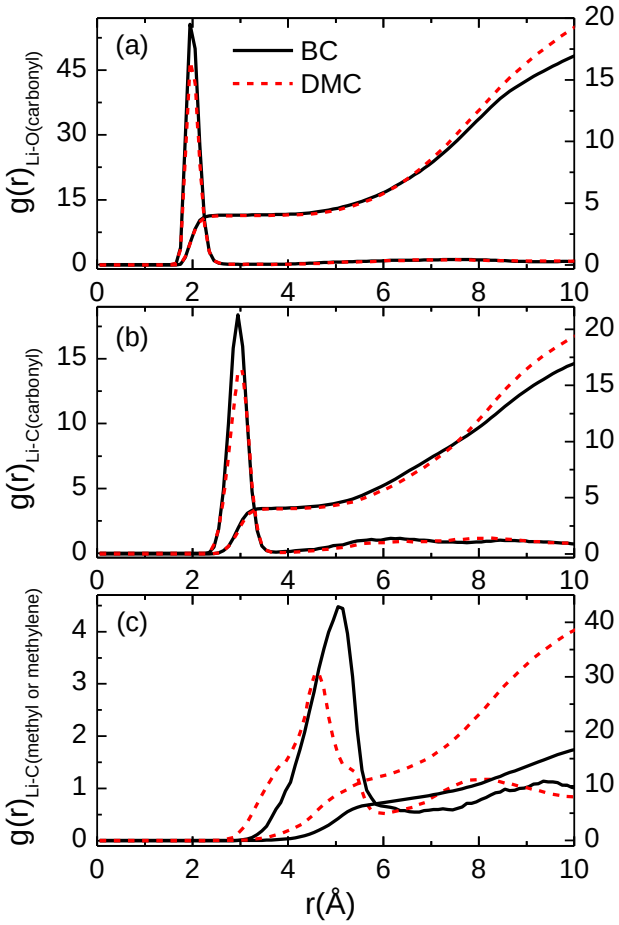


Figure 4.2. RDF profiles and integral of g(r) of Li+ in BC (black solid line) and in DMC (red dashed line). (a) g(r) between Li+ and carbonyl oxygen, (b) g(r) between Li+ and carbonyl carbon, (c) g(r) between Li+ and methyl or methylene carbon.

The RDF between lithium and the carbon of methyl group of DMC, and the methylene group of the cycle in BC were also calculated (Figure 4.2(c)) and Scheme 4.1). In contrast to the RDF of the oxygen and carbon atoms of the carbonyl group, the RDFs of carbon of the methyl

and methylene group of the carbonates show a striking difference between DMC and BC. In the case of DMC, the RDF shows a first peak with multiple shoulders and a maximum at 4.6 Å and a featureless second peak more asymmetric at 8.0 Å. Two peaks are also observed in the RDF of BC, but they are both relatively featureless and located at 5.1 Å and 9.5 Å. In addition, both DMC and BC RDF show a first minimum at ~6 Å and ~7 Å, respectively, which indicates the presence of a defined first solvation shell. The differences between BC and DMC account for the existence of different methyl groups in DMC due to the presence of the cis-trans isomer (Figure 4.1) that are not present in the coordinated BC molecules, while the peak positions arise from the different molecular size of BC and DMC.

The integral of the g(r) shows that there are 7 methylene groups of BC and 12 methyl group of DMC within the first solvation shell of lithium. The results indicate that the first solvation shell of BC contains 7 molecules of the carbonate, whereas DMC has 6 molecules of the carbonate in the same location. While this result appears to contradict the RDF of the carbonyl atoms, the presence of more than 4 molecules in the first solvation shell demonstrates that groups of the molecules in second solvation shell insert and/or intercalate into the first solvation shell. Note that intercalation is defined here as the molecule being located within the first solvation shell, while insertion corresponds to parts of the solvent molecule being buried in the first solvation shell. To differentiate between intercalation and insertion within the first solvation shell the RDF of the methyl and cyclic methylene group of the carbonates is decomposed between carbonate that have or do not the carbonyl oxygen solvating Li+. The result shows that the methylene group of BC molecules not having the carbonyl solvating Li+ are in closer proximity to Li+ than those corresponding to carbonates solvating Li+. In contrast, the methyl groups of DMC are further away

than the closest methyl groups of carbonates solvating Li+. Thus, there are three BC molecules intercalating into the first solvation shell, but the extra DMC molecules are inserting parts of the molecule into the first solvation shell. To visualize the observed intercalation process, a "representative" snapshot of the AIMD trajectory, illustrating the composition of the first peak in the RDF, is shown in Figure 4.3.

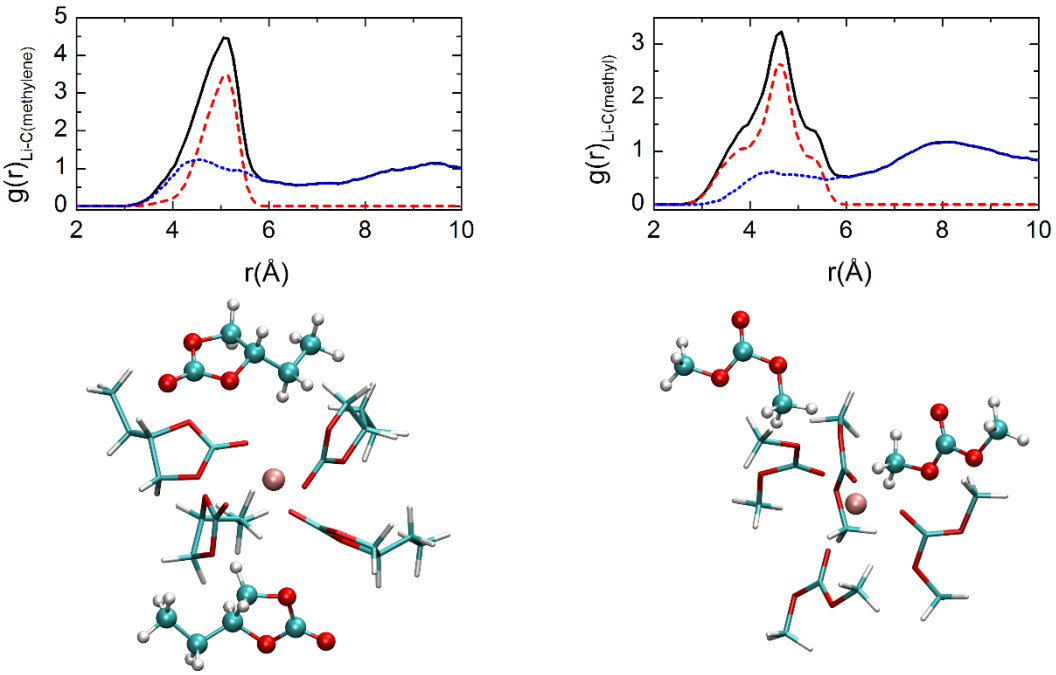


Figure 4.3. RDF between Li+ and DMC methyl or BC methylene carbon. Left and right panels correspond to BC and DMC, respectively. The solid black line corresponds to all groups, the dashed red line to those groups of carbonates coordinating Li+, and the dotted blue line to carbonates not directly coordinating Li+. Snapshots on each side of the panel illustrate the intercalation and inserting processes.

The intercalation in BC comes from the strong dipole-diploe interaction as a result of its high dielectric constant, leading to a more organized and rigid solvation structure in BC than in DMC. This result explains the slower(faster) solvation dynamics at lower(higher) Li+ concentration observed in the previous 2DIR study,[21] due to a decrease(increase) of the number of intercalated carbonate molecules when the lithium concentration is increased(decreased). The

observation of BC intercalation is also in agreement with the previous Raman and NMR studies.[9, 68]

The RDFs show that BC and DMC have different solvation structures. To study the effect of the molecular structure of the carbonate on the structural arrangement of the Li+ tetrahedral solvation shell, the order parameter:

$$q = 1 - \frac{3}{8}\sum_{j=1}^{3}\sum_{k=j+1}^{4}\left\{\cos\left(\phi_{jik}\right) + \frac{1}{3}\right\}^2,$$

was used to measure how tetrahedral the solvation structure formed by the carbonate molecules is. In this order parameter, $\phi_{jik}$ is the angle between the *j* and *k* vertices and the center of the tetrahedron "*i*".[69] For this order parameter, q is unity when the structure is strictly tetrahedral and q is zero when the four surrounding objects are randomly positioned.[69] The distribution of the q for $O_C$ in BC and DMC show very similar single distributions with extensive overlap in the whole q range (Figure 4.4) and same mean value (Table 4.1). The mean values of the q distributions demonstrate that the four $O_C$ form a tetrahedral structure around Li+, which is close to a perfect tetrahedron. A similar picture emerges from the q distribution of the carbon atom of the carbonyl group (Figure 4.4). However, the q distributions of $C_C$ are less tetrahedral than $O_C$ since their average is lower (Table 4.1), but is still fairly tetrahedral.

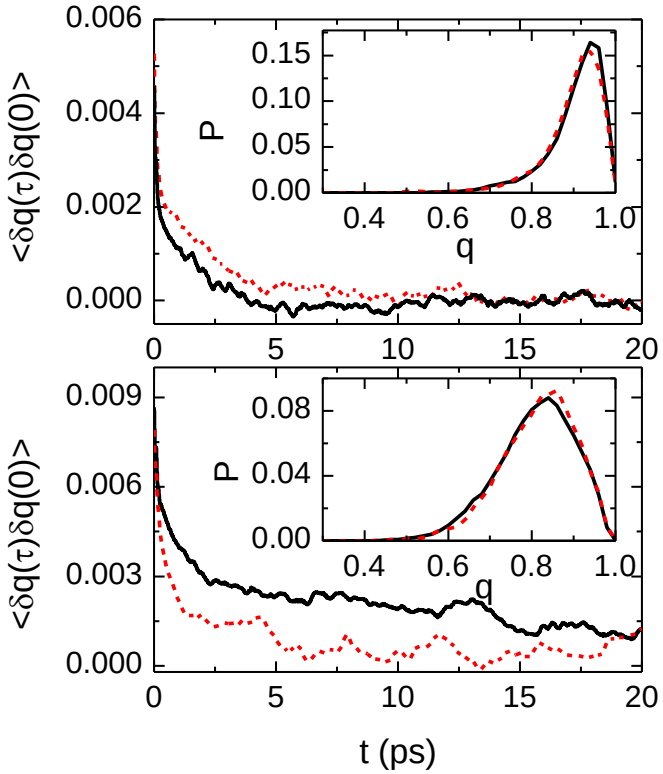


Figure 4.4. Distributions and autocorrelation functions of the tetrahedral parameter q for BC (black solid line) and DMC (red dashed line) samples. Top and bottom panel correspond to coordinated carbonyl oxygens ($O_C$) and coordinated carbonyl carbon ($C_C$). Inset show the distribution function.

The dynamics of the first solvation shell is derived from the autocorrelation function of the q factor defined as: $\langle \delta q(t) \delta q(0) \rangle$, where $\delta q(t) = q(t) - \langle q \rangle$. The autocorrelations of q for the oxygen atoms show a very similar time evolution for both carbonates (i.e., a very fast process followed a slower one) with a similar decorrelation exponential times for both carbonates (Figure 4.4 and Table 4.1). The autocorrelation demonstrates that the motions of the coordinated oxygens around lithium ions are very similar in both systems. In contrast, the autocorrelation function of q for $C_C$ exhibits a significant difference between BC and DMC. In this case, much faster decorrelation dynamics is observed for DMC compared to BC, which is evidenced in the characteristic times of 20 ps and 2 ps for BC and DMC, respectively. Notably, a similar timescale has been deduced from previous 2DIR experiments on similar systems.[21]

Table 4.1. Average values and fitting parameters of tetrahedral parameter q

| Geometrical factor | | Sample | |
|---|---|---|---|
| | | BC | DMC |
| q of $O_C$ | <q> | 0.90 | 0.90 |
| | τ (ps) | ~2 | ~2 |
| q of $C_C$ | <q> | 0.81 | 0.81 |
| | τ (ps) | ~20 | ~2 |
| Li-$O_C$ distance | <d> | 2.03 | 2.04 |
| | τ (ps) | ~1.8 | ~1.3 |
| $O_C$-Li-$O_C$ angle | <θ> | 108.8 | 109.2 |
| | τ (ps) | ~2.0 | ~2.5 |
| Li-$O_C$-$C_C$ angle | <θ> | 132.9 | 134.4 |
| | τ (ps) | ~5.0 | ~2.6 |
| $C_C$-Li-$C_C$ angle | <θ> | 104.8 | 108.4 |
| | τ (ps) | ~22 | ~6 |
| FFCF from exp. | τ (ps) | 12.8±0.1 | 1.4±0.1 |

The autocorrelation function of the q factor for the DMC $C_C$ also shows a ~4 ps oscillation, which is better observed in the residuals of its bi-exponential fitting (Figure 4.5) and is not observed in its cyclic analogue. The oscillation in the autocorrelation reveals a periodic motion that affects the tetrahedral structure of the coordinated carbons in this timescale. Due to the simplicity of the studied system, it is fair to assume that the oscillation is caused by the close proximity between the cation and the anion in DMC due to the formation of SSIPs. To test this hypothesis, the autocorrelation function of the distance between Li+ and the phosphorus atom of the anion was calculated. As in the q factor, an oscillation with a period of 7 ps is observed in the autocorrelation of the DMC system, but not in BC. Note that the factor of two between the oscillation periods observed in the autocorrelation of the q factor and the Li-anion distance arises from the definition of q (Figure 4.6). To simplify the process, assuming the PF6- only pushing the

two nearby carbons in a scissoring-like motion, the evolution of q along the change of C-O-C angle is shown in Figure 4.6. One period of lithium oscillation, which is inserting in and then getting out of the solvation shell, is in corresponding to the angle change from 40 to -40, then from -40 back to 40. From Figure 4.6, q experiences two cycles within one cycle of Li-PF6 distance change, which explains the factor of 2 between the oscillation periods. Thus, the oscillation in the q autocorrelation indicates that the anion disturbs the tetrahedral structure by pushing the nearby carbonyl groups back and forth while alternating between two different structures related to SSIPs (see Figure 4.12).

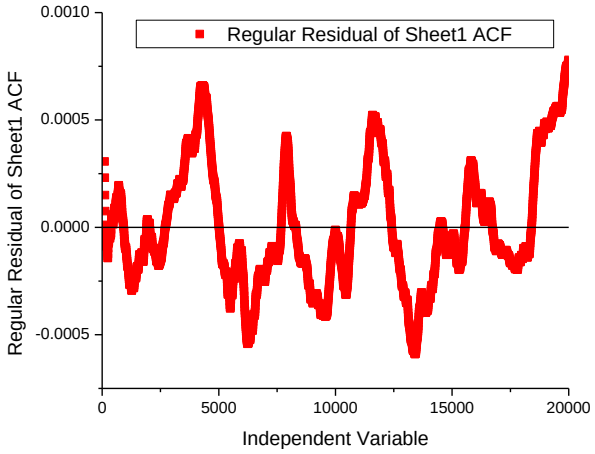


Figure 4.5. The residuals of the bi-exponential fitting of the ACF of $q_C$ of DMC.

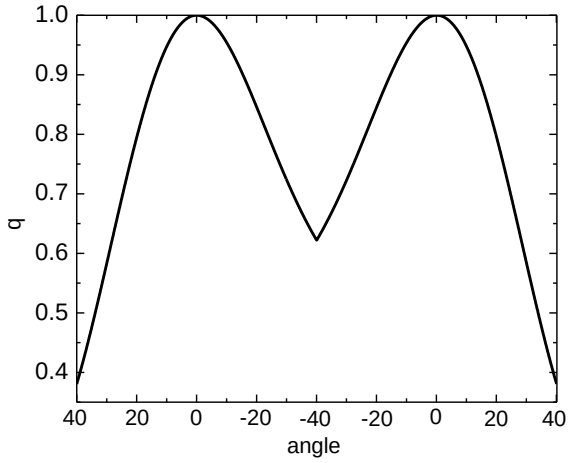


Figure 4.6. Variation of q during the insertion of a $PF_6^-$ anion in the $Li(DMC)_4^+$.

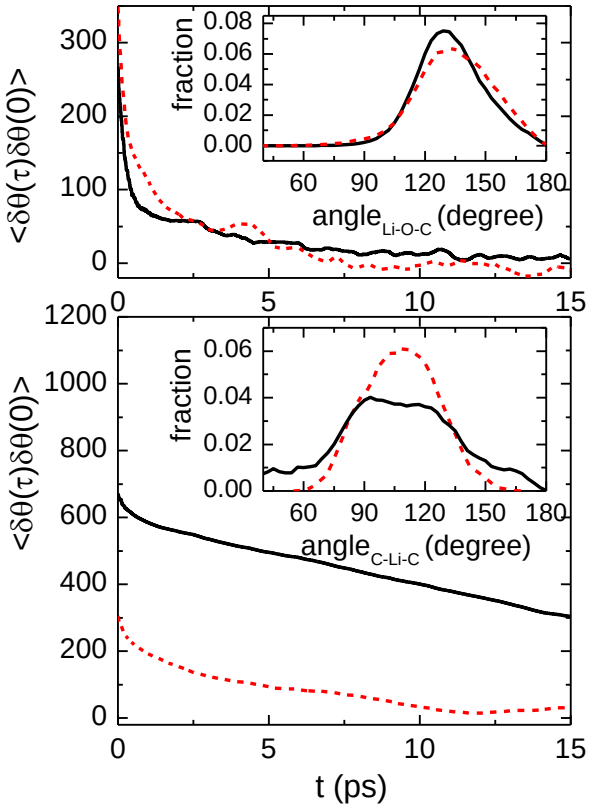


Figure 4.7. Distributions and autocorrelation functions of the Li-$O_C$-$C_C$ (top panel), and $C_C$-Li-$C_C$ (bottom panel) for BC (black solid line) and DMC (red dashed line) samples.

An examination of the different geometrical parameters, such as Li-$O_C$ distance and $O_C$-Li-$O_C$ angles confirms the results derived from the q factor, in which the Li-$O_C$-$C_C$ geometrical factor exhibits the largest difference between samples for their distributions and dynamics (see Table 4.1, and Figure 4.8 for the Li-$O_C$ distance and Figure 4.9 for $O_C$-Li-$O_C$ angle). While BC and DMC Li-$O_C$-$C_C$ angle distributions depart significantly from the 180$^o$ expected for a perfect tetrahedral structure (Table 4.1), the DMC solvation shell presents a much broader and asymmetric distribution for the Li-$O_C$-$C_C$ angle than BC. This result indicates that the DMC carbonyl carbons undergo larger spatial fluctuations than BC, which are related to the formation of SSIPs (see next section). The dynamics of the Li-$O_C$-$C_C$ autocorrelation function reveals two dynamical processes in which the slow has a characteristic time of ~3 ps and ~5 ps for DMC and BC, respectively. The difference in Li-$O_C$-$C_C$ bending dynamics evidences the slower carbonyl motions of the BC-Li+ solvation shell, due to intercalation which is not present in the DMC solvation shell.

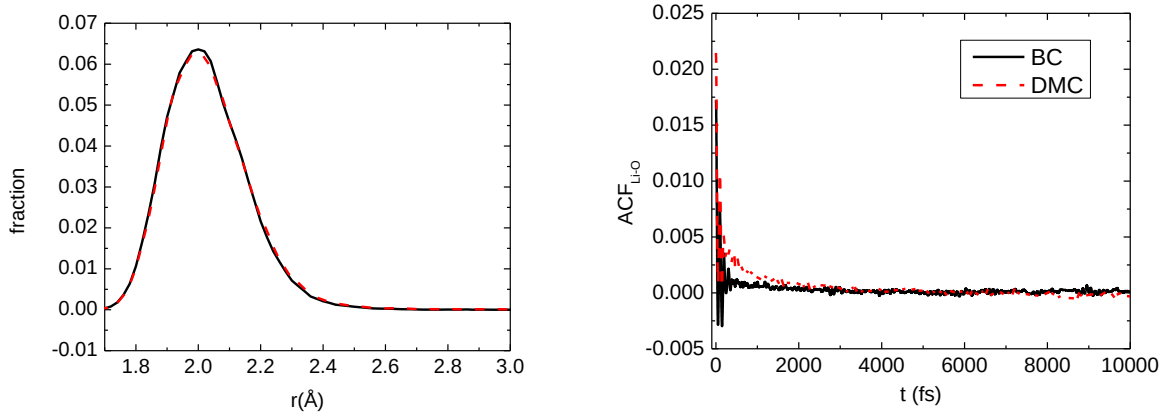


Figure 4.8. Distributions (left) and autocorrelation functions of the distance between Li and $O_C$ in BC (black, solid) and in DMC (red, dash).

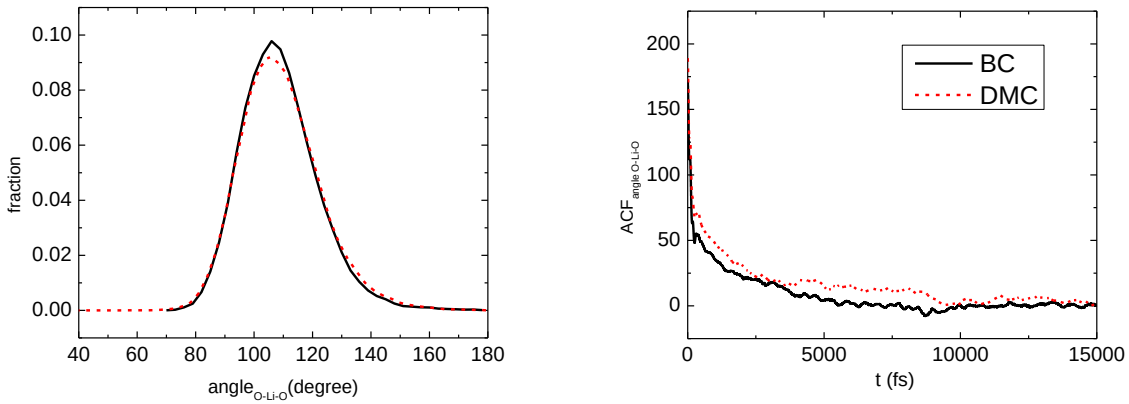


Figure 4.9. Distributions (left) and autocorrelation functions of $O_C$-Li-$O_C$ angle in BC (black, solid) and in DMC (red, dash).

A more evident distortion of the BC solvation shell is observed by studying the $C_C$-Li-$C_C$ angle. The mean values (standard deviations) of $C_C$-Li-$C_C$ angle are 104.8 (30.4) and 108.4 (17.9) for BC and DMC solvation shells, respectively. The result shows that BC has a more tilted geometry than DMC when coordinated to Li+. Interestingly, the $C_C$-Li-$C_C$ angle has a much broader distribution for BC than DMC. The difference in the distributions arises from the intercalation of the second solvation shell, which forces the carbonyl carbons to depart from the tetrahedral structure. The characteristic times of ~22 ps for BC and ~6 ps of DMC derived from the autocorrelation function of the $C_C$-Li-$C_C$ angle also shows the striking differences between BC and DMC solvation shells. The slow dynamics is compatible with the intercalation observed in the BC samples since the compact BC solvation shell requires the displacement of one intercalated BC molecule to produce large motions of the BC molecules in the Li+ solvation shell.

The results showed so far demonstrate that the solvent molecules beyond the first solvation shell play a role in the solvation of the lithium by either inserting the groups or by intercalating themselves in the first solvation shell. However, unlike the solvent molecules in the first solvation

shell of Li+, the solvent molecules in the second solvation shell undergo larger changes in its position due to the lack of a strong interaction with Li+. The fast dynamics of the molecules in the second solvation shell is directly observed in the time evolution of their orientational dynamics which are 10 and 4 times faster than those in the first solvation shell for DMC and BC samples, respectively (Figure 4.10). The orientational autocorrelation time of carbonate molecules was estimated by averaging the scalar product of the normalized dipole $\vec{\mu}_i$ of each carbonate molecule (i) in the system as

$$C_1(t) = \langle \vec{\mu}_i(t)\vec{\mu}_i(0)\rangle = \frac{1}{N}\sum_{i=1}^{N} cos\big(\theta_i(t)\big)$$

where $\theta_i(t)$ is the angle between the dipole of the molecule at 0 time and time *t*. the results are shown in Figure 4.10, and the decorrelation times derived from the fittings of the values in Figure 4.10 with a function of the form:

$$f(t) = \sum a_i exp(-t/\tau_i)$$

are presented in Table 4.2.

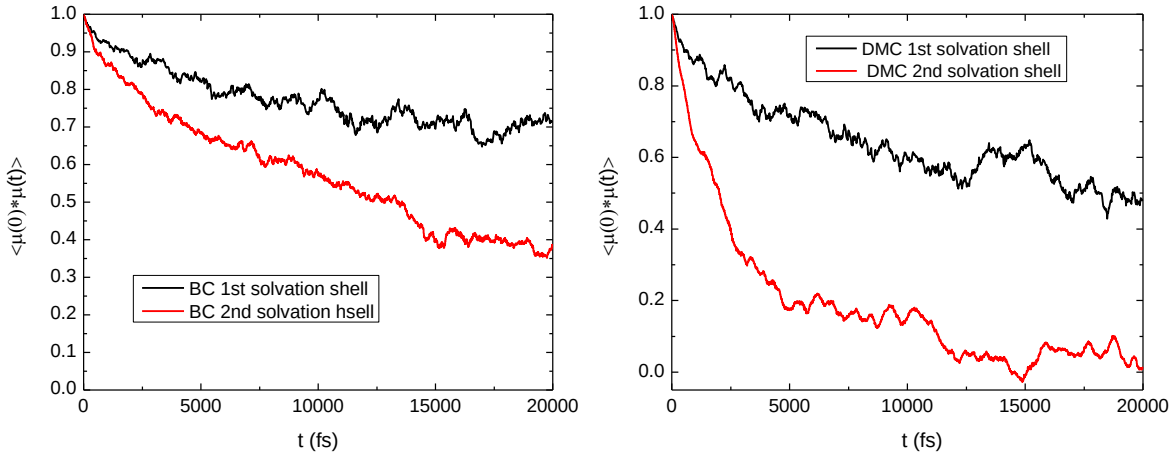


Figure 4.10. Orientational autocorrelation of the different solvation shells of Li+ for DMC (left panel) and BC (right panel) samples. The black and red lines correspond to the first and second solvation shell of Li+, respectively.

Table 4.2 Fitting parameters for orientational autocorrelation of the different solvation shells of Li+ for DMC and BC samples.

| Sample | $a_1$ | $\tau_1$ (ps) | $a_2$ | $\tau_2$ (ps) | $a_3$ | $\tau_3$ (ps) | $\langle\tau\rangle$ (ps) |
|---|---|---|---|---|---|---|---|
| BC 1st SS | 0.04±0.01 | 0.2±0.1 | 0.13±0.01 | 3.6±0.5 | 0.83±0.01 | 91±7 | 76±6 |
| BC 2nd SS | 0.13±0.01 | 0.8±0.1 | 0.86±0.01 | 22.6±0.1 | -- | -- | 19.7±0.1 |
| DMC 1st SS | 0.21±0.01 | 2.8±0.3 | 0.75±0.01 | 48±2 | -- | -- | 38±2 |
| DMC 2nd SS | 0.62±0.01 | 1.5±0.1 | 0.38±0.01 | 8.1±0.5 | -- | -- | 4.0±0.3 |

Overall, the presented results show that the dynamics of the first solvation shell of Li+ is controlled by both the second solvation shell and the anion. In the case of DMC, the motions of the solvation shell are essentially two, one which is exclusively driven by the motion $PF_6^-$ ion and another given by stochastic fluctuations in system. In contrast, the Li+ solvation shell of BC only present a motion related to thermal fluctuations because of the intercalation of BC molecules into the first solvation shell, which hinders the formation of SSIPs and consequently its influence in the dynamics of the Li+ solvation shell deformation.

### 4.3.2. Anion solvation

The structure of the solvation shell of hexafluorophosphate anion was also investigated. The RDF between lithium and the phosphorus atom for BC and DMC samples are displayed in 4.11. The RDFs show significant differences between the two systems. First, the first peak of the DMC RDF is wider and more asymmetric than that of BC. Second, the location of the peak maxima is also different: 6.1 Å for DMC and at 8.2 Å for BC. The peak maxima demonstrate that the interaction between lithium and the anion is inhibited by the presence of BC molecules, but not by linear carbonates. According to the RDF of the Li-$O_C$, the second solvation shell ends at ~7.5 Å. Consequently, the anion positions at 8 Å and 6 Å are assigned to free ion and solvent separated ion pairs, respectively. Note that this assignment is similar to that previously derived from IR experiments.[20] Thus, the dominant species for the anion are free ions in BC and SSIPs in DMC. Although DMC shows predominantly SSIPs, the RDF of Li-P presents a shoulder at 7.0 Å. This latter peak corresponds to free ions in DMC. However, some of the free ions are not completely "free" since they present a $CH_3$--F interaction that stabilizes their structure similar to an SSIP (Figure 4.11). In addition, the shoulder at ~6 Å in the BC RDF demonstrates that the anion has a small probability of forming SSIPs in BC.

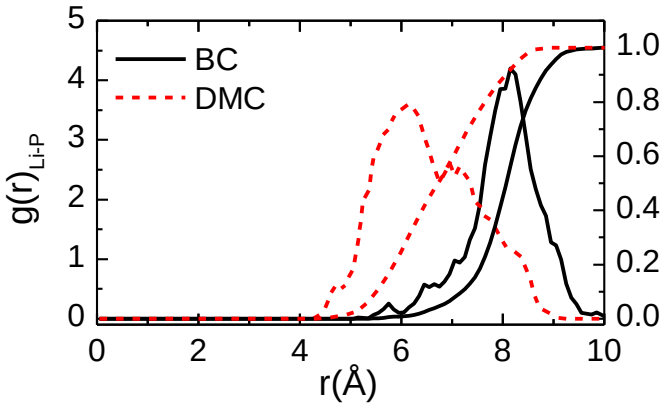


Figure 4.11. RDF between lithium ion and the phosphorus atom of $PF_6^-$ ion for BC (black solid line) and DMC (red dashed lines) samples.

The RDF shows that the anion is present in both free and SSIP in DMC, but mainly as free ions in BC. The lack of SSIPs in the cyclic carbonate and the observation of SSIPs and free ions in the linear carbonate is in agreement with previous experimental studies.[21] The molecular mechanism for the inhibition of the SSIP formation in cyclic carbonates could arise from a difference in the energetics of the SSIP formation. However, previous studies have shown that linear and cyclic carbonates have similar ion pair energetics when only accounting for 4 carbonates in the solvation shell.[31] However, the RDF of the carbonates indicates that BC has ~7 carbonates in the first solvation shell due to the intercalation. The presence of 7 BC molecules creates a denser solvation shell around Li+ which not only limits the interaction between the cation and the anion, but also requires the expulsion of more than one BC molecule to create CIPs. In addition, the intercalated BC molecules appear to have their dipole moment pointing away from Li+, making it energetically unfavorable to position the counter ion closer to Li+ due to the repulsive ion-dipole interaction. Finally, the RDFs of both systems do not show anions at distances less than 4 Å from Li+. The result indicates that contact ion pairs are not the most favorable counterion species in dilute solutions, irrespective of the carbonate structure.

Due to the limited time window explored by the canonical AIMD simulation, the probability of forming different anionic species was studied by computing the potential of mean force (PMF) from AIUS simulations. Figure 4.13 shows the calculated PMF for a Li-P reaction coordinate. Both carbonate samples exhibit a potential well with a minimum centered at ~3 Å, which is related to the formation of CIPs. An extra potential minimum is observed at ~3.6 Å in Li-P PMFs for DMC, which is less noticeable in BC. This minima at ~3.6 Å is assigned to a SSIP; i.e., four carbonate molecules and the anion in the Li+ solvation shell (Figure 4.12). Overall, the energy barriers of ~1.5 kcal/mol are observed in DMC and BC systems, which are well within thermal energy. Moreover, the energy difference between CIP, SSIPs and free ions is also within ~1 kcal/mol indicating that the ion pair formation does not impart a large energy stabilization of the system.

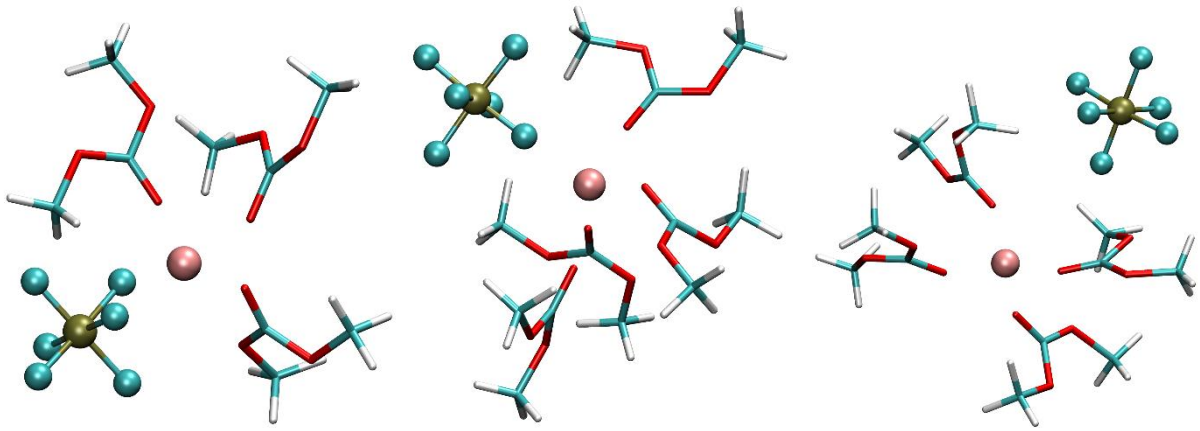

Figure 4.12. Representative snapshots of the lithium ion first solvation shell in DMC for the distance Li+ to P of: ~3 Å (left), ~3.6 Å (middle), and 6 Å (right).

The normalized probability of finding the phosphorus atoms of the anion at distance r of Li+ computed from the Boltzmann distribution function is shown in Figure 4.13. While it appears that CIP have a large probability because of the radial distribution, the space integrated probability (Figure 4.13) shows that the CIP only account for ~14% in DMC and ~12% in BC. However, the

most significant difference in the integrated probability is the formation of SSIPs in DMC. For the cutoff of range of 3.4-6.4 Å (Figure 4.11), the SSIP population accounts for 46% and 40% in DMC and BC, respectively, and the free ion population is 40% in DMC and 48% in BC. These results, along with the RDF of Li-P from the canonical AIMD, support the previous experimental data that the lithium ion exists predominantly as SSIP in DMC, while in BC it exists predominantly as free.[20] Note that the semi-qualitative agreement between experiment and theory could arise from the relatively small time window sampled in our AIUS because of the high computational cost of the methodology.

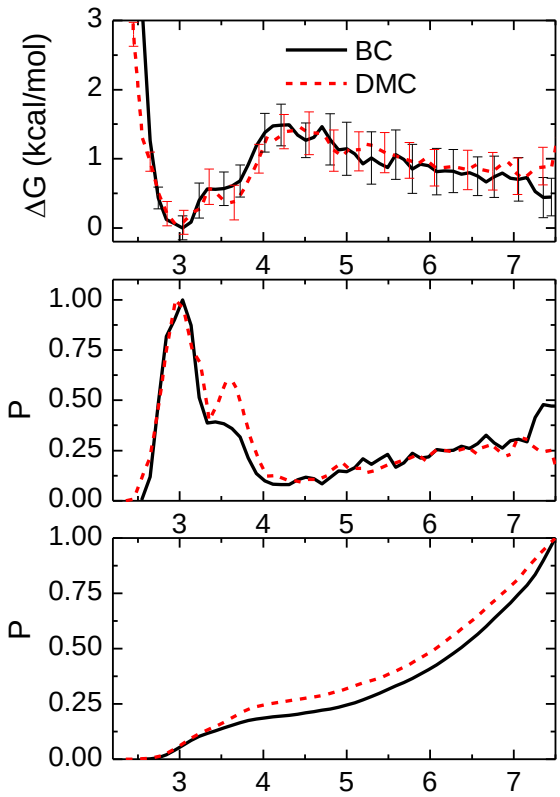


Figure 4.13. Ion pairing in BC and DMC. PMF of ion pairing process (top panel), probability distribution of $PF_6^-$ existing at the distance of r of lithium ion (middle panel), and integrated probability of $PF_6^-$ existing in a sphere with a radius of r (bottom panel) for BC (black solid line) and DMC (red dashed lines) samples.

### 4.3.3. Solvent exchange

The canonical AIMD trajectory revealed that solvent exchange is a slow dynamical process since there is only one occurrence in the 200 ps trajectory of the BC-Li+ system and it is not observed in the DMC trajectory. Thus, the canonical AIMD strongly suggests a slow solvent exchange rate, which is in agreement with a previous theoretical study.[2] However, the observed slow dynamics also prevents us from estimating the rate constant value because of the large statistical error. To estimate the chemical exchange rate, the structural arrangement of the solvation coordinate in BC giving rise to the only solvent exchange event observed in the BC trajectory is used. This structural arrangement is likely to represent the geometry of transition state (TS).

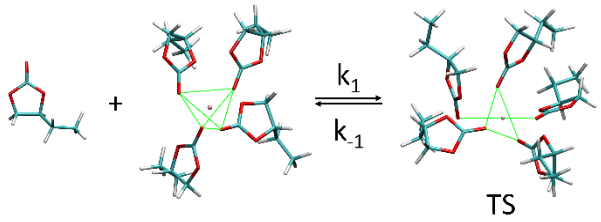


Figure 4.14. Kinetic scheme for chemical exchange including the transition state (TS) geometry observed in the BC trajectory.

The observed transition state (Figure 4.14) shows that the carbonate molecules adopt a trigonal bipyramid in which the incoming carbonate approximates to the Li+ through an axial position. While this solvent configuration (i.e., bipyramidal geometry of the carbonates) does not appear frequently in the trajectory, the solvent configuration showing five carbonates in the Li+ solvation shell does. Therefore, one can use the appearance of the TS during the canonical trajectory to obtain the lower limit of the time scale for the solvent exchange dynamics. To this end, it is assumed that the complex containing 5 carbonate molecules and one Li+ undergoes chemical exchange as depicted by the following mechanism

$$BC + C_4 \underset{k_{-1}}{\overset{k_1}{\rightleftharpoons}} C_5(TS) \underset{k_{-2}}{\overset{k_2}{\rightleftharpoons}} C_4' + BC',$$

where $C_4'$ and $C_4$ are the Li+ with four carbonates in its first solvation shell, $C_5$ is the five-carbonates configuration, and $BC'$ is the carbonate interchanged during the solvent exchange process. In addition, $k_i$ are the rate constants of the depicted kinetics steps. Since the concentration of BC does not change in the solution during the process, the equation can be simplified as,

$$C_4 \underset{k_{-1}}{\overset{k_1}{\rightleftharpoons}} C_5(TS) \underset{k_{-2}}{\overset{k_2}{\rightleftharpoons}} C_4'.$$

In this case, the concentration evolution can be solved as:

$$[C_5(t)] = A_0 k_1 \left[\frac{k_{-2}}{\gamma_1\gamma_2} - \frac{k_{-2}-\gamma_1}{\gamma_1(\gamma_2-\gamma_1)} e^{-\gamma_1 t} + \frac{k_{-2}-\gamma_2}{\gamma_2(\gamma_2-\gamma_1)} e^{-\gamma_2 t}\right],$$

$$[C_4'(t)] = A_0 k_1 k_2 \left[\frac{1}{\gamma_1\gamma_2} - \frac{1}{\gamma_1(\gamma_2-\gamma_1)} e^{-\gamma_1 t} + \frac{1}{\gamma_2(\gamma_2-\gamma_1)} e^{-\gamma_2 t}\right],$$

where $\gamma_1\gamma_2 = k_{-1}k_{-2} + k_1k_2 + k_1k_{-2}$; $\gamma_1 + \gamma_2 = k_1 + k_{-1} + k_2 + k_{-2}$, with the boundary condition of $[C_4(0)] = A_0$ $[C_5(0)] = 0$, and $[C_4'(0)] = 0$. In addition, the final state and the initial state are actually identical, and so: $k_1 = k_{-2}$, $k_2 = k_{-1}$, and $k_1 \ll k_{-1}$.

Thus,

$$[C_5(t)] = A_0 k_1 \left[\frac{1}{2k_{-1}} - \frac{1}{k_1 + 2k_{-1}} e^{-(k_1+2k_{-1})t}\right],$$

$$[C_4'(t)] = 0.5A_0(1 - e^{-k_1 t}).$$

From this mechanism, one can demonstrate that the solvent exchange rate is given by the rate of making the transition state; i.e., $k_1$

The rate of making the $C_5$ was obtained from the time intervals between the appearances of the $C_5$ from the AIMD trajectory. In this case, the $C_5$ was strictly defined as the Li+ coordinated with five carbonates in which all carbonates have the carbonyl carbon within 3.5 Å of the Li+. The time intervals between the appearances of two different $C_5$ configurations are displayed in 4.15. The time intervals show that the BC solvation shell is more likely to adopt the $C_5$ configuration than DMC. In addition, it is observed the presence of time intervals with time windows of 0.5 ps. These short time intervals correspond to the oscillation in the structure that do not completely lose the $C_5$ configuration. In contrast, the longtime intervals observed in the trajectory relate to the time required to form the five carbonate structure. The average time for forming $C_5$ configuration in BC and in DMC are found to be 27 ps and 60 ps, respectively. Based on the results calculated from the time intervals, the rate of chemical exchange (or equivalent $1/k_1$) is estimated to be $(27\ ps)^{-1}$ for BC and $(60\ ps)^{-1}$ for DMC. Overall, the solvent exchange dynamics in DMC-Li+ system is much slower than that of BC-Li+ complex. It is likely that the intercalation of the second solvation shell in BC might help to rearrange the molecules in the first solvation shell in a geometry close to that of the TS. In contrast, the less extended solvation shell formed by the DMC limits the insertion of the fifth carbonyl group required for the solvent exchange process to occur.

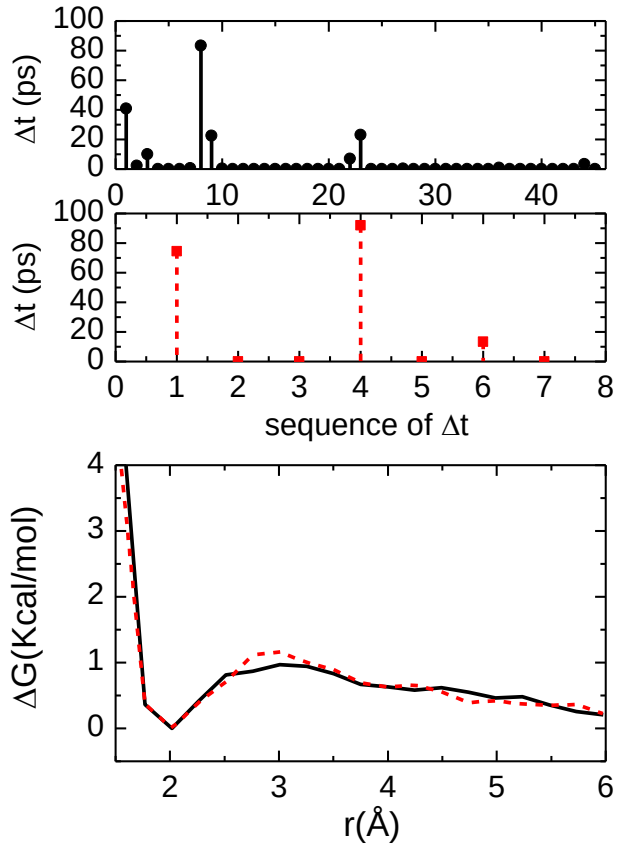


Figure 4.15. Time intervals between TS in BC (left) and in DMC (right). PMF of the solvent exchange for BC (black solid line) and DMC (red dashed line).

The predicted solvation exchange process is much slower than the 5 ps proposed experimentally and theoretically.[18, 19] However, it is possible that the short time window of the canonical trajectory is not sufficient to appropriately sample the solvent exchange process. To this end, AIUS was performed in both DMC and BC systems. The PMFs of the solvent exchange for BC and DMC are shown in Figure 4.15. Surprisingly, the solvent exchange process for BC and DMC show a similar energy barrier of ~1 kcal/mol. To estimate the solvent exchange rate from the PMF, Kramer's theory is used. In Kramer's theory, the rate constant of a transition state is given by

$$k = \frac{\omega_0 \omega_b}{2\pi\gamma} e^{-\frac{E^*}{k_B T}},$$

where $E^*$ is the transition state energy barrier, $\gamma$ is the friction coefficient, and $\omega_0$ and $\omega_b$ are the oscillation frequencies at the bottom of the well and at the transition state, respectively. In this case, the solvent exchange rate is computed for the breaking process, since the forming process requires the oscillation frequency of the final state, which is not available due to the limit of the box size. However, the PMF shows that the potential well of the final state for making a bond is much flatter than that of the initial state, indicating that the making process should be slower than the breaking process. Using the oscillation frequencies, $\omega_0$ and $\omega_b$, obtained by assuming the harmonic potential, the characteristic time of breaking is found to be on a range of 100-370 ps for BC, and of 20-60 ps for DMC. Although the energy barrier of ~1 kcal/mol does not fulfill the one of the hypothesis of Kramer's theory, the observed characteristic time is similar to that predicted from the kinetics of the TS in canonical simulations. Thus, the solvent exchange rates derived from the rate of making and breaking the TS and Kramer's theory confirm that the rates are much longer than the ones previously derived from experiment.[18]

### 4.4. Conclusions

The *ab initio* molecular simulations presented here show the similarities and differences in the structure and dynamics of the lithium solvation shell in cyclic and linear carbonates. A tetrahedral coordination number was found for the lithium ion in both DMC and BC solutions. In addition, it is observed that the methyl groups of various DMC molecules insert into the lithium ion first solvation shell. In contrast, three BC molecules intercalate in the first solvation shell of the lithium ion for this cyclic carbonate. The intercalation of BC molecules leads to a more rigid

and more organized solvation shell in BC than DMC. The speciation of Li+ is also affected by the chemical nature of the carbonate, where the intercalation of BC molecules appears to inhibit the association of Li+ with the counterion in BC. The PMF derived from AIUS shows that Li+ exists predominantly as free in BC and SSIPs in DMC, and that CIPs only account for a small fraction of the total population (~10%). In addition, the canonical AIMD and AIUS via Kramer's theory predict a slow solvent exchange dynamic in both DMC and BC with characteristic times ranging from fifty to hundreds of picoseconds. Overall, this work gives a description of the structure and dynamics of the lithium solvation shell in cyclic and in linear carbonates occurring in picosecond time scales. In addition, it demonstrates that the carbonate molecular structure affects the speciation of Li+ and solvent exchange dynamics.

### 4.5. References


1. Garche, J., et al., *Encyclopedia of electrochemical power sources*. 2013: Newnes.
2. Ganesh, P., D.-e. Jiang, and P.R.C. Kent, *Accurate Static and Dynamic Properties of Liquid Electrolytes for Li-Ion Batteries from ab initio Molecular Dynamics.* The Journal of Physical Chemistry B, 2011. **115**(12): p. 3085-3090.
3. Peled, E., *The Electrochemical Behavior of Alkali and Alkaline Earth Metals in Nonaqueous Battery Systems—The Solid Electrolyte Interphase Model.* Journal of The Electrochemical Society, 1979. **126**(12): p. 2047-2051.
4. Wang, J., et al., *Superconcentrated electrolytes for a high-voltage lithium-ion battery.* Nature Communications, 2016. **7**: p. 12032.
5. Yamada, Y. and A. Yamada, *Review—Superconcentrated Electrolytes for Lithium Batteries.* Journal of The Electrochemical Society, 2015. **162**(14): p. A2406-A2423.
6. Soetens, J.-C., et al., *Molecular dynamics simulation and X—ray diffraction studies of ethylene carbonate, propylene carbonate and dimethyl carbonate in liquid phase.* Journal of Molecular Liquids, 2001. **92**(3): p. 201-216.

7. Fujii, K., et al., *Long-Range Ion-Ordering in Salt-Concentrated Lithium-Ion Battery Electrolytes: A Combined High-Energy X-ray Total Scattering and Molecular Dynamics Simulation Study.* The Journal of Physical Chemistry C, 2017. **121**(41): p. 22720-22726.

8. Yang, L., A. Xiao, and B.L. Lucht, *Investigation of solvation in lithium ion battery electrolytes by NMR spectroscopy.* Journal of Molecular Liquids, 2010. **154**(2): p. 131-133.

9. Bogle, X., et al., *Understanding Li+–Solvent Interaction in Nonaqueous Carbonate Electrolytes with 17O NMR.* The Journal of Physical Chemistry Letters, 2013. **4**(10): p. 1664-1668.

10. Matsubara, K., R. Kaneuchi, and N. Maekita, *13C NMR estimation of preferential solvation of lithium ions in non-aqueous mixed solvents.* Journal of the Chemical Society, Faraday Transactions, 1998. **94**(24): p. 3601-3605.

11. Cazzanelli, E., et al., *Raman and NMR analysis of LiClO4 concentrated solutions in ethylene carbonate-propylene carbonate.* Solid State Ionics, 1996. **86-88**: p. 379-384.

12. Kondo, K., et al., *Conductivity and Solvation of Li+ Ions of LiPF6 in Propylene Carbonate Solutions.* The Journal of Physical Chemistry B, 2000. **104**(20): p. 5040-5044.

13. Burba, C.M. and R. Frech, *Spectroscopic Measurements of Ionic Association in Solutions of LiPF6.* The Journal of Physical Chemistry B, 2005. **109**(31): p. 15161-15164.

14. Giorgini, M.G., et al., *Solvation Structure around the Li+ Ion in Mixed Cyclic/Linear Carbonate Solutions Unveiled by the Raman Noncoincidence Effect.* The Journal of Physical Chemistry Letters, 2015. **6**(16): p. 3296-3302.

15. Aroca, R., et al., *Vibrational Spectra and Ion-Pair Properties of Lithium Hexafluorophosphate in Ethylene Carbonate Based Mixed-Solvent Systems for Lithium Batteries.* Journal of Solution Chemistry, 2000. **29**(10): p. 1047-1060.

16. Maeda, S., et al., *Local Structure of Li+ in Concentrated Ethylene Carbonate Solutions Studied by Low-Frequency Raman Scattering and Neutron Diffraction with 6Li/7Li Isotopic Substitution Methods.* The Journal of Physical Chemistry B, 2017. **121**(48): p. 10979-10987.

17. Klassen, B., et al., *Raman Spectra and Transport Properties of Lithium Perchlorate in Ethylene Carbonate Based Binary Solvent Systems for Lithium Batteries.* The Journal of Physical Chemistry B, 1998. **102**(24): p. 4795-4801.

18. Lee, K.-K., et al., *Ultrafast fluxional exchange dynamics in electrolyte solvation sheath of lithium ion battery.* Nature Communications, 2017. **8**: p. 14658.

19. Liang, C., K. Kwak, and M. Cho, *Revealing the Solvation Structure and Dynamics of Carbonate Electrolytes in Lithium-Ion Batteries by Two-Dimensional Infrared Spectrum Modeling.* The Journal of Physical Chemistry Letters, 2017. **8**(23): p. 5779-5784.

20. Fulfer, K.D. and D.G. Kuroda, *Ion speciation of lithium hexafluorophosphate in dimethyl carbonate solutions: an infrared spectroscopy study.* Physical Chemistry Chemical Physics, 2018. **20**(35): p. 22710-22718.

21. Fulfer, K.D. and D.G. Kuroda, *Solvation Structure and Dynamics of the Lithium Ion in Organic Carbonate-Based Electrolytes: A Time-Dependent Infrared Spectroscopy Study.* The Journal of Physical Chemistry C, 2016. **120**(42): p. 24011-24022.

22. Fulfer, K.D. and D.G. Kuroda, *A comparison of the solvation structure and dynamics of the lithium ion in linear organic carbonates with different alkyl chain lengths.* Physical Chemistry Chemical Physics, 2017. **19**(36): p. 25140-25150.

23. Pollard, T.P. and T.L. Beck, *Structure and polarization near the Li+ ion in ethylene and propylene carbonates.* The Journal of Chemical Physics, 2017. **147**(16): p. 161710.

24. Flores, E., et al., *Solvation structure in dilute to highly concentrated electrolytes for lithium-ion and sodium-ion batteries.* Electrochimica Acta, 2017. **233**: p. 134-141.

25. Kumar, N. and J.M. Seminario, *Lithium-Ion Model Behavior in an Ethylene Carbonate Electrolyte Using Molecular Dynamics.* The Journal of Physical Chemistry C, 2016. **120**(30): p. 16322-16332.

26. Takeuchi, M., et al., *Ion–ion interactions of LiPF6 and LiBF4 in propylene carbonate solutions.* Journal of Molecular Liquids, 2009. **148**(2): p. 99-108.

27. Bhatt, M.D., M. Cho, and K. Cho, *Interaction of Li+ ions with ethylene carbonate (EC): Density functional theory calculations.* Applied Surface Science, 2010. **257**(5): p. 1463-1468.

28. Borodin, O., et al., *Competitive lithium solvation of linear and cyclic carbonates from quantum chemistry.* Physical Chemistry Chemical Physics, 2016. **18**(1): p. 164-175.

29. Borodin, O. and G.D. Smith, *Quantum Chemistry and Molecular Dynamics Simulation Study of Dimethyl Carbonate: Ethylene Carbonate Electrolytes Doped with LiPF6.* The Journal of Physical Chemistry B, 2009. **113**(6): p. 1763-1776.

30. Ponnuchamy, V., S. Mossa, and I. Skarmoutsos, *Solvent and Salt Effect on Lithium Ion Solvation and Contact Ion Pair Formation in Organic Carbonates: A Quantum Chemical Perspective.* The Journal of Physical Chemistry C, 2018. **122**(45): p. 25930-25939.

31. Seo, D.M., et al., *Role of Mixed Solvation and Ion Pairing in the Solution Structure of Lithium Ion Battery Electrolytes.* The Journal of Physical Chemistry C, 2015. **119**(25): p. 14038-14046.

32. Chapman, N., et al., *Spectroscopic and Density Functional Theory Characterization of Common Lithium Salt Solvates in Carbonate Electrolytes for Lithium Batteries.* The Journal of Physical Chemistry C, 2017. **121**(4): p. 2135-2148.

33. Doucey, L., et al., *A study of the Li/Li+ couple in DMC and PC solvents: Part 1: Characterization of LiAsF6/DMC and LiAsF6/PC solutions.* Electrochimica Acta, 1999. **44**(14): p. 2371-2377.

34. Zhang, B., et al., *FTIR spectroscopic studies of lithium tetrafluoroborate in propylene carbonate+diethyl carbonate mixtures.* Spectrochimica Acta, Part A, 2014. **122**: p. 59-64.

35. Jiang, B., et al., *The Anion Effect on Li+ Ion Coordination Structure in Ethylene Carbonate Solutions.* The Journal of Physical Chemistry Letters, 2016. **7**(18): p. 3554-3559.

36. Allen, J.L., et al., *Combined quantum chemical/Raman spectroscopic analyses of Li+ cation solvation: Cyclic carbonate solvents-Ethylene carbonate and propylene carbonate.* Journal of Power Sources, 2014. **267**: p. 821-830.

37. Giorgini, M.G., et al., *Solvation Structure around the Li+ Ion in Mixed Cyclic/Linear Carbonate Solutions Unveiled by the Raman Noncoincidence Effect.* Journal of Physical Chemistry Letters, 2015. **6**(16): p. 3296-3302.

38. Arslanargin, A., et al., *Models of Ion Solvation Thermodynamics in Ethylene Carbonate and Propylene Carbonate.* The Journal of Physical Chemistry B, 2016. **120**(8): p. 1497-1508.

39. Chaudhari, M.I., et al., *Scaling Atomic Partial Charges of Carbonate Solvents for Lithium Ion Solvation and Diffusion.* Journal of Chemical Theory and Computation, 2016. **12**(12): p. 5709-5718.

40. Postupna, O.O., et al., *Microscopic Structure and Dynamics of LiBF4 Solutions in Cyclic and Linear Carbonates.* The Journal of Physical Chemistry B, 2011. **115**(49): p. 14563-14571.

41. von Wald Cresce, A., et al., *Anion Solvation in Carbonate-Based Electrolytes.* The Journal of Physical Chemistry C, 2015. **119**(49): p. 27255-27264.

42. Takeuchi, M., et al., *Free-Energy and Structural Analysis of Ion Solvation and Contact Ion-Pair Formation of Li+ with BF4– and PF6– in Water and Carbonate Solvents.* The Journal of Physical Chemistry B, 2012. **116**(22): p. 6476-6487.

43. Ong, M.T., et al., *Complex ion dynamics in carbonate lithium-ion battery electrolytes.* The Journal of Physical Chemistry C, 2017. **121**(12): p. 6589-6595.

44. Ong, M.T., et al., *Lithium Ion Solvation and Diffusion in Bulk Organic Electrolytes from First-Principles and Classical Reactive Molecular Dynamics.* The Journal of Physical Chemistry B, 2015. **119**(4): p. 1535-1545.

45. Tang, Z.-K., J.S. Tse, and L.-M. Liu, *Unusual Li-Ion Transfer Mechanism in Liquid Electrolytes: A First-Principles Study*. The Journal of Physical Chemistry Letters, 2016. **7**(22): p. 4795-4801.

46. Tachikawa, H. and S. Abe, *Solvent Stripping Dynamics of Lithium ion solvated by ethylene carbonates: A direct ab-initio molecular (AIMD) Study.* Electrochimica Acta, 2014. **120**: p. 57-64.

47. Li, T. and P.B. Balbuena, *Theoretical Studies of Lithium Perchlorate in Ethylene Carbonate, Propylene Carbonate, and Their Mixtures.* Journal of The Electrochemical Society, 1999. **146**(10): p. 3613-3622.

48. Tachikawa, H., *Mechanism of Dissolution of a Lithium Salt in an Electrolytic Solvent in a Lithium Ion Secondary Battery: A Direct Ab Initio Molecular Dynamics (AIMD) Study.* ChemPhysChem, 2014. **15**(8): p. 1604-1610.

49. Jorn, R., et al., *Atomistic Modeling of the Electrode–Electrolyte Interface in Li-Ion Energy Storage Systems: Electrolyte Structuring.* The Journal of Physical Chemistry C, 2013. **117**(8): p. 3747-3761.

50. Li, T., et al., *Hydration and vibrational dynamics of betaine (N,N,N-trimethylglycine).* The Journal of Chemical Physics, 2015. **142**(21): p. 212438.

51. Jorn, R. and R. Kumar, *Breaking the Scales: Electrolyte Modeling in Metal-Ion Batteries.* Interface, 2017. **26**(1): p. 55-59.

52. VandeVondele, J., et al., *QUICKSTEP: Fast and accurate density functional calculations using a mixed Gaussian and plane waves approach.* Computer Physics Communications, 2005. **167**(2): p. 103-128.

53. Grimme, S., *Semiempirical GGA-type density functional constructed with a long-range dispersion correction.* Journal of Computational Chemistry, 2006. **27**(15): p. 1787-1799.

54. Goedecker, S., M. Teter, and J. Hutter, *Separable dual-space Gaussian pseudopotentials.* Physical Review B, 1996. **54**(3): p. 1703-1710.

55. Lippert, G., et al., *Response Function Basis Sets: Application to Density Functional Calculations.* Journal of Physical Chemistry, 1996. **100**(15): p. 6231-6235.

56. Perdew, J.P., K. Burke, and M. Ernzerhof, *Generalized Gradient Approximation Made Simple.* Physical Review Letters, 1996. **77**(18): p. 3865-3868.

57. Logan, E.R., et al., *A Study of the Transport Properties of Ethylene Carbonate-Free Li Electrolytes.* Journal of the Electrochemical Society, 2018. **165**(3): p. A705-A716.

58. Hwang, S., et al., *Ionic Conduction and Solution Structure in LiPF6 and LiBF4 Propylene Carbonate Electrolytes.* The Journal of Physical Chemistry C, 2018. **122**(34): p. 19438-19446.

59. Frisch, M.J., et al., *Gaussian 09, Revision D.01*. 2013: Wallingford, CT.

60. Martínez, L., et al., *PACKMOL: A package for building initial configurations for molecular dynamics simulations.* Journal of Computational Chemistry, 2009. **30**(13): p. 2157-2164.

61. Plimpton, S., *Fast Parallel Algorithms for Short-Range Molecular Dynamics.* Journal of Computational Physics, 1995. **117**(1): p. 1-19.

62. Jorgensen, W.L., D.S. Maxwell, and J. Tirado-Rives, *Development and Testing of the OPLS All-Atom Force Field on Conformational Energetics and Properties of Organic Liquids.* Journal of the American Chemical Society, 1996. **118**(45): p. 11225-11236.

63. Kumar, S., et al., *THE weighted histogram analysis method for free-energy calculations on biomolecules. I. The method.* Journal of Computational Chemistry, 1992. **13**(8): p. 1011-1021.

64. Boczko, E.M. and C.L. Brooks III, *Constant-temperature free energy surfaces for physical and chemical processes.* Journal of Physical Chemistry, 1993. **97**(17): p. 4509-4513.

65. Grossfield, A., *"WHAM: the weighted histogram analysis method", version 2.0.9.1.*

66. Ferrenberg, A.M. and R.H. Swendsen, *Optimized Monte-Carlo Data-Analysis.* Physical Review Letters, 1989. **63**(12): p. 1195-1198.

67. Soetens, J.-C., C. Millot, and B. Maigret, *Molecular Dynamics Simulation of Li+BF4- in Ethylene Carbonate, Propylene Carbonate, and Dimethyl Carbonate Solvents.* The Journal of Physical Chemistry A, 1998. **102**(7): p. 1055-1061.

68. Brodin, A. and P. Jacobsson, *Dipolar interaction and molecular ordering in liquid propylene carbonate: Anomalous dielectric susceptibility and Raman non-coincidence effect.* Journal of Molecular Liquids, 2011. **164**(1): p. 17-21.

69. Chau, P.L. and A.J. Hardwick, *A new order parameter for tetrahedral configurations.* Molecular Physics, 1998. **93**(3): p. 511-518.

# CHAPTER 5
# MOLECULAR STRUCTURE OF A CONDUCTIVE AND "NON-IONIC" MIXTURE OF MOLECULAR SOLVENTS

## 5.1. Introduction

Proton delocalization plays a critical role in the structure and function of both aqueous solution and biological macromolecules. In the system of excess aqueous proton and water, strong evidence for proton delocalization with a low-barrier, double-minimum potential energy surface (PES) in Zundel-like cation motif was found by 2DIR and pump-probe spectroscopies.[1, 2] It implies a possible mechanism of proton transport in water that is responsible for the high conductivity of the excess proton water system. In terms of macromolecules, the role of low-barrier hydrogen bond (LBHB) in catalysis processes, which is an abnormally short hydrogen bond with a proton transfer barrier of the same order as zero-point energy, has been discussed for a long time. Unusually high prevalence of LBHB was found in the enzymes with transition state analog, and many scientists insist that the low-barrier hydrogen bond contributes to enzymic catalysis by stabilizing its transition state energy through quantum resonance.[3-9] Meanwhile, the delocalization of excess protons along the conducting wire was also found in the membrane enzymes, and the fluctuation of soliton in the molecule chain under the condition of strong coupling is the mechanism of proton transfer in the conducting channel.[10-13] Similarly, the delocalization of excess proton through the Grotthuss hopping mechanism in the hydrophilic domain pocket was found to be the reason for the high proton mobility in proton-conducting membranes as Nafion.[14] Other applications of proton delocalization appear as manipulating the isotopic fractionation factor by utilizing the low barrier potential and the different zero-point energy of isotopes.[15]

Attractions have been drawn to a system composed of acetic acid (HAc) and N-methylimidazole ($C_1$Im). A Brønsted acid-base mixture of weak acid HAc and weak base $C_1$Im with an extremely low ionicity was found to have a conductivity 4 orders of magnitude higher than its neat acid and 2 orders of magnitude higher conductivity than its neat base. This high conductivity is unexpected since the conductivity of the acid-base mixture is believed to be related to the ΔpKa between the two components, which indicates the concentration of ions. Raman spectroscopy showed that electrically neutral molecular species predominantly exist in the equimolar mixture,[16] in which the conductivity of 4 mS/cm was found.[17] Moreover, measurements of different molar ratios of this HAc/$C_1$Im mixture have been conducted to obtain the conductivity curve, and then two electrical conductivity maxima were found in the curve, at xHAc=0.65 and xHAc=0.85 respectively.[18, 19] This double-maxima is unique compared with other conductive acid/base mixtures such as pyridine/acetic acid, trimethylamine/acetic acid, water/acetic acid, etc.,[18] indicating a specific mechanism of electric conductivity.

Efforts were made to explain the unique proton activities and electric conductivity in this system. By looking into the Waldon plot, and conducting simple DFT energy calculations, Umebayashi and co-workers claimed that the system is a good or superionic liquid with a specific conductive mechanism such as the Grotthuss mechanism. ΔpKa value, which is pKa($C_1$HIm+) - pKa(HAc), is as small as 2.4 in this system, precluding the complete proton transfer. On the other hand, they claimed that the energy difference between the molecule complexes and ion pairs is approximately 7 kJ/mol, which is comparable to the thermal energy. This small energy difference enables fast proton transfer followed by the reorientation of surrounding neutral molecules, implying a specific proton conduction.[16] Moreover, recent *ab initio* molecular dynamics simulation provided evidence of the Grotthuss mechanism in the equimolar mixture, herein the

content of neutral species is 75-80%.[20] The energy surface of the proton transfer after zero-point energy correction showed a barrierless profile with a 7 kJ/mol energy difference between the two configurations.[20] However, nuclear magnetic resonance (NMR) experiments demonstrated completely different results. Enthalpy change of -9.33 kJ/mol, and entropy change of 11.29 $J\cdot(mol\cdot K)^{-1}$ in proton transfer process were calculated by temperature-dependent NMR, along with an ionicity of 92.8% obtained from concentration-dependent NMR.[21] This work was based on the simple assumption that the proton exists either in single HAc molecule or in a single $C_1HIm^+$ ion.

This barrierless energy profile indicates a probability that the proton delocalization exists in the HAc/$C_1$Im mixture. In the past thirty years, there have been numerous experimental and theoretical studies uncovering proton delocalization in low-barrier or barrierless potential for both homonuclear and heteronuclear hydrogen bonds. In the case of the weak homonuclear hydrogen bond, formation energy is small (~20 kJ/mol) and the distance between two electronegative atoms is far (>2.8 Å for O-O). The hydrogen is in a double-well potential, attached to either one electronegative atom closely by a covalent bond and far away from the other. As two electronegative atoms get closer, the barrier between two potential wells decreases and eventually can be overcome by the zero-point energy.[22] In this case, the shared proton is described to move freely between the two electronegative atoms and be bonded covalently to them.[23] An even closer distance between two atoms results in a single-well potential.[22] Similar trend has also been observed for heteronuclear hydrogen bonds.[22]

In this project, we looked into the structures and dynamics in the HAc/$C_1$Im mixture by FTIR, NMR, and DFT computational technique. The existence of proton delocalization in different structures is then discussed.

## 5.2. Experimental and theoretical methods

### 5.2.1. Sample preparation

1-methylimidazole (99% pure, Alfa Aesar) was dried over molecular sieves 4A for several days, and acetic acid glacial from VWR was dried by desiccant-anhydrous drierite (10-20 mesh no indicate) from W.A. Hammond Drierite Company, Ltd. for more than three days.[16] Mixtures were prepared at $C_1$Im to HAc molar ratio of 100:1, 20:1, 10:1, 2:1, 1:1, 1:2, and 1:5. The drying process and sample preparation process were all performed in a nitrogen-filled glovebox, and the final mixtures were checked by the Karl Fisher titration to ensure a water content less than 100 ppm.

### 5.2.2. Linear infrared spectroscopy

Fourier transformed infrared spectroscopy (FTIR) were collected on a Bruker Tensor 27 equipped with a liquid nitrogen cooled narrow band MCT detector, with a resolution of 0.5 $cm^{-1}$. Sample cells for FTIR were prepared by sandwiching samples two $CaF_2$ windows and operated in the $N_2$-filled glovebox. Attenuated total reflection (ATR) – FTIR were run on a Bruker Tensor 27 spectrometer equipped a room temperature DTGS detector, mid-IR source (4000 to 400 $cm^{-1}$), and a KBr beamsplitter. The maximum resolution is 1 $cm^{-1}$. The standard sample cell, which is a Pike Miracle single-bounce attenuated total reflectance (ATR) cell equipped with a ZnSe single crystal, was used for measurements. All ATR data were collected as an average over 16 scans at a resolution of 4 $cm^{-1}$.

### 5.2.3. Conductivity and viscosity measurements

Electrical conductivity was measured with a conductivity meter (YSI 3200 conductivity instrument). Viscosity was measured with a viscometer (Brookfield, DV-II+ Pro).

### 5.2.4. Density functional theory (DFT) calculations

DFT calculations of optimization and frequency calculation in vacuum were performed by Gaussian 16 software at PBE level with 6-311++G basis set.[24] Initial configurations were built by Avogadro[25] with classical force field MMFF94, and were firstly optimized using a 6-311G basis set. To investigate the potential well, distance scan of O-H was performed. Optimization energy at MP2 level with 6-311++G was also calculated for comparison.

### 5.2.5. *Ab initial* molecular dynamics simulation (AIMD)

AIMD simulations were carried out by using CP2K package (version 5.1).[26] The electronic structure was calculated via Quickstep module[26] using the PBE functional with the D2 dispersion scheme[27] and the TZV2P basis set, with Goedecker-Teler-Hutter (GTH) pseudopotentials.[28-30] Periodic boundary conditions were applied to all the systems, and the Nosé-Hoover thermostat was used to keep the temperature as a constant of 300 K with the temperature damping constant of 100 fs. A self-consistent field (SCF) convergence criterion was set to $5.0 \times 10^{-7}$ Hartree. The four systems with different molar fractions of HAc were performed by four boxes, with 72 HAc molecules for pure acetic acid (system 1), 60 HAc and 10 $C_1$Im for x(HAc)=0.85 (system 2), 42 HAc and 21 $C_1$Im for x(HAc)=0.67 (system 3), and 1 HAc and 51 $C_1$Im for very diluted solution (system 4). Cubic boxes with box size of ~19 Å were applied for all the systems. System 2 and 3 are representative of the mixture at its two conductivity maximums.[18, 19]

Boxes were prepared by Packmol,[31] and Optimized Potential for Liquid Simulations-all atom (OPLS-aa) forced field[32] was applied. The system first underwent an energy minimization, a 10 ns NVT, a 10 ns NPT, and a 10 ns NVT process using Large-scale Atomic/Molecular

Massively Parallel Simulator (LAMMPS) software package[33] and OPLS-aa force field. Initial configurations for AIMD simulation were obtained by taking three random snapshots separated by more than 200 ps from the second NVT process of the classical MD simulation to assure equilibrium and better sampling. In the AIMD, each system has 3 trajectories, each with different initial configuration. The systems were equilibrated for ~4 ps, followed by a 100 ps productive run for system 2 and 3, and a 35 ps productive run for system 1 and 4. In all cases, the time step of AIMD simulation is 0.5 fs.

### 5.3. Results

Conductivity measurement results of HAc/$C_1$Im mixture at different HAc molar fractions are plotted in Figure 5.1. In agreement with previous studies, two maximums occur at around 65% and 85%, with the conductivity several orders higher than pure HAc or $C_1$Im. [18, 19] Conductivity increases slowly and linearly in the range of $0 < x(HAc) < 0.4$, and experiences fast increase after $x(HAc) > 0.4$, indicating an obvious change of dominant hydrogen bond network structure at x(HAc)=~0.4. In the x(HAc) range of 0.4 - 0.9, two maximums emerge with an obvious drop in between at 0.75. At $x(HAc) > 0.9$, solution conductivity experiences a fast linear decreasing.

There are two types of conduction mechanisms in the solution. One is the “vehicle” mechanism, where the charge transfers with the diffusion of carrier ions, determined by ionicity and viscosity; the other is the Grotthuss-like mechanism, where the charge is transported through the hydrogen-bond network by bond shifting without large translations of the proton. The conductivity of sodium acetate and acetic acid mixture at the molar fraction of $x(NaAc) = 0.04$ was measured at room temperature, and it is 0.26 mS/cm. According to the previous study, in HAc/pyridine mixture, the degree of ionization reaches 0.04 at $x(HAc) = 0.7$.[34] Consider the similar pKa of pyridine and $C_1$Im, the degree of ionization of two should not deviate too much. In

this case, if the "vehicle" mechanism is dominant in the HAc/$C_1$Im mixture, the conductivity of HAc/$C_1$Im at x(HAc)=0.7 should be at the same scale as the conductivity of HAc/NaAc at x(NaAc)=0.04, since they have the same ion concentration. Considering the high viscosity of HAc/$C_1$Im, HAc/NaAc mixture is supposed to have even higher conductivity than the HAc/$C_1$Im mixture at the same degree of ionicity. However, in reality, the HAc/NaAc mixture has a much lower conductivity (0.26 mS/cm) compared to the HAc/$C_1$Im mixture (7.9 mS/cm), ruling out the "vehicle" mechanism.

Comparing the conductivity curve with the viscosity curve measured for the mixture in Figure 5.1, it can be seen that the maximum of viscosity occurs at the same concentration range of the maximum conductivity, which implies that the conductivity is not mainly dependent on the diffusion of ions in the solution. This result is in agreement with the possible Grotthuss proton conduction mechanism proposed by several groups previously.[20, 35] Viscosity at the concentration of the maximum conductivity is around 10 times higher than that of the pure acetic acid or methyl imidazole, indicating a highly ordered structure with stronger interaction among molecules at this concentration. Walden product shown in Table 5.1 provides a single maximum at x(HAc)=0.75. This demonstrates that the concentration of charge carrier, which is proton in this case, reaches its maximum at x(HAc)=0.75. However, the high viscosity at the same molar fraction decreases the conductivity, resulting in a local minimum, and two maximums at each side of x(HAc)=0.75.

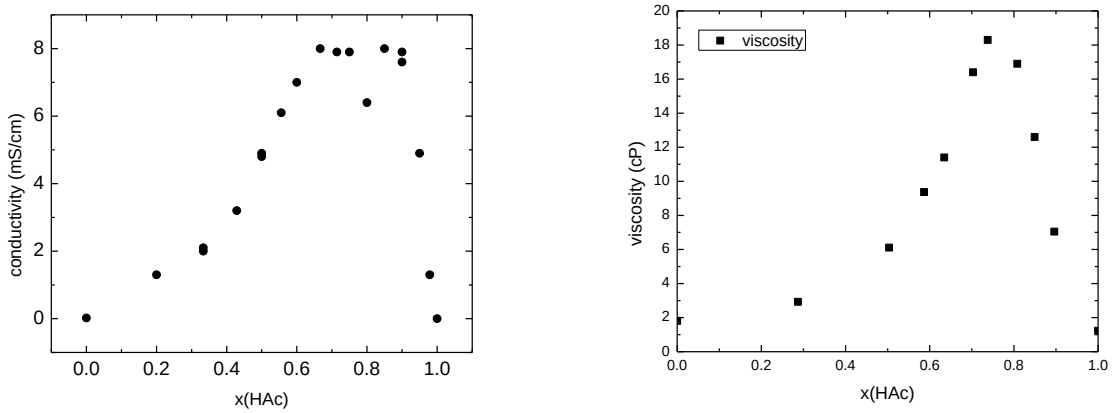


Figure 5.1. Conductivity and viscosity of HAc and $C_1$Im mixture at different molar ratio

Table 5.1. Walden product of HAc and $C_1$Im mixture at different molar ratio

| x(HAc) | conductivity(mS/cm) | viscosity (cP) | Walden product |
|---|---|---|---|
| 0.65 | 8.0 | 11.4 | 91.2 |
| 0.70 | 7.9 | 16.4 | 129.56 |
| 0.75 | 7.9 | 18.3 | 144.57 |
| 0.80 | 6.4 | 16.9 | 108.31 |
| 0.85 | 8.0 | 12.6 | 101.14 |

The ATR-FTIR spectra of HAc/$C_1$Im mixture at different molar ratios in the frequency range of 1600-3800 $cm^{-1}$ are shown in Figure 5.2. The sharp peak centered at ~1700 $cm^{-1}$ is the absorption of COO asymmetric stretching mode in HAc,[36] which is in agreement with the decrease of the peak height as the decrease of HAc concentration. At very low molar fraction of HAc, there only exists absorption of the H motion in $C_1$Im at ~2900 $cm^{-1}$ and 3100 $cm^{-1}$. As the HAc concentration increases, three broadband peaks, located at ~1900 $cm^{-1}$, 2500 $cm^{-1}$, and 3000 $cm^{-1}$ respectively, increase and then decrease. The 1900 and 2500 $cm^{-1}$ peaks reach maximum at the molar ratio HAc to $C_1$Im 2:1 (x(HAc)=67%), while the 3000 $cm^{-1}$ peak reaches its maximum at x(HAc)=83%, indicating two different dominant structures in the different mixtures. Although it is on top of the pure acetic acid $CH_3$ peak as shown at the bottom of Figure 5.2, the peak at 3000 $cm^{-1}$ arising from the mixture is still clear. All three peaks have an extremely large bandwidth of around 1000 $cm^{-1}$, which is similar to the broadband IR absorption observed for the excess proton

motions in water. To look into the absorption at low HAc concentration with better signal to noise ratio, FTIR spectra were measured with thicker spacers, and are shown in Figure 5.3 after the subtraction of the $C_1$Im background. The noises in the range of 2900 $cm^{-1}$ to 3150 $cm^{-1}$ result from the subtraction of over absorption in the $C_1$Im range. It is interesting that although the broadband peaks grow with the increasing concentration of HAc, the ratio of peaks at 1900 and 2500 $cm^{-1}$ keeps as constant. This indicates that in much diluted HAc mixtures, there exist two main structures, and the area ratio of these two does not vary with HAc concentration.

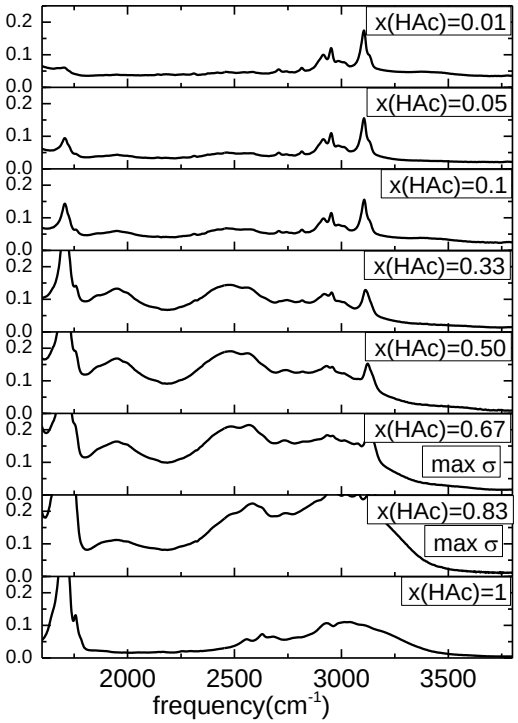


Figure 5.2. ATR-FTIR spectra of HAc and $C_1$Im mixture at different molar ratio.

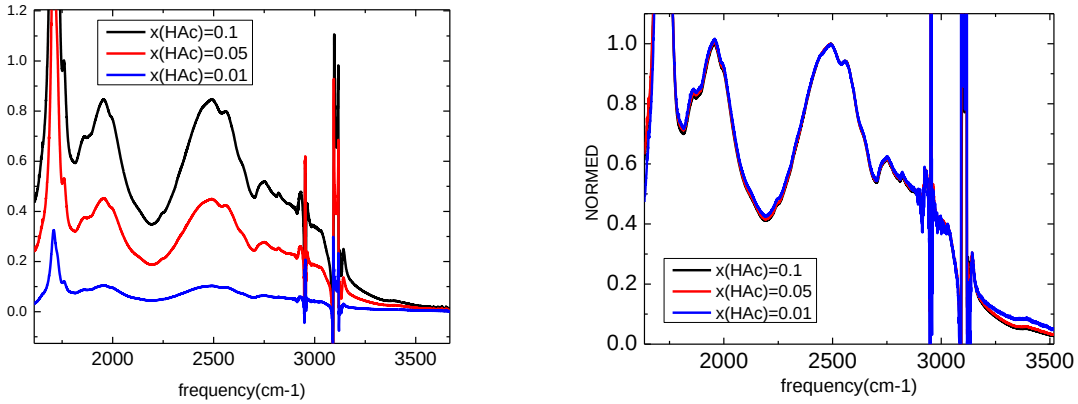


Figure 5.3. FTIR spectra of HAc and $C_1$Im mixture at small x(HAc).

## 5.4. Discussions

### 5.4.1. Assignment of infrared peaks

Previous studies on delocalized excess protons in water have built a relationship between broadband FTIR peaks and motions of excess protons. Although the assignment of Eigen and Zundel species of proton is still under debate, the broadband peak centered at 1200 $cm^{-1}$ is mostly assigned as the stretching motion of the strongly bound proton in Zundel arrangement, [2, 37-40] 1750 $cm^{-1}$ peak is attributed to bending motions of aqueous proton complex,[38, 39, 41-45] and the peaks at 2500 $cm^{-1}$ and 3000 $cm^{-1}$ are assigned to flanking water OH stretches in different aqueous proton water cluster configurations.[1, 37, 38, 41-44, 46-48] To this end, DFT frequency calculation was implemented to investigate the corresponding motion of IR absorption in this HAc/$C_1$Im system.

To simulate the system near the maximum conductivity area, based on our AIMD simulation, previous Raman and *ab initio* molecular dynamics studies,[16, 20] acetic acid chains of length L=1-5 with $C_1$Im as their terminate were interrogated. Chains with L>5 were not calculated because from previous study and our own MD simulation, the proportion of L>5 chains

in all the mixtures is negligible. As shown in Figure 5.4, there exist two kinds of structure arrangement, each with an energy local minimum. DFT frequency computational results of planar Figure 5.4(a) structures are shown in Figure 5.5(a), and the results of Figure 5.4(b) are shown in Figure 5.5(b).

Figure 5.4. Two arrangements of HAc and $C_1$Im complex

In the frequency range of 1500 ~1750 $cm^{-1}$, absorptions with small infrared intensity less than 1000 km/mol are generated from the coupling between the COO stretching and proton bending. Single proton stretching motion displays a high infrared intensity of around 2000 – 3000 km/mol, standing out from other motions in this frequency range, which have intensities on the scales of tens and hundreds. Hydrogen bond proton in the HAc molecule adjacent to $C_1$Im is denoted as the $1^{st}$ proton, and the other protons in the complex are denoted as $2^{nd}$, $3^{rd}$, $4^{th}$, and $5^{th}$ protons from $C_1$Im side to the other. The stretching motion of the $1^{st}$ proton has an extremely strong absorption at ~2500 $cm^{-1}$ in both two structures at L=1. At L>1, infrared absorption of this stretching locates at frequency of around 1800 $cm^{-1}$ with highest intensity at L=2. The stretching frequency of $2^{nd}$ proton locates at ~ 3000 $cm^{-1}$ in structure (a) at L<4 and structure (b), which in structure (a) at L>3 it locates at ~2300 $cm^{-1}$. The rest proton stretch modes locate at ~ 3000 $cm^{-1}$ with intensity of around 1000 km/mol. Based on the calculation, the 1900 $cm^{-1}$, 2500 $cm^{-1}$, and 3000 $cm^{-1}$ peaks in infrared spectra at x(HAc) > 0.1 can be assigned to stretching of the $1^{st}$ proton at L>1, $1^{st}$ proton at L=1, $2^{nd}$ proton at L>3, and the rest protons respectively. This assignment agrees with the fact that the 1900 $cm^{-1}$ peak reaches its maximum at x(HAc) =0.65 and decreases to 0 at x(HAc)=1, while the 2500 $cm^{-1}$ and 3000 $cm^{-1}$ peaks keep increasing until reaching its

maximum at x(HAc)=0.85. The reason for this is that at lower HAc concentration, increasing of HAc molar fraction leads to the increasing of concentration of L=1 and L=2 structures, while at higher concentration, chain length increasing becomes a competing effect and causes the 1900 $cm^{-1}$ absorption to decrease.

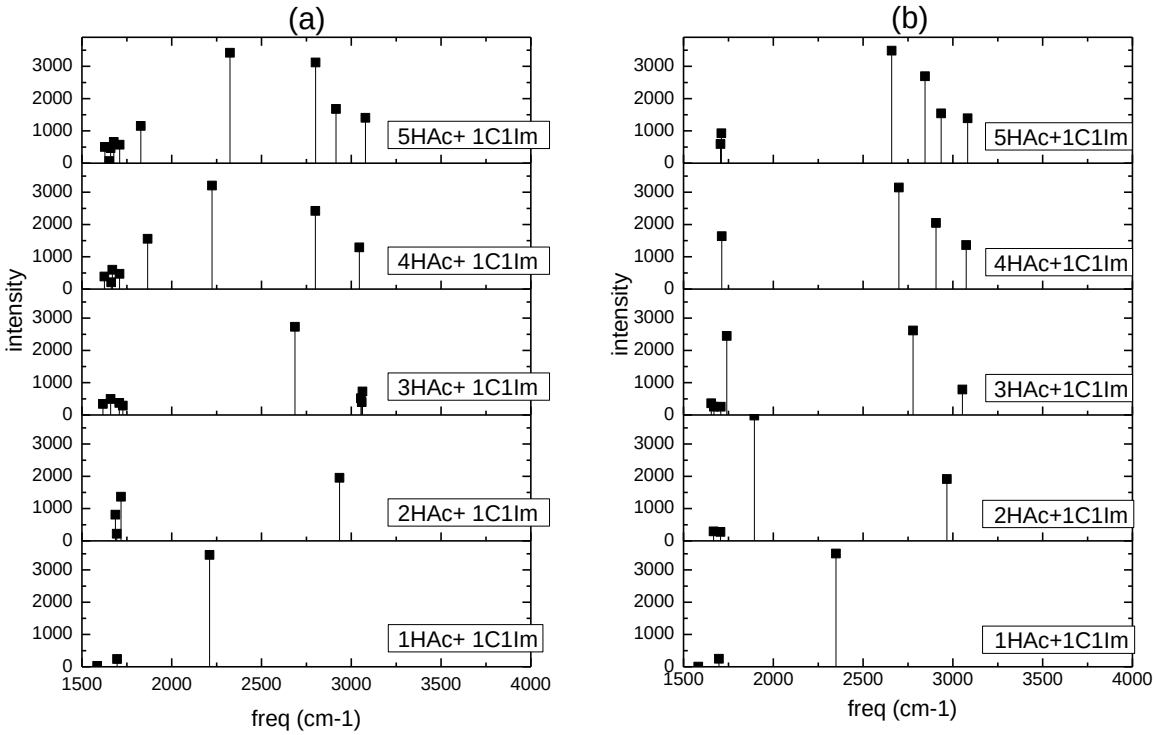


Figure 5.5. DFT frequency calculation of planar linear HAc/$C_1$Im chain at chain length L=1-5.

The two kinds of planar complex arrangements (Figure 5.4) give an informative indication on the assignment of FTIR peak location. However, the extremely broad bandwidth cannot be explained by these simplified models. Since the C-H···O hydrogen bond is a relatively weak interaction, it is reasonable to consider the frequency shift arising from rotational conformers along O-H···N hydrogen bond. To investigate the existence of 3D rotational conformers, distribution on the angle between normal vector of $C_1$Im plane defined by hydrogen acceptor N and the two

adjacent C, and the normal vector of HAc plane defined by the carboxylate group COO, are calculated from AIMD trajectory.

Radial distribution function (RDF) between hydroxyl H in HAc and the hydrogen bond acceptor N in $C_1$Im and its integral calculated from AIMD simulation are compared with previous AIMD results to check the reproducibility. Plots of RDFs are shown in Figure 5.6. There are two obvious solvation shell located at 0.95 Å – 1.35 Å and 1.35 Å – 2.25 Å, respectively. The first maximum locates at 1.05 Å, and the second is at 1.55 Å, which are all in agreement with previously published AIMD studies.[20]

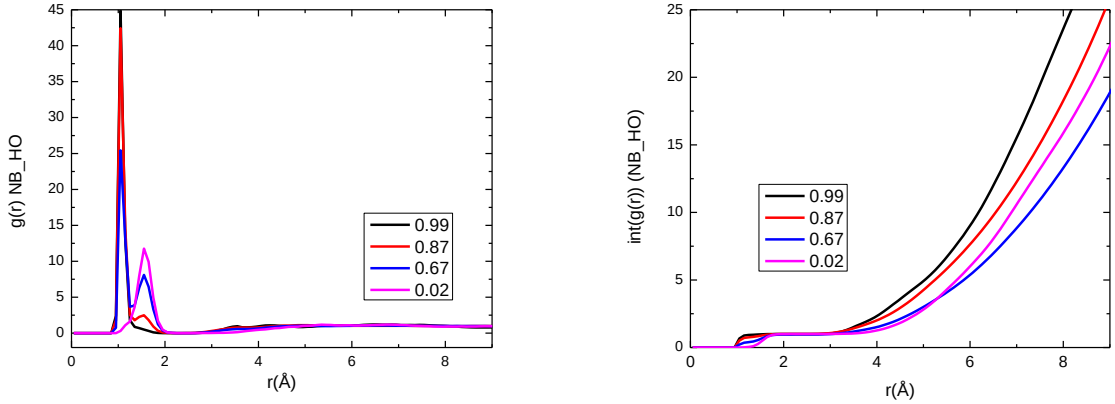


Figure 5.6. Radial distribution function between hydroxyl H in HAc and the hydrogen bond acceptor N in $C_1$Im and its integral.

From the normal vector angle distribution shown in Figure 5.7, instead of 0 and 180 degrees, the two maximums of distribution locate at 30 and 120 degrees at small x(HAc), or at 70 and 150 degrees at high x(HAc), which indicates two free energy minimums in hydrogen bond rotating coordinate. The structures at minimum energy are non-planar, which might result from the solvation shell energy stabilization. The carbonyl oxygen in HAc is energetically more favorable to form a hydrogen bond with another HAc in the solvation shell, compared with forming

C-H···O hydrogen bond with $C_1Im$. Besides, the broad distribution demonstrates the existence of 3D structure and free rotating along the hydrogen bond.

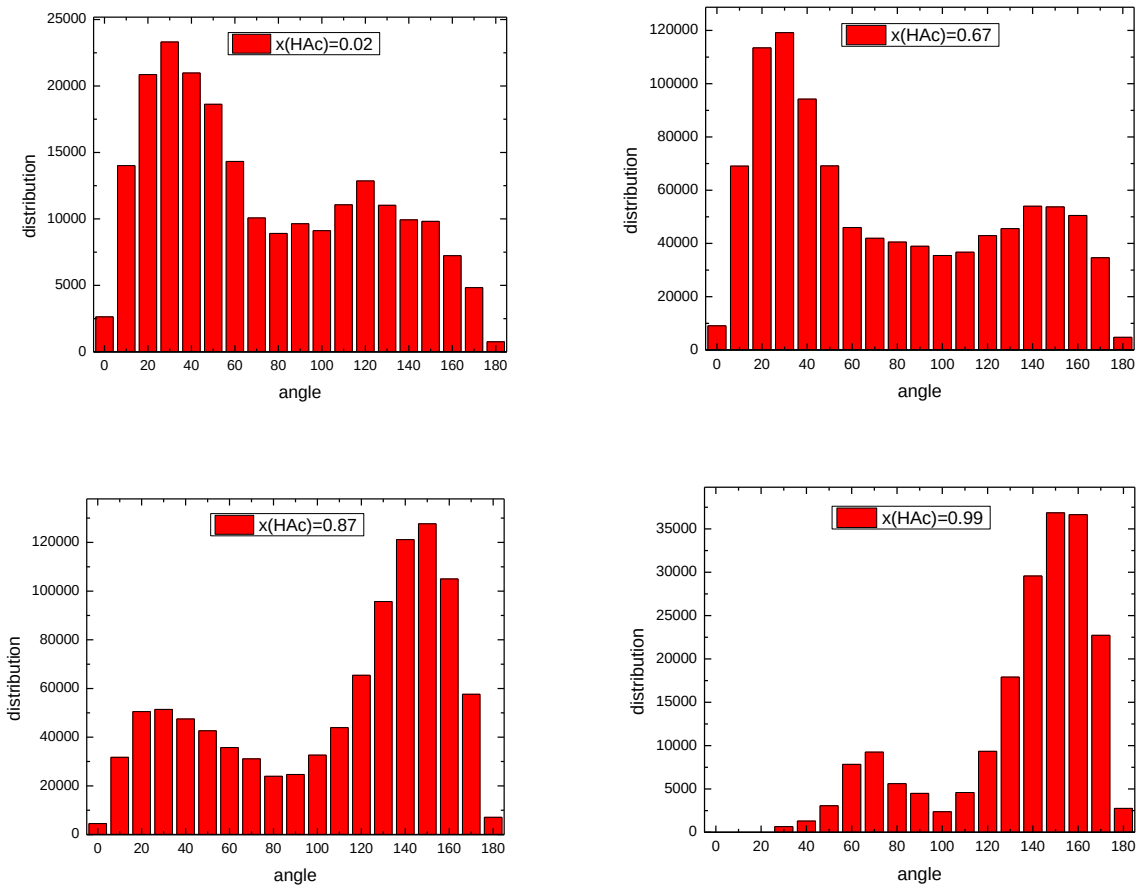


Figure 5.7. Distribution of AIMD frames on the angle between normal vectors of HAc and $C_1Im$ plane at different x(HAc).

The existence of 3D conformers is also confirmed by the rotation energy surfaces calculated as a function of dihedral angle in different structures observed in AIMD. There are mainly two types of rotation. One is the rotation of $C_1Im$, the other is rotation of terminal HAc in the chain. 1HAc+1 $C_1Im$, 2HAc+1$C_1Im$, and 3HAc+1$C_1Im$ structures were investigated as representative species in highly concentrated HAc solution. The energy surfaces along rotational coordinate of those representative structures are shown in Figure 5.8. Energy barrier of rotation is

found to be about 4 kcal/mol, which is possible to be overcome by thermal energy and local environmental energy variation. This result supports the existence of conformation change in the solution.

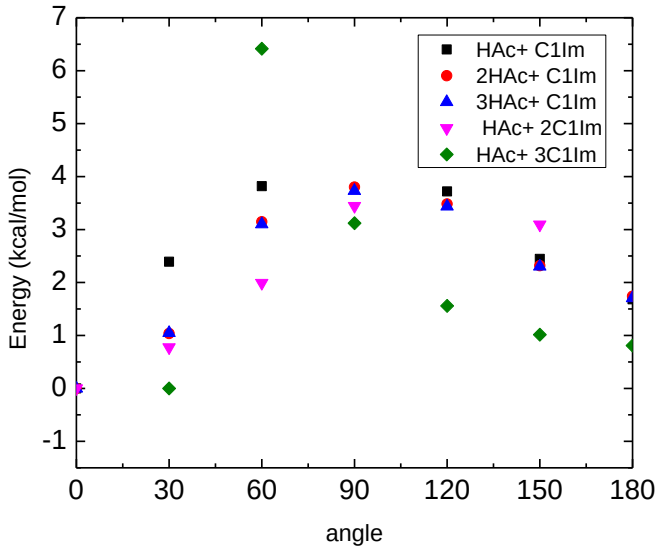


Figure 5.8. Energy vs. dihedral angle. (a) HAc+ $C_1$Im (black square); (b) 2HAc+ $C_1$Im (red dot); (c) 3HAc+ $C_1$Im (blue triangle); (d) HAc+ 2$C_1$Im (magenta obtriangle); (e) HAc+ 2$C_1$Im (green diamond).

DFT frequency computational results of two types of rotation in 2HAc+ $C_1$Im, which is the most concentrated species in the conductive mixture, are shown in Figure 5.9 (a) and 5.11 (b). Results of $C_1$Im rotation in HAc+$C_1$Im, 3HAc+$C_1$Im are displayed in Figure 5.9 (c) and (d). The hydrogen stretching mode maintains a strong absorption compared with other vibrational modes in all structures at all conformations. Frequency shift of ~300 $cm^{-1}$ is observed in all cases, which indicates that the variance of conformation explains the homogenous broadening component of the broad band in FTIR spectra.

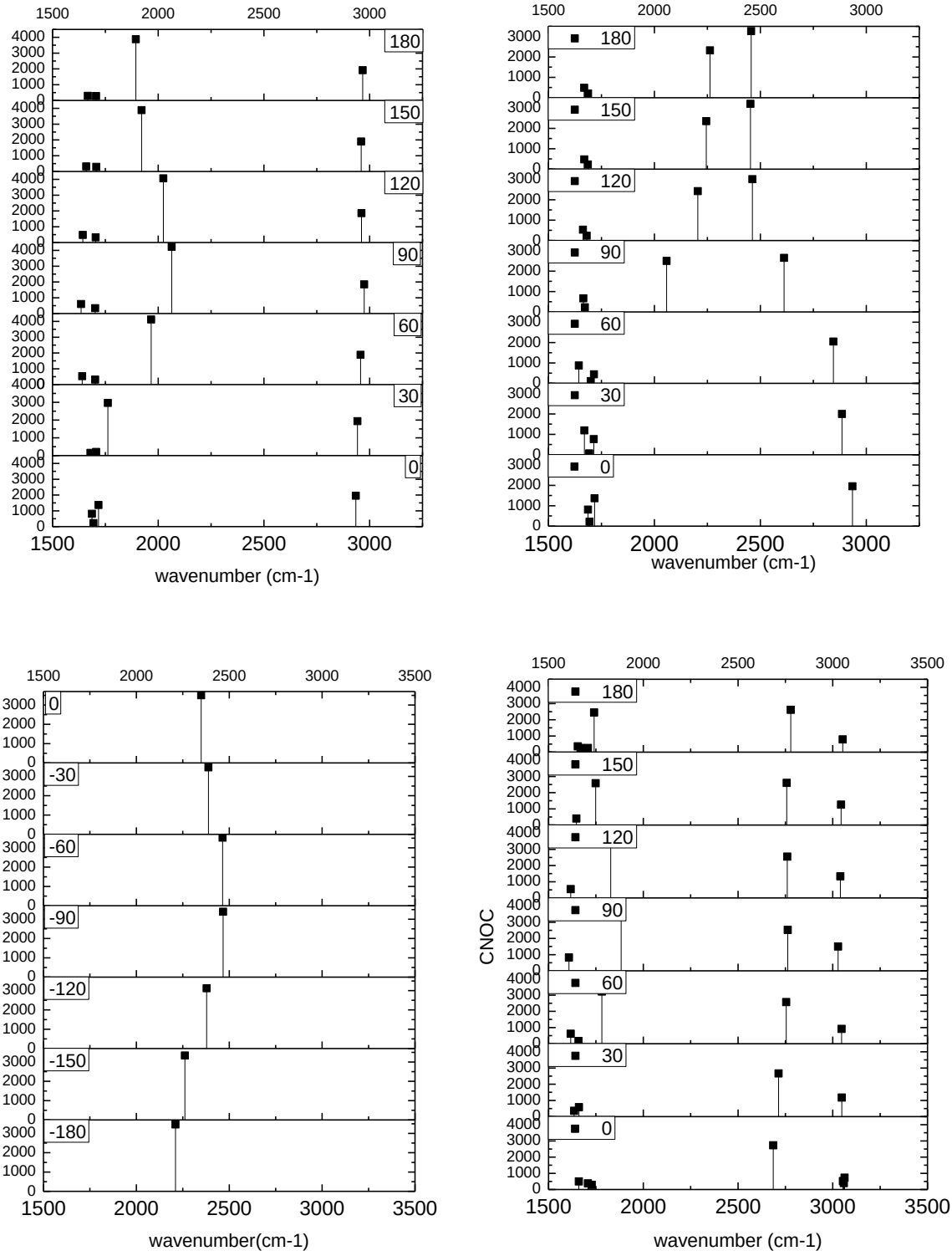


Figure 5.9. DFT frequency calculation of conformers in different complexes: (a) 2HAc+ $C_1$Im; (b) 2HAc+ $C_1$Im; (c) HAc+ $C_1$Im; (d)3HAc+ $C_1$Im.

There is one more question on the assignment of the FTIR peaks. From Figure 5.2(b), it is observed that even at x(HAc)=0.01, the 1900 $cm^{-1}$ and 2500 $cm^{-1}$ peak still exist, and the intensity ratio between those two remains exactly the same at low concentration from X(HAc)=0.1 to x(HAc)=0.01. Statistically, at such concentration, the probability of two HAc meeting to form L=2 chain is negligible. In terms of chemical equilibrium, as x(HAc) decreases, the equilibrium shifts to L=1 side, with changes of concentration ratio between L=1 and 2. This indicates that there are other structures in this diluted solution contributing to the 1900 $cm^{-1}$ and 2500 $cm^{-1}$ infrared absorption. Since it is highly concentrated $C_1$Im solution, structures of one HAc bonded with two and three $C_1$Im molecules were considered. Solvation shell structures of HAc obtained from AIMD are investigated to seek for the possible complexes existing at small x(HAc).

Distributions of number of carbonyl C (in HAc, denote as CT) and the number of C (between two N in $C_1$Im, denote as CR) in the first solvation shell of CT are calculated. RDF among CT is computed to determine the solvation shell cutoff and shown in Figure 5.10 (top). RDF at three molar fractions all have the first solvation shell within 4.85 Å, the second solvation shell at ~6.8 Å, followed by the third solvation shell. An extra sharp peak appears in the range of 3.5-4.0 Å at x(HAc)=0.02, and decreases fast as x(HAc) increases. Looking into the AIMD trajectory, this peak arises from the structure that one HAc stacks on top of another, forming two parallel layers (a snapshot inserted in Figure 5.10). The $C_1$Im in the solvation shell of HAc might block the formation of this structure. From the integrated g(r), increasing number of HAc at the cutoff 4.85 Å is observed as the increase of x(HAc). 2.2, and 3.3 HAc are found to exist in the first solvation shell at x=0.67 and 0.85 respectively, and coordination number of 4 is found at x(HAc)=0.99 and 1.0.

RDF between CT and CR are also calculated and plotted in Figure 5.10 (bottom). The first minimum is located at 4.85 Å, which is the same position as the minimum of RDF between CT and CT. The second minimum is located at 7.25 Å, indicating a thicker second solvation shell composed of $C_1Im$ compared with that composed of HAc. This difference can be explained by the larger volume/radius of $C_1Im$ compared to HAc. The number of $C_1Im$ in the first solvation shell is 0.1, 0.6, 1.4, and 3.0 at x(HAc)=0.99, 0.85, 0.67, 0.02. Therefore, in very diluted HAc solution (x(HAc)=0.02), there are 3 $C_1Im$ molecules in the first solvation shell of HAc on average, indicating a big amount of 1HAc+2$C_1Im$ and 1HAc+3$C_1Im$ complexes existing in the diluted solutions.

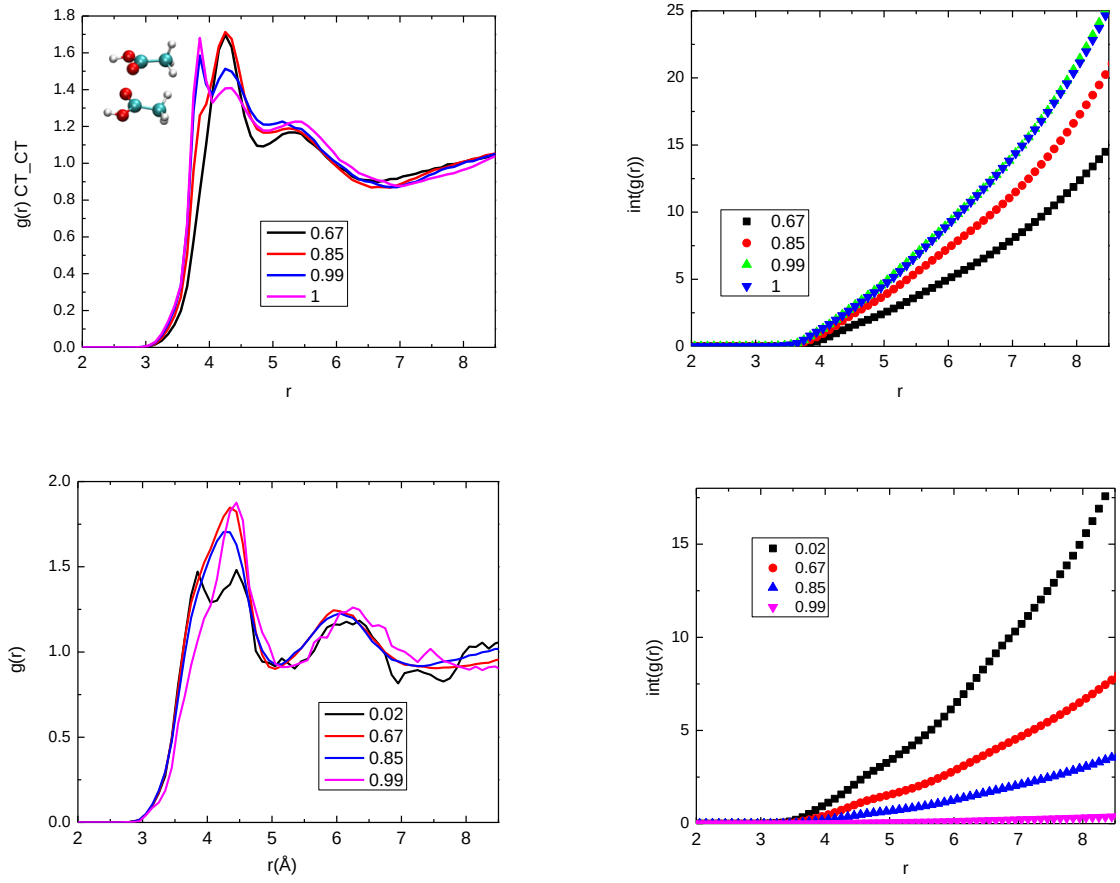


Figure 5.10. RDF and its integral between CT and CT (top), CT and CR (bottom).

In addition, the integrated g(r) shows the number of $C_1Im$ in first solvation shell of HAc decreases as the increasing of x(HAc). This indicates as x(HAc) increases, HAc molecules come into the first solvation shell while $C_1Im$ molecules are leaving from the first solvation shell.

Similar to HAc chain terminated with $C_1Im$, different spatial arrangements of $1HAc+2C_1Im$ and $1HAc+3C_1Im$ complexes due to the formation of C-H···O hydrogen bond are all investigated. Calculated frequencies are shown in Figure 5.12 and the corresponding structures in Figure 5.13. It can be observed from the plot that $1HAc+2C_1Im$ structure has an absorption at 1800 $cm^{-1}$ (Figure 5.12(b) and 5.12(b)) with high intensity, and $1HAc+3C_1Im$ structure produces two high-intensity IR absorption at ~2300 $cm^{-1}$ (Figure 5.12(e-f) and 5.12(e-f)). Therefore, it can be assumed that at small x(HAc), the absorption centered at 1900 $cm^{-1}$ can be assigned to proton stretching of $1HAc+2C_1Im$ structure, and the absorption centered at 2500 $cm^{-1}$ can be assigned to proton stretching of $1HAc+3C_1Im$ structure. The unchanged ratio between those two peaks at different x(HAc) indicates that the two structures have same Gibbs free energy. The energy change of breaking C-H···O hydrogen bond between HAc and the third $C_1Im$ can be compensated by the energy change of hydrogen bond network rearrangement in the solvation shell of HAc.

Conformations of these dominant species in diluted HAc solution are investigated to understand the broad infrared peaks. $1HAc+2C_1Im$ and $1HAc+3C_1Im$ complexes in Figure 5.14(b) and 5.14(f) are taken as representative species. The energy surfaces of rotation along hydrogen bond are shown in Figure 5.8(d) and 5.8(e), where the energy barrier is on the same order of thermal energy. Histogram of the number of nitrogen in the first solvation shell of carbonyl carbon in the diluted HAc solution shown in Figure 5.11 (top left) confirms the existence of $1HAc+2C_1Im$ and $1HAc+3C_1Im$ complexes at small x(HAc). DFT frequency calculations are performed on the conformations of these two complexes rotating along the hydrogen bond, and the results are shown

in Figure 5.14. Frequency shifts of ~300 $cm^{-1}$ are observed for the two complexes, which is responsible for the FTIR broad bandwidth.

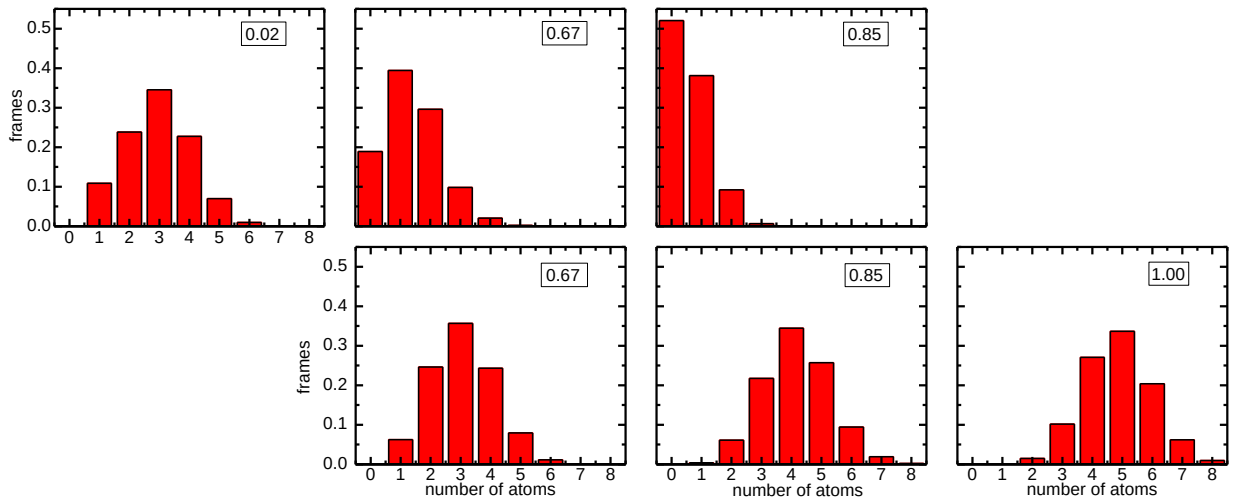


Figure 5.11. Histograms of number of carbonyl C (bottom) and N (top) in the first solvation shell of C.

Based on DFT calculation and FTIR study, it can be assumed that at x(HAc)<0.1, the dominant species in mixture that responsible for the broad bands are 1HAc+2$C_1$Im (1800 $cm^{-1}$) and 1HAc+3$C_1$Im (2300 $cm^{-1}$), and their concentrations increase as x(HAc) increases. In molar fraction range 0.1<x(HAc)<0.65, the dominant species are 1HAc+1$C_1$Im (2300 $cm^{-1}$) and 2HAc+1$C_1$Im (1800 $cm^{-1}$ and 3000 $cm^{-1}$). At x(HAc)>0.65, 2HAc+$C_1$Im chains and longer chains become two competing components in the mixture.

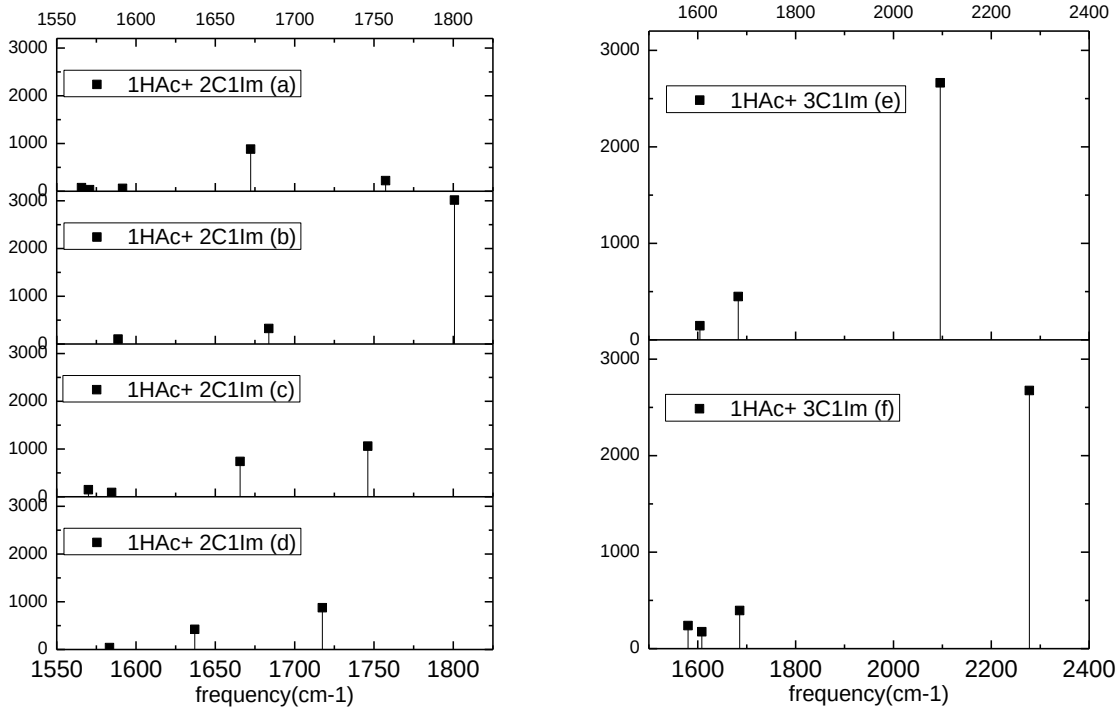


Figure 5.12. DFT frequency calculation results of HAc and $C_1$Im complexes.

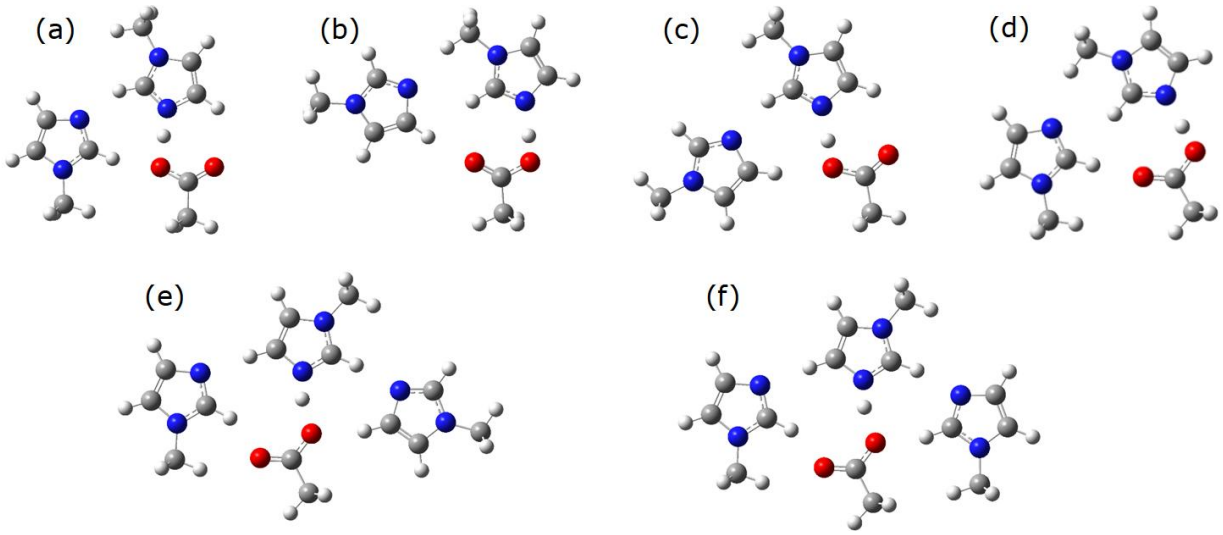


Figure 5.13. Structures of complexes taken in DFT frequency calculation.

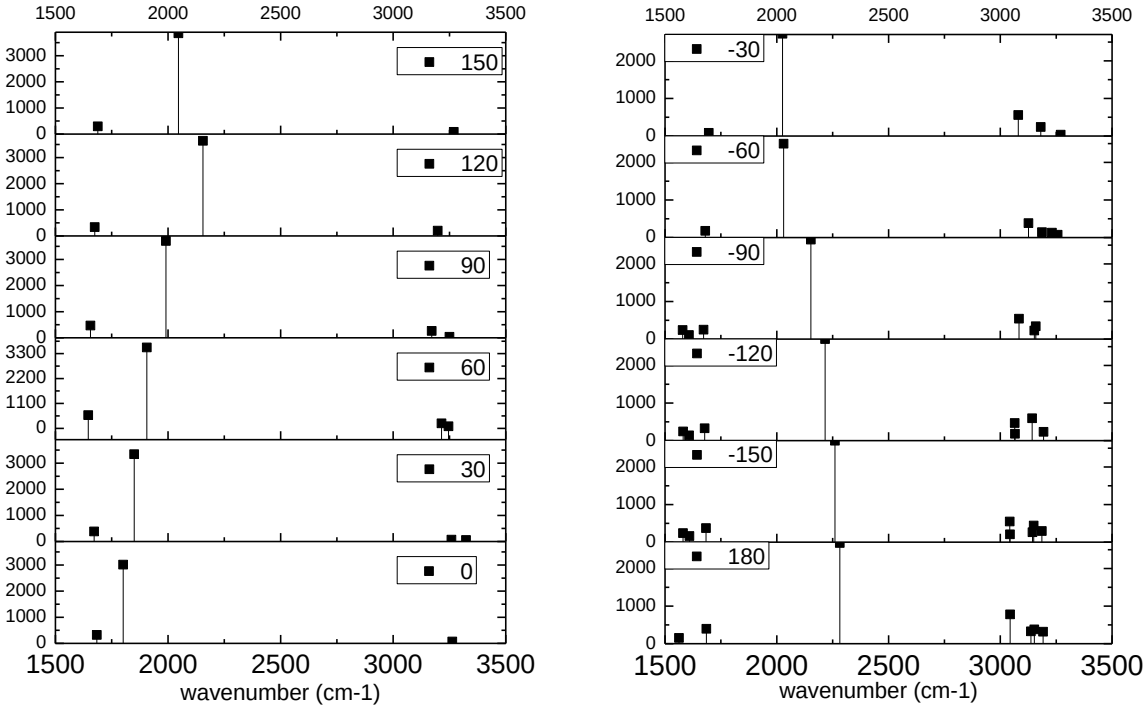


Figure 5.14. DFT calculation of conformers in different complexes: (a) HAc+ $2C_1Im$; (b) HAc+$3C_1Im$.

### 5.4.2. Delocalization of protons from computational calculation

The coordinate of proton motion in the proton stretching mode investigated by DFT calculation before is the same as the coordinate of proton delocalization. It can be observed from the DFT calculation results that proton between HAc and $C_1Im$ is delocalized. When the HAc chain gets longer, a second delocalized proton appears between the first and second HAc. The third delocalized proton appears at L>3.

Radial distribution function between hydroxyl H in HAc and the hydrogen bond acceptor N in $C_1Im$ and its integral are shown in Figure 5.6. There are two obvious solvation shells, which are in agreement with the previous AIMD studies.[20] The first solvation shell is corresponding to the delocalized protons which deviate from the initial positions near oxygen. Previous Raman study supports this assignment with the fact that the ions are negligible in this mixture.[16] The

second solvation shell composes of the protons on the O side. The two solvation shells are overlapped without any zero probability point in between, which proves proton delocalization. Integrated g(r) gives the ensemble average number of H in the first solvation shell of N to be 0.79, 0.45, and 0.1 at x(HAc)=0.86, 0.67, and 0.02 respectively. This strongly supports the existence of proton delocalization in all molar ratio of mixtures and indicates that at least 79% and 45% of protons in $C_1$Im -HAc complexes are delocalized. The two states of protons can also be observed from the trace of OH distance in the AIMD trajectory in Figure 5.15. However, the statics results from our simple canonical ensemble MD simulation only give information on free energy and remove the influence from entropy change of the system. To remove the effect of entropy, DFT calculation at T=0 K is needed.

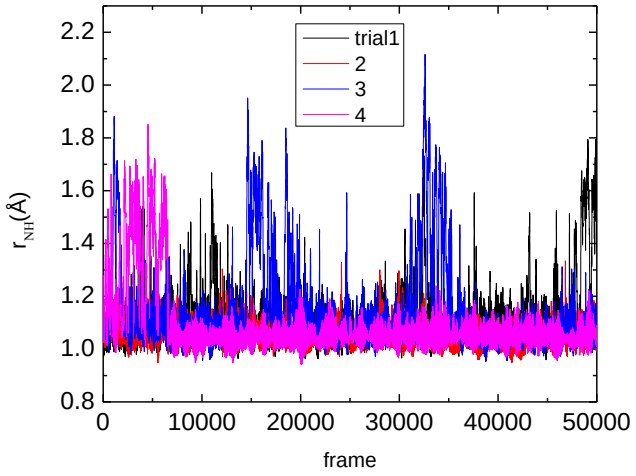


Figure 5.15. Trace of OH distance in 4 trials in the mixture at x(HAc)=0.02.

The energy surface of scanning the proton from the oxygen side to the nitrogen side is calculated by Gaussian 16. Energy surfaces of the 1$^{st}$ proton in pure HAc-HAc dimer chain, HAc-$C_1$Im chain, and HAc-HAc- $C_1$Im chain are compared in Figure 5.16(a). Proton is confined in a narrow single well close to oxygen in the HAc dimer chain. When $C_1$Im replaces one HAc

molecule, energy at r(OH)=1.5Å decreases from ~30 kcal/mol to ~4.7 kcal/mol, forming a second energy minimum close to the nitrogen atom. Taking account of the estimated zero-point vibrational energy of the proton vibrational motion, which is about 5.4 kcal/mol, the same scale as the energy difference between the two local minimums, the proton can be considered to be in a state that it moves back and forth freely from the oxygen side to the nitrogen side. This delocalized quantum state is neither a mixture of simple acid and base molecules (HAc and $C_1Im$), nor a mixture of two ions ($Ac^-$ and $HC_1Im^+$), as the previous classical understanding of the system. In fact, the solution is composed of HAc-C1Im complexes at different chain lengths, whose H-bonded proton is delocalized, and the excess HAc or $C_1Im$ as a solvent. It's the first time that proton delocalization with a neutral complex formation is observed in a simple mixture of two types of molecules, which can be utilized in chemical reactions such as polymerization.

Pump-probe spectroscopy results confirmed the existence of proton delocalization with the obvious inversed anharmonicity, which can only come from a flat-bottom steep potential well of the delocalized proton.[1, 2]

Based on the discussion in the last section and previous studies, [20, 35] the HAc/$C_1Im$ mixture adopts a Grotthuss-like proton conduction mechanism, which in this case indicates that the delocalized proton initiates the Grotthuss-like conduction mechanism. The proton delocalization can explain the overlapped x(HAc) position of the viscosity maximum and the Walden product maximum. At the maximum of Walden product, there exists the highest concentration of charge carrier, which is the delocalized proton. As a result, the concentration of HAc- $C_1Im$ complexes reaches its maximum, leading to the strongest overall intermolecular interaction and hydrogen bond network, and thus a maximum of viscosity.

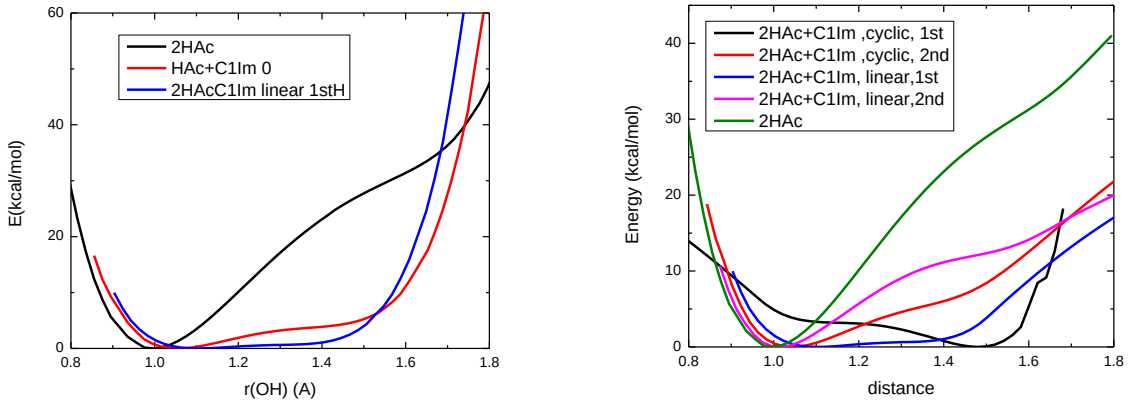


Figure 5.16. Potential energy surfaces of different complexes on proton stretching coordinate.

Looking back into Figure 5.16(a), compared with HAc+ $C_1$Im structure, 2HAc+ $C_1$Im displays an even lower potential energy of around 1.7 kcal/mol at r(OH) = 1.45 Å. Considering the zero-point vibrational energy and thermal energy, 2HAc+ $C_1$Im has a barrierless flat-bottom potential well. As the energy barrier decreases, which means proton gets more delocalized, the minimum position at the oxygen side shifts further away from oxygen from r(OH)=1.00 Å to 1.10 Å, while the second minimum near N shifts from N to O at the same time from r(OH)=1.6 Å to 1.45 Å, demonstrating the delocalized proton prefers to distribute in the middle area between O and N, instead of the local position close to O or N. The comparison among different structures indicates that forming a hydrogen bond with a $C_1$Im molecule delocalizes the acid proton, and increasing of the chain length L helps to stabilize the delocalized proton.

The influence of different spatial arrangements on proton delocalization is investigated and plotted in Figure 5.16(b). The energy surface of 1$^{st}$ proton in 2HAc+ $C_1$Im complex is modified by the structure while it's barrierless in both structures. In the linear complexes, the energy minimum is located close to the oxygen side. In the cyclic complexes, the minimum shifts to the

position close to the nitrogen side. Meanwhile, the second proton is localized in the linear structure and a lot more delocalized in the cyclic structure.

From the AIMD trajectory, it is observed that structures of 2HAc+ $C_1$Im and 3HAc+ $C_1$Im have a much higher concentration compared with other complexes at the x(HAc) of maximum conductivity. It can be inferred that the concentration of 2HAc+ $C_1$Im and 3HAc+ $C_1$Im determines the Walden product. This is because the delocalized proton in these structures has a flat-bottom barrierless potential well as shown in the last part, so the protons can vibrate from O side to N side, initiating the Grotthuss-like mechanism. Thus the concentration of 2HAc+ $C_1$Im and 3HAc+ $C_1$Im complexes determines the conductivity.

### 5.5. Summary

In the system of acetic acid and methylimidazole mixture, solvation structure and dynamics were investigated by linear the non-linear spectroscopies and computational calculation. The high-absorption broad-band peaks in infrared spectroscopy were assigned to proton stretching mode in HAc/$C_1$Im complexes. Dominant species at high x(HAc) were demonstrated to be HAc chain ended with a $C_1$Im terminal molecule, while the dominant species at very low x(HAc) were found to be HAc+2$C_1$Im and HAc+3$C_1$Im complexes. Conformers of complexes arising from rotation around hydrogen bonds were proved to exist and are responsible for the large bandwidth of proton stretching mode in infrared spectroscopy. The most impressive finding is the existence of proton delocalization. A flat-bottom potential energy surface of proton stretching is obtained from both DFT calculation and pump-probe experiment, which proves the existence of proton delocalization in the hydrogen bond between HAc and $C_1$Im. It is the first time that proton delocalization is observed in a simple mixture of two molecules. This project provides a new method to generate

proton delocalization and start a polymerization by mixing a weak acid and a weak base with similar proton affinity.

### 5.6. References


1. Fournier, J.A., et al., *Broadband 2D IR spectroscopy reveals dominant asymmetric H5O2+ proton hydration structures in acid solutions.* Nature Chemistry, 2018. **10**(9): p. 932-937.

2. Dahms, F., et al., *Large-amplitude transfer motion of hydrated excess protons mapped by ultrafast 2D IR spectroscopy.* Science, 2017. **357**(6350): p. 491-495.

3. Cleland, W. and M. Kreevoy, *Low-barrier hydrogen bonds and enzymic catalysis.* Science, 1994. **264**(5167): p. 1887-1890.

4. Cleland, W.W., *Low-barrier hydrogen bonds and low fractionation factor bases in enzymic reactions.* Biochemistry, 1992. **31**(2): p. 317-319.

5. Wang, L., et al., *Quantum delocalization of protons in the hydrogen-bond network of an enzyme active site.* Proceedings of the National Academy of Sciences, 2014. **111**(52): p. 18454-18459.

6. Cleland, W.W., P.A. Frey, and J.A. Gerlt, *The Low Barrier Hydrogen Bond in Enzymatic Catalysis.* Journal of Biological Chemistry, 1998. **273**(40): p. 25529-25532.

7. Katz, B.A., et al., *Contribution of Multicentered Short Hydrogen Bond Arrays to Potency of Active Site-Directed Serine Protease Inhibitors.* Journal of the American Chemical Society, 2002. **124**(39): p. 11657-11668.

8. Rajagopal, S. and S. Vishveshwara, *Short hydrogen bonds in proteins.* The FEBS Journal, 2005. **272**(8): p. 1819-1832.

9. Frey, P., S. Whitt, and J. Tobin, *A low-barrier hydrogen bond in the catalytic triad of serine proteases.* Science, 1994. **264**(5167): p. 1927-1930.

10. Stuchebrukhov, A.A., *Mechanisms of proton transfer in proteins: Localized charge transfer versus delocalized soliton transfer.* Physical Review E, 2009. **79**(3): p. 031927.

11. Krumhansl, J.A. and J.R. Schrieffer, *Dynamics and statistical mechanics of a one-dimensional model Hamiltonian for structural phase transitions.* Physical Review B, 1975. **11**(9): p. 3535-3545.

12. Davydov, A., *"Solitons in Molecular Systems"(Reidel, Dordrecht, 1991).*

13. Bountis, T., *Proton transfer in hydrogen-bonded systems*. Vol. 291. 2012: Springer Science & Business Media.

14. Petersen, M.K., et al., *Excess proton solvation and delocalization in a hydrophilic pocket of the proton conducting polymer membrane Nafion.* The Journal of Physical Chemistry B, 2005. **109**(9): p. 3727-3730.

15. Kreevoy, M.M. and T.M. Liang, *Structures and isotopic fractionation factors of complexes, A1HA2.* Journal of the American Chemical Society, 1980. **102**(10): p. 3315-3322.

16. Doi, H., et al., *A New Proton Conductive Liquid with No Ions: Pseudo-Protic Ionic Liquids.* Chemistry – A European Journal, 2013. **19**(35): p. 11522-11526.

17. MacFarlane, D.R., et al., *Lewis base ionic liquids.* Chemical Communications, 2006(18): p. 1905-1917.

18. Treble, R.G., K.E. Johnson, and E. Tosh, *The volatilities and conductivities of ionic liquids — GC–MS methodology and preliminary studies of acetic acid – base systems.* Canadian Journal of Chemistry, 2006. **84**(6): p. 915-924.

19. Yoshimura, N., et al., *Electronic States of Acetic Acid in a Binary Mixture of Acetic Acid and 1-Methylimidazole Depend on the Environment.* The Journal of Physical Chemistry B, 2019. **123**(6): p. 1332-1339.

20. Ingenmey, J., S. Gehrke, and B. Kirchner, *How to Harvest Grotthuss Diffusion in Protic Ionic Liquid Electrolyte Systems.* ChemSusChem, 2018. **11**(12): p. 1900-1910.

21. Chen, K., et al., *Equilibrium in Protic Ionic Liquids: The Degree of Proton Transfer and Thermodynamic Properties.* The Journal of Physical Chemistry B, 2018. **122**(1): p. 309-315.

22. Hibbert, F. and J. Emsley, *Hydrogen Bonding and Chemical Reactivity*, in *Advances in Physical Organic Chemistry*, D. Bethell, Editor. 1990, Academic Press. p. 255-379.

23. Gilli, P., et al., *Evidence for resonance-assisted hydrogen bonding. 4. Covalent nature of the strong homonuclear hydrogen bond. Study of the O-H--O system by crystal structure correlation methods.* Journal of the American Chemical Society, 1994. **116**(3): p. 909-915.

24. Frisch, M.J., et al., *Gaussian 16 Rev. C.01*. 2016: Wallingford, CT.

25. Hanwell, M.D., et al., *Avogadro: an advanced semantic chemical editor, visualization, and analysis platform.* Journal of Cheminformatics, 2012. **4**(1): p. 17.

26. VandeVondele, J., et al., *Quickstep: Fast and accurate density functional calculations using a mixed Gaussian and plane waves approach.* Computer Physics Communications, 2005. **167**(2): p. 103-128.

27. Grimme, S., *Semiempirical GGA-type density functional constructed with a long-range dispersion correction.* Journal of Computational Chemistry, 2006. **27**(15): p. 1787-1799.

28. Goedecker, S., M. Teter, and J. Hutter, *Separable dual-space Gaussian pseudopotentials.* Physical Review B, 1996. **54**(3): p. 1703-1710.

29. Lippert, G., et al., *Response Function Basis Sets: Application to Density Functional Calculations.* The Journal of Physical Chemistry, 1996. **100**(15): p. 6231-6235.

30. Perdew, J.P., K. Burke, and M. Ernzerhof, *Generalized Gradient Approximation Made Simple.* Physical Review Letters, 1996. **77**(18): p. 3865-3868.

31. Martínez, L., et al., *PACKMOL: A package for building initial configurations for molecular dynamics simulations.* Journal of Computational Chemistry, 2009. **30**(13): p. 2157-2164.

32. Jorgensen, W.L., D.S. Maxwell, and J. Tirado-Rives, *Development and Testing of the OPLS All-Atom Force Field on Conformational Energetics and Properties of Organic Liquids.* Journal of the American Chemical Society, 1996. **118**(45): p. 11225-11236.

33. Plimpton, S., *Fast Parallel Algorithms for Short-Range Molecular Dynamics.* Journal of Computational Physics, 1995. **117**(1): p. 1-19.

34. Aravindakshan, N.P., et al., *The origin of the conductivity maximum vs. mixing ratio in pyridine/acetic acid and water/acetic acid.* The Journal of Chemical Physics, 2018. **149**(9): p. 094505.

35. Watanabe, H., et al., *Possible Proton Conduction Mechanism in Pseudo-Protic Ionic Liquids: A Concept of Specific Proton Conduction.* The Journal of Physical Chemistry B, 2019. **123**(29): p. 6244-6252.

36. Herman, R.C. and R. Hofstadter, *Vibration Spectra and Molecular Structure V. Infra-Red Studies on Light and Heavy Acetic Acids.* The Journal of Chemical Physics, 1938. **6**(9): p. 534-540.

37. Daly, C.A., et al., *Decomposition of the Experimental Raman and Infrared Spectra of Acidic Water into Proton, Special Pair, and Counterion Contributions.* The Journal of Physical Chemistry Letters, 2017. **8**(21): p. 5246-5252.

38. Biswas, R., et al., *IR spectral assignments for the hydrated excess proton in liquid water.* The Journal of Chemical Physics, 2017. **146**(15): p. 154507.

39. Asmis, K.R., et al., *Gas-Phase Infrared Spectrum of the Protonated Water Dimer.* Science, 2003. **299**(5611): p. 1375-1377.

40. Headrick, J.M., et al., *Spectral Signatures of Hydrated Proton Vibrations in Water Clusters.* Science, 2005. **308**(5729): p. 1765-1769.

41. Thämer, M., et al., *Ultrafast 2D IR spectroscopy of the excess proton in liquid water.* Science, 2015. **350**(6256): p. 78-82.

42. Dahms, F., et al., *The Hydrated Excess Proton in the Zundel Cation H5O2+: The Role of Ultrafast Solvent Fluctuations.* Angewandte Chemie International Edition, 2016. **55**(36): p. 10600-10605.

43. Kim, J., et al., *The vibrational spectrum of the hydrated proton: Comparison of experiment, simulation, and normal mode analysis.* The Journal of Chemical Physics, 2002. **116**(2): p. 737-746.

44. Xu, J., Y. Zhang, and G.A. Voth, *Infrared Spectrum of the Hydrated Proton in Water.* The Journal of Physical Chemistry Letters, 2011. **2**(2): p. 81-86.

45. Vendrell, O., F. Gatti, and H.-D. Meyer, *Full dimensional (15-dimensional) quantum-dynamical simulation of the protonated water dimer. II. Infrared spectrum and vibrational dynamics.* The Journal of Chemical Physics, 2007. **127**(18): p. 184303.

46. Carpenter, W.B., et al., *Picosecond Proton Transfer Kinetics in Water Revealed with Ultrafast IR Spectroscopy.* The Journal of Physical Chemistry B, 2018. **122**(10): p. 2792-2802.

47. Fournier, J.A., et al., *Snapshots of Proton Accommodation at a Microscopic Water Surface: Understanding the Vibrational Spectral Signatures of the Charge Defect in Cryogenically Cooled H+(H2O)n=2–28 Clusters.* The Journal of Physical Chemistry A, 2015. **119**(36): p. 9425-9440.

48. Wolke, C.T., et al., *Spectroscopic snapshots of the proton-transfer mechanism in water.* Science, 2016. **354**(6316): p. 1131-1135.

# APPENDIX: COPYRIGHT INFORMATION

## AIP Publishing LLC

*Your Window to Possible*

## Permission to Reuse Content

REUSING AIP PUBLISHING CONTENT

Permission from AIP Publishing is required to:

- republish content (e.g., excerpts, figures, tables) if you are not the author
- modify, adapt, or redraw materials for another publication
- systematically reproduce content
- store or distribute content electronically
- copy content for promotional purposes

To request permission to reuse AIP Publishing content, use RightsLink® for the fastest response or contact AIP Publishing directly at rights@aip.org (mailto:rights@aip.org) and we will respond within one week:

For RightsLink, use Scitation to access the article you wish to license, and click on the Reprints and Permissions link under the TOOLS tab. (For assistance click the "Help" button in the top right corner of the RightsLink page.)

To send a permission request to rights@aip.org (mailto:rights@aip.org), please include the following:

- Citation information for the article containing the material you wish to reuse
- A description of the material you wish to reuse, including figure and/or table numbers
- The title, authors, name of the publisher, and expected publication date of the new work
- The format(s) the new work will appear in (e.g., print, electronic, CD-ROM)
- How the new work will be distributed and whether it will be offered for sale

Authors do **not** need permission from AIP Publishing to:

- quote from a publication (please include the material in quotation marks and provide the customary acknowledgment of the source)
- reuse any materials that are licensed under a Creative Commons CC BY license (please format your credit line: "Author names, Journal Titles, Vol.#, Article ID#, Year of Publication; licensed under a Creative Commons Attribution (CC BY) license.")
- reuse your own AIP Publishing article in your thesis or dissertation (please format your credit line: "Reproduced from [FULL CITATION], with the permission of AIP Publishing")
- reuse content that appears in an AIP Publishing journal for republication in another AIP Publishing journal (please format your credit line: "Reproduced from [FULL CITATION], with the permission of AIP Publishing")

# LIST OF REFERENCES


Afroz, T., et al., *Structural interactions within lithium salt solvates: acyclic carbonates and esters.* The Journal of Physical Chemistry C, 2015. **119**(13): p. 7022-7027.

Akio, S. and T. Yoshihiro, *NMR Studies on Reorientational Motion of Hydrated D2O Molecules in Tetraalkylammonium Bromide Dilute Aqueous Solutions.* Bulletin of the Chemical Society of Japan, 1990. **63**(11): p. 3255-3259.

Albanese, D., et al., *Key role of water for nucleophilic substitutions in phase-transfer-catalyzed processes: A mini-review.* Industrial & engineering chemistry research, 2001. **40**(11): p. 2396-2401.

Alexander, R., et al., *Solvation of ions. XIV. Protic-dipolar aprotic solvent effects on rates of bimolecular reactions. Solvent activity coefficients of reactants and transition states at 25°.* Journal of the American Chemical Society, 1968. **90**(19): p. 5049-5069.

Allen, J.L., et al., *Combined quantum chemical/Raman spectroscopic analyses of Li+ cation solvation: Cyclic carbonate solvents-Ethylene carbonate and propylene carbonate.* Journal of Power Sources, 2014. **267**: p. 821-830.

Allen, M.P. and D.J. Tildesley, *Computer simulation of liquids*. 2017: Oxford university press.

Andrews, S.S. and S.G. Boxer, *Vibrational Stark Effects of Nitriles II. Physical Origins of Stark Effects from Experiment and Perturbation Models.* The Journal of Physical Chemistry A, 2002. **106**(3): p. 469-477.

Aravindakshan, N.P., et al., *The origin of the conductivity maximum vs. mixing ratio in pyridine/acetic acid and water/acetic acid.* The Journal of Chemical Physics, 2018. **149**(9): p. 094505.

Arnett, E.M., B. Chawla, and N.J. Hornung, *The hydration of anions in nonaqueous media.* Journal of Solution Chemistry, 1977. **6**(12): p. 781-818.

Aroca, R., et al., *Vibrational spectra and ion-pair properties of lithium hexafluorophosphate in ethylene carbonate based mixed-solvent systems for lithium batteries.* Journal of Solution Chemistry, 2000. **29**(10): p. 1047-1060.

Arslanargin, A., et al., *Models of Ion Solvation Thermodynamics in Ethylene Carbonate and Propylene Carbonate.* The Journal of Physical Chemistry B, 2016. **120**(8): p. 1497-1508.

Asbury, J.B., et al., *Water Dynamics: Vibrational Echo Correlation Spectroscopy and Comparison to Molecular Dynamics Simulations.* The Journal of Physical Chemistry A, 2004. **108**(7): p. 1107-1119.

Ashihara, S., et al., *Vibrational couplings and ultrafast relaxation of the O–H bending mode in liquid H2O.* Chemical physics letters, 2006. **424**(1-3): p. 66-70.

Asmis, K.R., et al., *Gas-Phase Infrared Spectrum of the Protonated Water Dimer.* Science, 2003. **299**(5611): p. 1375-1377.

Auerbach, D.I., et al., *Impacts of ocean CO 2 disposal on marine life: I. A toxicological assessment integrating constant-concentration laboratory assay data with variable-concentration field exposure.* Environmental Modeling & Assessment, 1997. **2**(4): p. 333-343.

Bagchi, S., et al., *2D-IR Experiments and Simulations of the Coupling between Amide-I and Ionizable Side Chains in Proteins: Application to the Villin Headpiece.* Journal of Physical Chemistry B, 2009. **113**(32): p. 11260-11273.

Bakker, H., *Structural dynamics of aqueous salt solutions.* Chemical reviews, 2008. **108**(4): p. 1456-1473.

Bakker, H.J., M.F. Kropman, and A.W. Omta, *Effect of ions on the structure and dynamics of liquid water.* Journal of Physics-Condensed Matter, 2005. **17**(45): p. S3215-S3224.

Bakker, H.J., *Structural dynamics of aqueous salt solutions.* Chemical Reviews, 2008. **108**(4): p. 1456-1473.

Banerjee, P., S. Yashonath, and B. Bagchi, *Rotation driven translational diffusion of polyatomic ions in water: A novel mechanism for breakdown of Stokes-Einstein relation.* Journal of Chemical Physics, 2017. **146**(16): p. 164502.

Banno, M., K. Ohta, and K. Tominaga, *Ultrafast Dynamics of the Carbonyl Stretching Vibration in Acetic Acid in Aqueous Solution Studied by Sub-Picosecond Infrared Spectroscopy.* The Journal of Physical Chemistry A, 2008. **112**(18): p. 4170-4175.

Banno, M., K. Ohta, and K. Tominaga, *Vibrational dynamics of acetate in D2O studied by infrared pump-probe spectroscopy.* Physical Chemistry Chemical Physics, 2012. **14**(18): p. 6359-6366.

Barthel, J., et al., *Non-aqueous electrolyte solutions in chemistry and modern technology*, in *Physical and inorganic chemistry*. 1983, Springer. p. 33-144.

Bazewicz, C.G., et al., *Expanding the utility of 4-cyano-l-phenylalanine as a vibrational reporter of protein environments.* The Journal of Physical Chemistry B, 2012. **116**(35): p. 10824-10831.

Belieres, J.-P. and C.A. Angell, *Protic Ionic Liquids: Preparation, Characterization, and Proton Free Energy Level Representation.* The Journal of Physical Chemistry B, 2007. **111**(18): p. 4926-4937.

Bell, R.P., *The theory of reactions involving proton transfers.* Proceedings of the Royal Society of London. Series A-Mathematical and Physical Sciences, 1936. **154**(882): p. 414-429.

Benjamin, I., *Mechanism and Dynamics of Ion Transfer Across a Liquid-Liquid Interface.* Science, 1993. **261**(5128): p. 1558-1560.

Bhatt, M.D., M. Cho, and K. Cho, *Interaction of Li+ ions with ethylene carbonate (EC): Density functional theory calculations.* Applied Surface Science, 2010. **257**(5): p. 1463-1468.

Biswas, R., et al., *IR spectral assignments for the hydrated excess proton in liquid water.* The Journal of Chemical Physics, 2017. **146**(15): p. 154507.

Blomgren, G.E., *Properties and structures of electrolyte solutions for lithium batteries.* Journal of Power Sources, 1985. **14**(1): p. 39-44.

Bockris, J.O.M. and A.K. Reddy, *Modern electrochemistry 2B: electrodics in chemistry, engineering, biology and environmental science*. Vol. 2. 2000: Springer Science & Business Media.

Boczko, E.M. and C.L. Brooks III, *Constant-temperature free energy surfaces for physical and chemical processes.* Journal of Physical Chemistry, 1993. **97**(17): p. 4509-4513.

BODEN, R.M. and B. RM, *A mild method for preparing trans-alkenes; crown ether catalysis of the Wittig reaction.* 1975.

Bogle, X., et al., *Understanding Li+–solvent interaction in nonaqueous carbonate electrolytes with 17O NMR.* The journal of physical chemistry letters, 2013. **4**(10): p. 1664-1668.

Bohets, H. and B.J. van der Veken, *On the conformational behavior of dimethyl carbonate.* Physical Chemistry Chemical Physics, 1999. **1**(8): p. 1817-1826.

Borodin, O. and G.D. Smith, *Quantum chemistry and molecular dynamics simulation study of dimethyl carbonate: ethylene carbonate electrolytes doped with LiPF6.* The Journal of Physical Chemistry B, 2009. **113**(6): p. 1763-1776.

Borodin, O., et al., *Competitive lithium solvation of linear and cyclic carbonates from quantum chemistry.* Physical Chemistry Chemical Physics, 2016. **18**(1): p. 164-175.

Bountis, T., *Proton transfer in hydrogen-bonded systems*. Vol. 291. 2012: Springer Science & Business Media.

Boyd, R.W., *Nonlinear optics*. 2003: Elsevier.

Brak, K. and E.N. Jacobsen, *Asymmetric Ion-Pairing Catalysis.* Angewandte Chemie International Edition, 2013. **52**(2): p. 534-561.

Brodin, A. and P. Jacobsson, *Dipolar interaction and molecular ordering in liquid propylene carbonate: Anomalous dielectric susceptibility and Raman non-coincidence effect.* Journal of Molecular Liquids, 2011. **164**(1): p. 17-21.

Burba, C.M. and R. Frech, *Spectroscopic Measurements of Ionic Association in Solutions of LiPF6.* The Journal of Physical Chemistry B, 2005. **109**(31): p. 15161-15164.

Car, R. and M. Parrinello, *Unified approach for molecular dynamics and density-functional theory.* Physical review letters, 1985. **55**(22): p. 2471. 62

Carey, D.M. and G.M. Korenowski, *Measurement of the Raman spectrum of liquid water.* The Journal of chemical physics, 1998. **108**(7): p. 2669-2675.

Carpenter, W.B., et al., *Picosecond Proton Transfer Kinetics in Water Revealed with Ultrafast IR Spectroscopy.* The Journal of Physical Chemistry B, 2018. **122**(10): p. 2792-2802.

Castro, P. and M. Huber, *Marine biology. WCB*. 1997, McGraw-Hill, New York.

Cazzanelli, E., et al., *Raman and NMR analysis of LiClO4 concentrated solutions in ethylene carbonate-propylene carbonate.* Solid State Ionics, 1996. **86-88**: p. 379-384.

Chapman, N., et al., *Spectroscopic and Density Functional Theory Characterization of Common Lithium Salt Solvates in Carbonate Electrolytes for Lithium Batteries.* The Journal of Physical Chemistry C, 2017. **121**(4): p. 2135-2148.

Chau, P.L. and A.J. Hardwick, *A new order parameter for tetrahedral configurations.* Molecular Physics, 1998. **93**(3): p. 511-518.

Chaudhari, M.I., et al., *Scaling Atomic Partial Charges of Carbonate Solvents for Lithium Ion Solvation and Diffusion.* Journal of Chemical Theory and Computation, 2016. **12**(12): p. 5709-5718.

Chen, H.L., et al., *Vibrational Energy Transfer: An Angstrom Molecular Ruler in Studies of Ion Pairing and Clustering in Aqueous Solutions.* Journal of Physical Chemistry B, 2015. **119**(12): p. 4333-4349.

Chen, K., et al., *Equilibrium in protic ionic liquids: The degree of proton transfer and thermodynamic properties.* The Journal of Physical Chemistry B, 2017. **122**(1): p. 309-315.

Cho, M., *Two-dimensional optical spectroscopy*. 2009: CRC press.

Choi, J.-H. and M. Cho, *Vibrational solvatochromism and electrochromism of infrared probe molecules containing C≡O, C≡N, C=O, or C−F vibrational chromophore.* The Journal of Chemical Physics, 2011. **134**(15): p. 154513.

Chuntonov, L., et al., *Kinetics of Exchange between Zero-, One-, and Two-Hydrogen-Bonded States of Methyl and Ethyl Acetate in Methanol.* Journal of Physical Chemistry B, 2015. **119**(12): p. 4512-4520.

Cleland, W. and M. Kreevoy, *Low-barrier hydrogen bonds and enzymic catalysis.* Science, 1994. **264**(5167): p. 1887-1890.

Cleland, W.W., *Low-barrier hydrogen bonds and low fractionation factor bases in enzymic reactions.* Biochemistry, 1992. **31**(2): p. 317-319.

Cleland, W.W., P.A. Frey, and J.A. Gerlt, *The Low Barrier Hydrogen Bond in Enzymatic Catalysis.* Journal of Biological Chemistry, 1998. **273**(40): p. 25529-25532.

Cole, R.B. and A.K. Harrata, *Solvent effect on analyte charge state, signal intensity, and stability in negative ion electrospray mass spectrometry; implications for the mechanism of negative ion formation.* Journal of the American Society for Mass Spectrometry, 1993. **4**(7): p. 546-556.

Collins, K.D. and M.W. Washabaugh, *The Hofmeister Effect and the Behavior of Water at Interfaces.* Quarterly Reviews of Biophysics, 1985. **18**(4): p. 323-422.

Costard, R., et al., *Ultrafast phosphate hydration dynamics in bulk H2O.* Journal of Chemical Physics, 2015. **142**(21): p. 212406.

Cowan, M., et al., *Ultrafast memory loss and energy redistribution in the hydrogen bond network of liquid H 2 O.* Nature, 2005. **434**(7030): p. 199-202.

Cox, M., M. Hidalgo, and M. Valiente, *Solvent Extraction for the 21st Century.* SCI, London, 2001.

Cringus, D., et al., *Hydrogen bonding and vibrational energy relaxation in water− acetonitrile mixtures.* The Journal of Physical Chemistry B, 2004. **108**(29): p. 10376-10387.

Czurlok, D., et al., *Femtosecond 2DIR spectroscopy of the nitrile stretching vibration of thiocyanate anions in liquid-to-supercritical heavy water. Spectral diffusion and libration-induced hydrogen-bond dynamics.* Physical Chemistry Chemical Physics, 2015. **17**(44): p. 29776-29785.

D'Angelo, P., et al., *Combined XANES and EXAFS analysis of Co2+, Ni2+,and Zn2+ aqueous solutions.* Physical Review B, 2002. **66**(6): p. 064209.

Dahms, F., et al., *Large-amplitude transfer motion of hydrated excess protons mapped by ultrafast 2D IR spectroscopy.* Science, 2017. **357**(6350): p. 491-495.

Dahms, F., et al., *The Hydrated Excess Proton in the Zundel Cation H5O2+: The Role of Ultrafast Solvent Fluctuations.* Angewandte Chemie International Edition, 2016. **55**(36): p. 10600-10605.

Daly, C.A., et al., *Decomposition of the Experimental Raman and Infrared Spectra of Acidic Water into Proton, Special Pair, and Counterion Contributions.* The Journal of Physical Chemistry Letters, 2017. **8**(21): p. 5246-5252.

Darensbourg, M.Y., *Ion pairing effects on transition metal carbonyl anions.* Prog. Inorg. Chem, 1985. **33**: p. 221-274.

Davydov, A., *"Solitons in Molecular Systems"(Reidel, Dordrecht, 1991).*

Del Ben, M., et al., *Bulk liquid water at ambient temperature and pressure from MP2 theory.* The Journal of Physical Chemistry Letters, 2013. **4**(21): p. 3753-3759.

Ding, Y., A.A. Hassanali, and M. Parrinello, *Anomalous water diffusion in salt solutions.* Proceedings of the National Academy of Sciences of the United States of America, 2014. **111**(9): p. 3310-3315.

Doi, H., et al., *A New Proton Conductive Liquid with No Ions: Pseudo-Protic Ionic Liquids.* Chemistry – A European Journal, 2013. **19**(35): p. 11522-11526.

Doucey, L., et al., *A study of the Li/Li+ couple in DMC and PC solvents: part 1: characterization of LiAsF6/DMC and LiAsF6/PC solutions.* Electrochimica acta, 1999. **44**(14): p. 2371-2377.

Eisenman, G. and J.A. Dani, *An introduction to molecular architecture and permeability of ion channels.* Annual review of biophysics and biophysical chemistry, 1987. **16**(1): p. 205-226.

Evans, M.G. and M. Polanyi, *Inertia and driving force of chemical reactions.* Transactions of the Faraday Society, 1938. **34**(0): p. 11-24.

Fafarman, A.T., et al., *Quantitative, directional measurement of electric field heterogeneity in the active site of ketosteroid isomerase.* Proceedings of the National Academy of Sciences, 2012. **109**(6): p. E299-E308.

Falk, M., *Frequencies of H O H, H O D and D O D bending fundamentals in liquid water.* Journal of Raman Spectroscopy, 1990. **21**(9): p. 563-567.

Fayer, M.D., et al., *Water Dynamics in Salt Solutions Studied with Ultrafast Two-Dimensional Infrared (2D IR) Vibrational Echo Spectroscopy.* Accounts of Chemical Research, 2009. **42**(9): p. 1210-1219.

Fecko, C.J., et al., *Ultrafast Hydrogen-Bond Dynamics in the Infrared Spectroscopy of Water.* Science, 2003. **301**(5640): p. 1698-1702.

Ferrenberg, A.M. and R.H. Swendsen, *Optimized Monte-Carlo Data-Analysis.* Physical Review Letters, 1989. **63**(12): p. 1195-1198.

Flores, E., et al., *Solvation structure in dilute to highly concentrated electrolytes for lithium-ion and sodium-ion batteries.* Electrochimica Acta, 2017. **233**: p. 134-141.

Fournier, J.A., et al., *Broadband 2D IR spectroscopy reveals dominant asymmetric H5O2+ proton hydration structures in acid solutions.* Nature Chemistry, 2018. **10**(9): p. 932-937.

Fournier, J.A., et al., *Snapshots of Proton Accommodation at a Microscopic Water Surface: Understanding the Vibrational Spectral Signatures of the Charge Defect in Cryogenically Cooled H+(H2O)n=2–28 Clusters.* The Journal of Physical Chemistry A, 2015. **119**(36): p. 9425-9440.

Franks, F., *Water a comprehensive treatise: volume 4: aqueous solutions of amphiphiles and macromolecules*. 2013: Springer Science & Business Media.

Frey, P., S. Whitt, and J. Tobin, *A low-barrier hydrogen bond in the catalytic triad of serine proteases.* Science, 1994. **264**(5167): p. 1927-1930.

Fried, S.D., S. Bagchi, and S.G. Boxer, *Measuring electrostatic fields in both hydrogen-bonding and non-hydrogen-bonding environments using carbonyl vibrational probes*. Journal of the American Chemical Society, 2013. **135**(30): p. 11181-11192.

Frisch, M.J., et al., *Gaussian 09, Revision D.01*. 2013: Wallingford, CT.

Frisch, M.J., et al., *Gaussian 16 Rev. C.01*. 2016: Wallingford, CT.

Fujii, K., et al., *Long-Range Ion-Ordering in Salt-Concentrated Lithium-Ion Battery Electrolytes: A Combined High-Energy X-ray Total Scattering and Molecular Dynamics Simulation Study.* The Journal of Physical Chemistry C, 2017. **121**(41): p. 22720-22726.

Fulfer, K.D. and D.G. Kuroda, *A comparison of the solvation structure and dynamics of the lithium ion in linear organic carbonates with different alkyl chain lengths.* Physical Chemistry Chemical Physics, 2017. **19**(36): p. 25140-25150.

Fulfer, K.D. and D.G. Kuroda, *Ion speciation of lithium hexafluorophosphate in dimethyl carbonate solutions: an infrared spectroscopy study.* Physical Chemistry Chemical Physics, 2018. **20**(35): p. 22710-22718.

Fulfer, K.D. and D.G. Kuroda, *Solvation Structure and Dynamics of the Lithium Ion in Organic Carbonate-Based Electrolytes: A Time-Dependent Infrared Spectroscopy Study.* The Journal of Physical Chemistry C, 2016. **120**(42): p. 24011-24022.

Fulmer, E.C., F. Ding, and M.T. Zanni, *Heterodyned fifth-order 2D-IR spectroscopy of the azide ion in an ionic glass.* Journal of Chemical Physics, 2005. **122**(3): p. 034302.

Gaffney, K.J., et al., *H-bond switching and ligand exchange dynamics in aqueous ionic solution.* Chemical Physics Letters, 2011. **504**(1-3): p. 1-6.

Gale, G., et al., *Femtosecond dynamics of hydrogen bonds in liquid water: A real time study.* Physical review letters, 1999. **82**(5): p. 1068.

Ganesh, P., D.-e. Jiang, and P.R.C. Kent, *Accurate Static and Dynamic Properties of Liquid Electrolytes for Li-Ion Batteries from ab initio Molecular Dynamics.* The Journal of Physical Chemistry B, 2011. **115**(12): p. 3085-3090.

Garche, J., et al., *Encyclopedia of electrochemical power sources*. 2013: Newnes.

Garcia-Celma, J.J., et al., *Specific anion and cation binding to lipid membranes investigated on a solid supported membrane.* Langmuir, 2007. **23**(20): p. 10074-10080.

Gavras, I. and H. Gavras, *'Volume-expanded'hypertension: the effect of fluid overload and the role of the sympathetic nervous system in salt-dependent hypertension.* Journal of hypertension, 2012. **30**(4): p. 655-659.

Giammanco, C.H., P.L. Kramer, and M.D. Fayer, *Dynamics of Dihydrogen Bonding in Aqueous Solutions of Sodium Borohydride.* Journal of Physical Chemistry B, 2015. **119**(8): p. 3546-3559.

Gilli, P., et al., *Evidence for resonance-assisted hydrogen bonding. 4. Covalent nature of the strong homonuclear hydrogen bond. Study of the O-H--O system by crystal structure correlation methods.* Journal of the American Chemical Society, 1994. **116**(3): p. 909-915.

Giorgini, M.G., et al., *Solvation Structure around the Li+ Ion in Mixed Cyclic/Linear Carbonate Solutions Unveiled by the Raman Noncoincidence Effect.* Journal of Physical Chemistry Letters, 2015. **6**(16): p. 3296-3302.

Goedecker, S., M. Teter, and J. Hutter, *Separable dual-space Gaussian pseudopotentials.* Physical Review B, 1996. **54**(3): p. 1703-1710.

Gouaux, E. and R. MacKinnon, *Principles of selective ion transport in channels and pumps.* science, 2005. **310**(5753): p. 1461-1465.

Grimme, S., *Semiempirical GGA-type density functional constructed with a long-range dispersion correction.* Journal of Computational Chemistry, 2006. **27**(15): p. 1787-1799.

Grossfield, A., *"WHAM: the weighted histogram analysis method", version 2.0.9.1*.

Guo, Q., et al., *Line shape analysis of two-dimensional infrared spectra.* Journal of Chemical Physics, 2015. **142**(21): p. 212427.

Hajari, T., P. Ganguly, and N.F.A. van der Vegt, *Enthalpy-Entropy of Cation Association with the Acetate Anion in Water.* Journal of Chemical Theory and Computation, 2012. **8**(10): p. 3804-3809.

Hamm, P. and M. Zanni, *Concepts and methods of 2D infrared spectroscopy*. 2011: Cambridge University Press.

Hamm, P., M. Lim, and R.M. Hochstrasser, *Non-Markovian dynamics of the vibrations of ions in water from femtosecond infrared three-pulse photon echoes.* Physical Review Letters, 1998. **81**(24): p. 5326-5329.

Han, S.-D., et al., *Solvate structures and computational/spectroscopic characterization of LiPF6 electrolytes.* The Journal of Physical Chemistry C, 2015. **119**(16): p. 8492-8500.

Hansen, J., et al., *Climate response times: Dependence on climate sensitivity and ocean mixing.* Science, 1985. **229**(4716): p. 857-859.

Hanwell, M.D., et al., *Avogadro: an advanced semantic chemical editor, visualization, and analysis platform.* Journal of Cheminformatics, 2012. **4**(1): p. 17.

Headrick, J.M., et al., *Spectral Signatures of Hydrated Proton Vibrations in Water Clusters.* Science, 2005. **308**(5729): p. 1765-1769.

Heilweil, E.J., et al., *Vibrational energy relaxation of the cyanide ion in aqueous solution.* The Journal of Chemical Physics, 1982. **76**(11): p. 5632-5634.

Herman, R.C. and R. Hofstadter, *Vibration Spectra and Molecular Structure V. Infra-Red Studies on Light and Heavy Acetic Acids.* The Journal of Chemical Physics, 1938. **6**(9): p. 534-540.

Hibbert, F. and J. Emsley, *Hydrogen Bonding and Chemical Reactivity*, in *Advances in Physical Organic Chemistry*, D. Bethell, Editor. 1990, Academic Press. p. 255-379.

Hodgkin, A.L. and A.F. Huxley, *A Quantitative Description of Membrane Current and Its Application to Conduction and Excitation in Nerve.* Journal of Physiology-London, 1952. **117**(4): p. 500-544.

Hofmeister, F., *Zur Lehre von der Wirkung der Salze.* Archiv für experimentelle Pathologie und Pharmakologie, 1888. **24**(4): p. 247-260.

Hofmeister, F., *Zur lehre von der wirkung der salze.* Naunyn-Schmiedeberg's Archives of Pharmacology, 1888. **25**(1): p. 1-30.

Houriez, C., M. Meot-Ner, and M. Masella, *Simulated Solvation of Organic Ions II: Study of Linear Alkylated Carboxylate Ions in Water Nanodrops and in Liquid Water. Propensity for Air/Water Interface and Convergence to Bulk Solvation Properties.* Journal of Physical Chemistry B, 2015. **119**(36): p. 12094-12107.

Huerta-Viga, A., et al., *A salt-bridge structure in solution revealed by 2D-IR spectroscopy.* Physical Chemistry Chemical Physics, 2014. **16**(30): p. 15784-15786.

Hundhammer, B. and T. Solomon, *Determination of standard Gibbs energies of ion partition between water and organic solvents by cyclic voltammetry: Part I.* Journal of electroanalytical chemistry and interfacial electrochemistry, 1983. **157**(1): p. 19-26.

Hwang, S., et al., *Ionic Conduction and Solution Structure in LiPF6 and LiBF4 Propylene Carbonate Electrolytes.* The Journal of Physical Chemistry C, 2018. **122**(34): p. 19438-19446.

Ingenmey, J., S. Gehrke, and B. Kirchner, *How to harvest Grotthuss diffusion in protic ionic liquid electrolyte systems.* ChemSusChem, 2018. **11**(12): p. 1900-1910.

Ito, K. and H.J. Bernstein, *THE VIBRATIONAL SPECTRA OF THE FORMATE, ACETATE, AND OXALATE IONS.* Canadian Journal of Chemistry, 1956. **34**(2): p. 170-178.

Jenkins, H.D.B. and Y. Marcus, *Viscosity B-Coefficients of the Aqueous Cyanide and Azide Ions.* Journal of Solution Chemistry, 1993. **22**(1): p. 95-98.

Jewett, A.I., Z.Y. Zhuang, and J.E. Shea, *Moltemplate a Coarse-Grained Model Assembly Tool.* Biophysical Journal, 2013. **104**(2): p. 169a-169a.

Jiang, B., et al., *The Anion Effect on Li+ Ion Coordination Structure in Ethylene Carbonate Solutions.* The Journal of Physical Chemistry Letters, 2016. **7**(18): p. 3554-3559.

Jickells, T., et al., *Global iron connections between desert dust, ocean biogeochemistry, and climate.* science, 2005. **308**(5718): p. 67-71.

Jimenez, R., et al., *Femtosecond solvation dynamics of water.* Nature, 1994. **369**(6480): p. 471-473.

Joint, I., S.C. Doney, and D.M. Karl, *Will ocean acidification affect marine microbes?* The ISME journal, 2011. **5**(1): p. 1-7.

Jones, L.H. and E. Mclaren, *Infrared Spectra of Ch3coona and Cd3coona and Assignments of Vibrational Frequencies.* Journal of Chemical Physics, 1954. **22**(11): p. 1796-1800.

Jorgensen, W.L., D.S. Maxwell, and J. Tirado-Rives, *Development and Testing of the OPLS All-Atom Force Field on Conformational Energetics and Properties of Organic Liquids.* Journal of the American Chemical Society, 1996. **118**(45): p. 11225-11236.

Jorgensen, W.L., et al., *Comparison of Simple Potential Functions for Simulating Liquid Water.* Journal of Chemical Physics, 1983. **79**(2): p. 926-935.

Jorn, R. and R. Kumar, *Breaking the Scales: Electrolyte Modeling in Metal-Ion Batteries.* Interface, 2017. **26**(1): p. 55-59.

Jorn, R., et al., *Atomistic Modeling of the Electrode–Electrolyte Interface in Li-Ion Energy Storage Systems: Electrolyte Structuring.* The Journal of Physical Chemistry C, 2013. **117**(8): p. 3747-3761.

Jow, T.R., et al., *Electrolytes for lithium and lithium-ion batteries*. Vol. 58. 2014: Springer.

Kameda, Y., et al., *Solvation structure of Li+ in concentrated LiPF6− propylene carbonate solutions.* The Journal of Physical Chemistry B, 2007. **111**(22): p. 6104-6109.

Katz, B.A., et al., *Contribution of Multicentered Short Hydrogen Bond Arrays to Potency of Active Site-Directed Serine Protease Inhibitors.* Journal of the American Chemical Society, 2002. **124**(39): p. 11657-11668.

Kim, H. and M. Cho, *Infrared probes for studying the structure and dynamics of biomolecules.* Chemical reviews, 2013. **113**(8): p. 5817-5847.

Kim, J., et al., *The vibrational spectrum of the hydrated proton: Comparison of experiment, simulation, and normal mode analysis.* The Journal of Chemical Physics, 2002. **116**(2): p. 737-746.

Kim, Y.S., et al., *2D IR provides evidence for mobile water molecules in beta-amyloid fibrils.* Proceedings of the National Academy of Sciences of the United States of America, 2009. **106**(42): p. 17751-17756.

Kindt, J. and C. Schmuttenmaer, *Far-infrared dielectric properties of polar liquids probed by femtosecond terahertz pulse spectroscopy.* The Journal of Physical Chemistry, 1996. **100**(24): p. 10373-10379.

Klassen, B., et al., *Raman Spectra and Transport Properties of Lithium Perchlorate in Ethylene Carbonate Based Binary Solvent Systems for Lithium Batteries.* The Journal of Physical Chemistry B, 1998. **102**(24): p. 4795-4801.

Koeppen, B.M. and J.T. Hansen, *Netter's Atlas of Human Physiology*. 2002: Elsevier Inc.

Kohn, W. and L.J. Sham, *Self-Consistent Equations Including Exchange and Correlation Effects.* Physical Review, 1965. **140**(4A): p. A1133-A1138.

Kondo, K., et al., *Conductivity and Solvation of Li+ Ions of LiPF6 in Propylene Carbonate Solutions.* The Journal of Physical Chemistry B, 2000. **104**(20): p. 5040-5044.

Kramer, P.L., J. Nishida, and M.D. Fayer, *Separation of experimental 2D IR frequency-frequency correlation functions into structural and reorientation-induced contributions.* Journal of Chemical Physics, 2015. **143**(12): p. 124505.

Kreevoy, M.M. and T.M. Liang, *Structures and isotopic fractionation factors of complexes, A1HA2.* Journal of the American Chemical Society, 1980. **102**(10): p. 3315-3322.

Kropman, M.F. and H.J. Bakker, *Vibrational relaxation of liquid water in ionic solvation shells.* Chemical Physics Letters, 2003. **370**(5): p. 741-746.

Krumhansl, J.A. and J.R. Schrieffer, *Dynamics and statistical mechanics of a one-dimensional model Hamiltonian for structural phase transitions.* Physical Review B, 1975. **11**(9): p. 3535-3545.

Kubo, R., *A Stochastic Theory of Line Shape*, in *Advances in Chemical Physics*. 2007, John Wiley & Sons, Inc. p. 101-127.

Kubo, R., *A stochastic theory of line shape.* Stochastic processes in chemical physics, 1969. **15**: p. 101-127.

Kumar, N. and J.M. Seminario, *Lithium-Ion Model Behavior in an Ethylene Carbonate Electrolyte Using Molecular Dynamics.* The Journal of Physical Chemistry C, 2016. **120**(30): p. 16322-16332.

Kumar, R., J.R. Schmidt, and J.L. Skinner, *Hydrogen bonding definitions and dynamics in liquid water.* Journal of Chemical Physics, 2007. **126**(20): p. 204107.

Kumar, S., et al., *THE weighted histogram analysis method for free-energy calculations on biomolecules. I. The method.* Journal of Computational Chemistry, 1992. **13**(8): p. 1011-1021.

Kunz, W., *Specific ion effects in colloidal and biological systems.* Current Opinion in Colloid & Interface Science, 2010. **15**(1-2): p. 34-39.

Kuo, C.-H., et al., *Correlation of the Vibrations of the Aqueous Azide Ion with the O−H Modes of Bound Water Molecules.* Journal of Physical Chemistry B, 2007. **111**(50): p. 14028-14033.

Kuroda, D.G. and R.M. Hochstrasser, *Dynamic structures of aqueous oxalate and the effects of counterions seen by 2D IR.* Physical Chemistry Chemical Physics, 2012. **14**(18): p. 6219-6224.

Kuroda, D.G. and R.M. Hochstrasser, *Two-dimensional infrared spectral signature and hydration of the oxalate dianion.* The Journal of chemical physics, 2011. **135**(20): p. 204502.

Kuroda, D.G., D.Y. Vorobyev, and R.M. Hochstrasser, *Ultrafast relaxation and 2D IR of the aqueous trifluorocarboxylate ion.* Journal of Chemical Physics, 2010. **132**(4): p. 044501.

Kuroda, D.G., et al., *Vibrational dynamics of a non-degenerate ultrafast rotor: The (C12,C13)-oxalate ion.* Journal of Chemical Physics, 2013. **139**(16): p. 164514.

Kwac, K. and M. Cho, *Molecular dynamics simulation study of N-methylacetamide in water. I. Amide I mode frequency fluctuation.* The Journal of chemical physics, 2003. **119**(4): p. 2247-2255.

Kwac, K. and M.H. Cho, *Molecular dynamics simulation study of N-methylacetamide in water. II. Two-dimensional infrared pump-probe spectra.* Journal of Chemical Physics, 2003. **119**(4): p. 2256-2263.

Kwak, K., et al., *Frequency-frequency correlation functions and apodization in two-dimensional infrared vibrational echo spectroscopy: A new approach.* Journal of Chemical Physics, 2007. **127**(12): p. 124503.

Laage, D. and J.T. Hynes, *A molecular jump mechanism of water reorientation.* Science, 2006. **311**(5762): p. 832-835.

Laage, D. and J.T. Hynes, *On the Residence Time for Water in a Solute Hydration Shell: Application to Aqueous Halide Solutions.* The Journal of Physical Chemistry B, 2008. **112**(26): p. 7697-7701.

Ladanyi, B.M. and R.M. Stratt, *Short-Time Dynamics of Solvation: Linear Solvation Theory for Polar Solvents.* The Journal of Physical Chemistry, 1995. **99**(9): p. 2502-2511.

Laenen, R., C. Rauscher, and A. Laubereau, *Dynamics of local substructures in water observed by ultrafast infrared hole burning.* Physical review letters, 1998. **80**(12): p. 2622.

Lee, K.-K., et al., *Ultrafast fluxional exchange dynamics in electrolyte solvation sheath of lithium ion battery.* Nature Communications, 2017. **8**: p. 14658.

Levinger, N.E., P.H. Davis, and M. Fayer, *Vibrational relaxation of the free terminal hydroxyl stretch in methanol oligomers: Indirect pathway to hydrogen bond breaking.* The Journal of Chemical Physics, 2001. **115**(20): p. 9352-9360.

Li, T. and P.B. Balbuena, *Theoretical Studies of Lithium Perchlorate in Ethylene Carbonate, Propylene Carbonate, and Their Mixtures.* Journal of The Electrochemical Society, 1999. **146**(10): p. 3613-3622.

Li, T., et al., *Hydration and vibrational dynamics of betaine (N,N,N-trimethylglycine).* Journal of Chemical Physics, 2015. **142**(21): p. 212438.

Liang, C., K. Kwak, and M. Cho, *Revealing the Solvation Structure and Dynamics of Carbonate Electrolytes in Lithium-Ion Batteries by Two-Dimensional Infrared Spectrum Modeling.* The Journal of Physical Chemistry Letters, 2017. **8**(23): p. 5779-5784.

Lim, M. and R.M. Hochstrasser, *Unusual vibrational dynamics of the acetic acid dimer.* The Journal of Chemical Physics, 2001. **115**(16): p. 7629-7643.

Lin, I.C., et al., *Structure and Dynamics of Liquid Water from ab Initio Molecular Dynamics-Comparison of BLYP, PBE, and revPBE Density Functionals with and without van der Waals Corrections.* Journal of Chemical Theory and Computation, 2012. **8**(10): p. 3902-3910.

Lindquist, B.A., K.E. Furse, and S.A. Corcelli, *Nitrile groups as vibrational probes of biomolecular structure and dynamics: an overview.* Physical Chemistry Chemical Physics, 2009. **11**(37): p. 8119-8132.

Lippert, G., et al., *Response Function Basis Sets: Application to Density Functional Calculations.* Journal of Physical Chemistry, 1996. **100**(15): p. 6231-6235.

Logan, E.R., et al., *A Study of the Transport Properties of Ethylene Carbonate-Free Li Electrolytes.* Journal of the Electrochemical Society, 2018. **165**(3): p. A705-A716.

Lombard, J., *Once upon a time the cell membranes: 175 years of cell boundary research.* Biology Direct, 2014. **9**: p. 32.

Lucht, B.L., T. Markmaitree, and L. Yang, *Lithium–Ion Batteries.* Encyclopedia of Inorganic and Bioinorganic Chemistry, 2011.

MacFarlane, D.R., et al., *Lewis base ionic liquids.* Chemical Communications, 2006(18): p. 1905-1917.

Maeda, S., et al., *Local Structure of Li+ in Concentrated Ethylene Carbonate Solutions Studied by Low-Frequency Raman Scattering and Neutron Diffraction with 6Li/7Li Isotopic Substitution Methods.* The Journal of Physical Chemistry B, 2017. **121**(48): p. 10979-10987.

Mąkosza, M. and M. Wawrzyniewicz, *Reactions of organic anions. XXIV. Catalytic method for preparation of dichlorocyclopropane derivatives in aqueous medium.* Tetrahedron Letters, 1969. **10**(53): p. 4659-4662.

Mancinelli, R., et al., *Hydration of Sodium, Potassium, and Chloride Ions in Solution and the Concept of Structure Maker/Breaker.* The Journal of Physical Chemistry B, 2007. **111**(48): p. 13570-13577.

Mandal, A. and A. Tokmakoff, *Vibrational dynamics of aqueous hydroxide solutions probed using broadband 2DIR spectroscopy.* Journal of Chemical Physics, 2015. **143**(19): p. 194501.

Mandal, A., et al., *Collective vibrations of water-solvated hydroxide ions investigated with broadband 2DIR spectroscopy.* Journal of Chemical Physics, 2014. **140**(20): p. 204508.

Marcus, Y., *Effect of Ions on the Structure of Water: Structure Making and Breaking.* Chemical Reviews, 2009. **109**(3): p. 1346-1370.

Marcus, Y., *Ions in solution and their solvation*. 2015, Hoboken, New Jersey: John Wiley & Sons, Inc. x, 298 pages.

Martinez, L., et al., *PACKMOL: A Package for Building Initial Configurations for Molecular Dynamics Simulations.* Journal of Computational Chemistry, 2009. **30**(13): p. 2157-2164.

Matsubara, K., R. Kaneuchi, and N. Maekita, *13C NMR estimation of preferential solvation of lithium ions in non-aqueous mixed solvents.* Journal of the Chemical Society, Faraday Transactions, 1998. **94**(24): p. 3601-3605.

Mellink, W.A. and R. Kaptein, *Determination of the methyl group rotation energy barrier in some substituted tricyclo [3.1.0.02,6]hexanes by carbon-13 spinlattice relaxation.* Organic Magnetic Resonance, 1980. **13**(4): p. 279-281.

Meneton, P., et al., *Links between dietary salt intake, renal salt handling, blood pressure, and cardiovascular diseases.* Physiological reviews, 2005. **85**(2): p. 679-715.

Mikio, K., T. Kyoji, and I. Tadashi, *THE COEXTRACTION OF WATER WITH ALKALI AND ALKALINE EARTH METALS HEXANITRODIPKENYLAMINATES AND ANALOGOUS AMINATES.* Chemistry Letters, 1972. **1**(5): p. 417-420.

Missimer, T.M. and R.G. Maliva, *Environmental issues in seawater reverse osmosis desalination: Intakes and outfalls.* Desalination, 2018. **434**: p. 198-215.

Mizoguchi, K., Y. Hori, and Y. Tominaga, *Study on dynamical structure in water and heavy water by low-frequency Raman spectroscopy.* The Journal of chemical physics, 1992. **97**(3): p. 1961-1968.

Moilanen, D.E., et al., *Water inertial reorientation: Hydrogen bond strength and the angular potential.* Proceedings of the National Academy of Sciences, 2008. **105**(14): p. 5295-5300.

Morita, M., et al., *A Raman spectroscopic study of organic electrolyte solutions based on binary solvent systems of ethylene carbonate with low viscosity solvents which dissolve different lithium salts.* Journal of the Chemical Society, Faraday Transactions, 1998. **94**(23): p. 3451-3456.

Mukamel, S., *Principles of nonlinear optical spectroscopy*. Oxford series in optical and imaging sciences. 1995, New York: Oxford University Press. xviii, 543 p.

Mukamel, S., *Principles of nonlinear optical spectroscopy*. Vol. 29. 1995: Oxford university press New York.

Nara, M., H. Torii, and M. Tasumi, *Correlation between the vibrational frequencies of the carboxylate group and the types of its coordination to a metal ion: An ab initio molecular orbital study.* Journal of Physical Chemistry, 1996. **100**(51): p. 19812-19817.

Nelson, D.L., M.M. Cox, and A.L. Lehninger, *Lehninger principles of biochemistry*. Seventh edition. ed. 2017, New York, NY; Houndmills, Basingstoke: W.H. Freeman and Company ; Macmillan Higher Education. xxxiv, 1172, AS34, G20, I45 pages.

Nibbering, E.T. and T. Elsaesser, *Ultrafast vibrational dynamics of hydrogen bonds in the condensed phase.* Chemical Reviews, 2004. **104**(4): p. 1887-1914.

Ohmine, I. and H. Tanaka, *Fluctuation, relaxations, and hydration in liquid water. Hydrogen-bond rearrangement dynamics.* Chemical reviews, 1993. **93**(7): p. 2545-2566.

Ohtaki, H. and T. Radnai, *Structure and dynamics of hydrated ions.* Chemical Reviews, 1993. **93**(3): p. 1157-1204.

Ong, M.T., et al., *Complex ion dynamics in carbonate lithium-ion battery electrolytes.* The Journal of Physical Chemistry C, 2017. **121**(12): p. 6589-6595.

Ong, M.T., et al., *Lithium Ion Solvation and Diffusion in Bulk Organic Electrolytes from First-Principles and Classical Reactive Molecular Dynamics.* The Journal of Physical Chemistry B, 2015. **119**(4): p. 1535-1545.

Osakai, T., A. Ogata, and K. Ebina, *Hydration of Ions in Organic Solvent and Its Significance in the Gibbs Energy of Ion Transfer between Two Immiscible Liquids.* The Journal of Physical Chemistry B, 1997. **101**(41): p. 8341-8348.

Osakai, T., et al., *Proton NMR Study on Selective Hydration of Anions in Nitrobenzene.* The Journal of Physical Chemistry B, 2000. **104**(50): p. 12021-12027.

Palese, S., et al., *Femtosecond optical Kerr effect studies of water.* The Journal of Physical Chemistry, 1994. **98**(25): p. 6308-6316.

Park, E.S., et al., *Vibrational stark spectroscopy in proteins: A probe and calibration for electrostatic fields.* The Journal of Physical Chemistry B, 1999. **103**(45): p. 9813-9817.

Park, S., K. Kwak, and M.D. Fayer, *Ultrafast 2D-IR vibrational echo spectroscopy: a probe of molecular dynamics.* Laser Physics Letters, 2007. **4**(10): p. 704-718.

Parr, R.G., *Density functional theory of atoms and molecules*, in *Horizons of Quantum Chemistry*. 1980, Springer. p. 5-15.

Pazos, I.M., et al., *Ester Carbonyl Vibration as a Sensitive Probe of Protein Local Electric Field.* Angewandte Chemie International Edition, 2014. **53**(24): p. 6080-6084.

Pedrielli, P., G.F. Pedulli, and L.H. Skibsted, *Antioxidant mechanism of flavonoids. Solvent effect on rate constant for chain-breaking reaction of quercetin and epicatechin in autoxidation of methyl linoleate.* Journal of Agricultural and Food Chemistry, 2001. **49**(6): p. 3034-3040.

Peled, E., *The Electrochemical Behavior of Alkali and Alkaline Earth Metals in Nonaqueous Battery Systems—The Solid Electrolyte Interphase Model.* Journal of The Electrochemical Society, 1979. **126**(12): p. 2047-2051.

Perdew, J.P. and K. Schmidt, *Jacob's ladder of density functional approximations for the exchange-correlation energy.* AIP Conference Proceedings, 2001. **577**(1): p. 1-20.

Perdew, J.P., K. Burke, and M. Ernzerhof, *Generalized Gradient Approximation Made Simple.* Physical Review Letters, 1996. **77**(18): p. 3865-3868.

Petersen, M.K., et al., *Excess proton solvation and delocalization in a hydrophilic pocket of the proton conducting polymer membrane Nafion.* The Journal of Physical Chemistry B, 2005. **109**(9): p. 3727-3730.

Pitzer, K.S., *Potential Energies for Rotation About Single Bonds.* Discussions of the Faraday Society, 1951(10): p. 66-73.

Plimpton, S., *Fast Parallel Algorithms for Short-Range Molecular Dynamics.* Journal of Computational Physics, 1995. **117**(1): p. 1-19.

Pollard, T.P. and T.L. Beck, *Structure and polarization near the Li+ ion in ethylene and propylene carbonates.* The Journal of Chemical Physics, 2017. **147**(16): p. 161710.

Poloczanska, E., et al., *Climate change and Australian marine life.* Oceanography and marine biology, 2007. **45**: p. 407.

Ponnuchamy, V., S. Mossa, and I. Skarmoutsos, *Solvent and Salt Effect on Lithium Ion Solvation and Contact Ion Pair Formation in Organic Carbonates: A Quantum Chemical Perspective.* The Journal of Physical Chemistry C, 2018. **122**(45): p. 25930-25939.

Pörtner, H.-O., *Ecosystem effects of ocean acidification in times of ocean warming: a physiologist's view.* Marine Ecology Progress Series, 2008. **373**: p. 203-217.

Pörtner, H.O., M. Langenbuch, and B. Michaelidis, *Synergistic effects of temperature extremes, hypoxia, and increases in CO2 on marine animals: From Earth history to global change.* Journal of Geophysical Research: Oceans, 2005. **110**(C9).

Postupna, O.O., et al., *Microscopic Structure and Dynamics of LiBF4 Solutions in Cyclic and Linear Carbonates.* The Journal of Physical Chemistry B, 2011. **115**(49): p. 14563-14571.

Quiles, F. and A. Burneau, *Infrared and Raman spectra of alkaline-earth and copper(II) acetates in aqueous solutions.* Vibrational Spectroscopy, 1998. **16**(2): p. 105-117.

Rackley, S.A., *Chapter 12 - Ocean Storage*, in *Carbon Capture and Storage*, S.A. Rackley, Editor. 2010, Butterworth-Heinemann: Boston. p. 267-286.

Rahman, H.M.A., G. Hefter, and R. Buchner, *Hydration of Formate and Acetate Ions by Dielectric Relaxation Spectroscopy.* Journal of Physical Chemistry B, 2012. **116**(1): p. 314-323.

Rais, J., T. Okada, and J. Alexova, *Gibbs energies of transfer of alkali metal cations between mutually saturated water-solvent systems determined from extraction experiments with radiotracer Cs-137.* Journal of Physical Chemistry B, 2006. **110**(16): p. 8432-8440.

Rajagopal, S. and S. Vishveshwara, *Short hydrogen bonds in proteins.* The FEBS Journal, 2005. **272**(8): p. 1819-1832.

Rey, R., K.B. Møller, and J.T. Hynes, *Hydrogen Bond Dynamics in Water and Ultrafast Infrared Spectroscopy.* The Journal of Physical Chemistry A, 2002. **106**(50): p. 11993-11996.

Rezus, Y., D. Madsen, and H. Bakker, *Orientational dynamics of hydrogen-bonded phenol.* The Journal of chemical physics, 2004. **121**(21): p. 10599-10604.

Rezus, Y.L.A. and H.J. Bakker, *On the orientational relaxation of HDO in liquid water.* The Journal of Chemical Physics, 2005. **123**(11): p. 114502.

Riemer, P., *Greenhouse gas mitigation technologies, an overview of the CO2 capture, storage and future activities of the IEA Greenhouse Gas R&D programme.* Energy Conversion and Management, 1996. **37**(6): p. 665-670.

Robinson, R.A. and H.S. Harned, *Some aspects of the thermodynamics of strong electrolytes from electromotive force and vapor pressure measurements.* Chemical Reviews, 1941. **28**(3): p. 419-476.

Rose, D. and I. Benjamin, *Free Energy of Transfer of Hydrated Ion Clusters from Water to an Immiscible Organic Solvent.* Journal of Physical Chemistry B, 2009. **113**(27): p. 9296-9303.

Ruiz-Lopez, M., et al., *Solvent effects on the mechanism and selectivities of asymmetric Diels-Alder reactions.* Journal of the American Chemical Society, 1993. **115**(19): p. 8780-8787.

Sabela, A., et al., *Standard Gibbs energies of transfer of univalent ions from water to 1, 2-dichloroethane.* Electrochimica acta, 1992. **37**(2): p. 231-235.

Samec, Z., V. Mareček, and M.P. Colombini, *Standard Gibbs energies of transfer of alkali metal cations from water to 1, 2-dichloroethane: A critique.* Journal of electroanalytical chemistry and interfacial electrochemistry, 1988. **257**(1-2): p. 147-154.

Sandle, G., *Salt and water absorption in the human colon: a modern appraisal.* Gut, 1998. **43**(2): p. 294-299.

Sanyal, S.K. and S.K. Mandal, *Viscosity B-Coefficients of Alkyl Carboxylates.* Electrochimica Acta, 1983. **28**(12): p. 1875-1876.

Schleicher, K.E. and A. Bradshaw, *A Conductivity Bridge for Measurement of the Salinity of Sea Water1.* ICES Journal of Marine Science, 1956. **22**(1): p. 9-20.

Schuch, N. and F. Verstraete, *Computational complexity of interacting electrons and fundamental limitations of density functional theory.* Nature Physics, 2009. **5**(10): p. 732.

Schweighofer, K.J. and I. Benjamin, *Transfer of Small Ions across the Water/1,2-Dichloroethane Interface.* The Journal of Physical Chemistry, 1995. **99**(24): p. 9974-9985.

Seo, D.M., et al., *Role of Mixed Solvation and Ion Pairing in the Solution Structure of Lithium Ion Battery Electrolytes.* The Journal of Physical Chemistry C, 2015. **119**(25): p. 14038-14046.

Shalit, A., et al., *Terahertz echoes reveal the inhomogeneity of aqueous salt solutions.* Nature Chemistry, 2017. **9**(3): p. 273-278.

Singh, A., *Solvent Effect on the Enthalpy and Entropy of Activation for the Hydrolysis of Ethyl Cinnamate in Mixed Solvent System.* Journal of Phy. Chem. Biophys, 2017. **7**.

Skyner, R., et al., *A review of methods for the calculation of solution free energies and the modelling of systems in solution.* Physical Chemistry Chemical Physics, 2015. **17**(9): p. 6174-6191.

Smith, J.D., R.J. Saykally, and P.L. Geissler, *The Effects of Dissolved Halide Anions on Hydrogen Bonding in Liquid Water.* Journal of the American Chemical Society, 2007. **129**(45): p. 13847-13856.

Smith, J.W., et al., *X-Ray absorption spectroscopy of LiBF 4 in propylene carbonate: a model lithium ion battery electrolyte.* Physical Chemistry Chemical Physics, 2014. **16**(43): p. 23568-23575.

Soetens, J.-C., C. Millot, and B. Maigret, *Molecular Dynamics Simulation of Li+BF4- in Ethylene Carbonate, Propylene Carbonate, and Dimethyl Carbonate Solvents.* The Journal of Physical Chemistry A, 1998. **102**(7): p. 1055-1061.

Soetens, J.-C., et al., *Molecular dynamics simulation and X—ray diffraction studies of ethylene carbonate, propylene carbonate and dimethyl carbonate in liquid phase.* Journal of Molecular Liquids, 2001. **92**(3): p. 201-216.

Sonoda, M.T., et al., *A review on the dynamics of water.* Brazilian Journal of Physics, 2004. **34**(1): p. 3-16.

Steinel, T., et al., *Watching hydrogen bonds break: A transient absorption study of water.* The Journal of Physical Chemistry A, 2004. **108**(50): p. 10957-10964.

Stenger, J., et al., *Coherent response of hydrogen bonds in liquids probed by ultrafast vibrational spectroscopy.* The Journal of Physical Chemistry A, 2001. **105**(13): p. 2929-2932.

Stirnemann, G., et al., *Mechanisms of Acceleration and Retardation of Water Dynamics by Ions.* Journal of the American Chemical Society, 2013. **135**(32): p. 11824-11831.

Stuchebrukhov, A.A., *Mechanisms of proton transfer in proteins: Localized charge transfer versus delocalized soliton transfer.* Physical Review E, 2009. **79**(3): p. 031927.

Sullivan, B.P. and T.J. Meyer, *Kinetics and mechanism of carbon dioxide insertion into a metal-hydride bond. A large solvent effect and an inverse kinetic isotope effect.* Organometallics, 1986. **5**(7): p. 1500-1502.

Tachikawa, H. and S. Abe, *Solvent Stripping Dynamics of Lithium ion solvated by ethylene carbonates: A direct ab-initio molecular (AIMD) Study.* Electrochimica Acta, 2014. **120**: p. 57-64.

Tachikawa, H., *Mechanism of Dissolution of a Lithium Salt in an Electrolytic Solvent in a Lithium Ion Secondary Battery: A Direct Ab Initio Molecular Dynamics (AIMD) Study.* ChemPhysChem, 2014. **15**(8): p. 1604-1610.

Takeuchi, M., et al., *Free-Energy and Structural Analysis of Ion Solvation and Contact Ion-Pair Formation of Li+ with BF4– and PF6– in Water and Carbonate Solvents.* The Journal of Physical Chemistry B, 2012. **116**(22): p. 6476-6487.

Takeuchi, M., et al., *Ion–ion interactions of LiPF6 and LiBF4 in propylene carbonate solutions.* Journal of Molecular Liquids, 2009. **148**(2): p. 99-108.

Tang, Z.-K., J.S. Tse, and L.-M. Liu, *Unusual Li-Ion Transfer Mechanism in Liquid Electrolytes: A First-Principles Study.* The Journal of Physical Chemistry Letters, 2016. **7**(22): p. 4795-4801.

Thämer, M., et al., *Ultrafast 2D IR spectroscopy of the excess proton in liquid water.* Science, 2015. **350**(6256): p. 78-82.

Thogersen, J., et al., *Hydration Dynamics of Aqueous Nitrate.* Journal of Physical Chemistry B, 2013. **117**(12): p. 3376-3388.

Thrane, L., et al., *THz reflection spectroscopy of liquid water.* Chemical Physics Letters, 1995. **240**(4): p. 330-333.

Treble, R.G., K.E. Johnson, and E. Tosh, *The volatilities and conductivities of ionic liquids — GC–MS methodology and preliminary studies of acetic acid – base systems.* Canadian Journal of Chemistry, 2006. **84**(6): p. 915-924.

Turley, C., et al., *Reviewing the impact of increased atmospheric CO2 on oceanic pH and the marine ecosystem.* Avoiding dangerous climate change, 2006. **8**: p. 65-70.

van der Post, S.T. and H.J. Bakker, *The combined effect of cations and anions on the dynamics of water.* Physical Chemistry Chemical Physics, 2012. **14**(18): p. 6280-6288.

vanderSpoel, D. and H.J.C. Berendsen, *Molecular dynamics simulations of leu-enkephalin in water and DMSO.* Biophysical Journal, 1997. **72**(5): p. 2032-2041.

VandeVondele, J., et al., *QUICKSTEP: Fast and accurate density functional calculations using a mixed Gaussian and plane waves approach.* Computer Physics Communications, 2005. **167**(2): p. 103-128.

Vendrell, O., F. Gatti, and H.-D. Meyer, *Full dimensional (15-dimensional) quantum-dynamical simulation of the protonated water dimer. II. Infrared spectrum and vibrational dynamics.* The Journal of Chemical Physics, 2007. **127**(18): p. 184303.

Verlet, L., *Computer "Experiments" on Classical Fluids. I. Thermodynamical Properties of Lennard-Jones Molecules.* Physical Review, 1967. **159**(1): p. 98-103.

von Wald Cresce, A., et al., *Anion Solvation in Carbonate-Based Electrolytes.* The Journal of Physical Chemistry C, 2015. **119**(49): p. 27255-27264.

Vorobyev, D.Y., et al., *Water-Induced Relaxation of a Degenerate Vibration of Guanidinium Using 2D IR Echo Spectroscopy.* Journal of Physical Chemistry B, 2010. **114**(8): p. 2944-2953.

Waegele, M.M., M.J. Tucker, and F. Gai, *5-Cyanotryptophan as an infrared probe of local hydration status of proteins.* Chemical physics letters, 2009. **478**(4-6): p. 249-253.

Waegele, M.M., R.M. Culik, and F. Gai, *Site-specific spectroscopic reporters of the local electric field, hydration, structure, and dynamics of biomolecules.* The journal of physical chemistry letters, 2011. **2**(20): p. 2598-2609.

Walrafen, G., *Raman spectrum of water: transverse and longitudinal acoustic modes below. apprxeq. 300 cm-1 and optic modes above. apprxeq. 300 cm-1.* Journal of physical chemistry, 1990. **94**(6): p. 2237-2239.

Wang, J., et al., *Superconcentrated electrolytes for a high-voltage lithium-ion battery.* Nature communications, 2016. **7**: p. 12032.

Wang, L., et al., *Quantum delocalization of protons in the hydrogen-bond network of an enzyme active site.* Proceedings of the National Academy of Sciences, 2014. **111**(52): p. 18454-18459.

Watanabe, H., et al., *Possible Proton Conduction Mechanism in Pseudo-Protic Ionic Liquids: A Concept of Specific Proton Conduction.* The Journal of Physical Chemistry B, 2019. **123**(29): p. 6244-6252.

Watson, P.E., I.D. Watson, and R.D. Batt, *Total body water volumes for adult males and females estimated from simple anthropometric measurements.* The American Journal of Clinical Nutrition, 1980. **33**(1): p. 27-39.

Wick, C.D. and L.X. Dang, *Molecular Dynamics Study of Ion Transfer and Distribution at the Interface of Water and 1,2-Dichlorethane.* The Journal of Physical Chemistry C, 2008. **112**(3): p. 647-649.

Winstein, S., et al., *Salt effects and ion-pairs in solvolysis1.* Journal of the American chemical society, 1954. **76**(9): p. 2597-2598.

Wolke, C.T., et al., *Spectroscopic snapshots of the proton-transfer mechanism in water.* Science, 2016. **354**(6316): p. 1131-1135.

Woutersen, a., U. Emmerichs, and H. Bakker, *Femtosecond mid-IR pump-probe spectroscopy of liquid water: Evidence for a two-component structure.* Science, 1997. **278**(5338): p. 658-660.

Woutersen, S. and H.J. Bakker, *Hydrogen bond in liquid water as a Brownian oscillator.* Physical review letters, 1999. **83**(10): p. 2077.

Woutersen, S., U. Emmerichs, and H.J. Bakker, *Femtosecond Mid-IR Pump-Probe Spectroscopy of Liquid Water: Evidence for a Two-Component Structure.* Science, 1997. **278**(5338): p. 658.

Xu, J., Y. Zhang, and G.A. Voth, *Infrared Spectrum of the Hydrated Proton in Water.* The Journal of Physical Chemistry Letters, 2011. **2**(2): p. 81-86.

Xu, K., *Electrolytes and interphases in Li-ion batteries and beyond.* Chemical reviews, 2014. **114**(23): p. 11503-11618.

Xu, K., *Nonaqueous Liquid Electrolytes for Lithium-Based Rechargeable Batteries.* Chemical Reviews, 2004. **104**(10): p. 4303-4418.

Xu, W. and C.A. Angell, *Solvent-Free Electrolytes with Aqueous Solution-Like Conductivities.* Science, 2003. **302**(5644): p. 422-425.

Xuan, X., et al., *Vibrational spectroscopic studies on ion solvation of lithium perchlorate in propylene carbonate+ N, N-dimethylformamide mixtures.* Spectrochimica Acta Part A: Molecular and Biomolecular Spectroscopy, 2000. **56**(11): p. 2131-2139.

Yamada, Y. and A. Yamada, *Review—Superconcentrated Electrolytes for Lithium Batteries.* Journal of The Electrochemical Society, 2015. **162**(14): p. A2406-A2423.

Yang, L., A. Xiao, and B.L. Lucht, *Investigation of solvation in lithium ion battery electrolytes by NMR spectroscopy.* Journal of Molecular Liquids, 2010. **154**(2): p. 131-133.

Yoshimura, N., et al., *Electronic States of Acetic Acid in a Binary Mixture of Acetic Acid and 1-Methylimidazole Depend on the Environment.* The Journal of Physical Chemistry B, 2019. **123**(6): p. 1332-1339.

Yoshizawa, M., W. Xu, and C.A. Angell, *Ionic Liquids by Proton Transfer: Vapor Pressure, Conductivity, and the Relevance of ΔpKa from Aqueous Solutions.* Journal of the American Chemical Society, 2003. **125**(50): p. 15411-15419.

Zhang, B., et al., *FTIR spectroscopic studies of lithium tetrafluoroborate in propylene carbonate+diethyl carbonate mixtures.* Spectrochimica Acta, Part A, 2014. **122**: p. 59-64.

Zhang, Y.J. and P.S. Cremer, *Interactions between macromolecules and ions: the Hofmeister series.* Current Opinion in Chemical Biology, 2006. **10**(6): p. 658-663.

Zheng, J.R., et al., *Ultrafast carbon-carbon single-bond rotational isomerization in room-temperature solution.* Science, 2006. **313**(5795): p. 1951-1955.

Zimmermann, J., et al., *Cyano groups as probes of protein microenvironments and dynamics.* Angewandte Chemie International Edition, 2011. **50**(36): p. 8333-8337.

# VITA

Xiaoliu Zhang finished her undergraduate study and obtained the Bachelor of Science degree in the major of Analytical Chemistry from the University of Science and Technology of China in 2014. The same year, she came to Louisiana State University to pursue a doctorate degree under the guidance of Dr. Daniel Kuroda in physical chemistry. She anticipates graduating in summer of 2020.